Exploring methods for imaging dynamics in transmission electron microscopy

Raymond James Lamb

Submitted in fulfilment of the requirements for the
Degree of Doctor of Philosophy

School of Physics and Astronomy
College of Science and Engineering
University of Glasgow

September 2017

Abstract

Transmission electron microscopy (TEM) has enabled investigation of materials at atomic resolution and magnetic contrast in the nanometre regime. Progress in spherical aberration correction continues to push the limits of spatial resolution for this instrument and provides researchers unique methods of investigation in the area of materials physics. The drive towards realising nano devices requires both the spatial resolution to observe the system and the temporal resolution to understand how the system evolves in response to stimuli. The time resolution of TEM has classically been limited by both the number of electrons used to image and the noise generated by the imaging devices. In this thesis we explore methods of accessing time-resolved information from a JEOL ARM200cF - "MagTEM" through use of the active pixel sensor (APS) detector Medipix3 capable of single electron counting and noise-free readout. Investigations into both single-shot imaging and stroboscopic imaging are performed to assess the potential of time resolved imaging of dynamics processes in TEM.

Chapter 1 introduces the magnetic theory used to support the understanding of the magnetic dynamics imaged as part of this thesis. Starting with the individual magnetic energy terms contributing to the formation of magnetic ordering such as ferromagnetism we introduce how the competition between these terms results in the formation of magnetic structure. Magnetic domain walls are discussed with reference to both field-driven and current-driven dynamics. Finally, the anti-symmetric exchange term known as the Dzyaloshinskii-Moriya interaction (DMI) is introduced in order to discuss the magnetic skyrmion, which is a prominent feature of both chapters 3 and 4.

In chapter 2 we introduce the instrumentation used to both image and fabricate

samples used in the thesis with focus on TEM. The TEM is discussed section by section from the column components and lenses through imaging modes both structural and magnetic finishing with a broad overview of detector technology and the role of the APS Medipix3 within that field. Three primary methods of sample fabrication were used in this thesis; electron beam lithography (EBL), thin film metal deposition and focused ion beam (FIB) lithography which are discussed in turn, specifically their role in producing electron transparent specimens.

Chapter 3 presents the results of a detailed study into the magnetic dynamics of Cu_2OSeO_3 during a field induced phase transition between the helical and skyrmion phase using the Medipix3 camera. This experiment provided a system with dynamics in the low millisecond time-regime that would be difficult to resolve with a charge-coupled device (CCD) camera due to noise, therefore providing an ideal experiment to demonstrate the advantages of the Medipix3 detector and the limits of single-shot imaging. The chapter opens with a presentation of the quality of individual images captured during 10ms exposure imaging and presents a method of displaying the evolution of the magnetic state of the sample in time in a single figure termed a 'time-evolution profile'. Next, the specific dynamics present in the image stack are then investigated chronologically. First, evidence is presented of the appearance of isolated skyrmion-like meta-stable objects ahead of the skyrmion lattice during the phase transition. Second, the resolution of individual skyrmion positions on a frame-by-frame basis is processed into vector maps providing insight into the collective motion of skyrmions within the lattice. Finally, during rotation of the skyrmion lattice we observe formation of multi-domain skyrmion states in which 5-7 defects are present along the domain boundary. Analysis is performed on sequentially recorded frames containing 5-7 defects to investigate the mechanism of domain boundary motion during lattice rotation.

Continuing the investigation of single shot imaging of skyrmion lattice dynamics in chapter 4, we investigate high angle skyrmion lattice domain boundaries in the near room temperature helical material FeGe. The chapter starts with an investigation into the nucleation of the lattice boundaries and the effect of magnetic disorder in the helical state

prior to a field induced transition to the skyrmion phase. Imaging of the high angle domain boundary reveals the presence of a bi-stable defect moving between two positions. The defect appears to contain a paired skyrmion system changing position within a set of four neighbouring skyrmions along a single lattice vector. 2D Gaussian fitting is performed using the program Atomap to aid in the identification of the defect position and is processed using an Arrhenius law method to give an estimate of the energy barrier between the defect positions. The capability of the Medipix3 to correctly identify between defect positions enables construction of composite images with total exposure durations longer than the mean lifetime of the dynamic process. Finally, the frame-by-frame motion of the skyrmions during transition between defect sites is analysed to determine the effect of reorientation on the surrounding skyrmions.

In chapter 5 we investigate the potential of the Medipix3 detector to access sub-microsecond resolution stroboscopic imaging through evaluation of the time contribution of physical processes involved in the registering of a single electron count. The hardware of the Medipix3 is discussed with predictions of the temporal responses of key components such as the charge sensitive amplifier (CSA) and comparator followed by an investigation into the effect of charge sharing between pixels on this time response. In order to demonstrate the time resolution we characterise a simulated reproducible dynamic process by oscillating a 60keV electron beam using electrostatic deflection plates. Using this benchmark, the ultimate time resolution of the Medipix3 is determined for both single pixel mode (SPM) and charge summing mode (CSM).

The methodology for time resolved stroboscopic imaging developed in chapter 5 is applied to the real magnetic system FeRh during a temperature induced phase transition from anti-ferromagnetic to ferromagnetic in chapter 6. In this experiment the magnetic moment of a FeRh sample is investigated through small angle electron scattering in response to being heated using a DENSsolutions MEMS-based Wildfire heating chip. Initially static temperature images were taken using a Gatan Orius CCD camera before moving onto imaging the dynamic magnetic transition in response to a pulsed voltage source. Imaging is performed both in single-shot (1ms minimum) and stroboscopically (10μm minimum)

to demonstrate the applied limits of these methods. This experiment provides a method of investigating the thermal timescales at which in-situ thermal transitions can be driven using resistive heating.

Finally, chapter 7 contains a summary of the findings from results chapters 3 to 6 with a focus on the implication for time revolved TEM and the possible future work accessible using the developed methods.

Declaration

This thesis is a record of the work carried out by myself in the Department of Physics and Astronomy at the University of Glasgow during the period September 2013 - September 2017. The work described herein is my own apart from:

Access to Cu_2OSeO_3 material used in chapter 3 provided by Henrik M. Rønnow from École Polytechnique Fédérale de Lausanne. The modified skyrmion finding program used in chapter 3 was originally developed by Dr Rajeswari Jayaraman from the Lumes group, École Polytechnique Fédérale de Lausanne

Access to FeGe material used in chapter 4 was provided by the groups of Dr Yoshihiko Togawa of Osaka Prefecture University and Dr Yusuke Kousaka with students in Inoue (Katsuya) laboratory. The original program Atomap, modified to perform 2D Gaussian skyrmion finding in chapter 4, section 4.5 was originally developed by Dr Magnus Nord from the University of Glasgow.

The code written to perform temporal analysis on long exposure beam oscillation images in chapter 5, section 5.3 was provided by Dr Gary Paterson from the University of Glasgow.

Access to FeRh material used in chapter 6 was provided by Professor Christopher H. Marrows from the University of Leeds. The preparation of FeRh samples on DENSsolutions Wildfire chips from chapter 6 was performed by Dr Trevor Almeida from the University of Glasgow.

Some of the work presented in this thesis is also presented in the following papers:

1. **Imaging and controlling plasmonic interference fields at buried interfaces**
   Tom T. A. Lummen, Raymond J. Lamb, Gabriele Berruto, Thomas LaGrange, Luca

Dal Negro, F. Javier García de Abajo, Damien McGrouther, B. Barwick, and F. Carbone. Nature Communications, 7 (2016).

2. **Ultrafast imaging of plasmons in a transmission electron microscope,** Tom T. A. Lummen, Gabriele Berruto, Andrea Toma, Raymond J. Lamb, Damien McGrouther, and Fabrizio Carbone. International Society for Optics and Photonics, 9746 (2016).

This thesis has not previously been submitted for a higher degree.

Contents

[1] Skyrmion finding code adapted from the program 'Atomap', developed by Dr Magnus Nord, School of Physics & Astronomy, University of Glasgow

[2] Analysis performed by Dr Gary Paterson, Department of Physics & Astronomy, University of Glasgow

[3]Sample fabrication performed by Dr Trevor Almeida, Department of Physics & Astronomy, University of Glasgow

List of Figures

Nomenclature

AFM Anti-Ferromagnetic

APS Active pixel sensor

BELLE Beamwriter exposure layout for lithographic engineers

CCD Charge-coupled device

CFEG Cold field emission gun

CSA Charge sensitive amplifier

CSM Charge Summing Mode

DMI Dzyaloshinskii-Moriya interaction

DPC Differential phase contrast

DQE Detective quantum efficiency

DTEM Dynamic transmission electron microscopy

EBL Electron beam lithography

EPFL Ecole Polytechnique Fédérale de Lausanne

FEG Field emission gun

FFT Fast Fourier transform

FIB Focused ion beam

FM Ferromagnetic

FMR Ferromagnetic resonance

FWHM Full width at half maximum

IFFT Inverse fast Fourier transform

MAPS Monolithic active pixel sensors

MEMS Micro-electrical-mechanical system

MOKE Magneto-optical Kerr effect

MOS Metal-oxide semiconductor

MTF Modulation transfer function

PDF Probability distribution function

PEEM Photo-emission electron microscopy

PID Proportional–integral–derivative

PMT Photo multiplier tube

PSF Point spread function

PVD Physical vapour deposition

ROI Region of interest

SAES Small angle electron scattering

SNR Signal-to-noise ratio

SPM Single pixel mode

STEM Scanning transmission electron microscopy

TEM Transmission electron microscope

TEP Time evolution profile

XMCD X-ray magnetic circular dichroism

XRD X-ray diffraction

YAG Yttrium-aluminium garnet

List of Symbols

E	Total energy
E_{EX}	Exchange energy
E_{D}	Magnetostatic energy
E_{H}	Zeeman energy
E_{K}	Anisotropy energy
E_{λ}	Magnetostriction energy
S	Spin vector
J	Heisenberg exchange integral
H_{D}	Demagnetising field
H_{EX}	Externally applied field
M	Magnetic moment direction
μ_0	Vacuum permeability
M_{s}	Magnetic moment direction
T_{c}	Curie temperature
E_{DM}	DMI Energy
D	DMI vector
λ_H	Helical period

n	Topological number
T_{H}	Helical ordering Temperature
λ	Wavelength
λ_{e}	Electron Wavelength
h	Planks length
m_{e}	Electron mass
eV	Electron volt
c	Speed of light
J_{e}	Emission current density
A_{G}	Richardson constant
W	Work function
k	Boltzmann constant
e	Electron charge
B	Magnetic field
σ	Scattering cross section
p	Probability of electron scattering
N_{o}	Avogadro's constant
ρ	Density
t	Thickness
A	Atomic weight
λ_{fp}	Electron mean free path
β_{L}	Angle of electron deflection

ϕ	Phase shift
N	Enclosed magnetic flux
Δ	Defocus distance
K_{I}	Beam centre displacement
K_{α}	Beam radius
S	Signal
N	Noise
f	frequency
f_{Nyquist}	Nyquist frequency
λ_s	Inter-skyrmion distance
τ	State lifetime
f_0	Attempt frequency
E_a	Energy Barrier
$TH0$	Medipix3 pixel energy threshold
E_0	Electron energy upon arrival at detector
τ_{Rise}	Time constant of beam deflection
τ_{Fall}	Time constant of beam return from deflection
I_x	Beam intensity at x fraction of maximum during oscillation
$I_{Deflected}$	Beam intensity during deflection
$I_{Undeflected}$	Beam intensity during return from deflection
Δ_t	Transition duration between deflection states
T_t	AFM to FM transition temperature

Ψ_0	Electron wave function (Emitted)
Ψ_I	Electron wave function (Incident to sample)
Ψ_T	Electron wave function (Transmitted)

Chapter 1

Ferromagnetism and magnetic topology in thin ferromagnetic films

1.1 Introduction

Properties such as paramagnetism, ferromagnetism (FM), anti-ferromagnetism (AFM) and ferrimagnetism are all caused by electron wave-function interaction. In studies of magnetic materials it is important to consider that in the periodic table only three elements, iron, nickel and cobalt, exhibit ferromagnetic properties at room temperature. Therefore, the mechanism that causes ferromagnetism is an important starting point for any investigation into magnetism.

In a quantum mechanical model of an atom, each atomic shell state can be filled by up to two electrons with opposite spins according to the Pauli exclusion principle. When both states are filled the opposing magnetic moments of up and down spin states cancel so that there is no net magnetic moment. Exchange splitting in the spin up and down bands allows an imbalance of spin up and spin down electrons as the lowest energy states must be filled regardless of orientation. In the cases of iron, nickel and cobalt, unpaired electrons in the 3d sub-shell cause a net magnetic moment per atom [8]. The magnetic moment of an atom can be thought of as a tiny dipole with its own magnetic field. In ferromagnetic materials the magnetic moments align in an energetically preferable state. The net moment of the

sum of the magnetic moments from the atoms gives rise to the material's magnetic field. However, this picture of the local moment is not adequate to describe metals which have de-localised electrons. The band theory of ferromagnetism attempts to explain this and is an extension of the band theory of paramagnetism with the addition of exchange coupling between electrons. This theory was first proposed by Stoner in 1933 [9]. The energy band structure is a consequence of the overlap of atoms' atomic orbitals in crystal structures. An individual energy band refers to the energy an electron may have when in that solid, with band gaps covering a range of energies that are forbidden. In the specific case of the three ferromagnetic metals, a combination of narrow band widths and a large density of states leads to spontaneous splitting where it is energetically preferable for the population of the spin up and spin down bands to spontaneously split.

1.2 Magnetic energy terms

The energy contributing to a magnetic system is the sum of a number of separate energy terms which are affected by separate stimuli, however collectively give rise to the formation of magnetic structure within the specimen. This magnetic structure includes domain walls, topological structures such as skyrmions and magnetic transitions such as transformation between magnetic states. The total energy in the system E is the sum of: the exchange energy E_{EX} which attempts to align neighbouring spins parallel and is primarily responsible for ferromagnetism; the magnetostatic energy E_{D} which is the increase of magnetic charge on specimen surface and partially responsible for the splitting of large uniform magnetic regions into domains; the Zeeman energy E_{H} which causes the magnetic moments to tend to align with a magnetic field; the anisotropy energy E_{K} which causes the magnetic moment to align preferentially with the easy axis of a the material; and finally the magnetostriction energy E_{λ} which is influenced by the modification of the inter-atomic distance due to strain. The sum of these terms is given in equation 1.1. The magnetic system will naturally tend to minimise this number often giving rise the the aforementioned magnetic structure or magnetic dynamics. In the following sections each of these energy terms will be discussed

in detail.

$$E = E_{EX} + E_D + E_H + E_K + E_\lambda \tag{1.1}$$

1.2.1 Exchange energy

The first term, exchange energy E_{EX} is caused by the electron-electron correlation interaction and is primarily responsible for magnetic order in a material. In ferromagnetic materials the exchange interaction leads to parallel alignment of electron spin moments on adjacent atoms causing uniform magnetisation at a mesoscopic level. The exchange energy between two adjacent electrons with spins a and b is given by the dot product of the two vectors given in equation 1.2

$$E_{EX} = -2J_{ab} \cdot (\vec{S_a} \cdot \vec{S_b}) \tag{1.2}$$

where J is the Heisenberg exchange integral, which includes the magnitude and sign of the bonding interaction. $J > 0$ gives a preference to parallel alignment of spins which is the determining factor in ferromagnetism. Similarly $J < 0$ gives an anti-parallel preference and which gives rise to anti-ferromagnetism. The range of the exchange interaction is small and generally only extends as far as adjacent atoms, therefore in atomic systems the exchange energy contribution for an individual atom is given as the sum of the individual exchange interactions of nearest neighbours. The Heisenberg exchange described only explains the existence of ferromagnetism where the electrons are confined to their host atom, hence constituting a local moment. In metals, the valence electrons are delocalised and form bands. For some elements the 3d band (Co,Fe,Ni) can become non-degenerate in energy depending on the electron spin orientation and hence a permanent ferromagnetic moment is supported. This is also relatively common for the rare earth metals where 4f electrons are involved.

1.2.2 Magnetostatic energy

The second term E_{D}, is magnetostatic energy, this is a result of mesoscopic alignment of spin in ferromagnetism and is caused by the build-up of magnetic charge on the surface

areas of a material causing a diverging magnetic field. The generated field outside of the material is called the stray field and the internal field is called the demagnetisation field. The total magnetostatic field can be calculated as the sum of the integral of the magnetic volume charge and the integral of the magnetic surface charge shown in equation 1.3

$$\vec{H_{\mathrm{D}}} = -\frac{1}{4\pi}\int_V \nabla \cdot \vec{M}\frac{r}{r^3}\, dV \tag{1.3}$$

where $\vec{H_{\mathrm{D}}}$ is the demagnetising field. The magnetostatic energy, E_{D}, can then be calculated by integrating this over all space as shown in equation 1.4.

$$E_D = -\frac{\mu_0}{2}\int_V \vec{M} \cdot \vec{H}_D\, dV \tag{1.4}$$

Magnetostatic energy is reduced by a material splitting its magnetisation into regions (domains) of opposite magnetisation orientation causing alternating build-up of positive and negative charge at the surfaces of the material. This causes the total stray field to be decreased for a small increase in exchange energy as shown in figure 1.1. Figure 1.1A shows a uniformly magnetised material with large stray fields, figures 1.1B&C show the reduced stray field contribution due to the multi-domain states and figure 1.1D shows a landau flux close state with minimised stray field.

The magnetostatic energy gives rise to an apparent shape anisotropy which is caused by the non-uniform separation of magnetostatic charge in a non-symmetrical object. A large distance between the separated charges under an applied magnetic field causes a smaller energy contribution than separating charges that are closer to each other. Therefore in a rectangular material a magnetic field applied along its long axis would have a smaller anisotropy energy than if the same magnetic field was applied perpendicular.

1.2.3 Zeeman energy

The third term E_H is Zeeman energy caused by the interaction between a material and a magnetic field. The individual magnetic moments in a material seek to align parallel to the field to minimise energy. The magnetic orientation of the material with respect to the magnetic field causes either a positive or negative contribution by the Zeeman energy to

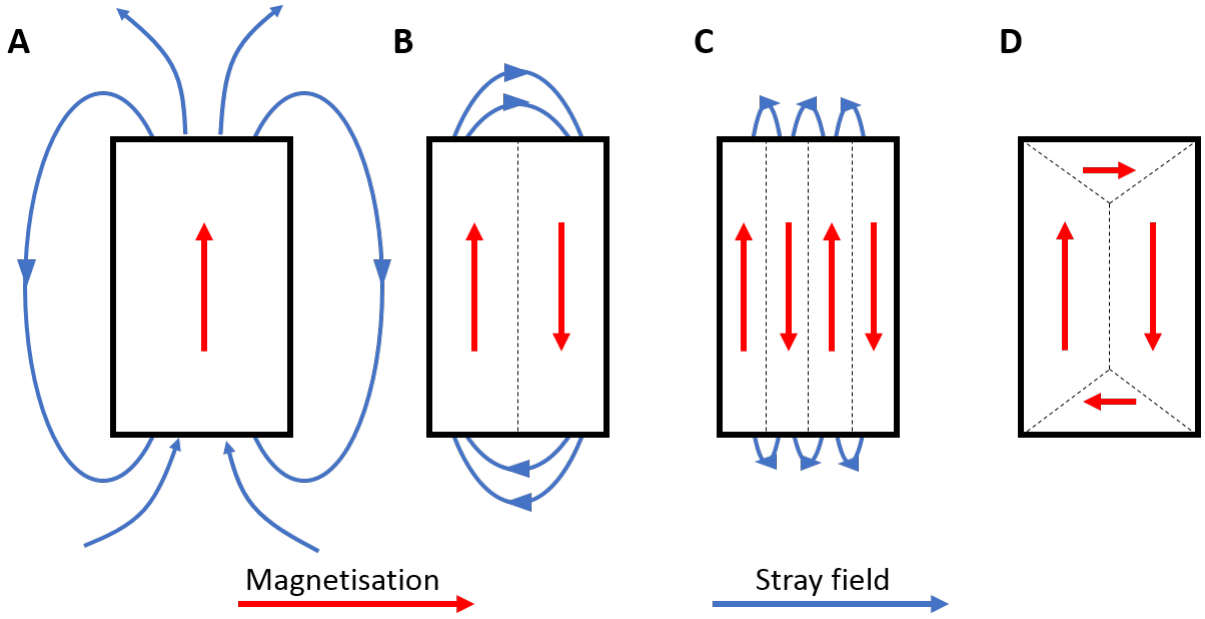

Figure 1.1: The process of reducing demagnetisation field by splitting regions of uniform magnetisation into smaller regions with different magnetisation directions.

the total energy. The total contribution of Zeeman energy to the system is given by:

$$E_H = -\mu_0 M_s \int \vec{H_{EX}} \cdot \vec{m}\ dV \tag{1.5}$$

where μ_0 is the permeability of free space, M_s is the material's saturation magnetisation (detailed below), H_{EX} is the external field, and $\vec{m}$ is the unit vector in the direction of the magnetisation which is integrated over the volume of the material.

Saturation magnetisation is the strength of applied field sufficient to cause all magnetic moments in a material to orientate uniformly. As a magnetic field is applied to a ferromagnetic material individual atoms change their magnetic orientation until the material reaches the point of saturation.

1.2.4 Magnetocrystalline anisotropy energy

The fourth term E_K is magnetocrystalline anisotropy energy, this contributes a directionally dependent energy term that is linked to the atomic ordering within a material. Magnetocrystalline anisotropy is predominantly caused by spin-orbit coupling which is

the interaction between the spin of an atom and the electrostatic field created by atomic ordering in a crystal structure. Due to the inter atomic spacing along crystallographic directions varying with the crystal structure geometry, the spin of an individual atom will have a lower energy contribution when aligning with specific directions called the 'easy axis'. Similarly, the directions in which the spin would contribute the largest amount of energy are referred to as the 'hard axis'. The easy and hard axis frequently lie along directions commonly lie along crystallographic axes of symmetry however intrinsic factors can contribute to this.

1.2.5 Magnetostriction energy

The final term E_λ is Magnetostriction which is the expansion/contraction of a material due to a magnetic field. The materials investigated in this project do not exhibit significant magnetostrictive properties and therefore this term will largely be ignored.

1.3 Magnetic Domains

A magnetic domain is a region within a magnetic material which has uniform magnetisation so that the magnetic moments of each atom are aligned with one another. When cooled below a temperature called the Curie temperature T_c, the magnetisation of a piece of ferromagnetic material spontaneously divides into many small regions called magnetic domains. This behaviour of spontaneous division originates from internal energy minimisation. In the previous section magnetostatic energy was shown to be minimised when regions of opposite magnetisation were aligned. When a domain wall is split the resulting smaller parallel domains cause smaller amounts of field outside the material. This would suggest that infinitely splitting the domains would minimise energy, however, there is competition with the Heisenberg exchange energy which in the case of a ferromagnet attempts to align the material spins. Therefore the stability of a domain is a balancing of these two energy terms.

1.4 Magnetic domain walls

The transition region between two adjacent domains is called a domain wall. Two domain wall structures to discuss are the Bloch wall and Néel wall. The difference between the two domain wall structures is the plane in which the magnetisation rotates in the transition between the two domains as shown in figure 1.2 [8, 10].

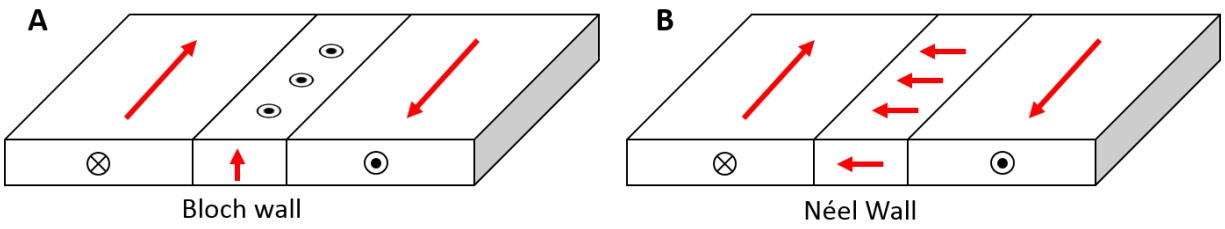

Figure 1.2: A diagram showing the magnetisation orientation of both Néel and Bloch walls

The interaction of the Bloch domain walls with the surface causes an area of high magnetostatic energy because of the high incident surface charge. In bulk magnetic materials the ratio of surface area to volume causes Bloch type domain walls to be energetically preferable. Magnetic thin films would gain a significant magnetostatic component from Bloch walls, however, the parallel direction in magnetism of the Néel wall type gives a much smaller magnetostatic contribution, and therefore in thin films Néel walls are often favourable.

Patterning of thin film material can allow for investigation into the properties of domain walls in confined geometries. In particular nanowire structures receive significant attention due to the complex interactions between the wire boundaries, shape and features artificially inserted into the wire. In planar nanowires domain walls have distinct classes of structure each with unique magnetic properties. The domain wall itself has a finite size and shape which is dependent on the intrinsic properties of the material and its geometry. The structure of a domain wall forming in a magnetic nanowire can be directly related to the wire geometry shown by the phase diagram in figure 1.3.

The two key structures at this scale of nanowire are transverse and vortex walls. Transverse walls are prominent at smaller length scales as the magnetostatic energy present

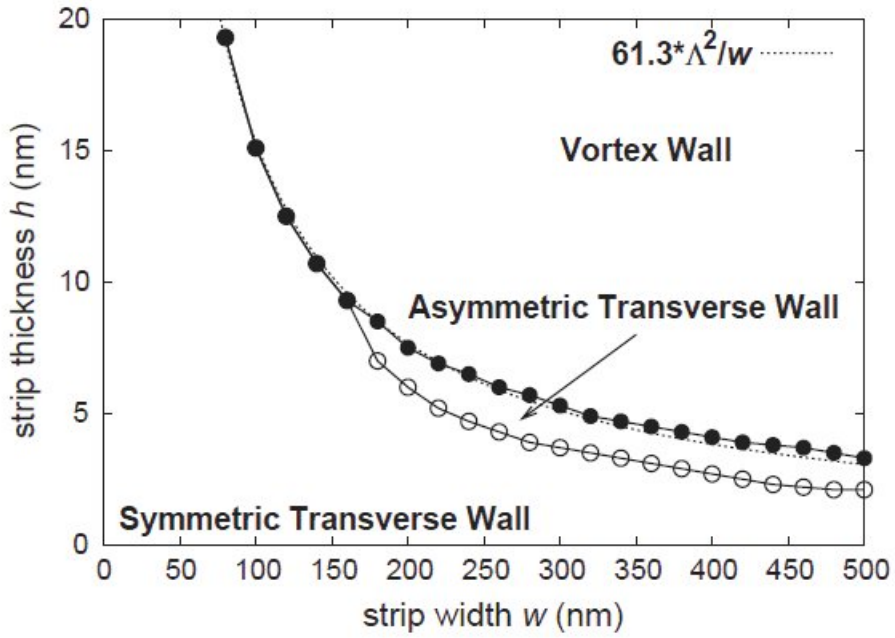

Figure 1.3: A diagram showing the effect of wire geometry on the formation of three common domain wall types. Image reproduced with permission of the rights holder, Elsevier [1].

in the smaller material component is not enough to overcome the exchange energy thus giving transverse walls a high stray field region. Vortex domains however minimise the magnetostatic energy by forming a closed loop, however this does cause an out-of-plane stray field from a point known as the vortex core. Both cases can additionally be classified by the direction of the domains which the domain wall separates. Where the domains point towards the domain wall, the term head-to-head is often used and conversely, when pointing away from the domain wall, tail-to-tail. Examples of head-to-head vortex and transverse domain walls are shown in figure 1.4.

1.5 Domain wall motion

In the previous section, a domain wall is considered to be a stationary quasi-particle. In practice this equilibrium state can be disrupted by the application of magnetic fields causing modification to the domain wall shape and motion. The fundamental mechanisms

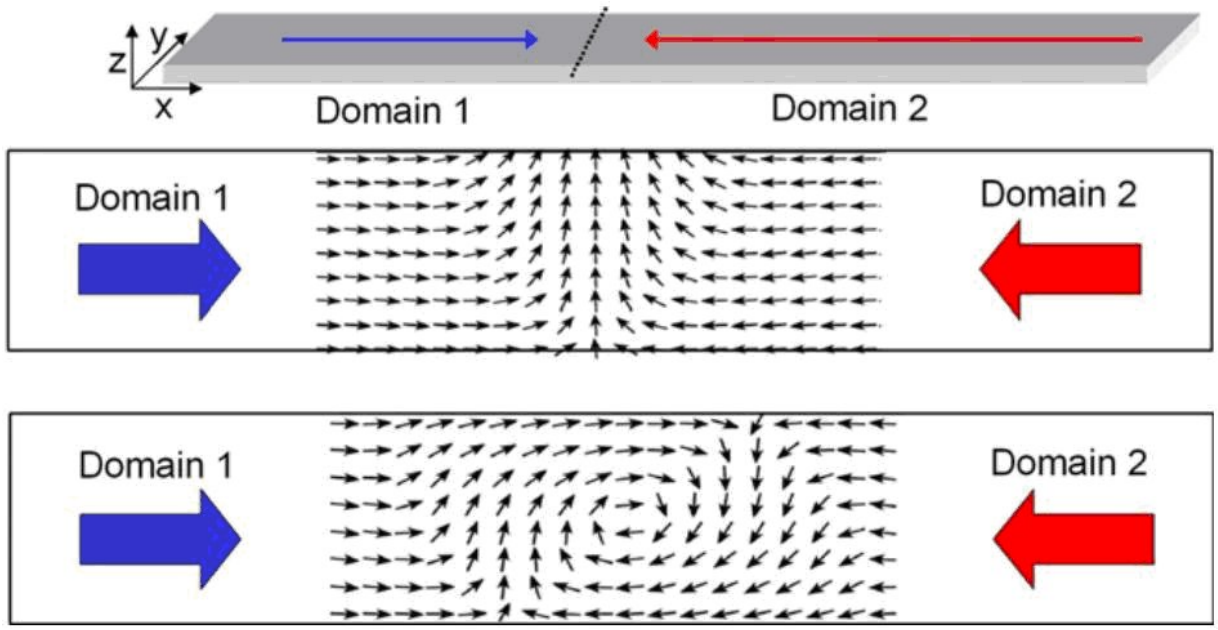

Figure 1.4: A figure showing the internal magnetic structure of a head-to-head transverse domain wall (Top) and a head-to-head vortex domain wall (Bottom). Image reproduced with permission of the rights holder, Taylor & Francis [2].

that cause field-induced domain wall motion are important in producing future spintronic devices.

Domain wall motion induced by magnetic fields is caused by unbalancing the magnetostatic and exchange energy terms. If a field is applied to a domain wall, the magnetic moments at the side of the domain which have opposite orientation to the field are rotated which causes the domain wall as a whole to appear to move with a translational motion. This process is theoretically reversible and changing the direction of the applied magnetic field should cause an opposite domain wall shift. This assumes that there is a uniform potential energy landscape. An energetically preferable location for a domain wall such as a notch or patch of edge roughness at a boundary is called a pinning site. A magnetic field applied to a domain wall at a pinning site will cause domain wall motion only once the required depinning field strength is reached where the pinning site geometry plays an important role on this value. Below this depinning field strength there is a deformation of the domain wall however once the field is removed the domain wall returns to its minimum

energy configuration.

The dynamic evolution of a domain wall and the domain wall velocity are proportional to the applied magnetic field. In a paper by Walker and Schryder the dynamics of a 180° domain wall is modelled for a one dimensional system [11]. This describes three regimes of motion. At low fields there is a linear relationship between applied field and domain wall velocity, this continues up to a point known as the Walker limit. The Walker limit is characterised by an abrupt reduction in the domain wall mobility at a specific applied current or field. The breakdown is predicted to occur due to canting in the plane of the domain wall causing procession and oscillation between domain wall types [12]. Specifically changing into a domain wall of opposite chirality [13]. Finally, if the magnetic field is far above the Walker field the relationship between velocity and field once again becomes linear, however, with a significantly reduced mobility. This three regime model can be seen in figure 1.5.

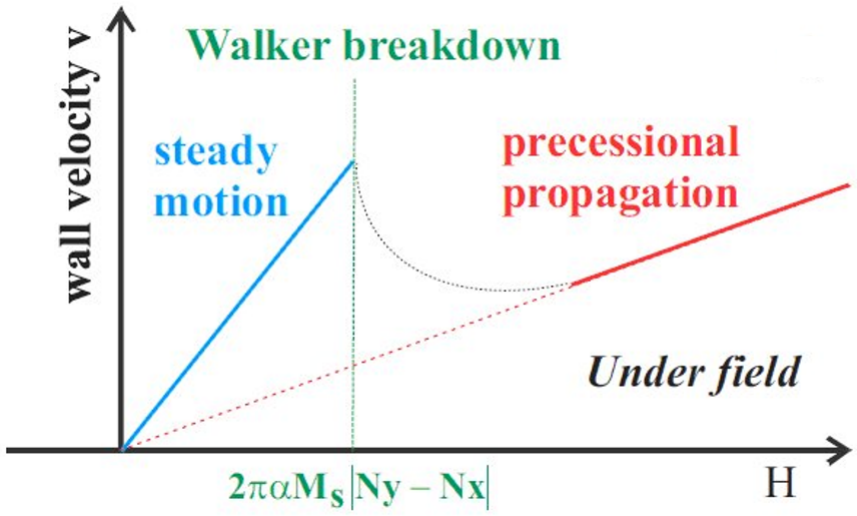

Figure 1.5: The Walker Breakdown walker limit illustrated under magnetic field. The image shows the transition between smooth propagation at low field values and turbulent propagation at large field values highlighting the decease in propagation velocity during the transition. Image reproduced with permission of the rights holder, EPL Letters [3]

The speed of domain wall propagation of up to hundreds of meters per second limits

the possibility of directly imaging this post breakdown propagation. However, indirect evidence from the pinning of a domain wall at a defined length along a wire has been shown to produce repeatable results [14].

1.6 Dzyaloshinskii–Moriya interaction

The exchange energy included in the energy terms presented in section 1.2 refers to only one part of the spin-exchange interaction. The spin-exchange interaction actually contains both a symmetric and anti-symmetric component where the anti-symmetric component is now known as the Dzyaloshinskii–Moriya interaction (DMI) [15, 16]. Whereas the symmetric exchange term prefers that neighbouring spins align parallel to one another, DMI prefers there to be some canting, where the spins are non-parallel. DMI originates from the spin orbit coupling between two neighbouring magnetic atoms and a third non-magnetic atom. The third atom causes the two neighbouring spins to favour aligning anti-parallel through the super-exchange mechanism in which the balanced spins of the third atom pair separately to the magnetic atoms causing indirect exchange. In many systems the DMI component may cancel to zero where the atomic arrangement is symmetric providing opposing energy contributions, this arrangement is said to have inversion symmetry. The impact of atomic geometry in DMI gives rise to two distinct cases - bulk DMI and interfacial DMI. Interfacial DMI is caused by the difference in atomic ordering between layers at a material interface. The discontinuity between materials causes DMI to be asymmetric and a net energy contribution to be observable especially where very thin layers are used [17]. In the majority of bulk materials the net DMI effect sums to zero due to inversion symmetry. However, some materials with broken space inversion symmetry have an inherent magnetic chirality such as those in the B20 crystal group. These chiral materials such as MnSi [18, 19], $Fe_{0.5}Co_{0.5}Si$ [20, 21] and FeGe [22] exhibit mesoscopic magnetic ordering due to the DMI effect [23, 24]. Bulk DMI contributions have been found in other non B20 materials such as Cu_2OSeO_3 with a $P2_13$ space group [25] and GaV_4S_8 with a R3m space group [26].

The DMI energy contribution to the system between a pair of adjacent spins is given

by equation 1.6:

$$E_{DM} = -2D_{ab} \cdot (\vec{S_a} \times \vec{S_b}) \tag{1.6}$$

where E_{DM} is the DMI energy, D_{ab} is the DMI vector, $\vec{S_a}$ and $\vec{S_b}$ are the spin vectors associated with atoms a and b respectively.

The competition between both the symmetric (exchange) and anti-symmetric (DMI) energies causes neighbouring spins to favour a canting angle between them with the magnitude of the angle related to the ratio of the two energies. This is shown in figure 1.6 in which a ferromagnetic system with zero DMI aligns spins parallel to one another and a system with non-zero DMI is canted to minimise energy, where the cross product of the two spins gives $E_{\mathrm{DM}} = E_{\mathrm{EX}}$ in equilibrium.

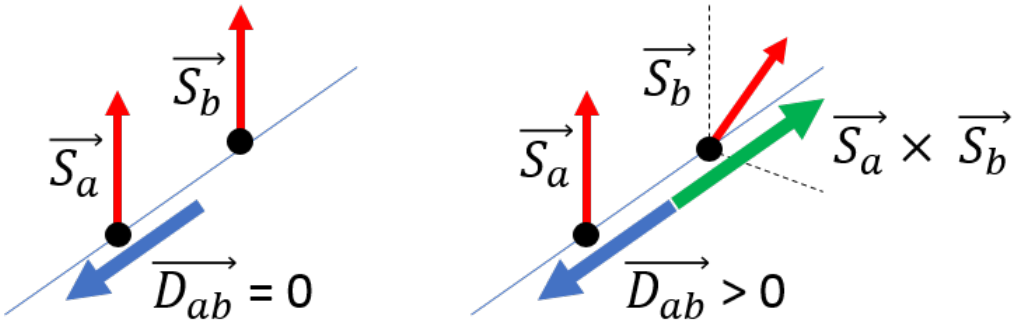

Figure 1.6: An example of neighbouring spins with both no DMI interaction in which the spins align parallel and DMI causing canting of neighbouring spins shown as a product of the two spins

The DMI has also been shown to change the profile of a domain wall with the application of an in-plane field potentially changing the domain wall dynamics [27]. There is also evidence that its effect can also be seen in domain tilting at the edges of nanowires which can lead to significantly altered domain wall dynamics including the Walker breakdown velocity [28].

Helical magnets exhibit magnetic ordering below a critical temperature $\mathrm{T_c}$. The helical phase emerges where the repeated canting of neighbouring spins form a magnetic helical spin texture aligned to a single $\vec{k}$-vector as shown in figure 1.7A where the helical spacing

λ is determined by the magnitude of the canting between neighbouring spins. Figure 1.7B shows a comparison of a second magnetic texture, the conical phase. The application of an applied field along the $\vec{k}$-vector of the helix causes the spin ordering to cant into the plane of the $\vec{k}$-vector in order to minimise the Zeeman energy contribution.

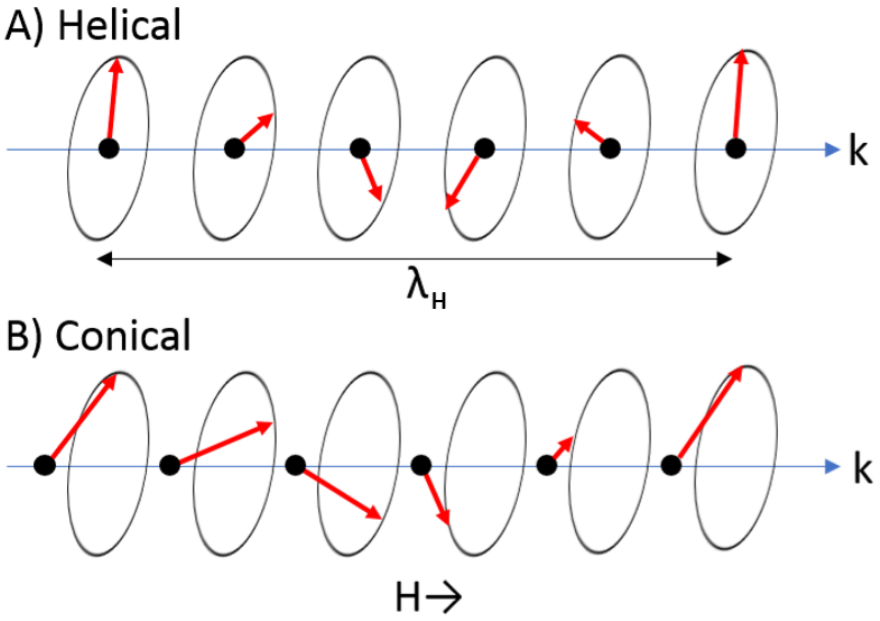

Figure 1.7: The magnetic ordering of the helical and conical phases along a single $\vec{k}$-vector. Figure A shows the rotation over one helical spacing λ_H. Figure B shows the conical phase as a result of applied field H, along the $\vec{k}$-vector.

1.7 Magnetic skyrmions

The origin of the term skyrmion comes from a particle theory paper by Tony Skyrme, a skyrmion is used to model a hypothetical particle which consists of a quantum superposition of baryons and resonance states as a topological soliton [29]. Due to the description as a topological soliton the term skyrmion has recently been used to describe a 3D magnetic state in which magnetic moments orientate out of a singularity referred to as the Bloch point. Magnetic skyrmions are a type of magnetic quasi-particle in which the magnetic

moments form a structure stabilised by its own topology. Skyrmions can be thought of as 2D domain walls with a 360° rotation with the domain wall forming a continuous twist around the central domain. Similar to magnetic domains, this magnetic twist exhibits two common structural forms: the Bloch skyrmion and the Néel skyrmion. Figure 1.8 shows the structure both Néel and Bloch skyrmions in the form of magnetic moment arrows. Figure 1.8A shows a Néel skyrmion, during rotation the spin lies in plane orthogonal to the central spin of the skyrmion in a similar manner to a Néel domain wall. This type of skyrmion is also referred to as a spiral skyrmion. Figure 1.8B shows a Bloch skyrmion, during rotation the spin lies in plane pointing inwards to the central spin of the skyrmion, like a Bloch domain wall. This type of skyrmion is also referred to as a hedgehog skyrmion.

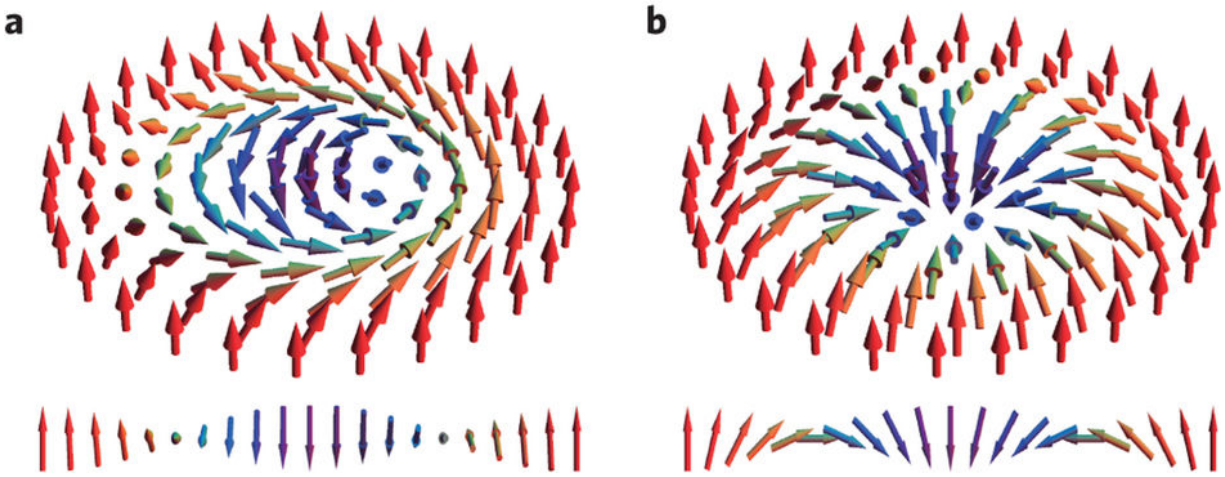

Figure 1.8: Skyrmions with the Néel form in figure A and with the Bloch form in figure B imaged in 2D and as a side profile. Image reproduced with permission of the rights holder, Springer Nature [4].

Skyrmions are discussed as being topologically stable. This concept comes about mathematically from the inability to unwrap the magnetisation without forming a magnetic discontinuity. Although this topology may cause energetic stability under certain conditions it does not prevent skyrmions from being both created and annihilated. The topological number or charge remains a useful metric for understanding the structure of skyrmions and specific regions with non-zero topological charge such as the ends of helical lines. The topological charge of a skyrmion can be calculated by the integral of the magnetic moments

of an area. Equation 1.7 shows the topological charge n, calculated for a 2D area where a topological number of 1 would be expected for both the skyrmions shown in figure 1.8

$$n = \frac{1}{4\pi} \int \mathbf{M} \cdot \left(\frac{\partial \mathbf{M}}{\partial x} \times \frac{\partial \mathbf{M}}{\partial y} \right) dxdy \tag{1.7}$$

Skyrmions have been demonstrated to be stable in both isolated states and as part of a skyrmion lattice where energetically favourable conditions cause the system to undergo a first order phase transition and spontaneously fill with skyrmions in a hexagonally close packed lattice. The skyrmion lattice is shown to be energetically favourable for only a small region on the field-temperature phase diagram. A schematic diagram showing the location of the skyrmion region is shown in figure 1.9

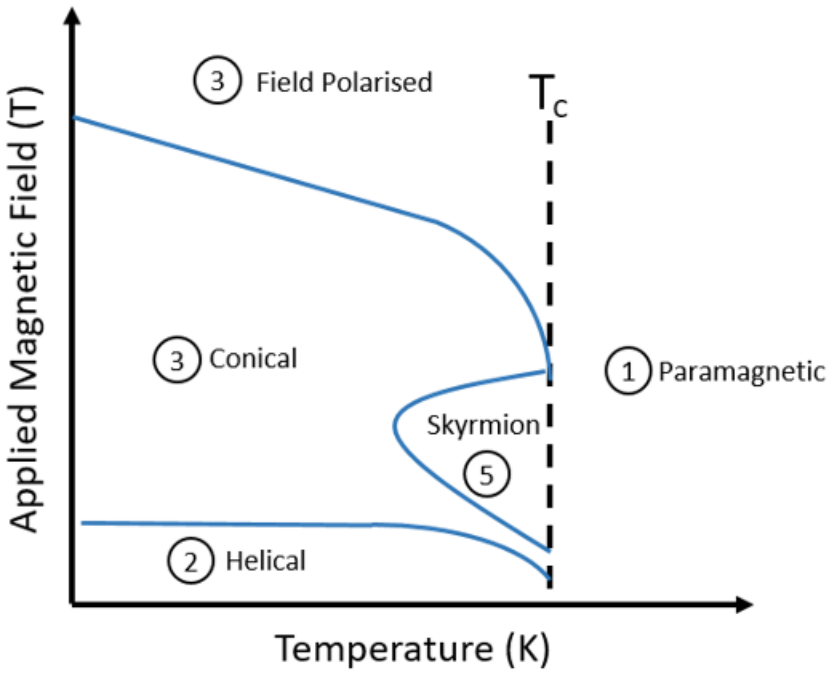

Figure 1.9: This schematic of the field-temperature phase diagram for a skyrmion supporting material indicates the locations of five important magnetic phases; Para-magnetic, Helical, Conical, Field Saturated and Skyrmion.

Label 1 of figure 1.9 shows the paramagnetic region of the $B-T$ graph. This area is above the critical temperature T_c and therefore the spontaneous fluctuation of magnetic

motion prevents any magnetic ordering to appear. Label 2 shows the Helical region of the $B-T$ graph. In this region where the temperature is below T_c and there is either a small applied field or no field applied the lowest energy state is helical. Label 3 shows the conical region of the $B-T$ graph in which the applied field is strong enough to cant the magnetic ordering into the plane of the helical direction. Label 4 shows the field polarised region of the $B-T$ graph in which the applied magnetic field is strong enough that the magnetic moment align with the direction of the magnetic field and the structure of the helical ordering is lost. Label 5 shows the Skyrmion region of the $B-T$ graph in which the temperature and applied field are within the correct ranges that skyrmion structure becomes the lowest energy configuration and spontaneous ordering of the hexagonal lattice appears. The specific temperature and fields at which this skyrmion region exists differ between materials however there is a trend for this this region being extended to lower temperatures as the host material is thinned from bulk. Bulk materials such as MnSi [30] exhibit the skyrmion phase at temperatures 26-28K with a maintained magnetic field of 0.1-0.25T. This prevents real world applications of skyrmions. However, progress is being made to increase the region of stability. Materials such as FeGe show the potential for near room temperature skyrmion lattice formation [31] with $T_c = 278$K with some studies showing magnetic ordering present as high as 300K [32].

Skyrmions have received significant attention in recent publications for the following attributes: topological stability, size modification [33], high mobility/current ratios and low pinning affinity [30]. These properties make skyrmions impressive candidates for future spintronic devices which have been envisioned as both memory storage on racetracks [34, 35] and binary logic operations performed by interaction of skyrmions in nanostructures [36, 37].

Chapter 2

Instrumentation

2.1 Introduction

This chapter gives an introduction to the instrumentation theory and its application to this project. Investigation into the magnetic dynamics was performed primarily using transmission electron microscopy (TEM) which is the focus of this chapter. The TEM is highlighted with reference to both the physical hardware of the column itself in section 2.2 and the principles of structural imaging modes and magnetic imaging modes in sections 2.3 and 2.4. The role and capabilities of specific electron detector technologies relevant to TEM is expanded to provide both background understanding and the limits of time resolved detection of electrons in section 2.5. Equipment providing *in situ* manipulation of magnetic field, temperature and electric current to samples inside the TEM are discussed in section 2.6. Finally, sample preparation techniques including bottom-up methods of electron beam lithography (EBL) with several types of metal deposition and top-down methods of lamella lift out using focused ion beam (FIB) lithography are covered in section 2.7.

Optical microscopes are limited in their spatial resolution due to the wave-particle nature of light [38]. The Rayleigh criterion defines the smallest distance resolved by

radiation of a specific wavelength [39]. This is given below in equation 2.1

$$\delta = \frac{0.61\lambda}{\mu sin\beta} \tag{2.1}$$

where δ is the resolution of the light microscope, λ is the wavelength of the radiation, μ is the refractive index of the medium and β is the collection semi-angle of the magnifying lens.

Optical microscope resolution is limited by the wavelength of light therefore an alternative particle was needed to increase the resolving power of instruments. Electrons have wavelengths corresponding to their energy, calculated using equation 2.2.

$$\lambda_e = \frac{h}{(2m_e eV)^{1/2}} \tag{2.2}$$

where λ_e is the wavelength of the electron, h is the Planck constant, m_e is the mass of an electron, eV is the accelerating potential in electron volts. Electrons having a low mass allow them to reach high energies when accelerated in an electric potential by increasing there momentum. TEM can accelerate electrons to voltages in the range 60keV - 1MeV, which cause the electrons to reach a velocity which is a significant fraction of the speed of light. Therefore, to correctly ascertain the wavelength of the accelerated electrons, relativistic corrections are included into the wavelength calculation as shown in equation 2.3.

$$\lambda_e = \frac{h}{(2m_e eV(1 + \frac{eV}{2m_e c^2})^{1/2}} \tag{2.3}$$

where c is the speed of light.

The first attempts at using electrons to create images happened directly after it was acknowledged that electrons could be focused similar to an optical lens by magnetic fields. The first dedicated electron lens was created in 1926 by Hans Busch [40] enabling the creation of the first electron microscope in 1931 [41] after which columns with compound lenses increased in complexity into the modern TEMs we have today. The wavelength of the electron however is not the limiting factor in modern TEM microscopes. Limits in resolution arise before 2.74pm (wavelength of a 200keV electron), currently TEM are limited to a resolution of approximately 0.5Å [42, 43].

TEM is a prominent feature of this project for collecting data on the magnetic ordering in samples, including but not limited to the structure and dynamics of skyrmions. TEM is a instrument in which a focused beam of electrons is transmitted through a thin sample from which information can be determined based on the interaction with the sample such as scattering events and deflections. The small feature sizes and intrinsically fast nature of the skyrmion dynamics required the use of different kinds of specialised TEMS: the JEOL ARM200cF - "MagTEM" at Glasgow university and the modified JEOL JEM-2100 at École Polytechnique Fédérale de Lausanne (EPFL).

2.2 TEM column

The internal components of a TEM column are briefly included as reference to explain the imaging modes and limitations of the experiments performed in this project. A simplified diagram showing only the key components of a TEM is shown in figure 2.1.

As shown in figure 2.1, the electrons are emitted from the electron gun. These electrons are accelerated down the optical axis of the TEM column by accelerating anodes creating an electric field. The electrons are focused by a series of lenses before reaching the sample depending on the imaging mode being performed and then projected by a series of post-specimen lenses to show either the real-space image or diffraction image with adjustable magnification. The transmitted beam contains two sets of data that are intrinsically linked, the diffraction image and the real-space image. The real-space image is what we associate more easily with the images produced by optical microscopes, where the x and y coordinates of the image directly correspond to directions in space. The diffraction pattern is an image taken in reciprocal space, where the axis represent momentum space rather than the physical space of real images. These diffraction patterns are Fourier transforms of the physical space image.

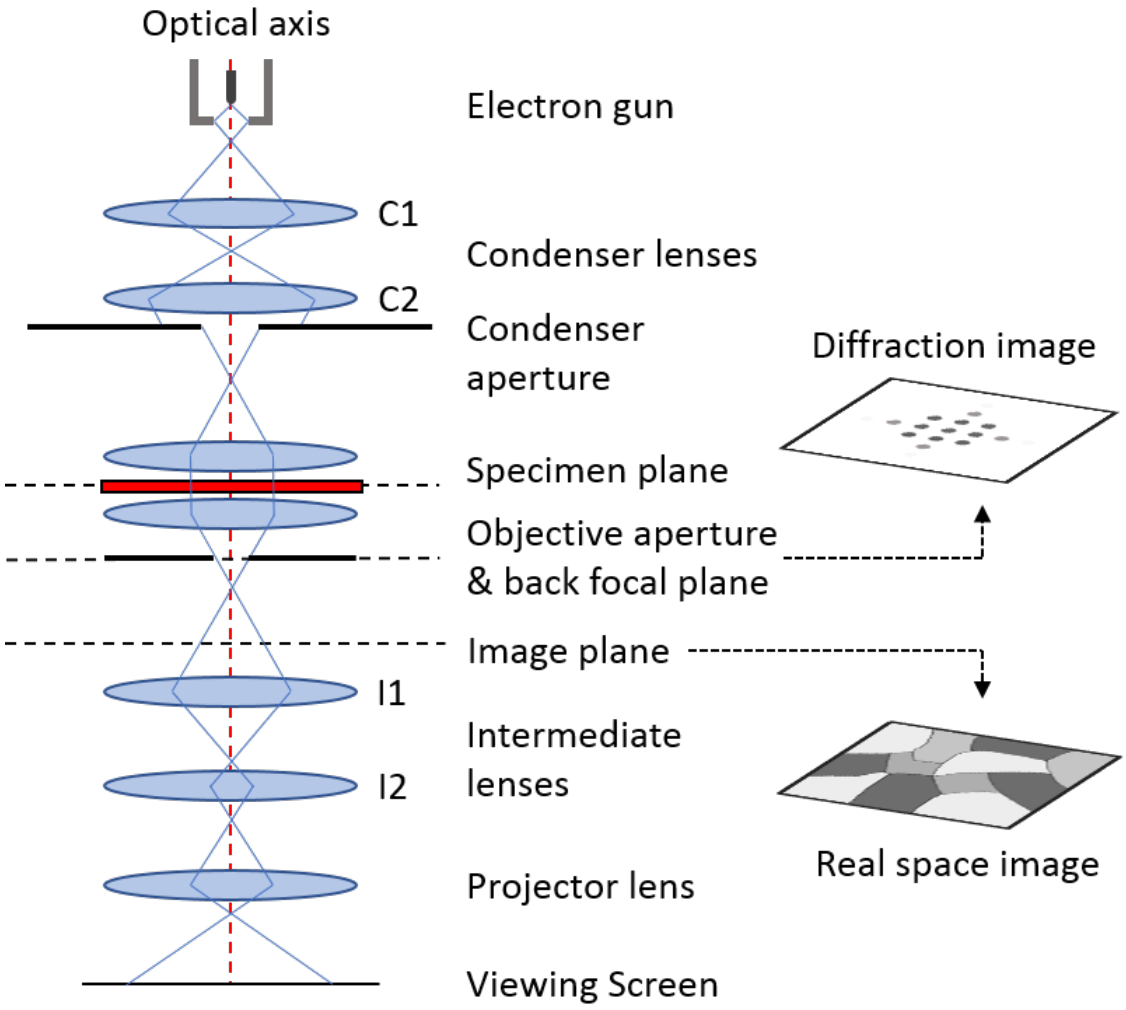

Figure 2.1: A schematic diagram of the main lenses and apertures in a TEM column. The position of the back focal plane and image plane are included with inserts showing the beam imaged in those planes.

2.2.1 Electron gun

The device that produces electrons and initially focuses them into a beam is called the electron gun. Within this electron gun the emission of electrons comes from a component called the electron source. Various electron source types exist, where the difference between them is the method in which the potential energy barrier, the work function of the material physically emitting the electrons is overcome. Three electron gun types are discussed here; electrons emitted by thermionic emission, by field emission and by photo-emission. The key components of these electron guns are shown in figure 2.2

Thermal emission of electrons has been a common form of electron production for decades. Thermal emission of electrons is caused when the thermal energy is higher than the work function of the material. The current density emitted by an electron source is proportional to the temperature as given in equation 2.4.

$$J_{\mathrm{e}} = A_G T^2 e \frac{-W}{kT} \tag{2.4}$$

where J_{e} is the emission current density, A_{G} is the Richardson constant, T is the temperature of the source, W is the work function of the material and k is the Boltzmann constant. Materials with low work functions and/or high operating temperatures such as tungsten and lanthanum hexaboride (LaB_6) are commonly chosen for the source tip. The characteristics of these sources are listed in table 2.1.

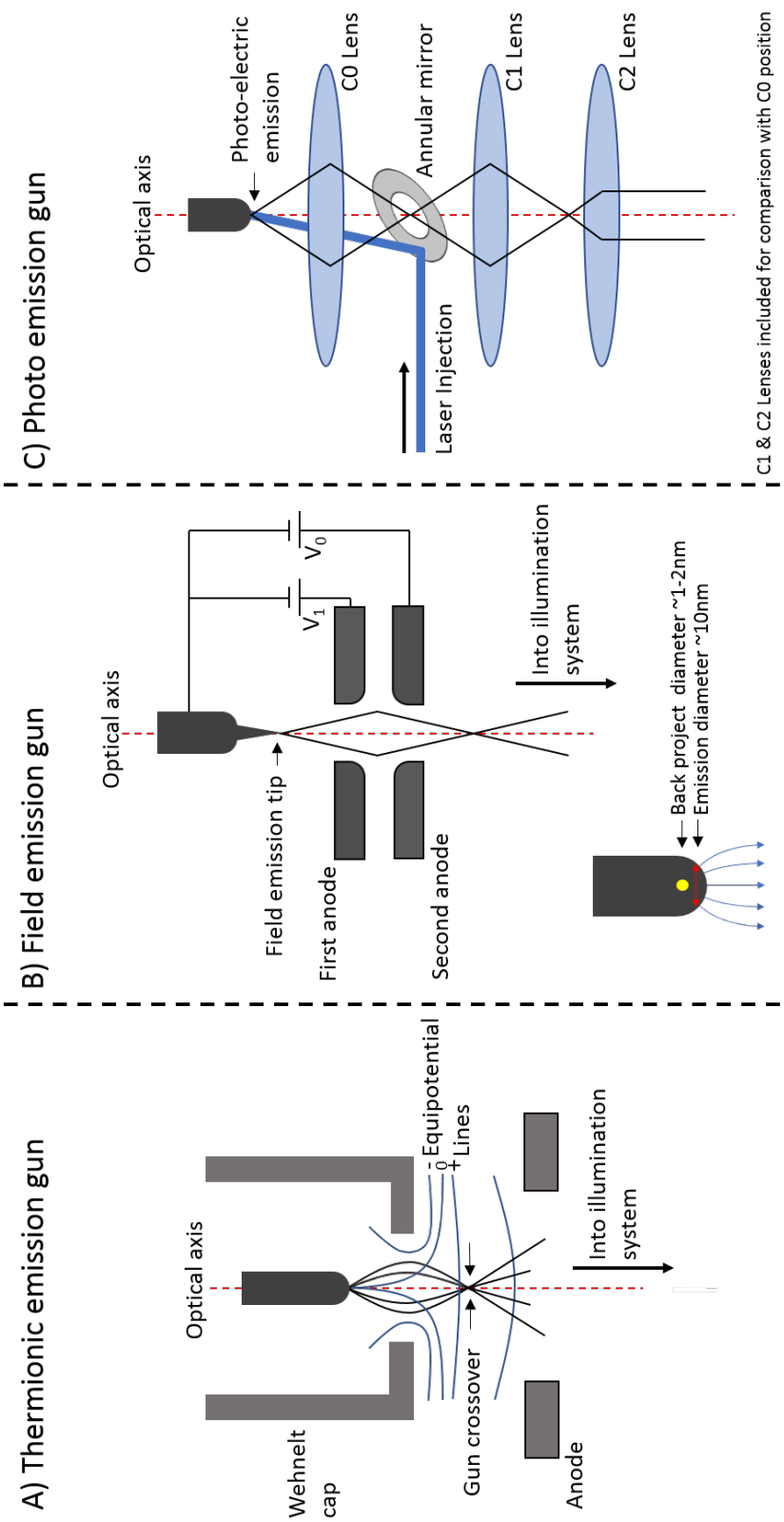

Figure 2.2: The key components and electron ray paths of three types of electron guns. Figure A shows a thermionic emission gun, figure B shows a field emission gun and figure C shows a photo emission gun including a commonly included C0 lens.

Directly after the thermionic source is the Wehnelt cap. This cylinder contains an aperture at one end which shapes an electrostatic field causing lensing of the newly emitted electrons forming the first gun crossover point. The biasing voltage applied to the Wehnelt cap affects the focusing and brightness of the beam. Where no biasing voltage is applied there is no crossover formed causing electrons emitted at high angles to be lost. Where the biasing voltage is high, electrons are deflected back by the strong electrostatic field at the aperture. The highest gun brightness is achieved when the Wehnelt is at an intermediate bias. Figure 2.2A shows the trajectories of four electrons focused by the Wehnelt cap. The equipotential lines are overlaid to better represent this lensing action. The bias of the Wehnelt is often automatically biased in response to the condition and parameters of the source, however in some microscopes it is favourable to alter the bias manually if there is a specific reason to allow electrons with more eccentric trajectories to pass through, typically in photo-emission sources where brightness is low. Thermionic emission guns such as those with LaB_6 or tungsten tips are characterised by having high total current emission. However, the emission area of the tip is relatively large compared to other emission methods which gives thermionic tips a lower temporal coherency and focusing spot size as shown in table 2.1, resulting in a lower overall brightness. Thermionic emission sources are therefore a useful tool for imaging large scale structural/magnetic features and experiments needing high source emission stability in instruments without the need for ultra high vacuum. A LaB_6 tip is fitted to the FEI Tecnai T20 TEM used in this thesis.

A modern technique for the production of electrons is through field emission. Using a strong magnetic field the electrons are stripped from the material through a process called Fowler–Nordheim tunnelling [44]. A field emission gun (FEG) uses a pair of anodes to create an extremely high electric potential at the tip of the emission source from which electron are extracted. This anode pair is shown in figure 2.2B. This method enables the emitting element to operate at a significantly lower temperature than other source tips. As shown in table 2.1 cold field emission guns (CFEG) operate around room temperature compared to the >1200K operating temperatures for the thermionic sources. The sharp tip used to create the high electric fields 10^9 Vm^{-1} causes the electrons to be emitted from

a very small point. This enables the CFEG to produce very bright beams with a high coherency which, as discussed later in 2.4, is an important factor in the quality of magnetic imaging. At the bottom of figure 2.2B the tip of the emission source is highlighted. This shows that the area that electrons are emitted from is of the order of 10nm. The emission area can be back projected to a point of diameter approximately 1-2nm. The primary disadvantage of field emission guns is the requirement to be installed in an high vacuum 10^{-6}Pa in the case of Schottky sources and ultra high vacuum 10^{-9}Pa in the case of cold field emission needed to prevent electrical discharge. This requirement for ultra high vacuum can cause and impact on emission current stability over the course of a day long TEM session. A cold field emission gun is fitted to the JEOL ARM200cF used in this thesis.

Finally, production of photo-electrons as a source for a TEM is an emerging technology [45], previously photo emitted electrons had been primarily used for photo-emission electron microscopy (PEEM) which is limited to surface-sensitive microscopy [46]. In photo-emission TEM the tip of the source is illuminated by a laser pulse, causing electrons to be emitted via the photoelectric effect. The illuminating laser is injected into the column and reflected by a mirror towards the photo-emission tip. This is shown in figure 2.2C where an annular mirror is shown to deflect the laser up while allowing electrons travelling along the optical axis to pass through. Dedicated photo cathodes are often produced from materials such as tantalum or copper. However, illumination of thermionic source tips such as LaB_6 and tungsten or field emission tips has been demonstrated [47]. The laser spot size which is usually on the order of 100μm causes the emission of electrons to occur in a large radius reducing the coherency of the beam [48]. The comparatively large area of source tip material over which photo-emission occurs and the presence of the laser mirror have motivated the inclusion of a condenser lens before their standard position after the accelerating anode. Figure 2.2C shows the C0 lens between the photo-emission source and the annular mirror used to capture electrons emitted with eccentric trajectories and for focusing though the annular mirror. The C1 & C2 lens have been included only in the photo-emission diagram to demonstrate their position compared to the C0 lens. Photo-emission sources have enabled time-resolved TEM imaging with the time resolution determined by the pulse

width of the injected laser. The pulse width of lasers can be in the order of ns to fs which allows the duration over which the specimen is exposed to the electron beam to occur periodically at durations the same order as the pulse width. However, the limitation on the number of electrons per pulse without causing significant space charge effects, and the ratio of emission and duty cycle determines the total counts produced via laser excited photo emission. It has been theoretically determined that electrons per pulse counts of 50,000 are possible without significant space charge for picosecond lasers [48].

Although not necessarily part of the electron optics, the accelerating anode stack is a major component in the TEM electron emission. This component increases the momentum and therefore energy of the electron from its emission momentum by acceleration in an electrostatic potential. The accelerating voltages used in this thesis for the JEOL ARM200cF are 200kV & 60kV. Both larger and smaller voltages are accessible in other instruments and have advantages for specific applications such as increased beam deflection.

2.2.2 Electron optics

Once the electron beam has been emitted into the column a series of magnetic lenses are used to both focus and position the beam. Unlike an optical microscope the series of lenses remain in a fixed position with respect to one other and the focal length of the lenses is altered by changing the applied current. The physics of magnetic lensing is an extension of Fleming's left hand rule and comes from the interaction of electrons with electromagnetic fields as described by the equation 2.5.

$$\vec{F} = e(\vec{E} + \vec{v} \times \vec{B}) \tag{2.5}$$

where $\vec{F}$ is the force on the electron, e is the charge of an electron, $\vec{E}$ is the electric field, $\vec{v}$ is the velocity of the electron and $\vec{B}$ is the magnetic field.

The optics in the TEM column can broadly be split into two sections, pre-specimen and post-specimen optics. In a standard TEM the lenses directly after the electron source are the condenser lenses. These lenses are used to form the electron beam probe and they help define many of its characteristics. Condenser lens one (C1) controls the spot size of

Characteristics of the principle electron sources					
	Units	Tungsten	LaB	Schottky FEG	Cold FEG
Work Function	eV	4.5	2.4	3.0	4.5
Richardson's Constant	A/m^2K^2	6 x 10^9	4 x ^{9}		
Operating temperature	K	2700	1700	1700	300
Current density (at 100kv)	A/m^2	5	10^2	10^5	10^6
Crossover Size	nm	$> 10^5$	10^4	15	3
Brightness (at 100kv)	A/m^2sr	10^{10}	5 x 10^{11}	5 x 10^{12}	10^{13}
Energy spread (at 100kv)	eV	3	1.5	0.7	0.3
Emission current stability	%/hr	<1	<1	<1	5
Vacuum	Pa	10^{-2}	10^{-4}	10^{-6}	10^{-9}
Lifetime	hr	100	1000	>5000	>5000

Table 2.1: A table directly replicated from 'Transmission Electron Microscopy', comparing the characteristics of two thermionic emitter materials and two types of field emission guns[39]

the beam, by forming a de-magnified image of the gun crossover. Adjusting the positioning of the gun crossover allows the user to balance between beam current and convergence angle when used in sequence with the condenser aperture. As the strength of the C1 lens is increased the distance to the gun crossover decreases causing more electrons to be removed by the condenser aperture resulting in a smaller probe size with a smaller convergence angle. Condenser lens two (C2) controls the focusing of the beam controlling the illuminated area and thus the intensity of the beam on the sample. When the magnification of the system is increased this requires the C2 lens to be strengthened to reduce the illuminated area to the size of the area of interest.

The objective lens which is located at the sample in the TEM has two purposes, to shape the probe or to provide magnetic stimulus to the sample. These two functions are typically not used together as the 1T or higher magnetic field caused by the objective lens while active can magnetize some magnetic samples. When active, the objective lens is used with the C2 lens to produce near parallel illumination of the sample which is useful for many of the imaging modes discussed later. The C2 lens is excited so that the crossover point is at the front focal plane of the objective lens, these lenses then work in tandem to spread the beam parallel across the sample. The weakly-excited objective lens uses the objective lens at only a fraction of the power for beam focusing, to provide an out-of-plane magnetic field to the sample and can be activated on the order of a few hundred milliseconds in the range of only a few tens of Oersted.

The intermediate and post-specimen projector lenses allow the user to specify both the magnification of a real-space image and the camera length of the diffraction pattern when projecting the back focal plane. Each lens in the series can be turned on/off and increased in strength to alter the focal point modifying the final magnification. To increase magnification more lenses must be turned on, however, each lens turned on causes a new crossover of the image causing the final image to reverse during known magnifications.

2.2.3 Specimen interaction

Scattering of electrons from atoms within the specimen sample is a complicated process with many possibilities some of which are shown in figure 2.3. Without modification or additional detectors, TEM is sensitive to transmitted electrons only with electrons reflected and X-rays produced at the sample often going undetected. The electrons that undergo scattering can generally be categorised into elastic and inelastic events. The scattering caused by an individual atom can be calculated as the sum of the cross sections of both elastic and inelastic scattering events as shown in equation 2.6 where the term "cross section" can be more literally thought of as a collision probability function.

$$\sigma_T = \sigma_{elastic} + \sigma_{inelastic} \tag{2.6}$$

The two key interaction locations at an atom are the nucleus and the electron cloud. The nucleus exists as a small cluster of subatomic particles that is both heavy compared to an electron and has a significantly larger total charge. Interactions between charged particles and an atomic nucleus was first explained by Ernest Rutherford in 1911 with the well known gold film experiment in which alpha particles incident to gold film were shown to scatter at all angles with decreasing probability as a function of the scattering angle. This effect was named "Rutherford Scattering" which is a form of Coulomb repulsion [49]. The electron cloud however exists as a probability distribution of electron charge due to the wavelike nature of electrons with properties such as the valence shell structure based on the atomic number of the atom.

Elastic scattering occurs where the incoming electron is deflected without a loss of energy. Multiple deflections causes the mean path of the electron to have some lateral component. The probability of elastic scattering has two key factors: the atomic number of the specimen material and the incoming electron energy. The scattering cross section increases as the square of the atomic number as the total positive charge of the atoms nucleus increases.

Inelastic scattering occurs where the energy of the incoming electron is not equal to the energy after deflection. The kinetic energy can be transferred to the atom through

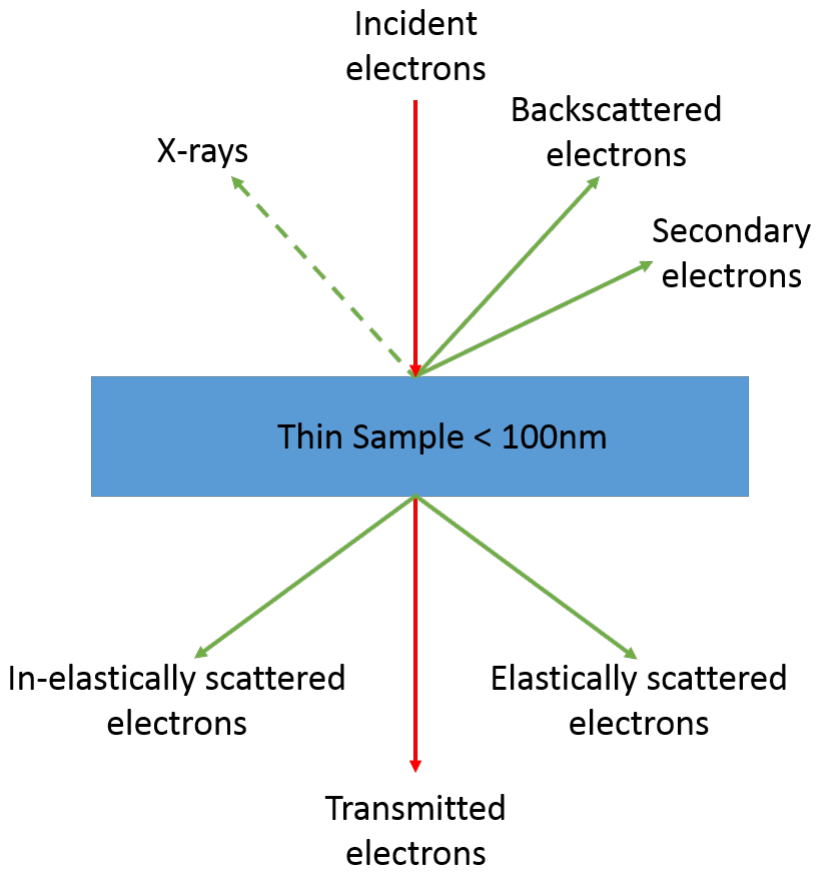

Figure 2.3: Interaction between the incident electron beam in a TEM and the sample can result in multiple resulting trajectories for the incident electron and electrons/x-rays generated from the sample itself.

multiple means however the creation of electron hole pairs is of particular importance when dealing with interaction with a semiconductor type material for the generation of electron hole pairs.

The probability of both elastic and inelastic scattering depend on the atoms per unit volume of the material. The probability of an electron scattering whilst passing through a material is shown in equation 2.7

$$p_e = \frac{N_o \sigma_T (\rho t)}{A} \tag{2.7}$$

where p_e is the probability of an electron scattering, N_o is Avogadro's number, σ_T is the cross section of the atom, ρ is the density, t is the thickness of the material and A is the

atomic weight of the atoms.

If the probability of interaction is known then the mean free path of the electron inside the material can be calculated. The mean free path of the electron in the material is important for the thickness-mass contrast produced in bright field imaging and for the implantation depth in detectors discussed in the following section. The mean free path is given in equation 2.8

$$\lambda_{fp} = \frac{A}{N_o \sigma_T \rho} \tag{2.8}$$

where λ_{fp} is the mean free path of the electron.

2.3 Structural imaging

The multitude of lenses and beam conditions in the TEM allows the user significant control over the information recorded. The first key imaging type is structural imaging where the geometric, crystalline and atomic structure of the material can be investigated. Key information about the sample is accessed by projecting either the image plane or the back focal plane onto the detector by the intermediate and projector lenses. Figure 2.4 shows how altering the strength of the intermediate lenses can change the plane imaged.

2.3.1 Bright-field imaging mode

Bright-field imaging is the most basic operational mode in the TEM. In bright-field imaging the beam is spread out at the objective lens to give broad beam illumination of a large area of the sample with electrons travelling near perpendicular to the sample plane. This illumination type is called "parallel beam illumination". An aperture is inserted directly after the objective lens into the back focal plane to ensure only electrons passing parallel though the objective lens pass through to form the first image in the intermediate lenses before projection. Figure 2.5A shows this in the form of a ray diagram. The rays forming the bright-field image are shown in orange and the rays blocked by the objective lens are shown in blue.

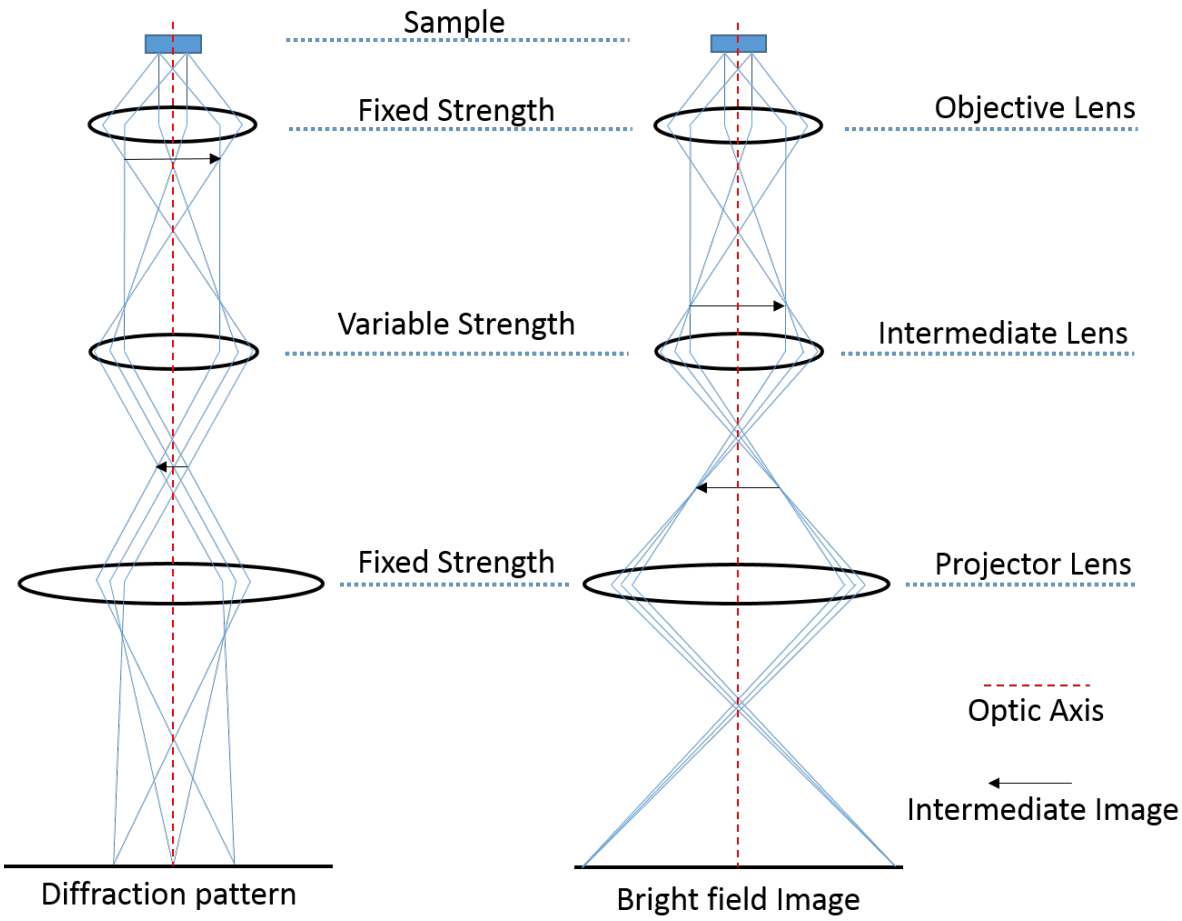

Figure 2.4: Projection of both the back focal plane showing the resulting diffraction pattern and the image plane showing the bright-field image as facilitated by the intermediate and projection lenses

Bright-field imaging is useful in accessing structural information and thickness measurements. However, it is not sensitive to any magnetic component of the sample. In bright-field imaging mode there are three principle contrast sources: amplitude contrast, diffraction contrast and phase contrast (important in high resolution TEM and discussed in section 2.4.2 with focus on magnetic imaging). Amplitude contrast is caused by the material of the specimen scattering the electrons which in turn produces contrast due to removal of electrons. The thickness of the sample directly influences the amount of elastic scattering. Thicker regions of the material will appear to have a lower intensity

than thinner sections. Similarly the density of the material will also impact the contrast by reducing the mean free path of the electrons as discussed previously in equation 2.8. Diffraction contrast is caused by electrons being lost from the transmitted beam due to Bragg scattering. This effect can be significant in highly crystalline material causing dark regions to appear at localised features such as dislocation or due to bending contouring in which a Bragg condition is reached by curvature in the sample. Although this causes dark regions due to loss of electrons, these electrons can be imaged by imaging specific regions in the back focal plane as discussed later in dark-field imaging.

Bright-field imaging as a technique is important in supporting results where bulk specimens have been prepared for the TEM using thinning techniques. Most thinning techniques provide some variation in the uniformity of the sample and therefore thickness measurements are important in interpreting results.

2.3.2 Diffraction imaging mode

Diffraction imaging is a parallel beam illumination technique for investigating the structural and crystalline properties of a material. In single crystal and polycrystalline materials, electrons are Bragg scattered according to the crystallographic planes present. The electrons are focused by the objective lens causing a diffraction pattern in the back focal plane. The series of intermediate lenses and projector lens then project the back focal plane onto the detector to view the diffraction pattern. Figure 2.5B shows the ray diagram indicating the crossover point of the back focal plane.

The theory of how diffraction patterns are created is linked to the wave-particle duality of electrons. The interference patterns produced by electrons which can be thought of as waves for the purpose of diffraction are accessed by projecting the back focal plane onto the viewing screen or detector. Bragg's law defines the possibility for a condition where the waves propagating through a material may constructively interfere based on the relative inter-atomic distance between the atoms in a crystal structure, the crystallographic planes present in the crystal and the wavelength of the incoming photon or, in this case, electron wavelength.

2.3.3 Dark-field imaging mode

In dark field imaging, rather than using the transmitted beam only electrons that have been scattered are imaged. This is done by using an aperture to block all but select group of electrons by centring the aperture over a single diffraction spot. Where the electron beam is incident to the specimen the diffraction spots are located off-axis meaning the position of the objective aperture must be moved to highlight a particular spot, this is called Off-axis dark field imaging shown in figure 2.5A. Alternatively tilting the beam causes the diffracted beam to appear off centre to the optic axis and the diffraction spot of interest to centre on the optic axis this method is called On-axis dark field imaging shown in figure 2.5B. The on-axis method is preferred as the off-axis method causes the diffracted beam to pass though the objective lens at a greater distance from the optical axis which will be susceptible to aberrations. Selecting only one diffraction spot results in an image where intensity is dependent on crystallographic orientation. This technique is often employed where the crystal grain size in polycrystalline materials is of interest. Alternatively it is used when identifying regions of damage to single crystal materials caused by the sample preparation method ion beam thinning. This technique was used in this project and will be discussed later.

2.4 Lorentz magnetic imaging

Lorentz imaging techniques use contrast produced by deflection of the electrons passing through the sample due to the classical Lorentz force. Electrons incident to the sample experience a force relative to the direction of magnetisation given by equation 2.9

$$\vec{F} = e(\vec{v} \times \vec{B}) \tag{2.9}$$

where $\vec{F}$ is the force on the electron, e is electron charge, $\vec{v}$ is electron velocity and $\vec{B}$ is the magnetic induction. The force on the electron causes a deflection from the beam path where the angle of deflection relative to the beam path is given by equation 2.10

$$\beta_L = \frac{e\lambda t(\vec{B} \times \vec{n})}{h} \tag{2.10}$$

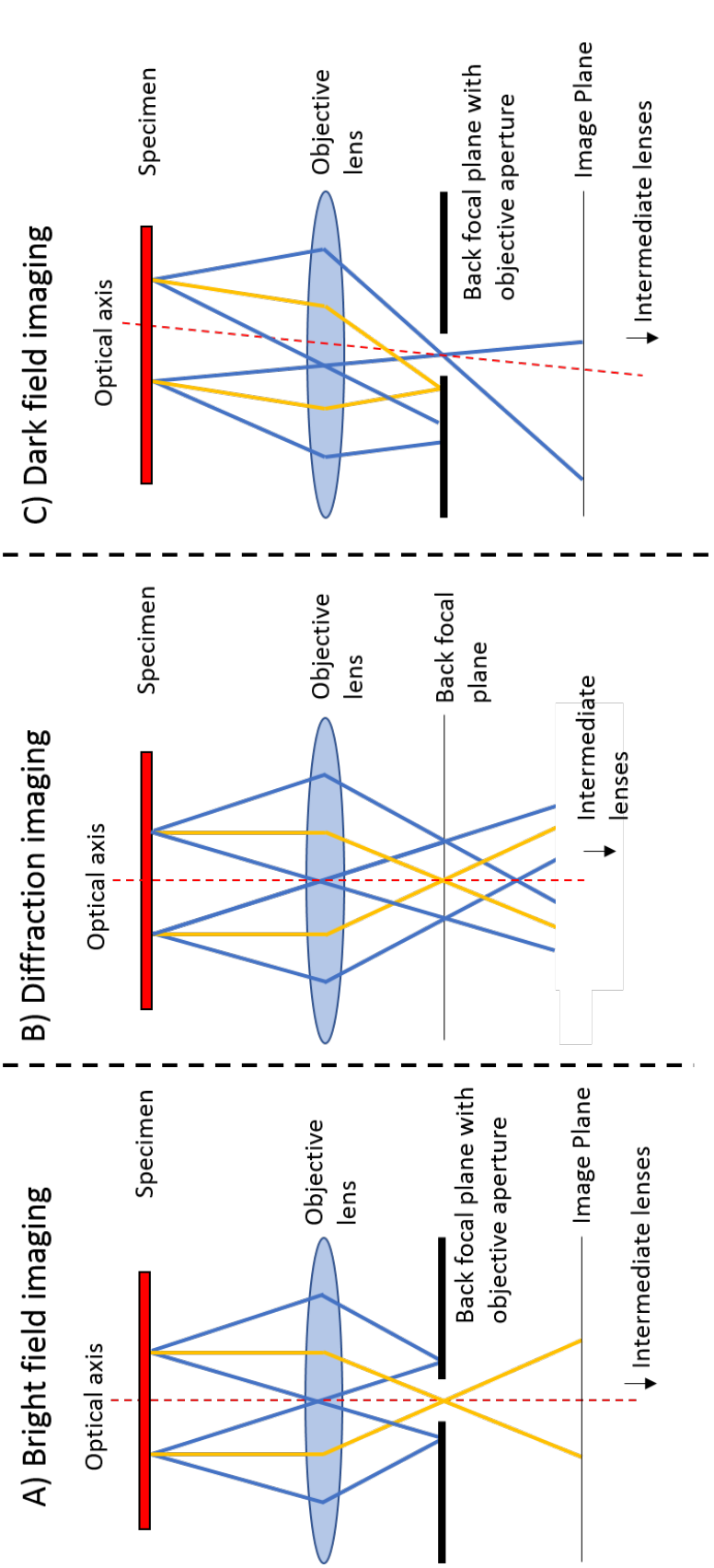

Figure 2.5: A ray diagram highlighting the role of the objective lens and objective aperture in capturing the image plane in bright-field imaging and the back focal plane in both diffraction imaging and dark-field imaging.

where β_L is the angle of deflection, t is the material thickness, $\vec{n}$ is the unit vector of the incident beam, λ is the electron wavelength and h is Planck's constant. The result of this Lorentz force on electrons passing through material with adjacent domains of anti-parallel magnetisation is shown in figure 2.6. Where the electron deflection in both domains is in an opposite direction from the domain boundary, there is a decrease in the electrons directly below the boundary, called a dark fringe. Alternatively, where the electron deflection of both domains is towards the domain boundary, there is an increase in the electrons creating a bright fringe. The particle-wave nature of electrons cause the electrons creating the bright fringe to form an interference pattern in the intensity.

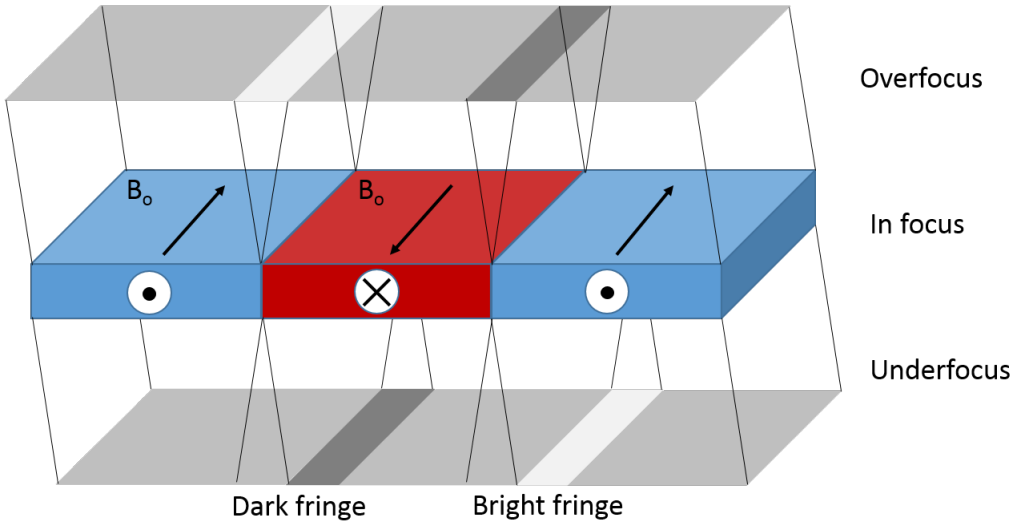

Figure 2.6: A diagram indicating the origins of contrast in Fresnel imaging mode

This classical approach to understanding electron interaction with a magnetic field is capable of revealing the basic principle of Fresnel mode. However, to properly understand quantitative Lorentz microscopy the electrons must be considered a quantum particle and therefore needs a particle-wave approach to fully understand the quantitative magnetic information available in Lorentz imaging. The quantum mechanical interpretation of figure 2.6 requires the theory created by Yakir Aharonov and David Bohm called the Aharonov-Bohm effect [50] .The Aharonov-Bohm effect is a phenomenon where a charged particle, which in this case is the electron, experiences a phase shift while passing through an electromagnetic potential. The phase shift between two electrons passing through

different regions of magnetisation is given by equation 2.11.

$$\phi = \frac{2\pi eN}{h} \tag{2.11}$$

where ϕ is the phase shift and N is the magnetic flux enclosed by the trajectories of the electrons. The phase shift in figure 2.6 between the point of entry and exit of a material is given by equation 2.12

$$\phi = \frac{2\pi et}{h} \int_{x_1}^{x_1} B_y(x)dx \tag{2.12}$$

where x_1 & x_2 are the points defining the integrated path.

2.4.1 Fresnel imaging

Fresnel mode imaging is an important tool in investigations into magnetic materials and the primary method of imaging used in this project. The technique uses a defocused beam to create an image of the plane Δ above or below the specimen plane. The technique is sensitive to the in-plane component of magnetisation only as the contrast is generated by deflection of the electron which does not occur where the local magnetisation is parallel. An example of the contrast produced by two 180° domain walls was shown previously in figure 2.6. This causes two regions of interest, the divergent (Dark) region and the convergent (Bright) region which highlight the domain wall boundaries in an image. Fresnel imaging with high beam coherency sources such as C-FEG enable imaging of the interference fringes created in the bright fringe where electrons with different phase shifts meet.

Fresnel imaging is an easy to perform technique, ideal for highlighting domain wall edges and skyrmion topology due to the symmetrical structure producing either white (under-focus) or black contrast (over-focus). The high contrast produced using Fresnel imaging makes it a good candidate for time resolved magnetic imaging where signal to noise ratio is limited. Fresnel imaging being an out-of-focus technique is limited in the spatial resolution available. Resolutions of approximately 10nm are available to this technique.

2.4.2 Differential phase-contrast imaging

Differential phase-contrast (DPC) imaging is a technique used in conjunction with scanning transmission electron microscopy (STEM). The technique was first proposed in 1974 by Dekkers and de Lang for high resolution TEM [51, 52] and subsequently adapted for magnetic imaging by Chapman [53, 54]. Modern DPC imaging has enabled the highest resolution imaging to date of any TEM technique, with structural imaging at sub Angstrom resolution and magnetic imaging with resolutions up to 0.3nm [55]. DPC uses a convergent probe focused onto the surface of the material. This probe is continuously rastered across the material using a pair of scan coils working in tandem to deflect the beam (First coil) and then realign the beam parallel to the optical axis (Second coil). The basic principle behind DPC can be understood by using a classic field induced deflection as the beam passes through the sample as previously shown in equation 2.10 or via the Aharonov-Bohm effect for quantitative magnetic information. For the purposes of this project we will use the classical approach, as no DPC simulations are being performed. The principle of DPC uses the deflection caused by the Lorentz force as in equation 2.10 to deflect the beam onto a multi-segment detector where the deflection is interpreted by the difference signals between segments. Figure 2.7 shows a diagrammatic approach of how the incoming probe is scanned across the surface of the material to create a DPC image. The incoming beam is shifted using a pair of scan coils to raster the probe across the sample. The probe is formed by using the objective lens in high resolution TEM and without when performing magnetic imaging to avoid saturation. The probe semi-angle α is increased as the magnification is increased. The probe is then deflected by the internal field and exits the sample with an angle of β_{L} . The pair of de-scan coils are then used to reform the beam out of the transmitted probe shifted back to its original position on the optical axis. The deflection of the beam β_{L} is then detected by the detector giving direct imaging of the direction of the internal field. The beam will experience no shift in two conditions; free space where a sample has not been inserted or a non magnetic sample will provide no deflection to the beam.

TEM column alignment in DPC unlike other high resolution imaging modes requires

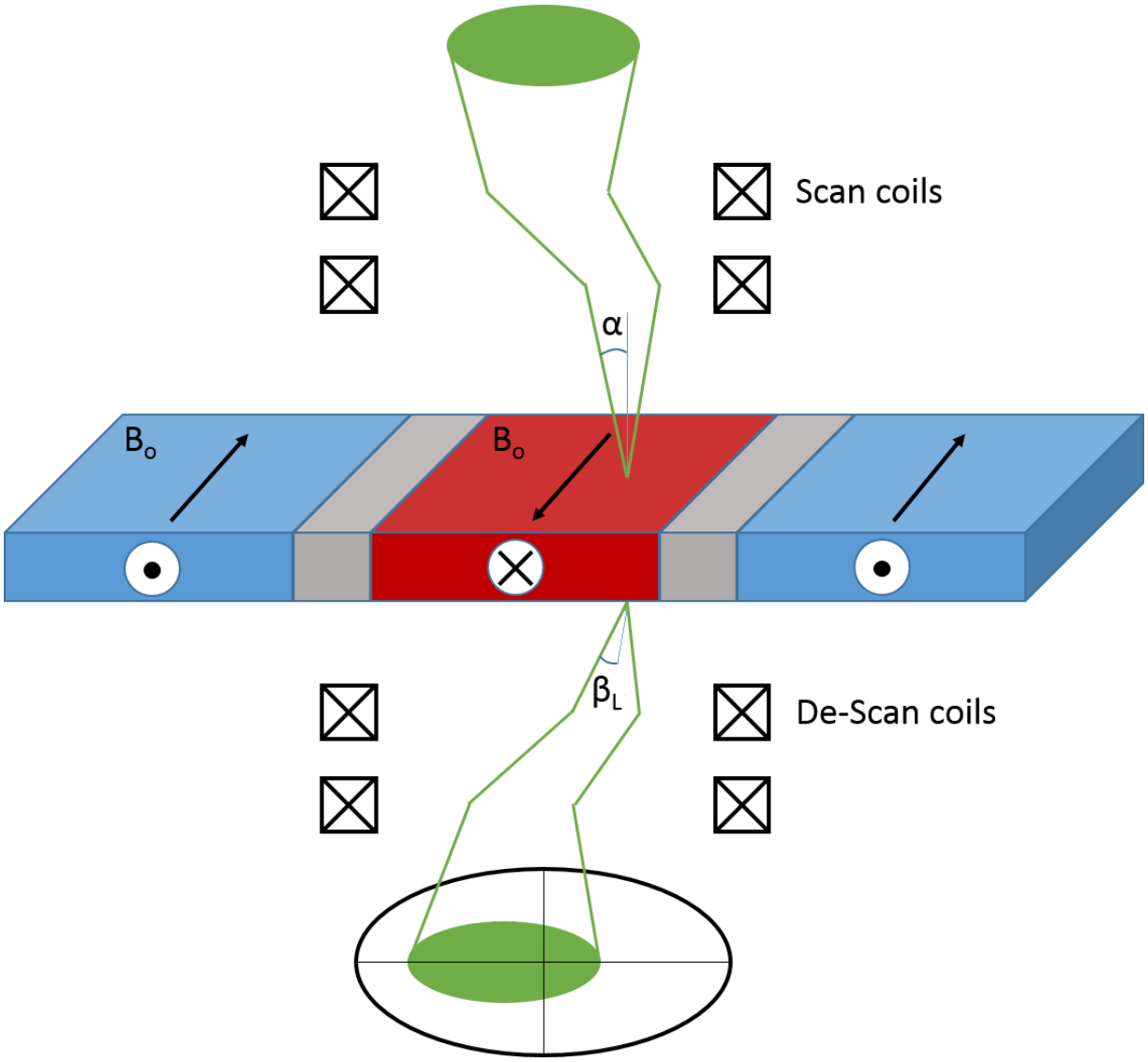

Figure 2.7: The detection of differential phase-contrast on a quadrant detector is illustrated. The convergent probe is rastered across the sample by the pairs of scanning coils allowing the convergent beam technique to image a large area.

the objective aperture to be removed which allows both the transmitted beam and electrons that have undergone diffraction to pass through. This ensures that not only the transmitted beam, but also the diffracted one are allowed to contribute to the image. DPC has been traditionally performed using a quadrant segmented detector. This means that two images relating to the difference between the opposing quadrants can be related and a contrast

image formed though summation of the four quadrants can produce a DPC image where the colour is proportional to the direction of deflection and colour intensity is proportional to electron intensity. This quadrant detector design has been shown to be improved by the 8 segment design discussed later in the detector chapter.

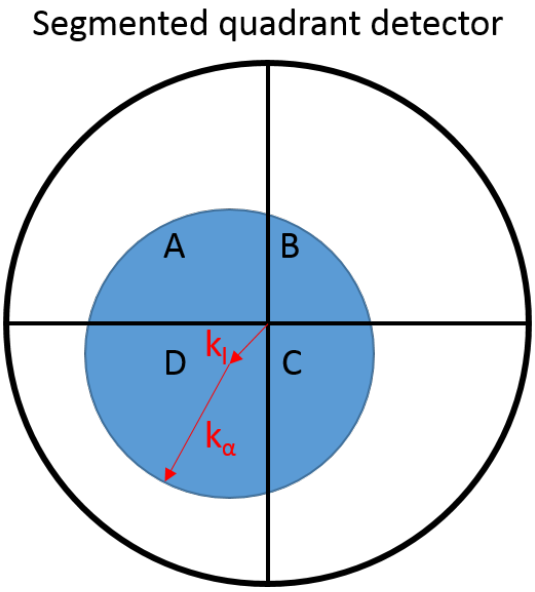

Figure 2.8: The displacement of the beam from the central position k_I and radius of the beam k_α determine the ratio of beam intensity distributed between the four quadrants of the detector (A-D)

$$Vertical = (A + B) - (C + D) \tag{2.13}$$

$$Horizontal = (A + D) - (B + C) \tag{2.14}$$

$$Intensity = (A + B + C + D) \tag{2.15}$$

Recent developments in direct electron detector technology have provided improvements in DPC imaging. Pixelated detectors have some improvements compared to the segmented detectors. The primary assumption of DPC imaging is that the disk projected from the sample onto the detector is a disk of uniform intensity. In reality because of diffraction

contrast in crystalline samples, there is contrast within the projected disk. This introduces a bias when using segmented detectors in which equations 2.13 & 2.14 do not accurately determine the geometric centre of the disk, k_I. Pixelated detectors allow more control of the interpretation of the deflection of the disk. Methods of computation using cross correlation and edge finding methods rather than simple centre of mass have been investigated and exhibit improvements compared to non-pixelated methods [56].

2.5 Electron detection technology

The significance of detector technology on the implementation of time-resolved magnetic imaging makes a brief understanding of both historical and currently competing technologies important. Starting with non-digital technologies such as photographic emulsion film and the electron-fluorescent viewing screen, followed by digital non-pixelated systems such as semiconductor detectors and scintillator photo-multiplier detectors. Finishing with a discussion on pixelated detectors, such as charge coupled devices (CCD) and active pixel sensor (APS) detectors [57, 58] which feature prominently in the research carried out within this thesis.

2.5.1 Non-digital electron detection

One of the most common methods of electron detection is via the retractable viewing screen which is standard on most TEM with the exception of some modern or specialised versions. The viewing screen uses a electron-fluorescent material such as Zinc sulphide (ZnS) to convert the electrons into photons which the user is able to interpret directly. ZnS is primarily chosen as a source of electron fluorescence as it has a comparatively long lifetime of 10ms compared to other compounds which can have as short as ns lifetimes. ZnS is commonly doped with a very small component of copper to give the electron-fluorescence a green hue. Although electron-fluorescent viewing screens do not provide a method of storing data about the sample it does provide an easy method of receiving visual feedback while calibrating the instrument.

Photographic emulsion has been used in TEM from the beginning and many TEM still have the faculty to use photographic emulsion. The photographic emulsion contains grains of silver halide of 4-5μm, which is an electron sensitive material. The grains are converted to silver granules when hit by an electron. The silver halide grains are suspended on a film until used. The small grain size gives the film a significantly higher resolution than many detectors before modern CCD cameras.

2.5.2 Scintillator-photomultiplier detectors

A scintillator-photomultiplier tube (PMT) detector counts electrons through a process where electrons are converted into photons through a short lifetime scintillation crystal such as doped yttrium-aluminium garnet (YAG). The photons emitted are then channelled into a photomultiplier tube which amplifies the intensity of the light signal by causing an avalanche effect through a sequence of dynodes responsible for multiplying incoming photons. These photons are then converted back into electrons and read out at a detector at the end of the photomultiplier tube. PMT detectors are very sensitive to low dose exposure due to the high gain in the system $>10^8$, which means that single electrons are easy to count and the detective quantum efficiency (DQE) of such a device is often greater than 0.9 for a modern instrument [39]. Due to the size of the photo-multiplier tube behind the scintillator, creating an array of these structures would be impractical and therefore they are generally not available as pixelated sensors for TEM applications. The time-resolution attainable in a PMT detector is fast compared to other methods of detection with scintillation crystals having mean lifetimes on the order of nanoseconds. Therefore, exposure times of 100ns are achievable making PMT detectors an attractive option for fast scanning transmission electron microscopy (STEM) detection.

2.5.3 Semiconductor detectors

Semiconductor technology involves the conversion of primary beam electrons into electron-hole pairs and the subsequent reading of these electron hole pairs as an electric signal to detect electrons. This section introduces non-pixelated semiconductor detectors as the

primary technology however semiconductor materials are also a major component of both charge coupled devices (CCD) and direct electron detectors discussed later in this section.

Semiconductor detectors commonly use silicon as the material of choice. However, in principle they can be constructed using any material capable of forming a positive-negative (p-n) junction. A p-n junction is the finite region between positive (p-doped) and negative (n-doped) material, where p-doped material contains excess holes in the conduction band and the n-doped material contains excess electrons. The finite region between the two doped materials contains no majority carriers which is referred to as the depletion region. As electrons from the incident beam interact with valence band electrons in the depletion region they are promoted to the conduction band across the band gap at a cost of 3.6eV for silicon. The promoted electron and hole left behind in the valence band collectively called the electron hole pair are separated by applying a bias across the p-n junction moving the oppositely charged pair in opposing directions. This charge is then measured and converted through a transimpedance amplifier to a more useful, proportional voltage signal.

Semiconductor detectors have some major advantages over other technologies. Advances in silicon processing has significantly reduced the cost of silicon based semiconductor detectors whilst increasing the complexity of the shapes to which the material can be cut, allowing for segmented detectors and detectors with central spot holes, both of which have important applications in TEM.

2.5.4 Charged coupled device

CCD cameras were a technological breakthrough in electron microscopy with widespread installation in TEMs during the late 90s. A diagram showing the principle components of a CCD chip is shown in figure 2.9. The first step of electron detection is to convert the incoming electron into a photon signal, the CCD is capped with a scintillation crystal, shown in blue in figure 2.9. The scintillation crystal is mounted onto fibre optic wires to collect and channel the emitted photons, shown in yellow in figure 2.9. The CCD chip shown in green, contains an array of cells isolated by an energy barrier. Incident photons are converted in these cells to electron-hole pairs and subsequently separated by a biasing

voltage. The charge of an individual cell increases near proportionally to the number of electron impacts electron. Figure 2.9 shows a 5x5 array of cells containing blue dots representing the charge generated by an electron impact. During the read-out step the charge is transferred to an analogue to digital conversion chip to be read out. The method of charge readout is dependent on the specific architecture of the CCD chip. In the case presented in figure 2.9, the readout is performed on a line by line basis by applying a potential across the cells to move the charge from one cell to the next. The charge is then transferred to a readout cell as shown by the dashed red line. The transfer of charge from cell to cell can cause noise to be added to the system where the perfect transfer of charge in not guaranteed.

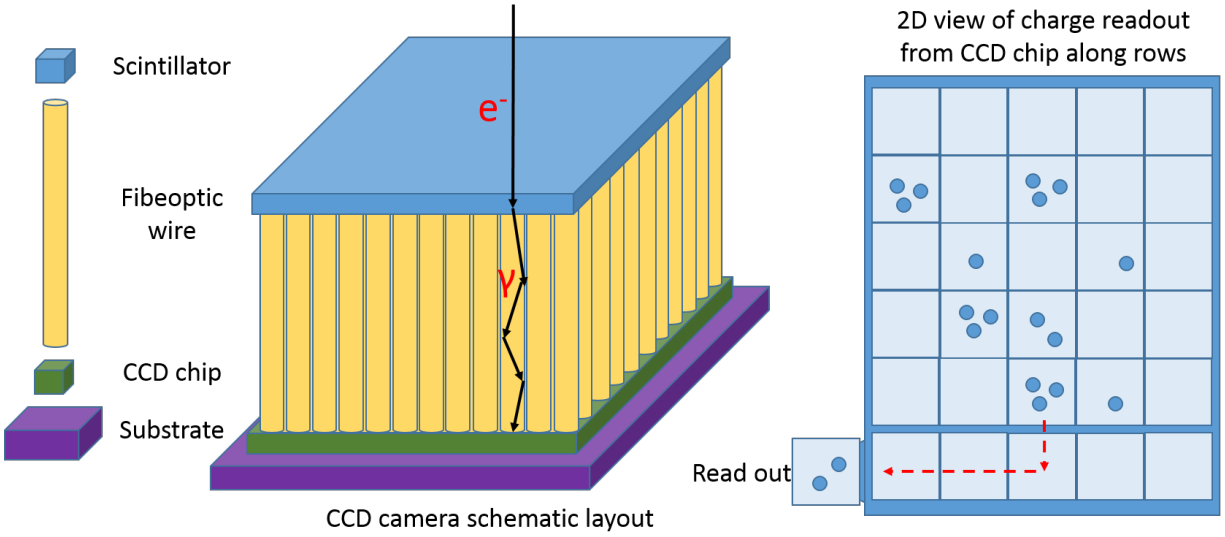

Figure 2.9: A schematic of a CCD camera highlighting the conversion of electrons into photons and the subsequent detection by the CCD chip. An example of the path between the potential well in which the charge of three electrons has been collected and the readout device is shown in red. An applied potential shifts the collected charge first down to a readout line and then across to the readout collector.

The clear advantage of this technology is the ability to reliably record images in a digital format. The substrate material of the CCD chip is often integrated with a Peltier cooling device which combats the thermal noise and can give DQE values of >0.6 [59, 60].

The resolvable frequencies of the detector are also an important consideration. As shown in equation 2.26 the size of the CCD cell ultimately determines the Nyquist frequency that can be resolved. Modern CCD chips have typical pixel sizes ranging from 15μm to 20μm [61, 62]. A disadvantage of CCD over other technologies is that the detectors are comparatively expensive, although since the technology was first commercialised the cost has decreased. A second disadvantage is that the charge in the pixels must be shifted along the array during the read-out step individually introducing a time delay caused by the time taken to shift the charge which prevents fast acquisition from one frame to another. The time required to perform the readout is an important factor in the maximum frames-per-second (FPS) for CCD cameras. The fibre-optic wire required to channel the photons into the CCD chip cause additional noise in the system. Cross-talk in the optical fibres, where transfer of photons from one fibre to another cause an effective blurring of the electrons being counted in each CCD cell. The physical material of the fibre-optic wire features impurities and potentially absorbs photons therefore reducing the overall gain of the system.

The focus on time-resolved imaging in this project is important when discussing CCD cameras as this technology is a common TEM feature and therefore the most likely candidate to compare when assessing future technologies for temporal resolution in digital imaging. In addition to the disadvantages discussed above that affect time-resolution the three major barriers to low time-resolution are the sources of noise affecting the signal-to-noise ratio (SNR) as discussed in equation 2.19; shot noise, thermal noise and readout noise. Readout noise is the most important factor here as there is no time component to the noise added. During the readout of the CCD chip imperfect transfer of the charge from cell to cell and during digital to analogue conversion prevents many CCD cameras from accessing single shot images below milliseconds.

2.5.5 Direct electron detection

The final detector discussed is the Direct Electron Detector which is a modern detector type with advantages over those previously discussed. This detector type is of major

importance in this project and is discussed at length later in the thesis as several calibrations and benchmarks were performed to reach some of the results that are presented. The section on direct electron detectors is split into technology called monolithic active pixel sensors (MAPS), which is currently of great scientific interest in improving TEM, and the detector which is used in this project, the Medipix3. The MAPS architecture is currently manufactured by three companies; Gatan, FEI and Direct Electron. Each company's product shows advantages and disadvantages against each other and previous CCD technology summarised concisely in the paper [57]. This section will briefly compare the difference in architecture between the MAPS technology and that of the Medipix3.

MAPS use an on-chip architecture where doped epitaxial layers are grown onto a substrate to provide a global depletion region which is then patterned with metal-oxide-semiconductor (MOS) devices to apply a bias in a local region forming a pixel. The thickness of the depletion layer is often thinner than the penetration depth of the primary beam electrons meaning that only a portion of the electron energy is converted into electron hole pairs before the incident beam electron is either stopped in the substrate or transmitted in the case of back-thinned MAPS. The electron hole pairs however do not spread over a large area due to the correlation between electron energy and scattering angle therefore the pixel size is not limited by electron stopping distance. The cost per pixel of MAPS technology is dropping quickly compared to other direct electron detectors meaning that much larger cameras are commercially available.

In comparison to the MAPS architecture, Medipix3 disconnects the CMOS pixel detector readout chip from the semiconductor sensor so that the full electron energy is deposited in the silicon material, then the electrons are channelled through the bump bonds into the pixel circuitry below. The thickness of the silicon material therefore must be thicker than used in MAPS. The advantages of this architecture is that there is reduced damage to the CMOS due to protection from high energy electrons by the silicon; increased gain by the detector as the majority of the energy is converted to electron hole pairs; reduced dead pixel space due to surface mounted circuitry which in turn helps determine DQE. The disadvantage of this architecture is that the increased complexity of the design increases

the cost per pixel and increased pixel size of the detector; the lateral spread of electrons in the Medipix3 architecture limits the minimum pixel size of the detector which is higher than can be achieved by MAPS.

The hardware of APS detectors promises improvement to the time-resolution of pixelated detectors such as CCD. The negligible read noise in the Medipix3 detector - discussed later in this chapter - enables the minimum exposure time of a single shot image to be reliably reduced to single millisecond timescales which is an improvement over CCD devices. A resolution of 1ms does not allow us to probe the fine dynamics of domain wall motion which are typically at the nanosecond time scale however opens up new fields of research such as confined systems of lattice skyrmion dynamics. APS technology has seen increased interest in the field of time-resolved imaging with dedicated time-resolved detectors such as Timepix3 capable of nanosecond resolution.

2.5.6 Electron detection and characterisation

In this project a Medipix3 direct electron detector has been used as the primary method of accessing time-resolved information. The key figures of merit in detector characterisation are briefly discussed highlighting those important to the research performed in this thesis. The sources of noise in the system are described in relation to the signal-to-noise ratio available for imaging which is an important aspect in chapters 3&4 where time-resolved single-shot imaging is performed and chapter 5 where nanosecond stroboscopic imaging is performed. Chapter 5 directly investigates the response of the detector and the impact of changing hardware variables. These changes are shown to alter the DQE and modulation transfer function (MTF) of the detector therefore these figures of merit are also discussed here for reference.

Noise is an important consideration in the detection of the image. The source and cause of the noise dictate how the conditions to provide the optimal imaging are found. Three main sources of noise in an image are; shot noise, dark noise and read noise. Shot noise is a consequence of the quantised charge of electrons. The fundamental physical processes that cause the emission of the electrons in the beam are random. Therefore, although the

average flux of electrons incident to the detector may be quantifiable, the distribution of the quantised charge of single electron counts in adjacent pixels will vary with a Poisson distribution shown in equation 2.16

$$P(m) = \frac{e^{-n} n^m}{m!} \tag{2.16}$$

where the probability of a single pixel receiving m electrons per unit time is related to the average number of electrons arriving at all pixels per unit time. The shot noise increases as the square root of the average number of electrons thus although a high flux signal will have a greater magnitude of variation in the Poisson distribution, the ratio to the intensity of the signal will be greater where there is higher flux. The signal to noise ratio is shown in equation 2.17

$$\frac{S}{N} = \frac{n}{\sqrt{n}} = \sqrt{n} \tag{2.17}$$

The shot noise being a property of the beam itself is sometimes referred to as signal noise as it is not generated in the detector itself, because of this it is also the only source of noise that cannot directly be modified by detector hardware engineering.

Dark noise, otherwise known as thermal noise is caused by electrons thermally generated in the detector material. Thermal electron generation is a statistically random event driven by the spontaneous creation of electron hole pairs within the depletion region of a semiconductor device causing a dark current. The dark noise is dependent on the temperature of the detector material with the number of thermally generated electrons varying as a Poisson distribution similar to shot noise.

Read noise is the noise added to the image during the conversion from the transfer of charge in the detector, conversion between charge and voltage and interpretation of that voltage as a discrete number of electron hits. Two of the primary contributions to read noise are the digital to analogue conversion of total charge in a single pixel to an electron hit count where the amplifier adds noise to pixels during conversion process. Secondly in a CCD detector because the pixels are shifted from one pixel to the next until reaching the amplifier there is a noise associated with the flow of charge between one potential well

and the next. These contributions are significantly impacted by the design choice of the detector hardware.

The total signal to noise of these primary sources of noise determines what ranges of exposures a signal with a specific signal to noise ratio can be obtained, where each source of noise is dominant in a different exposure range. The sum of the noises are expressed in equation

$$Total\ noise = \sqrt{\sqrt{PQ(e)t}^2 + \sqrt{Dt}^2 + N(r)^2} = \sqrt{PQ(e)t + Dt + N(r)^2} \tag{2.18}$$

$$SNR = \frac{PQ(e)t}{\sqrt{PQ(e)t + Dt + N(r)^2}} \tag{2.19}$$

The form of this signal to noise ratio has implication on the time-resolution available for given signal to noise ratio where the read noise is commonly large but not time dependent giving a read noise limited exposure at short timescales and electron limited exposure at longer timescales. The Medipix3 detector having an MAPS architecture is resistant to read noise which provides the means to access low exposure images by removing the time independent noise.

The next figure of merit which is also important is understanding the signal-to-noise of the whole system is the DQE. This is a measure of the ratio of SNR in and SNR out of the detector as a function of the spatial frequency of a signal as shown in equation 2.20.

$$DQE = \frac{SNR_{out}^2}{SNR_{in}^2} \tag{2.20}$$

where $\mathrm{SNR_{out}}$ is the SNR of the detected electrons and $\mathrm{SNR_{in}}$ is the SNR of the incident Poisson distribution of electrons. The DQE is clearly an important property of the detector especially in interest on time-resolved imaging. The upper limit on the intensity of the beam in a TEM means that for a single image DQE has a significant implication on the necessary image exposure for a given SNR.

The next figure of merit is the modulation transfer function, which is the ability of the detector to measure the contrast or modulation of specific frequencies contained within the

electron beam. The MTF for a given frequency is the ratio of detected intensity to initial intensity from a perfectly sinusoidal signal of that frequency. A sinusoidal signal shown in equation 2.21 is imaged by the detector. The modulation of the signal is the ratio of the AC component and the DC component as described in equation 2.22 with an example of the sinusoidal image signal shown in figure 2.10A. This is the same form as Michelson contrast often discussed in optical systems.

$$F(x) = a_0 + a_1 \sin(2\pi f x) \tag{2.21}$$

$$M_{in} = \frac{F_{max} - F_{min}}{F_{max} + F_{min}} = \frac{a_1}{a_0} \equiv \frac{AC}{DC} \tag{2.22}$$

The output signal of the detector can then be represented by a modulated version of the input signal where the form is the same, shown in equation 2.23. However because the intensity of high special frequencies are not detected with perfect efficiency the amplitude output signal AC component is suppressed as shown in equation 2.24

$$G(x) = b_0 + b_1 \sin(2\pi f x) \tag{2.23}$$

$$M_{out} = \frac{b(f)_1}{b_0} \leq M_{in} \tag{2.24}$$

where $b(f)_1$ approaches zero at the Nyquist frequency. Therefore the MTF is the ratio of the input signal modulation to the output signal modulations for all range of frequencies as shown in equation 2.25. An example MTF curve is shown in figure 2.10B. The impact on the image intensity for the same frequency varying signal given previously is given in figure 2.10C. It can be seen that high frequency information is lost as the image intensity decreases.

$$MTF(f) = \frac{M(f)_{Out}}{M(f)_{In}} \tag{2.25}$$

For pixelated detectors the highest spatial frequency that can be detected before aliasing occurs is dependent on the pitch of the detector pixels as shown in equation 2.26

$$f_{Nyquist} = \frac{1}{2 \times PixelSize(mm)} \tag{2.26}$$

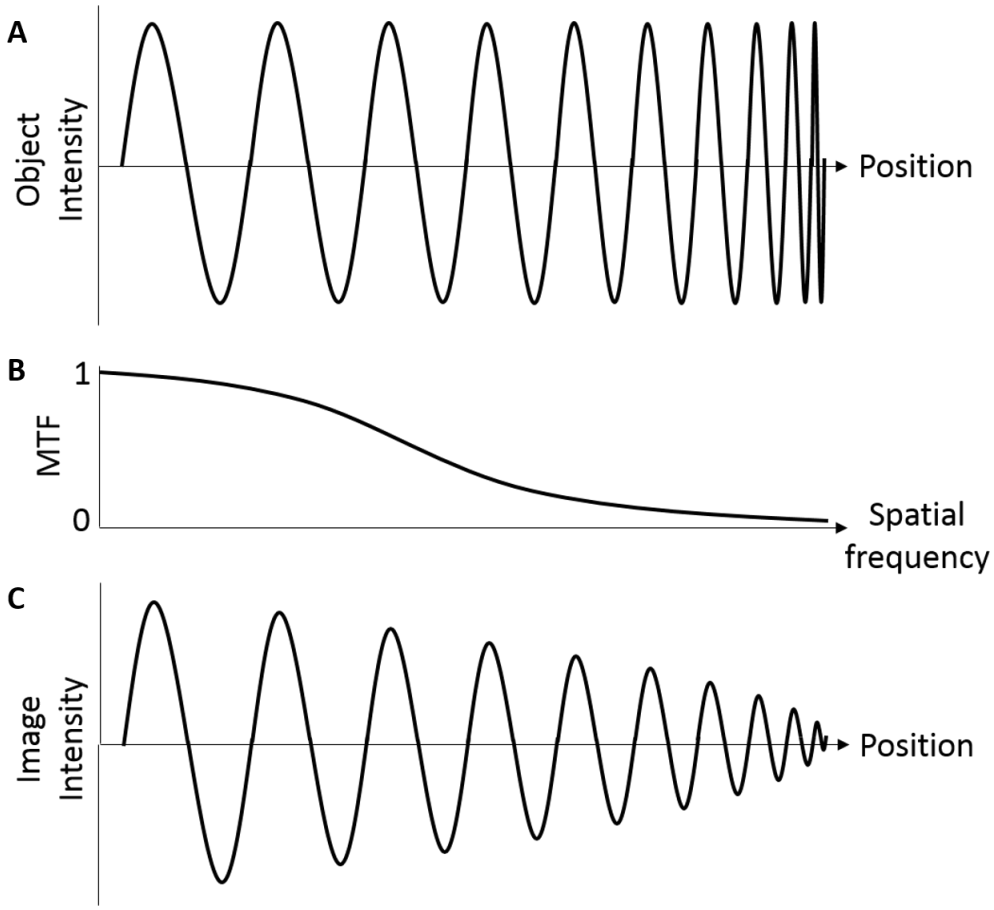

Figure 2.10: The effect of modulation transfer function on the transfer of information from object to image. The top figure shows an intensity spectrum with increasing frequency. The central graph shows the MTF as a function of spatial frequency. The bottom graph shows the reduced intensity for higher spatial frequencies.

2.6 TEM rods and in situ sample excitation

The materials used in this project exhibit many temperature dependent phenomena. To reach temperatures below room temperature a liquid nitrogen rod is used. The liquid nitrogen rod has a dewar connected at the externally accessible section which is then thermally contacted via copper cabling through the interior of the rod to the sample within the vacuum. The sample can be cooled to near the boiling point of liquid nitrogen, 77K. The sample temperature can be adjusted between the limits of base temperature and room temperature by using a proportional–integral–derivative controller (PID) connected

directly to a heating element at the tip of the rod. This device attempts to match the applied thermal energy with the energy lost through radiation/conduction primarily thus reaching thermal equilibrium. This can be stabilised to ±0.1K.

To access temperatures lower than 77K, a liquid helium rod can be used. Liquid helium has a boiling point of 4.2K which allows for a much larger range of temperatures to be accessed however the liquid helium rod comes with more technological challenges. Liquid helium is a super-fluid, this means containing the helium requires both a sealed storage container and rod dewar to control the movement of the helium and a pressure valve to release helium in the gas state. The difference in temperatures also mean that the time during which experimental temperatures can be maintained in the rod is significantly lower than liquid nitrogen only having about a 2 hour duration before refilling is necessary. It is possible to use the rod while connected to the main storage tank allowing vaporizing helium to be vented, however the physical connection causes vibrations to reach the sample and reduces contrast in the imaging.

To investigate material properties at high temperatures a Lightning D9+ rod produced by DENSsolutions is used. This rod provides eight electrical connections onto specially designed chips which provide in-situ TEM Biasing and Heating. In this thesis, the Lightning D9+ rod is used in combination with Wildfire nano-chips also produced by DENSsolutions. Wildfire chips feature electron-transparent windows adjacent to patterned nanowire structures designed to increase the temperature of the windows by Ohmic heating. The patterned nanowires enabled 4 point probe resistive measurements to enable heating at a rate of 200Kms^{-1} when monitored by the PID controller up to a temperature of 1773K.

An alternative method of sample heating to access the faster thermal timescales uses laser pulses injected into the TEM column. Laser pulses are focused onto the sample to cause rapid local heating. The timescale of this heating is determined by the pulse duration of the laser. Due to the interaction between photons and the sample material, heating from laser pulses on the timescale of picoseconds and below are not considered as pure thermal heating. At these short pulse durations the three temperature model is more accurate in describing the conversion of photon energy to thermal energy. Rather than considering the

energy in the sample as a single quantity the three temperature model considers energy of thermal electrons, spin response and lattice temperature as independent systems with transfer of energy between these systems occurring over separate timescales. Although laser induced heating is not featured in this thesis, it is discussed with regard to time resolved TEM imaging and a comparison to conventional heating.

The objective lens of the TEM microscope is usually turned off during most magnetic imaging modes due to the high magnetic field that is produced whilst active of approximately 1T as this would cause most magnetic materials to field polarize. A small amount of current can be applied to weakly excite the objective lens producing only a fraction of the magnetic field. The objective lens is best suited for static studies of applied magnetic field however the field can be increased with a timescale of 500ms accessing the ordered and lattice magnetic dynamics.

2.7 Sample fabrication

In sample fabrication there are two methods, these are known as the top-down or bottom-up approach. The top-down approach uses the modification of a bulk piece of material, processes such as etching and milling remove unwanted material to expose the pattern desired. The process is limited by the resolution of the tools you can use. The bottom-up approach is often described as nature's approach as it uses smaller components to build up to bigger ones. This method allows the smallest patterns to be created however the mass production of the bottom up approach is difficult. In this project both methods are used for creating the samples. Although there are many processes required such as sample cleaning and resist spinning, only major equipment will be discussed and how they impact the production of the project samples. The bottom-up method of Electron beam lithography with metal deposition and the top-down method of Focused ion beam (FIB) lithography.

2.7.1 Electron beam lithography

Electron Beam Lithography (EBL) is a technique where a focused electron beam weakens selected areas of an electron sensitive resist exposing a pattern created using computer software which allows these sections to be removed. This allows material to be deposited across the entire sample with only select areas having metal deposited on the nitride surface. Once the resist is removed only the areas etched before being metallised will remain. This process is shown in figure 2.11

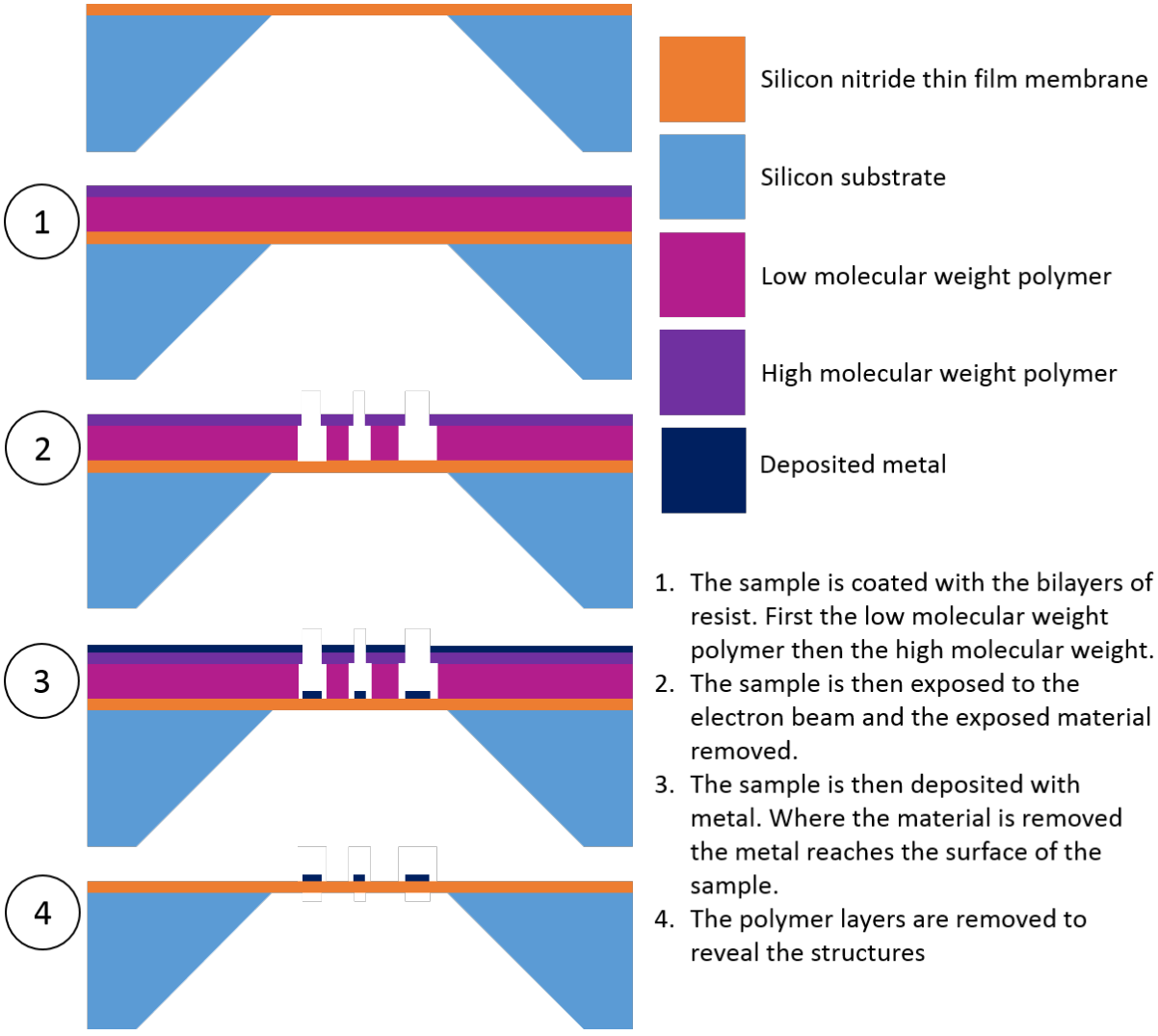

Figure 2.11: A step-by-step diagram demonstrating a bi-layer electron beam lithography technique used to create nanostructures

The key parameters when using an EBL tool include spot size, spot spacing and dose. These parameters must be individually tailored to suit the needs of the device being fabricated. Spot size and spacing define the theoretical resolution of the device however these must be weighed up against the beam writing time required. The dose of electrons used when writing the pattern is critical in correctly exposing the type and thickness of resist used, if the electron count is too small resist will remain post-processing and no metal will contact the membrane, too high dose will over expose the resist and an inflated image of the pattern will be removed. Although many standard recipes exist, additional factors, such as the material the resist is mounted on, can significantly alter the exposure. This is due to electron interactions differing in standard silicon wafer (for which many standards relate) and silicone nitride. Dose tests are a common first step when fabricating a new sample. Software created by Stephen Thoms, Beamwriter Exposure Layout for Lithographic Engineers (BELLE), allows the same pattern to be written in an array with each iteration using a different dose. This allows comparison and improvement to the dosage used. In this project EBL is performed on a Vistec VB6 UHR EWF electron beam lithography tool capable of spot size resolutions approximately 4nm.

2.7.2 Thin film metal deposition

The deposition of thin film metals during this project was performed using a combination of thermal evaporation and electron beam evaporation. These are both classified into the category of physical vapour deposition (PVD) techniques where the material is converted into a gas directed at the sample coating it upon impact.

Thermal evaporation uses a crucible in a vacuum chamber filled with pellets of the material to be deposited which is heated up till the material melts and subsequently evaporates onto the membrane which is secured at a known distance from the boat.

Electron beam evaporation has some advantages to standard thermal evaporation. The technique uses a solid ingot of the material which is bombarded by electrons where the kinetic energy of the electrons is converted into thermal energy causing the material to evaporate. The electrons are created by an electron gun commonly a thermal source which

is then focused into a beam. The beam is then deflected by static fields which position the beam onto the metal ingot. The evaporation by electrons can be finely controlled allowing the rate of deposition to be as low as 1nm per minute when used in conjunction with a thin film thickness monitor which is often a quartz crystal micro balance.

Both thermal and E-beam evaporation are considered to have good directionality, a quality that denotes the angle at which evaporated atoms reach the substrate which is important in EBL in preventing the side walls of the undercut being coated with metal causing unwanted flagging and problematic liftoff.

2.7.3 Focused ion beam lithography

The focused ion beam (FIB) in this project - FEI DualBeam FIB System - uses a 30kV gallium ion beam to accurately remove material via kinetic bombardment [63]. Ga^+ ions impacting the surface of a material impart kinetic energy causing sputtering of the material. This is show in figure 2.12. The construction of the FIB column is analogous to the TEM column. Although Ga^+ ions are positively charged and significantly heavier than electrons, the Lorentz force experienced allows them to be lensed similarly. The spot size that the beam is converged to controls the feature size created by removed material. The spot size of a modern FIB can be ~5nm which can create feature sizes of approximately 10nm. The rate which material is sputtered from the sample is controlled by an aperture in the column limiting the total intensity of Ga^+ ions reaching the sample. Therefore both small features and relatively large surfaces can be milled at a controllable rate. When the kinetic energy is given to the surface material there is a side effect of implantation of Ga^+ ions in the material causing changes to the near surface layers of the material. This side effect is predominantly considered to be a negative trait of FIB milling however it can be used to purposely alter the magnetic and structural properties of the material creating local alloying or defect sites.

The FIB has a few distinct roles in this project; preparation of electron transparent lamella for TEM and patterning thin film layers deposited through thermal evaporation for plasmonic experiments in collaboration with EPFL.

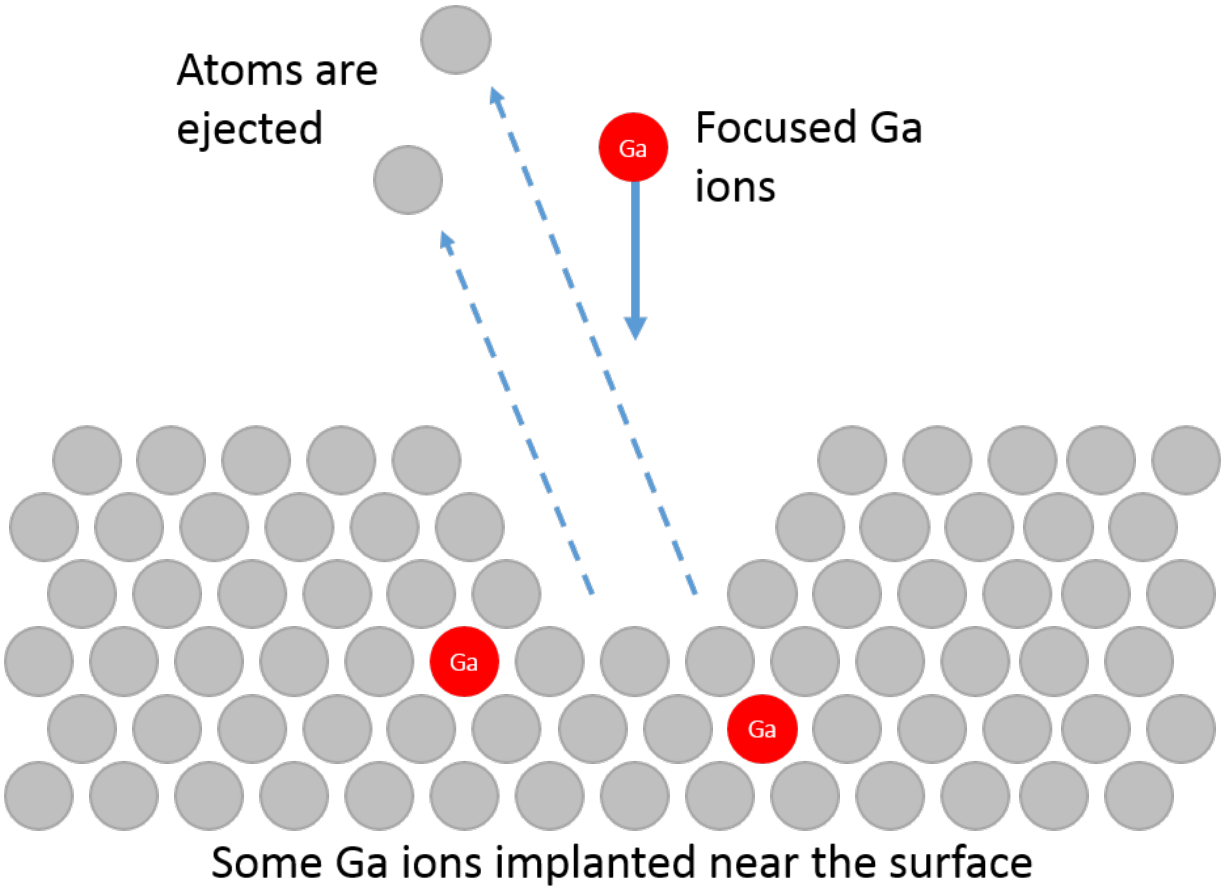

Figure 2.12: A diagram showing the removal of atoms from a material by accelerated Ga+ ions. The red Ga atoms in the material are implanted ions

The preparation of electron transparent samples from bulk material was performed by the following steps. The bulk crystal is glued onto a metal stub for use in the FIB. The bulk crystal is polished through conventional mechanical milling to reduce the size of the material and to remove any glue revealing the surface of the crystal. The FEI DualBeam FIB features a level of automation in sample preparation through the lift-out technique. Alignment markers in the form of crosses are milled into the material which are then identified through pattern recognition and used to align the area selected for milling. These alignment markers are shown in figure 2.13A at both sides of the lamella spaced 20μm apart. Next, due to the destructive nature of ion irradiation, electron beam deposited platinum is deposited onto the surface of the bulk material to provide a protective layer. This electron

beam deposited material is both soft to high dose irradiation and slow to deposit, however it allows ion beam platinum deposition over the top. The ion beam deposited material provides a hard protective layer that can be deposited at a much faster rate than the electron deposited material. This layer is increased to about 1-2um thick which is shown in shown figure 2.13A between the two alignment markers. Trenches are milled using a decreasing range of currents to isolate a lamella approximately 1μm thick. The milling is performed by first removing material in wide shallow cuts and then progressing towards the area that will form the lamella with increasingly deeper cuts forming a trapezoid shape on both sides of the lamella. As the material being removed approaches the lamella the beam current is reduced with the final beam current used typically being 1nA in this thesis. The beam current is reduced to prevent deep ion implantation into the lamella. This lamella is revealed after trench milling in figure 2.13A. The lamella is then undercut in an L shape incision so that only a single side of the lamella is still in contact with the bulk sample. Evidence of this can be seen in figure 2.13B where the lower trench has milling marks from the ion beam passing through the bottom of the material. The FIB at Glasgow is fitted with an Omniprobe device capable of manipulating small lamella of material allowing the sample to be removed from the surface of the material. Platinum is deposited connecting the lamella to the Omniprobe before the final side of the lamella is milled to disconnect it from the bulk crystal. The sample stage is lowered to isolate the lamella from the bulk material as shown in figure 2.13C. This lamella is then attached to a sample holder substrate, typically a copper sample holder featuring copper fingers or a Wildfire chip were used in this thesis. Figure 2.13D shows a copper finger with the previously removed lamella attached using platinum. At this point the lamella must be milled, ideally on both sides, using increasingly small beam currents to reduce the thickness of the material to below 100nm while reducing the damage caused by ion milling. A common procedure is to use a 300pA current down to 500nm, followed by a 100pA current down to approximately 100nm followed by a low keV polish in which the 30keV ion beam is reduced to 5keV and the surface is milled at a high angle of 7° to the surface to remove 10-20nm of material with minimal ion beam damage.

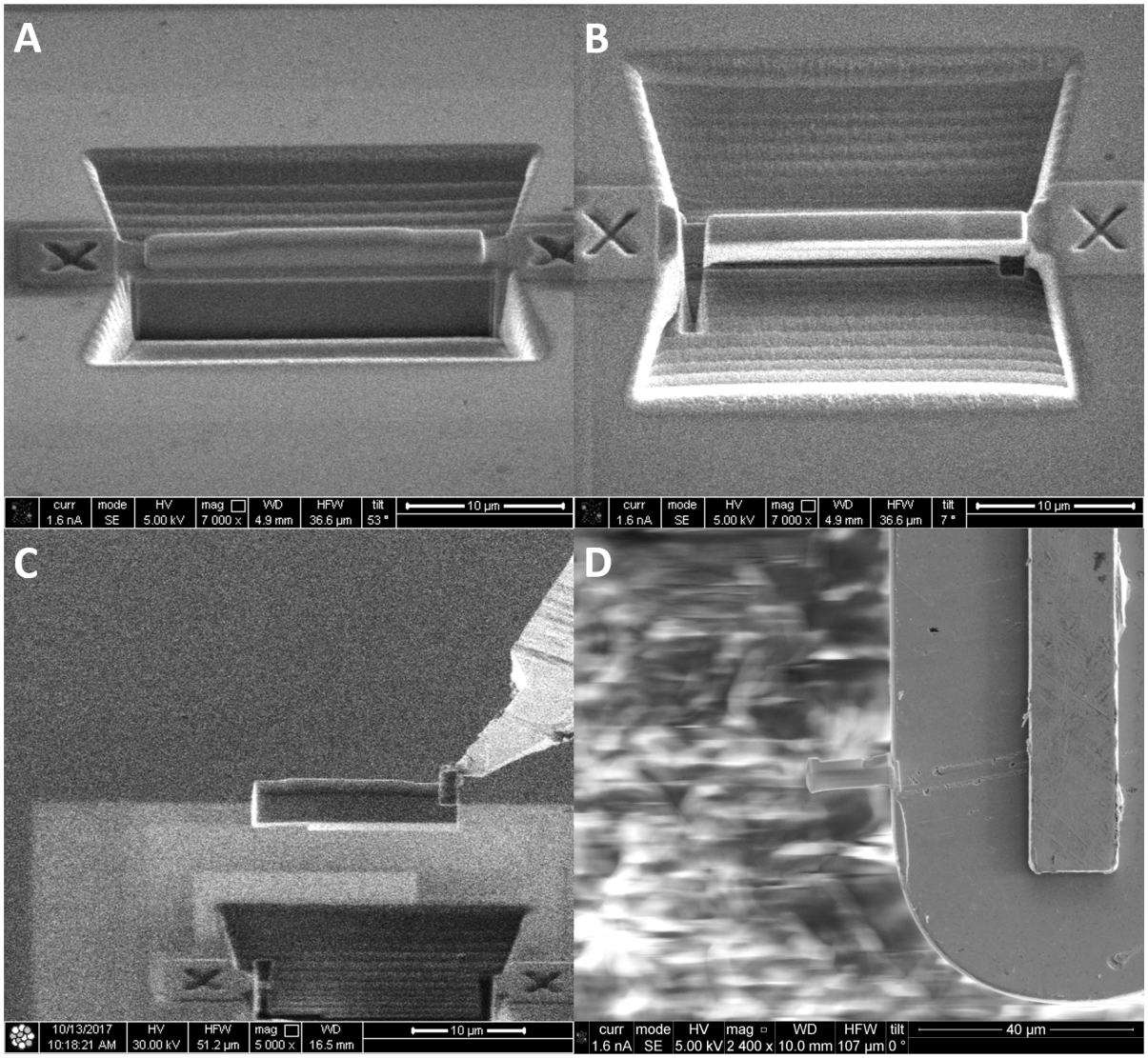

Figure 2.13: A typical example of the FIB lift-out process. Figure A shows the lamella revealed after trenches on both sides have been milled. Figure B shows the preparation to lift-out the lamella by creating an undercut in the material. Figure C shows the lamella cut free from the bulk material. Figure D shows the lamella after being joined to a substrate.

The FIB has been used in the production of nano-cavities for plasmonic work in collaboration with the LUMES group, EPFL, Switzerland. The FIB was used to accurately remove silver from the surface of a TEM membrane providing a clean and defined cavity while keeping the silicon nitride layer beneath the silver intact. This material removal is conducted in a series of linear cuts to create structures promoting plasmonic dynamics.

2.7.4 Plasmonic nano-structure fabrication

This section details the fabrication of plasmonic nanostructures as part of a collaboration with the Lumes group, École Polytechnique Fédérale de Lausanne (EPFL) as part of this thesis. The samples were designed with the purpose of demonstrating ultra-fast time resolved plasmonic excitation within the modified JEOL JEM-2100 TEM at EPFL. The planned fabrication included two separate types of plasmonic nano-structures.

In the first set of experiments, 40nm of gold was deposited onto Si_3N_4 by means of electron beam deposition as discussed in section 2.7.2 using bi-layer PMMA and electron beam lithography to define the structure geometry as discussed in section 2.7.1. These structures are shown in figure 2.14 which displays a sample containing three separate plasmonic designs referred to as; antennas, chains and bow-ties as part of this project. EBL enabled the gold nanostructures to have a resolution of approximately 10nm.

The second set of experiments used 40nm of silver deposited directly onto the Si_3N_4 and then patterned using the FIB, where material was removed using the Ga^+ ions in lines with a width of 50nm. Figure 2.15 shows some patterns written with the FIB for the purposes of plasmon interferometry. Figures 2.15A&B show how milling depth can be attained without damaging the Si_3N_4 layer and removing structural integrity from the sample. 2.15A shows a row of lines cut with different mill depths from left (Deeper) to right (Shallower) and imaged with electrons. The lines towards the left are slightly wider and have no remaining material. The lines towards the left are thinner however have some stray silver. All of the lines appear dark because the electron image was not sensitive to the Si_3N_4 layer. Figure 2.15B shows an image taken with the Ga^+ beam which is sensitive to the Si_3N_4 layer and proves that the layer remains intact for all depths shown in this image. Figures 2.15C&D show the designs similar to those found in Lin *et al.* [64], in which the cavity geometry promotes emission of plasmons in specific directions. Figure 2.15E shows extended cavities milled by overlapping lines to remove and area of material. The purpose of these cavities was to change the direction of incoming plasmons through reflection. Finally 2.15F shows some geometries designed for the purposes of investigating plasmon interferometry.

The work in collaboration with the Lumes group at EPFL resulted in papers published regarding the ultra-fast imaging of plasmonic samples in dynamic transmission electron microscopy [65, 66]

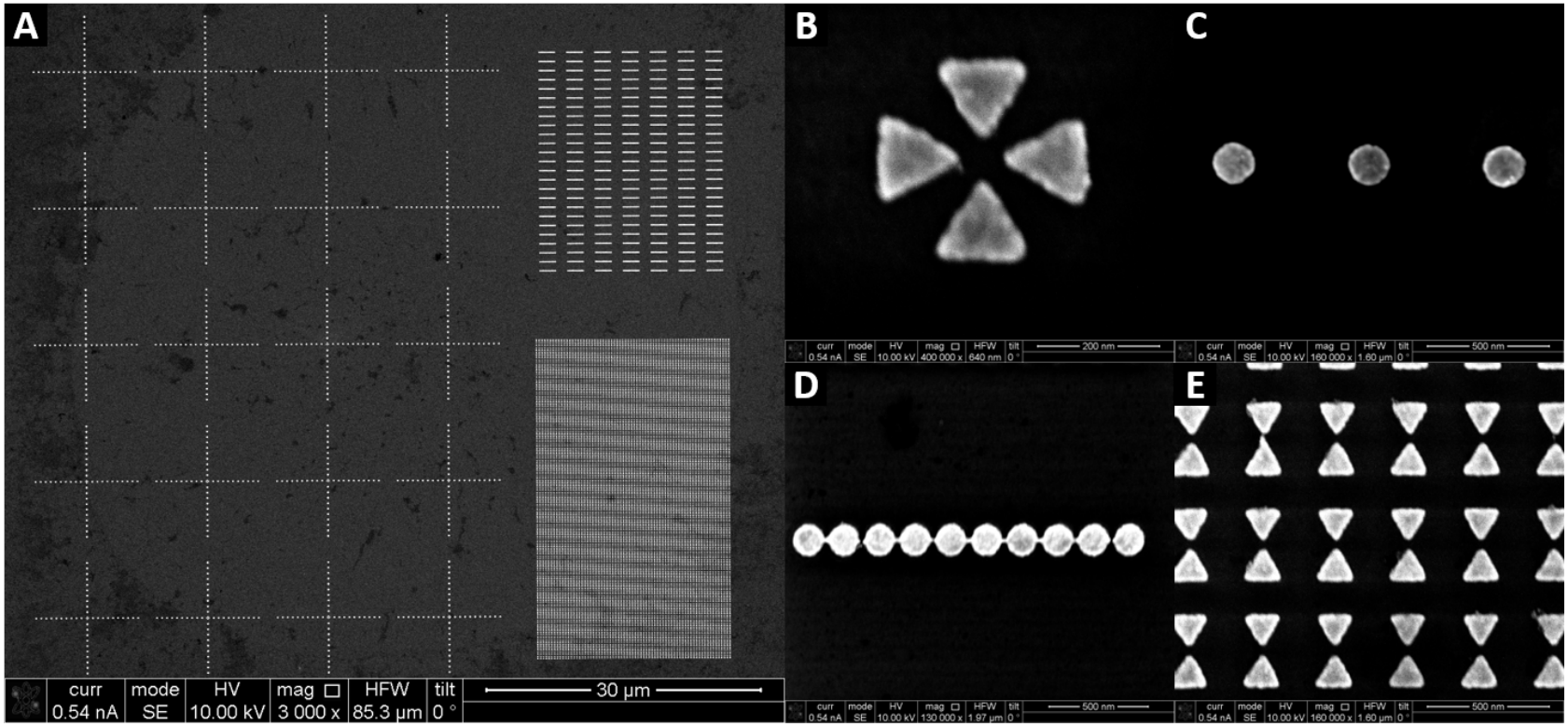

Figure 2.14: Gold plasmonic nanostructures deposited onto Si_3N_4 electron transparent windows. Figure A shows the layout of three nano-structure sets, Antennas, Chains and Bow ties. Figure B shows the centre of the antenna structure with figure C shows a close up of the surrounding gold disks. Figure D shows a set of 10 skyrmion disks in a chain. Figure E shows a magnified image of the bow tie design highlighting the gap between the two structures.

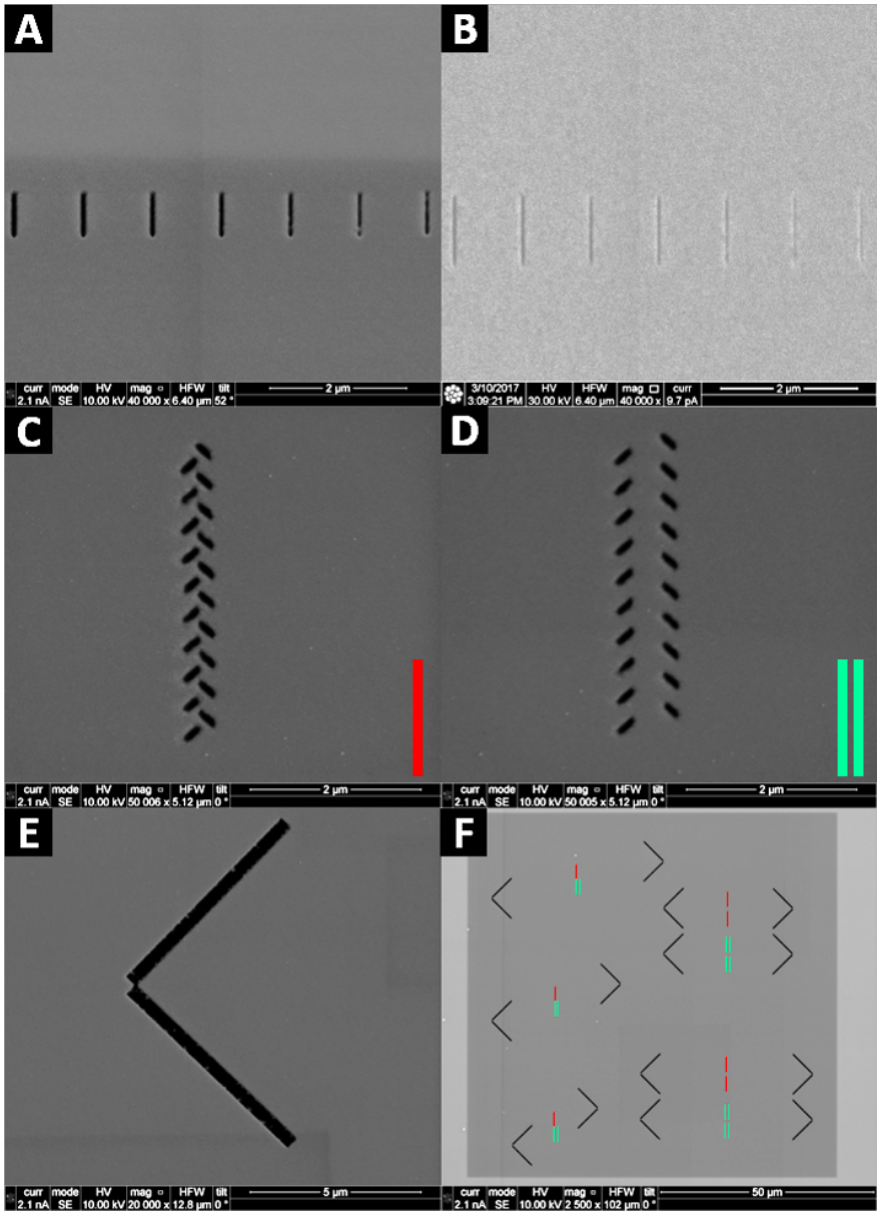

Figure 2.15: Silver thin-film patterned nano-structures deposited onto Si_3N_4 electron transparent windows. Figure A shows a FIB milling test section in which the depth is reduced from left to right imaged with the electron beam. Figure B shows the same section imaged with Ga^+. Figures C&D show patterned geometries designed to produced plasmons in specific directions. Figure E shows cavities designed to reflect the plasmons. Figure F shows an example of final experimental setup with plasmonic interferometers (Patterning is substituted for lines for clarity).

Chapter 3

Millisecond time-resolved skyrmion lattice dynamics in Cu_2OSeO_3

3.1 Introduction

In this chapter, the results of millisecond time-resolved Lorentz imaging performed on the magnetic chiral material copper oxyselenide Cu_2OSeO_3 during a magnetic field induced transition between the helical phase and skyrmion phase are presented. The introduction section 3.1, describes the time scales of magnetic dynamic processes and the instrumentation available for investigating those regimes. The potential role of time-resolved TEM is discussed, leading to a brief introduction to the current state of progress in the field of skyrmion lattice research. In section 3.2, the experimental method of controlling and imaging the magnetic phase transition in Cu_2OSeO_3 is detailed. In section 3.3, the Fresnel images taken using the Medipix3 detector are presented including details of the post processing performed. The image stack is processed and presented in a symmetry time space format to highlight the magnetic phase change in response to the time varying magnetic field. Three dynamical processes are identified and presented separately: skyrmion lattice rotation dynamics facilitated by 5-7 defects in section 3.7, helical to skyrmion phase transition dynamics in section 3.6, and meta-stable skyrmion creation and annihilation, where isolated skyrmions and skyrmion clusters appear over the space of 1-3 frames, before

disappearing in section 3.5.

Magnetic skyrmions are topologically stable quasi-particles. They have become a major field of research since their theoretical prediction in 2001 [67] and subsequent experimental discovery in 2009 [18]. This topological stability is afforded to magnetic skyrmions by the large energy barrier required to change the topological number, as this change requires a magnetic state similar to a discontinuity (or magnetic monopole). Skyrmions are shown to exhibit short range repulsion and long range attraction between one another, preventing skyrmions in confined nanostructures from annihilating each other and causing skyrmions to self-order in hexagonal lattices. Atomic crystal structures are held together in a similar manner with Pauli repulsion at short range where electron clouds repel and van der Waals force at long range. Although the energy scales and distances are different, the basic physics of this form of energy landscape is comparable. Research into skyrmions, therefore, provides a stable structure from which investigations into fundamental physical phenomena such as spin-orbit coupling and the Dzyaloshinskii-Moriya interaction (DMI) can be performed. Early investigations regarding skyrmions involved imaging skyrmion lattices at fixed magnetic fields and temperatures to map the phase space for which they appeared to spontaneously exist. Materials with the B20 crystal structure such as MnSi [18, 19], $Fe_{0.5}Co_{0.5}Si$ [20, 21]and FeGe [22] exhibit magnetic chirality caused by the asymmetric exchange coupling discussed fully in chapter 2. Recently, more exotic materials such as Cu_2OSeO_3, formed from a non-centrosymmetric $P2_13$ space group, display unique properties such as electrical insulation unlike the B20 crystal materials which are conductors [25]. Cu_2OSeO_3 therefore provides an interesting material for perusing purely spintronic applications where spin current rather than electrical current is dominant. The range over which the skyrmion phase space exists is primarily material dependent, but thin films are shown to exhibit a significantly broader skyrmion phase range than bulk materials. The response of skyrmions to external stimuli is of great scientific and engineering importance in realising skyrmion based magnetic memory. Many hardware architectures for integration of skyrmions with classic computer electronics have been proposed, where fine control of skyrmion creation with electric and/or magnetic fields is required. Examples

of skyrmions applied to computing include single skyrmions representing binary data on racetracks as a alternative to domain walls, where sidewall pinning is an inherent problem [34, 35, 68, 69, 70], and skyrmion logic gates providing entirely skyrmion-based binary operations which may even replace current processors [36, 71]. In order to realise these technologies the dynamic processes and timescales of skyrmions must be fully understood.

The dynamic processes in magnetism have a broad range of timescales from the precession of a single spin to the macroscale domain motion in bulk magnetic material. The techniques used to investigate these dynamic processes often require a trade-off between spatial resolution, temporal resolution and repeatability. The techniques used to probe magnetisation dynamics from femtoseconds to seconds are discussed here including the available spatial resolution.

The fastest magnetic timescales are accessed in the femtosecond regime with ultra fast laser pulses exploiting the magneto-optical Kerr effect (MOKE) [72, 73, 74] or X-ray magnetic circular dichroism (XMCD) [75, 76], where separation of the electron, spin and lattice temperatures give rise to dynamics between femtoseconds and tens of picoseconds [77]. This allows the bulk fundamental properties such as the phase of the material to be investigated, however, the advantage of ultra fast time resolution comes at the cost of spatial resolution. Both of these techniques are based on analysis of the absorption spectra from illumination of an area of material. This makes these techniques inapplicable to investigating dynamic processes where the position of a topological structure is of interest. The second drawback of these techniques is that they often need the process to be repeatable to perform pump-probe measurements for acceptable signal-to-noise levels at such short probe durations. A third technique which is rapidly developing due to emerging technology is dynamic transmission electron microscopy (DTEM). DTEM has the potential to open the field of ultra fast magnetism to spatially resolved imaging. The electron beam probe is driven by the photoelectric effect of pulsed lasers inside the TEM column. The temporal resolution of DTEM is therefore on par with optical techniques which have pulse widths between fs and ns. Although DTEM still requires the pump-probe element of ultra fast microscopy, the spatial resolution is significantly improved. DTEM has demonstrated

the ability to image plasmon excitations occurring on the femtosecond timescale [65, 66].

In the picosecond to nanosecond regime, understanding of the magnetic state can be accessed through ferromagnetic resonance (FMR) where MHz to GHz oscillating magnetic fields provide absorption spectra indicating the sample magnetisation [78, 79]. The spatial resolution of FMR is determined by the strength of the signal detectable and therefore the minimum size of the sample. FMR is often performed on bulk materials, thin films or repeated structures where, although the individual structure magnetisation is not probed, the average response provides understanding of the magnetic response of the individual structure.

Nucleation of topological structures such as magnetic skyrmions and domain walls occur in the nanosecond regime. These processes are often investigated through micro-magnetic simulations where meshes can be used to group many spins in nanometre volumes, in which the average spin is considered justifiably accurate. These simulations calculate the motion of spins through application of equations which predict the processional motion of spin, using models such as the Landau–Lifshitz–Gilbert equation [80]. These provide an important comparison when investigating dynamics on timescales with instruments unable to provide appropriate spatial resolution. Instruments such as neutron diffraction and X-ray diffraction (XRD) are capable of producing reciprocal space images sensitive to repetitive arrays of nanoscale topological objects at nanosecond temporal resolutions. However, these techniques are not sensitive to the real space variations in magnetism, making the instruments useful at investigating the phase response of materials but unable to fully resolve individual magnetic structures such as skyrmions. At the nanosecond time regime magneto-optical Kerr effect (MOKE) microscopy is capable of performing single shot imaging due to the intensity of lasers used and therefore an abundance of photons providing sufficient SNR to resolve local topology. The spatial resolution of MOKE is limited by the optical probe diameter which is limited by the wavelength of light.

The macro-scale motion of topological magnetic structures, such as skyrmion lattices and domains, have been investigated in time regimes from seconds to milliseconds. Skyrmion lattice dynamics simulated in nanodiscs are shown to rotate on a millisecond timescale in

the presence of a thermal gradient. Experimental investigations of FeGe nanodiscs show rotation three orders of magnitude slower over seconds [81].

Above the second time regime, the primary sources of magnetic dynamics are through creep motion where very low driving forces cause motion over long timescales [82, 83, 84]. The slow dynamics at these timescales provide an opportunity to investigate the spatial variation of topological objects in detail. Access to the finer internal structure and detail of skyrmions has typically been performed by TEM, where the highest resolution is achieved by DPC (differential phase contrast) imaging. As discussed in chapter 3, DPC is a scanning method which requires seconds to acquire a full image, making it unsuitable for dynamic imaging [85, 86]. Fresnel imaging as a parallel illumination mode is not limited in this way, making it a superior choice for imaging dynamic processes in a TEM. However, the time resolution is ultimately limited by the number of electrons contributing to an image due to noise.

The phase transition of skyrmion materials between the helical phase and the ordered skyrmion lattice phase is not well understood. Although their locations on the field-temperature graph have been mapped for many materials, the imaging techniques with the spatial resolution required to generate real-space images of skyrmion lattices do not have the time resolution required to dynamically image the process of skyrmion creation. Research performed using reciprocal space imaging methods of XRD and neutron diffraction have made progress in identifying dynamic processes in skyrmion lattices [87].

Control of skyrmion lattice rotation has been demonstrated with application of static magnetic fields in Cu_2OSeO_3 by Mochizuki at Aoyama Gakuin University, Japan. Their observations performed using Lorentz TEM suggest continuous rotation of the lattice attributed to magnons generated through beam heating [81]. Additional research using soft X-ray scattering has found evidence of multiple skyrmion domains present in the sample. During sample tilting in the presence of a magnetic field, the six-fold diffraction pattern associated with the skyrmion lattice split into eighteen spots. It is predicted that these spots are the superposition of three sets of six-fold symmetric patterns, each corresponding to a skyrmion domain [88].

The experiment proposed here presents the unique application of the Medipix3 detector in accessing millisecond single-shot real-space TEM images. The time resolution of TEM is pushed to the low millisecond regime by removing read noise from the image acquisition, increasing the signal-to-noise ratio for low duration exposures. The detector-based modification maintains the high quality spatial resolution capable of imaging the structure of an individual skyrmion. With access to real space information in the millisecond regime we hope to access information on the geometric motion of individual skyrmions during motion caused by both the phase transition and magnon induced rotation.

3.2 Experimental design

The investigation of the magnetic dynamics during the transition between helical phase and skyrmion phase in Cu_2OSeO_3 was investigated with Fresnel imaging in a JEOL ARM200cF (ARM). Sequential imaging is performed, triggered manually immediately before a manually operated field ramp causing the transition, performed at static temperature. This sequential imaging creates a time-resolved movie of the phase transition.

The Cu_2OSeO_3 bulk material was thinned to electron transparency using a focused ion beam (FIB) instrument in École Polytechnique Fédérale de Lausanne, Switzerland. The lamella of material is removed using a nano-manipulator and attached to a copper slot using tungsten. The sample was then inserted into the liquid helium rod to decrease the sample temperature below the critical temperature of the helical phase (60K) and the skyrmion temperature of Cu_2OSeO_3 - 20K.

The weakly-excited objective lens was used to provide a time varying field from 0 Gauss to 519 Gauss with the field saturated at ~3000ms. The change in the strength of the objective lens caused the trajectory of the beam to be altered during the field ramp, this caused a deflection the field of view by 300nm. The shift is observed during the initial field ramp in the helical phase, it has an average velocity of 0.42nm/ms equating to 4.6nm per frame in the helical phase, which compared to the periodicity of the helical lines (70nm) is small. During the transition between the helical phase to the skyrmion phase, the shift has

an average velocity of 0.08nm/ms equating to <1nm per frame which has minimal impact on the identification of skyrmions.

The CCD camera installed on the ARM, a Gatan Orius camera is unable to perform at a high frame rate of imaging with a maximum ~14 fps real-time, therefore, the Medipix3 direct electron detector was employed due to its maximum frame rate of 1200fps. The Medipix3 detector was also used in this experiment to maximise the signal-to-noise ratio in the images compared to that available by the CCD cameras which are limited by readout noise at fast exposures.

The effect of exposure time on the magnetic contrast was investigated for exposures between 10ms and 1ms. The sequential images are separated by a gap time of 1ms during the detector readout. Exposure of 10ms provided enough contrast to correctly identify the skyrmions above the background material both visually and through the use of computational peak finding. Data-sets were recorded in sequences of 1000 images with an exposure duration of 10ms per frame.

3.3 Individual skyrmion images

The time resolved data contains 1000 sequential images in a stack where each image is taken with an exposure of 10ms with a 1ms readout gap time between them, resulting in an 11s image stack. Figure 3.1 displays two frames A & B containing real space images and frames C & D containing reciprocal space images respectively. Figure 3.1A is frame 1 of the data-set showing the initial magnetisation landscape before any field is applied. The helical magnetic state is visible as alternating black and white stripes, as expected for Fresnel mode imaging. The direction and symmetry of the lines is shown in 3.1C as two spots with orientation perpendicular to the direction along the real image lines. Figure 3.1B is frame 803 of the data set, which is significantly after the field increase and therefore is taken in a static out-of-plane magnetic field of 519G. The skyrmion lattice is visible as a hexagonal array of black dots indicating the over-focused Fresnel mode condition. In the bottom left hand corner of the image, the edge of the sample can now be seen. As

discussed previously, the shift in the optical conditions due to the objective lens weak excitation has caused the field of view to shift to the edge of the sample. The six-fold hexagonal symmetry of the skyrmion lattice can be seen in 3.1D with more low spatial frequency noise due to the presence of the sample edge.

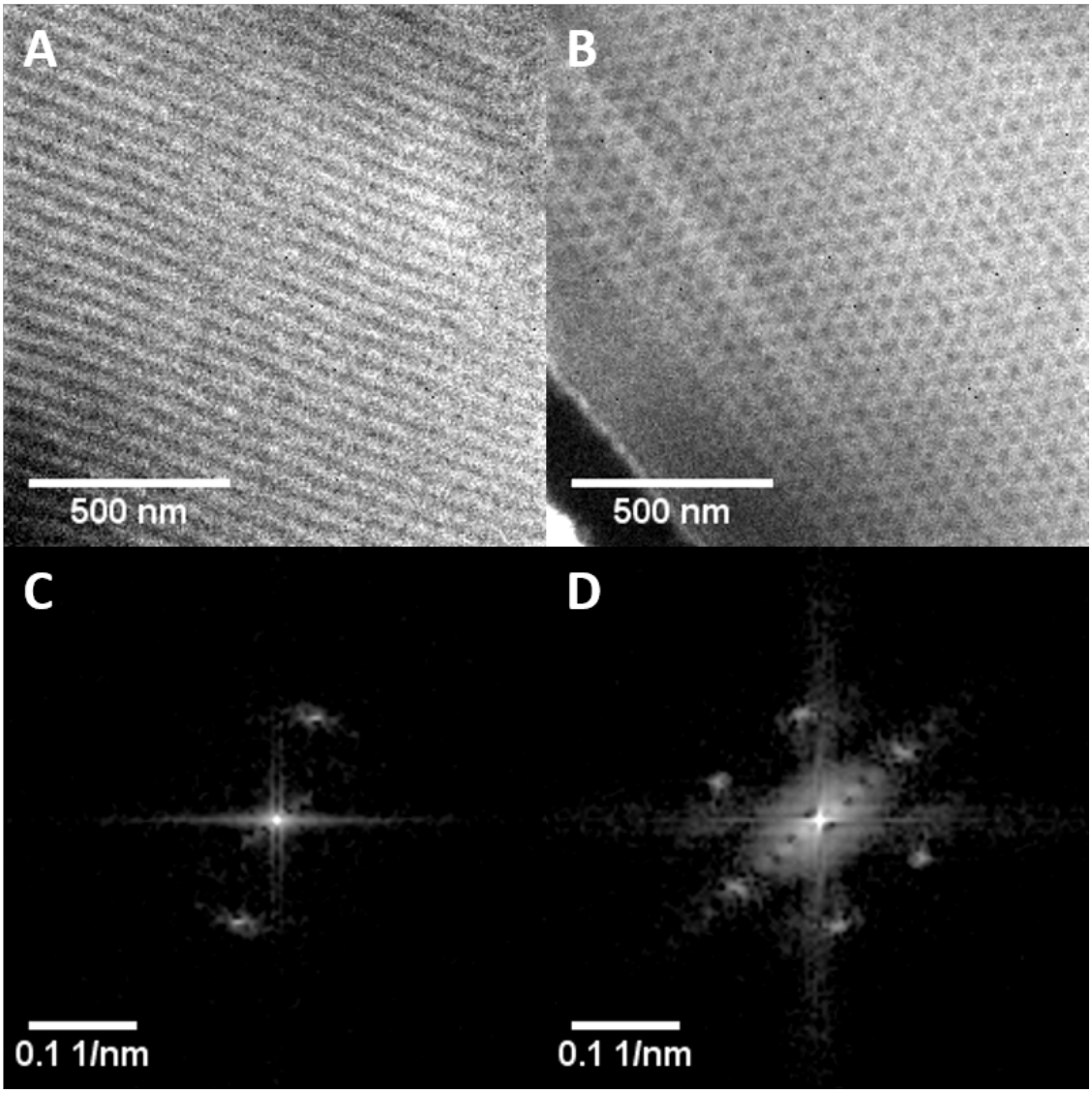

Figure 3.1: This figure highlights magnetic structure from both the helical phase in figure A (Frame 1) and the skyrmion phase in figure B (Frame 802). The reciprocal symmetry is shown for both magnetic phases in C & D respectively.

3.4 Projecting magnetic state information in time

To present the change in the magnetic state through time, the fast Fourier transform (FFT) images were used as they relate dominant spacings/periodicities and directions present in an image thereby presenting the magnetic structure in $\vec{k}$-space. The FFTs of each frame are radially unwrapped so that the bright spots align along an axis representing the $\vec{k}$-vector angle, and in the other axis representing position in $\vec{k}$-space. Now that the $\vec{k}$-space information is aligned in a single dimension, this allowed projection of a single $\vec{k}$-spacing or a range of $\vec{k}$-spacings over all orientations in time. This process is shown for a single frame in figure 3.2, where the real space image in figure 3.2A is fast Fourier transformed into figure 3.2B. Figure 3.2C shows the unwrapping of the FFT using red arrows to highlight the process. The red arrow which curves around the image at a constant distance from the centre of the FFT is unwrapped maintaining this distance till it is straight after being radially unwrapped, preserving the $\vec{k}$-space distance now along the x-axis. Finally, figure 3.2D shows the projection, in blue, of a single $\vec{k}$-space value through four unfolded FFTs. As the projection moves through the four images dominant $\vec{k}$-spacing spots can be seen to change between helical and skyrmion. These projections are referred to from here as the time evolution profile (TEP) of the image stack. Each TEP has an associated $\vec{k}$-spacing which it was projected through.

The $\vec{k}$-space slices can be stacked together, however, this does introduce some error into the image due to a mismatch in the contributing number of pixels. When the images are radially unwrapped, the number of pixels used to create the lower $\vec{k}$-space TEP is smaller than higher $\vec{k}$-space TEP. This is due to the change in the circumference of the circle for different $\vec{k}$-spacings when selecting a single isofrequency ring. Therefore, two images with very different $\vec{k}$-vectors will appear to blur when summed if the difference in circumference is too large. Three values of $\vec{k}$ = 0.0179 nm^{-1} (24px), $\vec{k}$ = 0.086 nm^{-1} (25px) and $\vec{k}$ = 0.0193 nm^{-1} (26px) are chosen as they incorporate most of the information to produce a good visual representation. The error can be calculated as the percentage difference between the circumferences of the circles. Where, $\vec{k}$ = 0.0179 nm^{-1} (24px) and $\vec{k}$ = 0.0193 nm^{-1} (26px) have a circumference length within 5% of $\vec{k}$ = 0.086 nm^{-1} (25px).

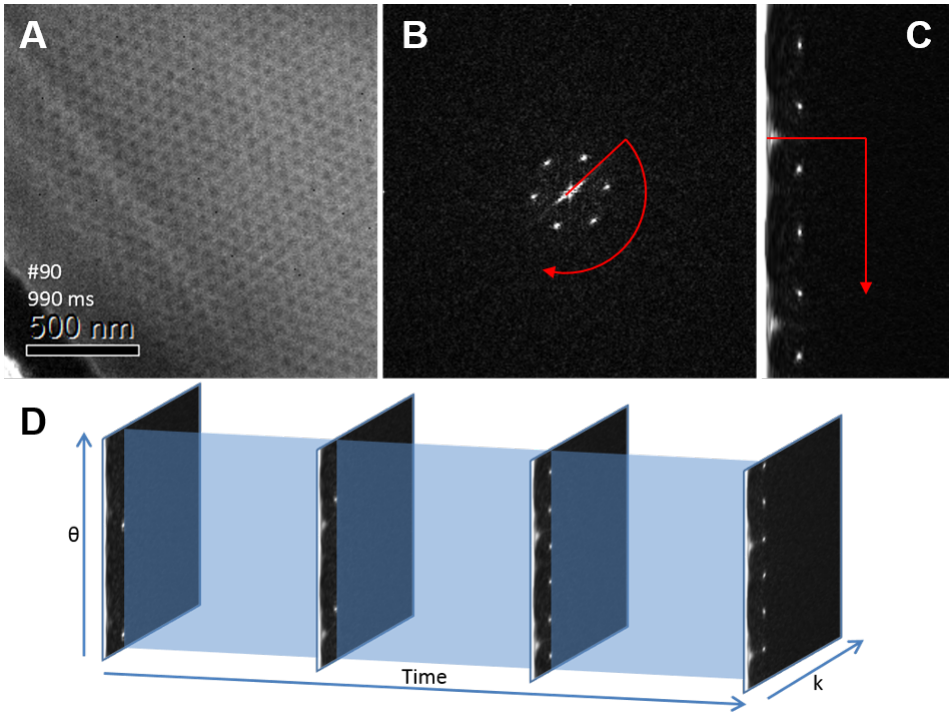

Figure 3.2: An example analysis of a real space image in figure A. The image is initially fast Fourier transformed to create figure B, this is followed by the application of a radial unwrapping function in figure C. This radial unwrapping is highlighted by the red arrow which in both images follows an isofrequency contour however is curved before the unwrap and straight afterwards. Finally the orthogonal projection in figure D, along with three other unwrapped images from other time slices, a projection is taken along the time axis to highlight the change in dominant $\vec{k}$-spacing spots quantity and position in time.

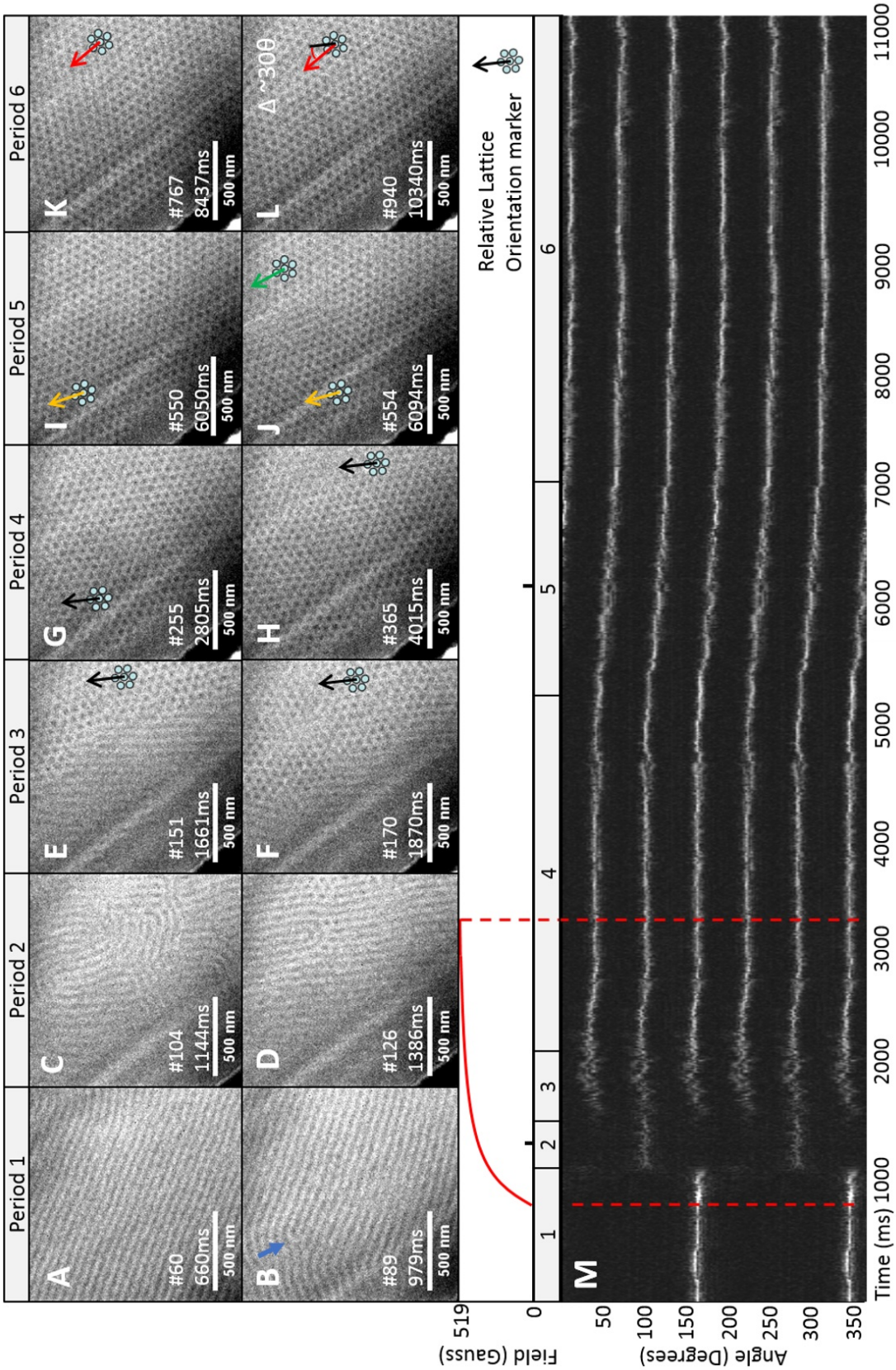

Figure 3.3: The TEP constructed from summation of $\vec{k}$-spacings $\vec{k} = 0.0179$ nm^{-1} (24px), $\vec{k} = 0.086$ nm^{-1} (25px) and $\vec{k} = 0.0193$ nm^{-1} (26px) overlaid with a plot of the applied field. The twelve insert images (A-L) cover the 6 periods of the movie. Panel B highlights a disclination with an arrow and panels (E-L) contain markers indicating the direction of the skyrmion lattices

The TEP presented in figure 3.3 highlights many of the processes happening during the experiment. The TEP in figure 3.3M is split up into six distinct phases, each of which have two example images shown in sub-figures 3.3A-L. The applied magnetic field during the transition is inferred by measuring the movement of the sample edge which is overlaid onto the figure 3.3M, in red, showing the ramp from 0 to 519G before remaining constant at this level.

Period 1 is the time frame while the helical state is in the same direction as the starting helical state. Figure 3.3A is a example of the helical structure found directly before the field ramp which is first observed in frame #65. The intensity of the dominant $\vec{k}$-spacing in the TEP during this phase appears to be greater than the other periods because the majority of the real space image is in the helical state with no sample edge contribution present in later images. Figure 3.3B shows a disclination - a line defect in which rotational symmetry is violated [89] - appearing in the previously uniform helical structure during the start of the field ramp. The disclination is highlighted by a blue arrow in the upper left hand corner of the image.

Period 2 includes the helical lattice during a reorientation of the helical lattice direction by 60°. This can be seen in figure 3.3M by a sudden change in the angle of the dominant $\vec{k}$-spacings. Figure 3.3C shows an example of the Transformation between the two is facilitated by buckling of the helical lines into a 'fingerprint-like' pattern. The exact cause of this reorientation is not fully understood; however, both the dominant $\vec{k}$-spacings of the first orientation and second orientation are present after the transformation into the skyrmion lattice, potentially suggesting this $\vec{k}$-spacing is energetically preferable. Figure 3.3D shows the end of period 2 where the skyrmion lattice begins to ingress from the right hand side. There is a single disclination at the boundary between the helical domain and skyrmion domain that persists for a small time into period 3.

Period 3 contains the duration in which there is temporary coexistence of the the helical and skyrmion phase. During this time segment the skyrmion lattice intrudes from the right hand side of the image, until the field of view shows only the skyrmion lattice. It is clear from the broadening of the dominant $\vec{k}$-spacings during period 3 in figure 3.3M that the

orientation of the skyrmion lattice is very unstable. This suggests rapid changes of the lattice orientation, or the presence of multiple orientations simultaneously. Figures 3.3E&F show the ingress of the skyrmion lattice at different stages during this period. The time difference between the two frames is 242ms (22 frames), in which the skyrmion domain front moves an average of 220nm (42px), equivalent to ~1nm/ms, which demonstrates the time resolution with which the imaging of the helical domain expulsion occurred. Both frames are overlaid with a lattice orientation marker which highlights one of the lattice vectors for comparison with other sub figures in later periods.

Period 4 is the first period of relative stability after the field ramp. The field change in this section is small, asymptotically reaching 519G. This period includes only small changes in the dominant $\vec{k}$-spacings, with the only permanent rotation soon after the phase transition. Figures 3.3G&H are spaced 1210ms (110 frames) apart and contain a skyrmion lattice with the same relative orientation.

Period 5 contains the rotation of the skyrmion lattice through 30° during which the lattice splits into two domains with different orientations. The splitting of the dominant $\vec{k}$-spacings from 6 peaks to 12 is visible in the figure 3.3M as small loops in the TEP. Figure 3.3I shows the skyrmion lattice after 11° of rotation directly before the appearance of the skyrmion lattice boundary, the lattice corresponding to an 11° rotation is identified by an orange arrow on the orientation marker. Figure 3.3J shows the system four frames later after the split. The left hand side of the frame remains at a 11° rotation compared to the original direction. The right hand side of the frame however has a 24 degree rotation compared to the original orientation (13° lattice boundary), this is shown as a green orientation marker. The mechanism facilitating the lattice rotation is discussed later.

Period 6 once again shows a period without rotation in the second stable skyrmion lattice orientation. At this point the lattice has rotated 30° compared to the orientation of period 4. This is indicated by a red orientation marker. Both figures 3.3K&J show the same relative angle with minimal dynamics between the images.

Line profiles are taken across the TEP for each frame, these line profiles are fitted using a peak finding tool to give information about the position and spread of the dominant

$\vec{k}$-spacings in time. Figure 3.4A shows the position of the FFT peak from the centre of the FFT image. The results show the periodicity of the lattice at 26px, before reaching a low of 23px during the transition, stabilising at 25px when in the skyrmion phase. This appears to show a response in the periodicity of the helical lattice in time to a rapidly changing field. The reorientation of the helical direction in phase 2 coincides with this decrease. The increased frustration in the helical pattern are likely to be the cause of this periodicity change. Figure 3.4B shows a broadening of the peaks fitted to the dominant $\vec{k}$-spacings. This is a combination of the helical pattern reorientation in period 2 and the co-existence of the helical lattice and skyrmion lattice simultaneously in period 3.

The combined TEP gives a good understanding of the evolution of the magnetic structure, however there is also important information in the individual $\vec{k}$-spacing TEP when it comes to discussing important physical occurrences in the experiment. Figure 3.5 shows the projection of six TEPs taken for $\vec{k}$-spacings between $\vec{k} = 0.0164$ nm^{-1} (22px) and $\vec{k} = 0.0201$ nm^{-1} (27px). The intensity is shown to be more prominent in a select band of $\vec{k}$-spacings. $\vec{k} = 0.0164$ nm^{-1} (22px) and $\vec{k} = 0.0171$ nm^{-1} (23px) are shown to have only a small amount of intensity showing that the majority of the symmetry information is at a longer frequency. Similarly, $\vec{k} = 0.0201$ nm^{-1} (27px) and $\vec{k}$-spacings above shows another decrease in intensity. The intensity in the images is most prominent for $\vec{k}$-spacings $\vec{k} = 0.0179$ nm^{-1} (24px) to $\vec{k} = 0.0193$ nm^{-1} (26px) justifying the previous summation of these three TEP. The prominence of the intensities in different $\vec{k}$-positions are shown to vary during different periods of the phase transition. The shift in the intensity towards lower $\vec{k}$-spacings appears to begin during the field ramp where $\vec{k} = 0.0179$ nm^{-1} (24px) sees an increase in intensity in the dominant $\vec{k}$-spacings.

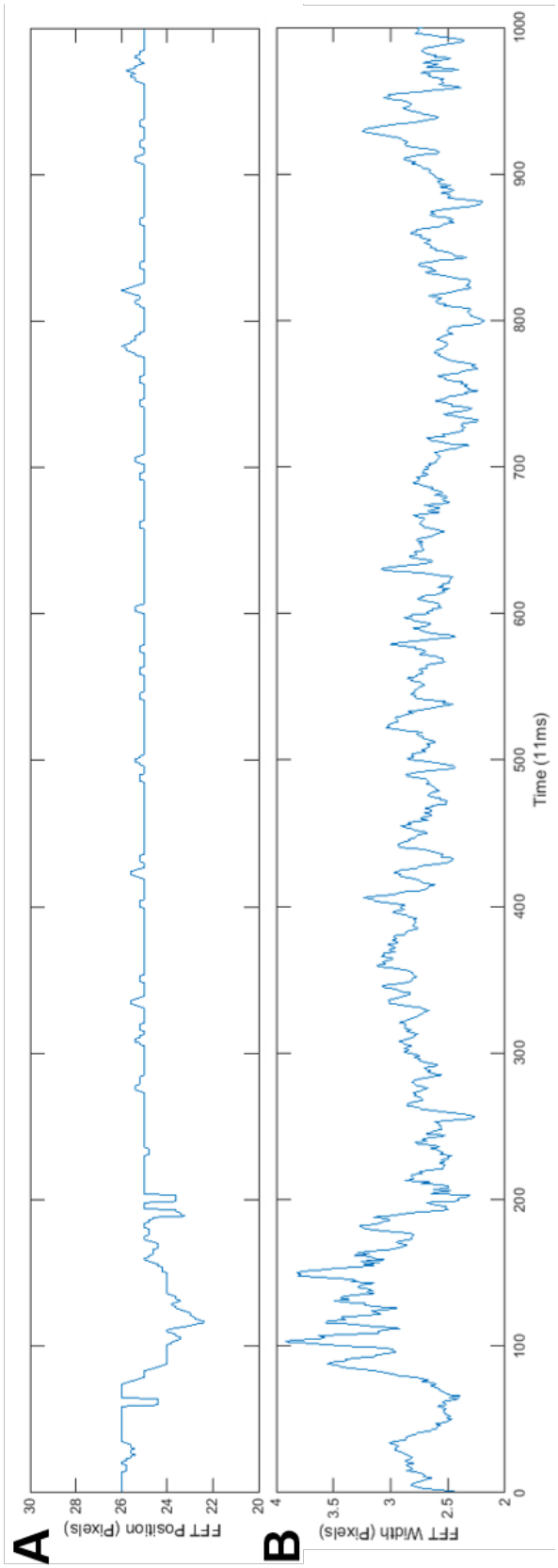

Figure 3.4: A figure showing peak finding analysis performed on the TEP shown in figure 3.3. Figure A shows the peak position along the $\vec{k}$-vector axis therefore showing the predominant reciprocal frequency in time. Figure B shows the full width half maximum of the FFT peak. This indicates the amount of variation in reciprocal frequency across the image.

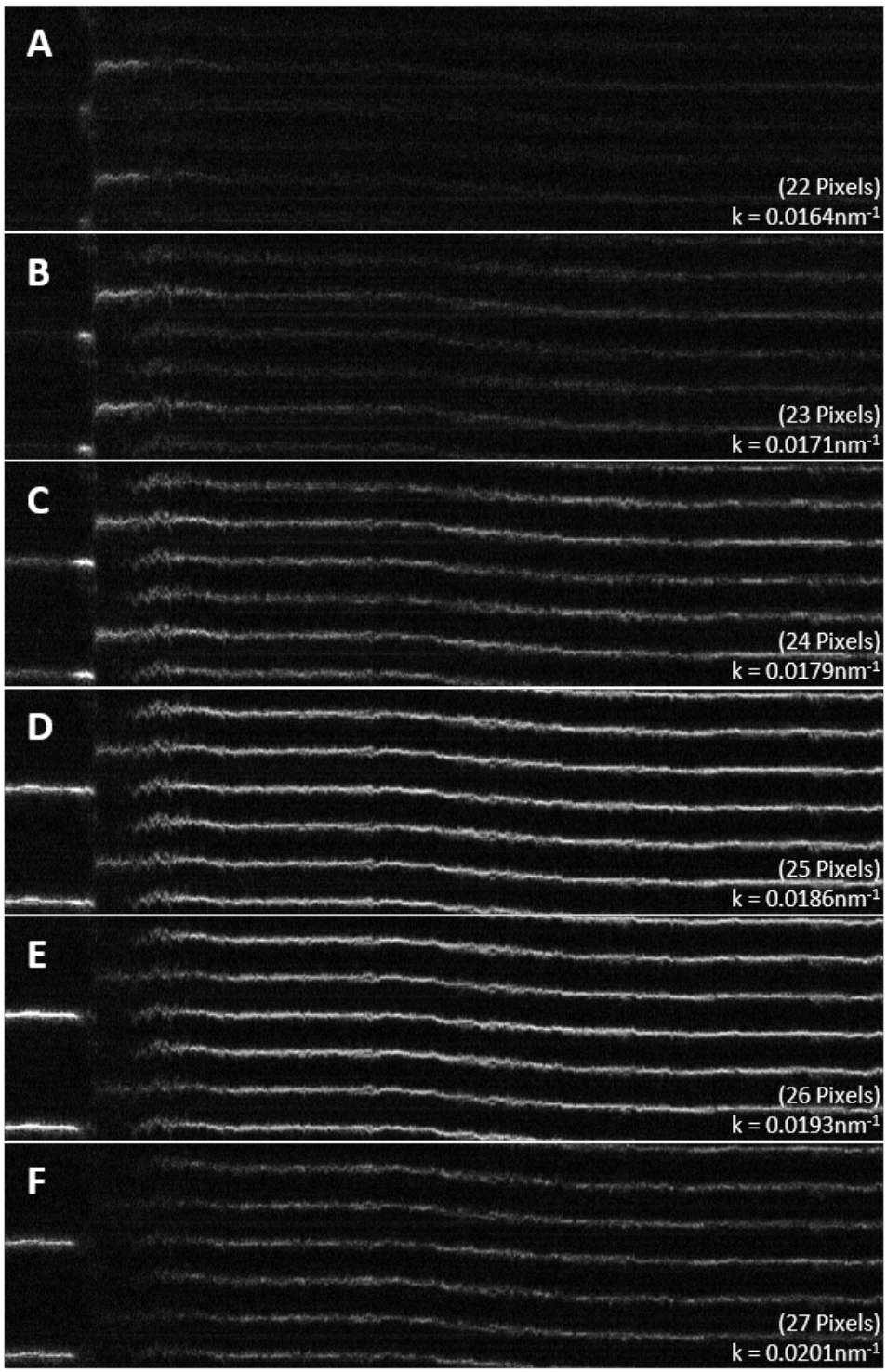

Figure 3.5: A set of images showing the orthogonal projections through a set of $\vec{k}$-spaces given inpx during a field induced transition from helical to skyrmion phase. The images show that the majority of the intensity is present in $\vec{k} = 0.0179$ nm^{-1} (24px) to $\vec{k} = 0.0193$ nm^{-1} (26px)

3.5 Skyrmion creation and annihilation

The skyrmion transition in period 3 shows the helical lattice being destroyed by the skyrmion lattice encroaching from right to left across frames #110 to frame #250. The creation of these skyrmions appears to happen out of the field of view imaged during these experiments. As discussed previously the millisecond timescale imaging performed here is orders of magnitude slower than the simulation predictions that skyrmion nucleation can occur on the nanosecond timescale [90]. However, individual frames recorded during the experiment feature transient objects whose appearance is consistent with that of skyrmions. These transient objects appear as distinct from the main skyrmion lattice. Figure 3.6 shows two frames with multiple isolated skyrmion-like objects appearing.

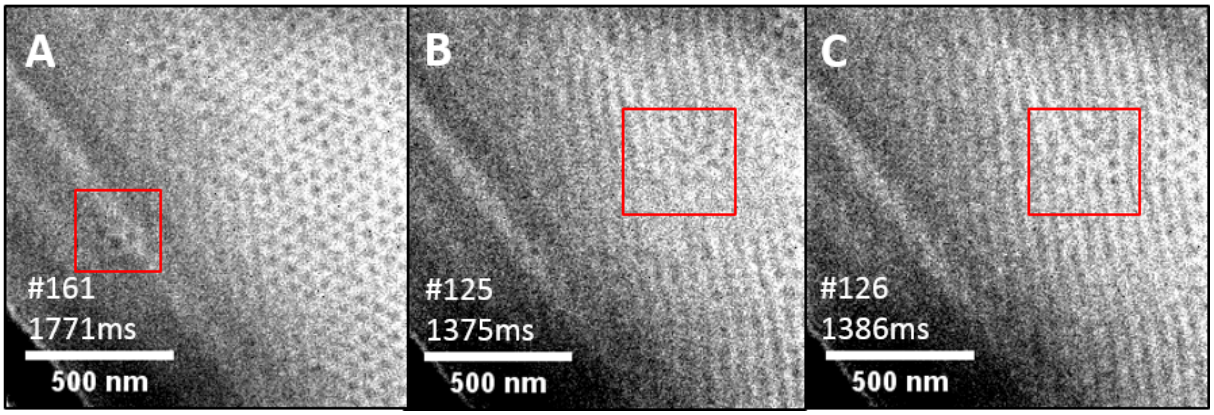

Figure 3.6: Examples of the appearance of transient skyrmion-like objects. Figure A shows a trio of three ahead of the skyrmion lattice. Figure B shows the state directly before the appearance of the objects near a $+\pi$ disclination. Figure C shows the following frame with several skyrmion-like objects appearing in close proximity to the $+\pi$ disclination.

Figure 3.6A shows frame 161 in which the skyrmion lattice has expelled a majority of the helical lines. The contrast of the left hand region of the image shows a significant decrease compared to the previous helical contrast level. This decrease in contrast is either associated with rapid motion blurring, the location of the helical lines, or with a canting of the helical direction which has been shown to co-exist with the skyrmion phase during tilting, however exhibits similar contrast [91]. These three skyrmion-like objects persist for

22ms (2 frames) after which the contrast from none of the three objects remains.

Figures 3.6B & C show the frames before and after the appearance of skyrmion like objects. The $+\pi$ disclination appears to be created during the reorientation of the helical lattice in frame #105, however it is the only helical feature to persist for a significant duration until frame #150, where the disclination migrates out of the field of view to the top on the frame. The topological structure of disclinations such as these have been investigated for both non-magnetic [92] and magnetic systems [93]. In the case of magnetic systems the $+\pi$ disclination appeared as a method of reducing energy at the boundary of non-parallel helical lattices. In this case it appears to function similarly between the helical and skyrmion lattice. To help with the discussion the structure two schematic diagrams of the pair of frames are shown in figure 3.7.

Figure 3.7A shows the $+\pi$ disclination at the boundary between the skyrmion and helical lattice. In the real space image there are no obvious signs of skyrmion-like contrast. The $+\pi$ disclination is approximately the width of four helical lines. Figure 3.7B shows the appearance of three skyrmion-like objects in close proximity to the $+\pi$ disclination in the helical lattice. The leftmost helical line end, topologically called a meron, appears to have receded and in the gap a single skyrmion-like object exists. The topological number appears to have changed in this region by -1. Similarly to the right is two skyrmion-like objects which have appeared changing the local topological number by -2.

The disclination creates a unique energy landscape that causes the skyrmion-like objects to reside where the helical lines intersect with the $+\pi$ defect creating a non-parallel helical boundary. The skyrmion-like objects occupy this position only temporarily, where the skyrmions appearing in frame 126 persist for three frames. However, the disclination tends to rapidly expand and shrink along the helical direction in response to the expanding skyrmion lattice, however this process occurs faster than the exposure. Skyrmions persisting outside of their predicted phase region on the field-temperature (B-T) graph have been previously identified in regions with non-parallel helical intersections causing clusters of skyrmion to appear stable. Both of these examples show that spontaneous creation of skyrmion-like objects appear to be a feature of the skyrmionic material when out of

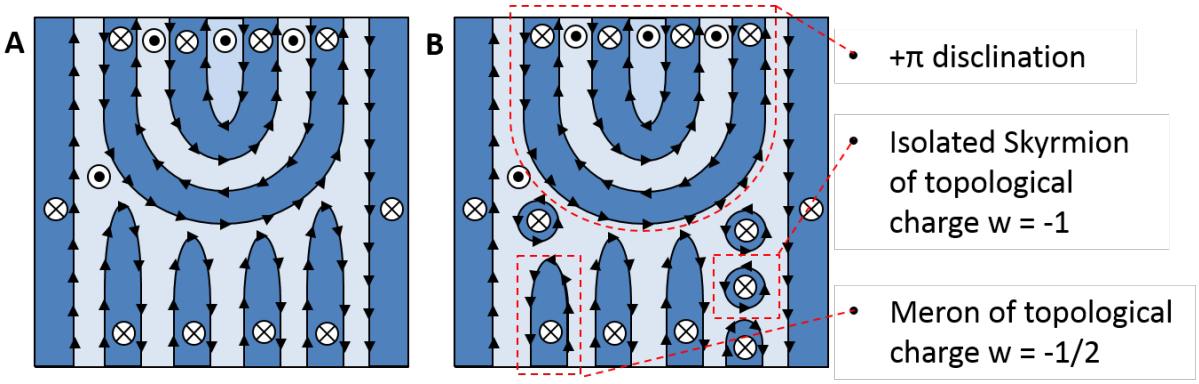

Figure 3.7: A pair of schematic diagrams representing the magnetic structure observed within the highlighted areas of figure 3.6B&C. Figure A, shows the state before the appearance of skyrmion-like objects. Figure B, shows the state after the appearance of skyrmion-like objects with predictions of the topology of key areas marked.

equilibrium caused by a rapidly changing magnetic field. This potentially enables skyrmion stability to be studied in this time regime using the Medipix3.

3.6 Analysis of skyrmion lattice transition dynamics

The transition from helical phase to skyrmion phase during period 3 of the TEP occurs in the field of view over the course of approximately 1375ms corresponding to 125 frames between frame #125 and frame #250. The early frames in the transition show very rapid motion which, due to the contrast level, are difficult to track at the individual skyrmion level. Later frames where the lattice structure has stabilised, provide better candidates for skyrmion finding and connecting single skyrmions in sequential frames. Although many results in this chapter focus on the latter part of the transition, it is important to understand both the quality and resolution of the images gathered during the transition. Figure 3.8 shows an extract of six images taken during the course of the transition. Figure 3.8A shows skyrmions only visible on the right hand edge of the image with the majority of the imaged area in the helical state. Figure 3.8B again shows skyrmions only at the right hand edge however there is the addition of structure in the helical lattice now in

the form of a $+\pi$ disclination , the structure of which is discussed in the previous section 3.5. The disclination persists for 352ms between frame#107 and frame #139 and exhibits significant mobility along the helical lines perpendicular to the skyrmion/helical boundary. The $+\pi$ disclination has a maximum velocity between frame #120 and frame#122 in which the disclination apex moves 180nm, equivalent to 8nm/ms. During frame #121 the disclination does not appear to be visible, caused by motion blurring. Figure 3.8C shows the skyrmion/helical boundary moving slightly further into the image and the 180°helical boundary removed from the image. Figure 3.8D shows approximately half of the image covered by skyrmions. In this frame the region of reduced contrast appears to contain a cluster of skyrmion-like objects discussed in the previous section 3.5. Figure 3.8E shows nearly the whole image filled with skyrmions, with figure 3.8F showing the imaged area completely in the skyrmion phase. Types of dynamic processes during the course of the transition are identified and discussed in depth in sections 3.6.1 and 3.6.2.

Two adjacent skyrmions in a lattice are nominally identical and therefore indistinguishable. If, during imaging these two skyrmions were to swap places, there would be nothing in the images to identify that this process had happened. Expanding this to an infinite plane of skyrmions, a shift by one lattice spacing along a lattice vector would also be indistinguishable. However, this experiment was performed on a real system that has boundaries such as the edge of the sample which provides a type of barrier which affects the skyrmion dynamics. Secondly, the skyrmion lattice does not appear to be perfectly rigid, the results of which are presented here and in the analysis of 5-7 defects in the following section. Therefore, by identifying regions of the skyrmion lattice in motion next to regions of the skyrmion lattice that appear to be stationary, a picture of the real dynamics can be formed. To determine the motion of individual skyrmions we must make the following assumptions. 1) New skyrmions are not created within the skyrmion lattice, 2) Neighbouring lines of skyrmions do not shift by more than a single lattice spacing relative to each other. This is explained and justified in detail later. The aim of this experiment was to use the real space information at millisecond time resolution to create vector maps of the skyrmion motion between frames in which the direction of the motion

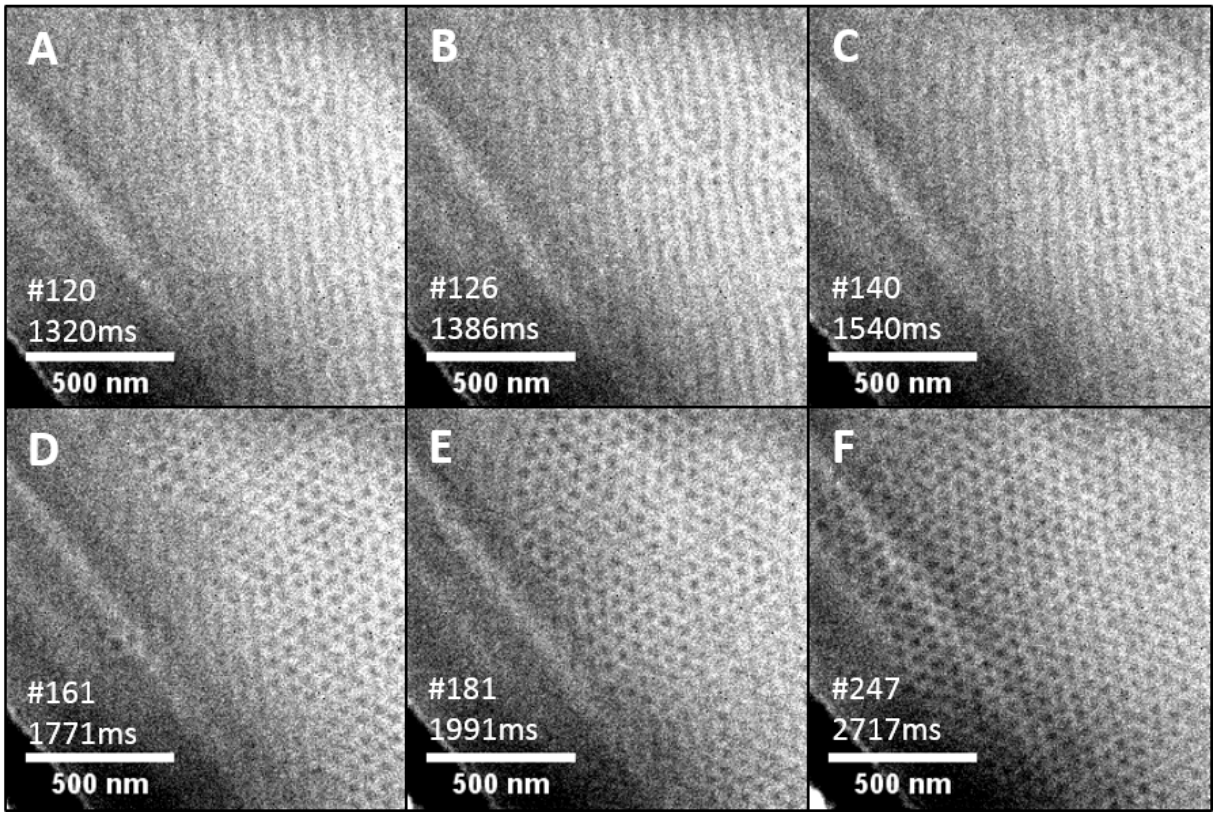

Figure 3.8: The figure shows six sequential frames highlighting the time resolution and duration of the transition from helical phase to skyrmion phase. The frame number and time from acquisition start are included.

into the following frame could be represented by an arrow. At first a computational nearest neighbour approach in which the skyrmion in a frame was matched to the closest skyrmion in the sequential frame appeared to produce justifiable vector maps for frames containing minimal motion, however frames containing significant motion caused anomalies. In order to computationally process the image stack, a more sophisticated matching method was required.

Analysis of sequential frames was performed by assuming that a skyrmion appearing in the same position in the next frame had not moved and was used as a fixed reference point for other skyrmions around it which did not appear to be stationary. Each skyrmion which had a stationary nearest neighbour was then assigned to the first 'motion index'. Any skyrmion which had not been matched was then checked for first motion index nearest

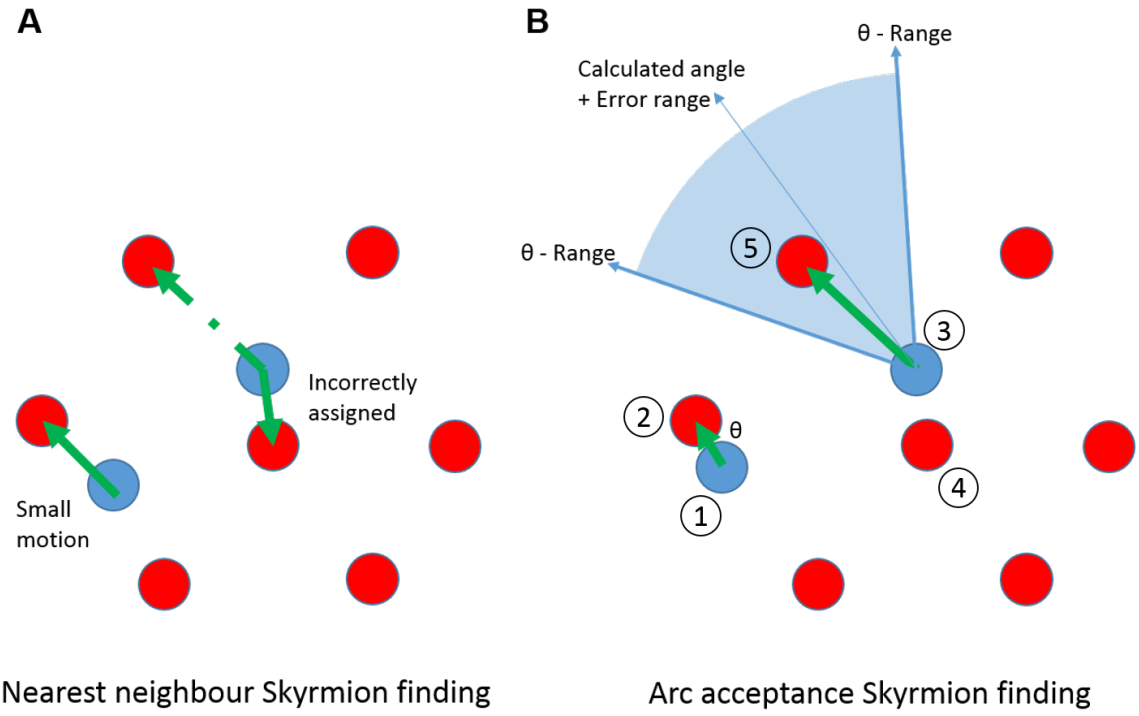

Figure 3.9: Examples of both the nearest neighbour and arc acceptance methods of linking skyrmions in sequential frames to create motion vectors

neighbours and if so, assigned to the second motion index. This process is continued until all skyrmions have been assigned. Skyrmions in the first index are connected to their nearest neighbours using a simple nearest neighbour match. All higher numbered indexes are then only matched with skyrmions in the same direction as the motion of the skyrmions in the index number below them. This method allows skyrmions with greater than a half lattice of motion to be connected providing there are some stationary skyrmions in the image. Figure 3.9 shows the application of this method where skyrmions in the current frame are shown in blue and the next frame in red. Figure 3.9A shows the connection using simple nearest neighbour matching. Figure 3.9B shows the arc acceptance method. To help with the explanation skyrmions from the first frame numbered 1 & 3 have been coloured in blue and the skyrmions from the second frame numbered 2, 4 & 5 have been coloured in red. The figure shows skyrmion 1, with a very close nearest neighbour skyrmion 2 connected by an angle θ. This connection influences the matching of the adjacent skyrmion

3. Although skyrmion 4 is the nearest neighbour of skyrmion 3 but it is not consistent with the local motion. The predicted motion is assumed to be close the angle θ and this creates a predicted arc to accept the closes skyrmion within. In this case the closest skyrmion within that arc is skyrmion 5. This method allows skyrmions to be connected at a distance between $\lambda_s/2$ and λ_s where λ_s is the standard inter-skyrmion distance.

The results of applying this arc method are presented in the following extracts showing frame pairs and the resulting vector maps created with discussion on the apparent dynamics and physical processes by which the dynamics are facilitated.

3.6.1 Lattice stretching via inter-skyrmion distance changes

Inter-skyrmion distance has been shown in previous research to be primarily dependent on the ratio between exchange energy and DMI. However, in this experiment we observe evidence of dynamics facilitated by a stretching of the inter-skyrmion distance over the duration of a single frame. Figure 3.10 shows the analysis performed on two sequential frames showing this motion. Figure 3.10A shows frame #218 and figure 3.10B shows frame #219. It is difficult to pick out the regions exhibiting motion visually in the real space images, however when image subtraction is performed the contrast indicative of motion is is clear. The difference image of frame #219 - frame #218 is shown in figure 3.10C. Figure 3.10D shows the skyrmion vector map created using the arc acceptance method code with a schematic representation of the map in the bottom left corner. Each skyrmion is represented with a red dot and position of the skyrmion in the next frame connected to by a coloured line. Any skyrmion without a line is stationary to within one pixel. These skyrmions are used as the first index. The line colours are used to denote the indexing colour scheme from green (second index) to cyan (sixth index). The skyrmions on the left hand side of the image outwith the skyrmion lattice indicated by the real space images are artefacts from the FFT filtering and can be ignored. There is a significant variation in the direction and magnitude of the motion vectors indicating the motion is not a 'slip' type dislocation in which adjacent skyrmion planes move laterally by one or more skyrmion lengths.

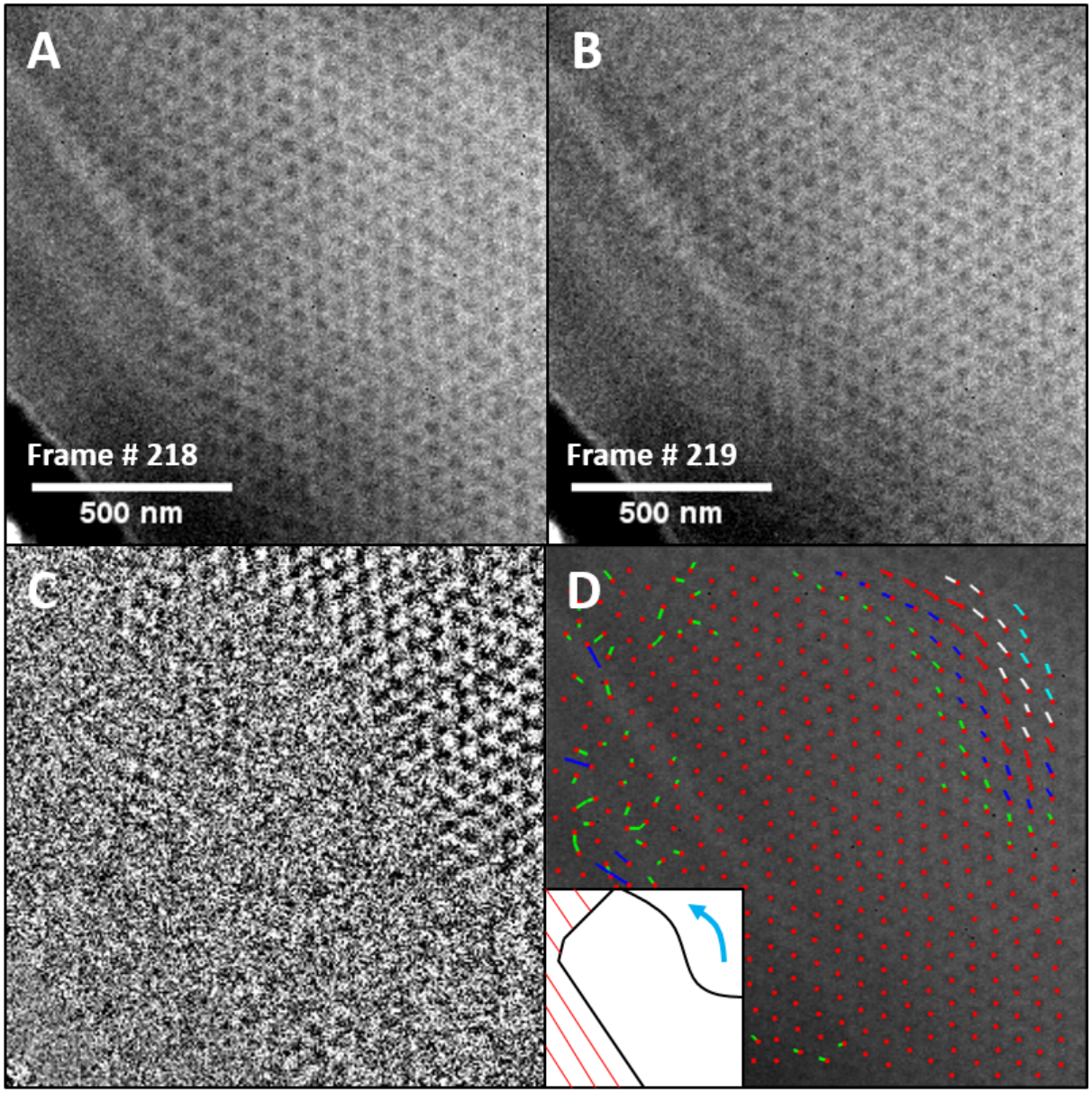

Figure 3.10: A pair of sequential frames showing rapid motion of skyrmions facilitated by a change of inter skyrmion spacing. Figures A & B show frames #218 & #219 respectively. Figure C shows a difference image of the two frames (C = B - A) in which motion is evident by the alternating black and white contrast in the top right hand corner. Figure D shows a vector map of the motion between the two frames using the arc acceptance method with schematic insert.

An example of this change in inter-skyrmion spacing is quantified in figure 3.11. Skyrmions along a single lattice vector are selected and blown up to highlight the spacing between skyrmions in red (frame 218) and in blue (frame 219). Figure 3.11B shows the change in spacing between the sequential skyrmion positions. The average inter-skyrmion distance in frame 218 is 10.81px where as 11ms later in frame 219 the average distance is 12.22px which is an increase of 13%. The skyrmions and their subsequent frame counterparts are labelled 1-6. Figure 3.11C shows the distance travelled by each skyrmion between frames. Skyrmion set 1 shows the smallest motion with only 1 pixel of motion and was chosen as the first skyrmion to label as skyrmions below show no motion. Skyrmions along the vertical plane increase in distance travelled causing a stretch in the inter-skyrmion distance. Skyrmion set 6 has the largest motion of 7 pixels.

The increase in inter-skyrmion distance happens while the magnetic field ramp is still increasing however the field rate of change is very small and unlikely to be the sole cause of the rapid increase in the inter-skyrmion spacing. The majority of the dynamics appear to be located outside of the field of view potentially meaning the magnitude of the stretching may be greater. The frame after has the skyrmion patch restored to the original inter-skyrmion distance. It can be postulated that outside the field of view either another stretched region or a defect has removed this strain. This suggests the potential to control inter-skyrmion distance through rapidly applied fields.

3.6.2 Multi-vector skyrmion lattice slip

In this extract, we observe evidence of skyrmion two slip planes along different lattice vectors situated between two regions of stationary skyrmions, shown in figure 3.12. Figure 3.12A & 3.12B show the real space images of frames #221 and #222 respectively. Figure 3.12C is the calculated difference image of frame #222-221. Figure 3.12D shows the vector map with the same indexing colour scheme as the previous figure 3.10. This figure shows two regions of stationary skyrmions separated by a region of skyrmion motion spanning the image. The motion appears to create a kinked linear flow with skyrmions on the right hand side of the image moving towards the bottom left corner and skyrmions on the left

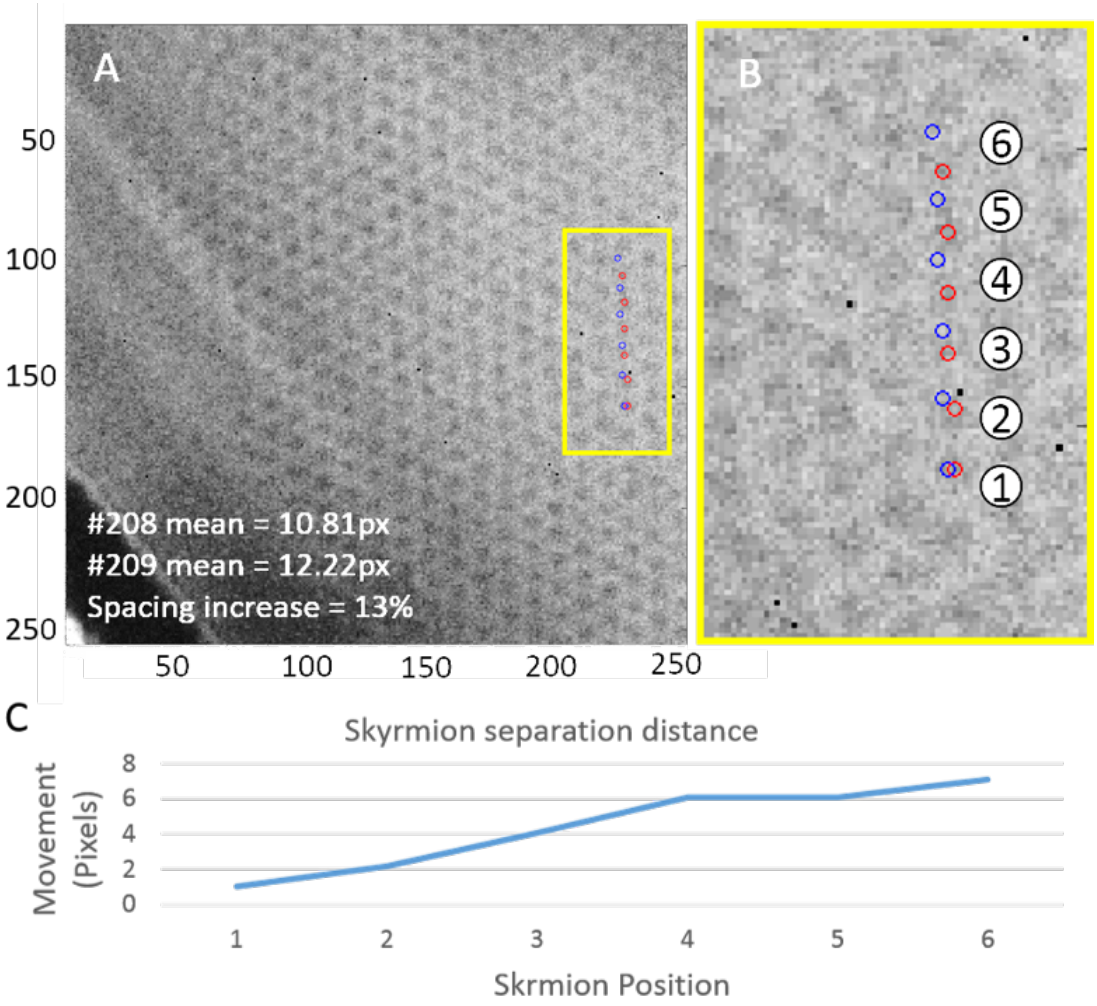

Figure 3.11: Figure A shows frame #218 of the movie with six skyrmions from the current frame (red) and subsequent frame #219 (blue). Figure B shows a zoomed image of these six skyrmions showing the increasing distance of motion from one frame to the next. Figure C shows a graph of the distance travelled by skyrmion position number

hand side moving towards the top left hand corner. The left side of the kink appears to show skyrmions moving farther than skyrmions to the right of the kink. Similar to the results of the previous section 3.6.1, this would suggest a temporary modification of the inter-skyrmion distance. The system shows this flow for only one frame before being stationary in the subsequent frames. It appears that the skyrmions closer to the centre of the slip region have larger displacement than the skyrmions immediately adjacent to the

stationary region, however, not enough to cause a full plane slip.

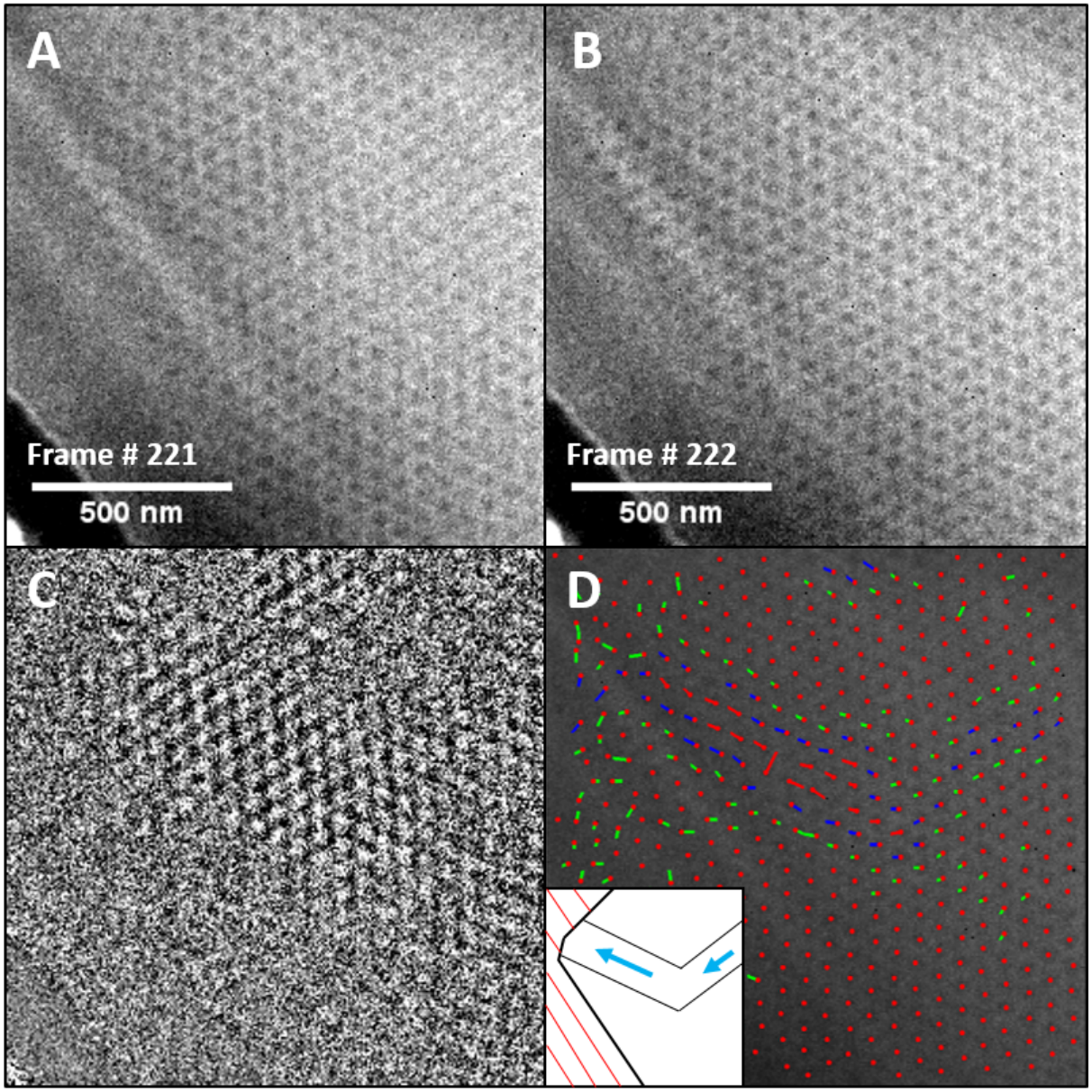

Figure 3.12: An example of kinked linear flow of skyrmions along multiple lattice vectors. Figures A&B show frames #221 & #222 respectively. Figure C shows a difference image of the two frames (C = B - A). Figure D shows a vector map of the motion between the two frames using the arc acceptance method with schematic insert.

3.7 Analysis of skyrmion lattice rotation dynamics

The possibility to obtain a multi-domain skyrmion lattice in Cu_2OSeO_3 has previously been detected via soft resonant elastic X-ray scattering [88]. Eighteen peaks are observed in the reciprocal space image and a prediction of the real space image is reconstructed using the intensity of each six-fold symmetry spot set. Although the reconstruction gives an idea of what the magnetic structure may look like, the location of the lattices themselves and the structure of the boundaries cannot be reconstructed through this method. This method of reconstruction is followed and expanded upon for comparison with the real space data. The dataset presented here is the first opportunity to see the real space evolution of individual skyrmion positions at the millisecond timescale.

3.7.1 Domain reconstruction via FFT masks

A single frame (#555) during the rotation segment of the movie is selected as having the largest splitting of the FFT peaks into two symmetry sets. Figure 3.13A shows the relative position of the frame on the TEP with figure 3.13B showing a magnified view of this section. Figure 3.13C shows the line profile of the TEP, clearly showing the presence of peak pairs. The separation of the peaks is calculated to be 9°.

To perform the reconstruction, both skyrmion lattices are selected using a six spot mask to highlight only the lattice in that orientation. A ring filter is also used as a noise reduced reference image maintaining the information of the lattice boundary. Figure 3.14A&C show the post masking FFT producing images D&F after inverse fast Fourier transformation (IFFT). These images are referred to for the rest of this analysis as domain 1 & 2 respectively. It is clearly seen that the boundary information is lost in both images, replaced by a reduction in contrast past the position of the boundary. Figure 3.14B&E, as expected, retain the boundary information; however, the position of the domains is less clear.

Both single domain images were passed through a peak finding tool with a threshold estimated by the distance to the boundary. The reconstruction shown in figure 3.15 is

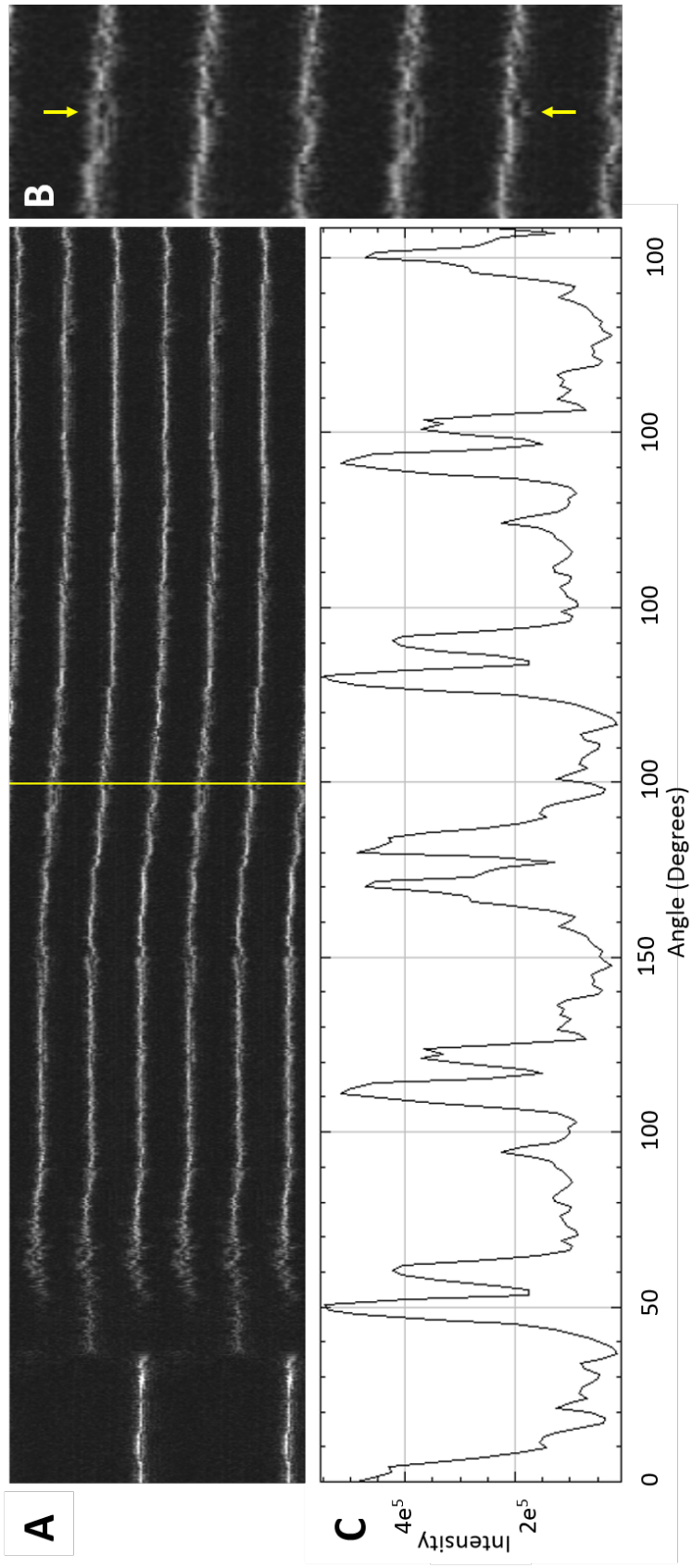

Figure 3.13: Figure A, shows the position of frame #555 on the TEP with figure B, showing a magnified image of this section. Figure C, shows the line profile taken from the TEP highlighted in yellow. The line profile shows a double peak structure rather than single peaks as expected by a single skyrmion lattice.

Figure 3.14: Isolating single skyrmion lattice domains via masked IFFT. Image A&C specifically filter the six-fold symmetry spots therefore creating an image where the domain with that specific orientation is highlighted in figures D&F respectively. Image B uses a ring filter to maintain all frequencies in the specified band maintaining the skyrmion domain boundary in Image E.

the superposition of both domain sets on the ring IFFT image. The identified skyrmions are mapped using a Delaunay triangulation function to attain boundaries and metrics for the domains. This method identifies the boundary to within a single skyrmion spacing where some skyrmions, such as those overlapping at the top and bottom, are identified as members of both lattices. However, masking of intermediate frequencies causes the skyrmions at some regions of the boundary to deviate by up to 5 pixels. Although spot masking does enable the identification of the skyrmion boundary, the precise position of defects within the boundary cannot be identified consistently. Therefore, the ring filtering is used in the following results of this section for identifying skyrmions to conserve the $\vec{k}$-space information at the boundary. Domain 1 is smaller containing 181 skyrmions across an area of 2.67x10^4 pixels calculated as 7.35x10^2 nm^2. Domain 2 contains 233 skyrmions across an area of 1.98x10^4 pixels calculated as 4.63x10^5 nm^2.

3.7.2 Rotation induced skyrmion lattice defects

A modified script similar to that used in a paper by Jayaraman Rajeswari involves rastering a search box across the image to find local maxima based on the calculated distance between skyrmions [94] preventing anomalous peak finding caused by noise. Both smoothing and masked ring IFFT techniques are used and produce skyrmion location results matching well to the apparent positions on both the raw and filtered image. The first defect identified in previous work was the 5-7 defect where one skyrmion has 5 nearest neighbours and an adjacent skyrmion has 7 nearest neighbours. A triangle is created between three points where the triangulation method is used to define the nearest neighbours for an individual skyrmion. A Delaunay triangle is created where three points can be connected by a circle and contain no other points. The Delaunay triangles can therefore be visualised as a mesh applied to the skyrmion location points which can be seen in figure 3.16A. Summing a single skyrmions membership to the Delaunay triangles, therefore, gives the number of nearest neighbours. The skyrmions are then colour coded by their number of nearest neighbours as shown in figure 3.16B, where blue shows typical lattice skyrmions with 6 nearest neighbours, red with 7 nearest neighbours and green with 5 nearest neighbours.

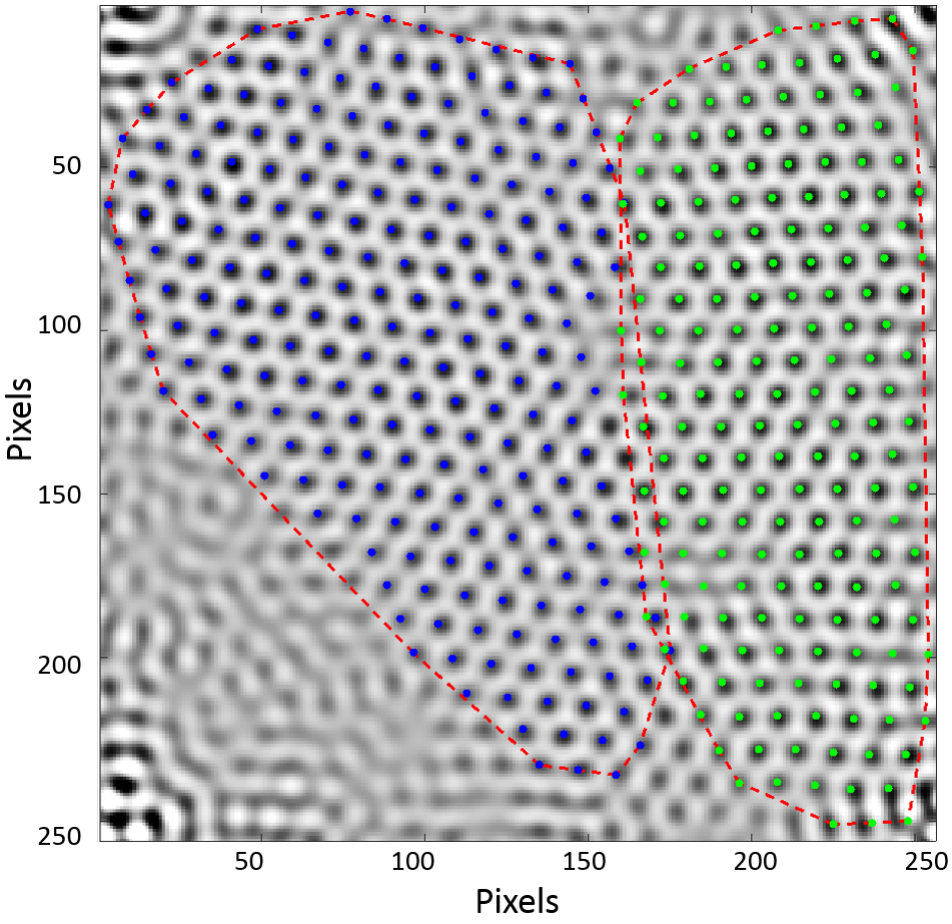

Figure 3.15: Skyrmion domains connected through a Delaunay triangulation method to highlight the lattice. Domains information is created via masked FFT reconstruction and overlaid onto a ring masked FFT image.

For the purpose of preventing confusion, skyrmions located at the border of the image with fewer nearest neighbours due to the field of view are coloured blue. The three red-green pairs can be distinctly seen in figure 3.16B separated vertically by 5 lattice planes each. The alignment of all three 5-7 defects in figure 3.16 appear to be parallel to the direction of the boundary where the obtuse angle between the two lattices is on the same side as the 7 nearest neighbour skyrmion.

As discussed in the introduction, the density of 5-7 defects along a defect is proportional to the relative misorientation of the two lattices forming the boundary. The relative angle of the lattices can be easily calculated by the difference between the two six-fold symmetry

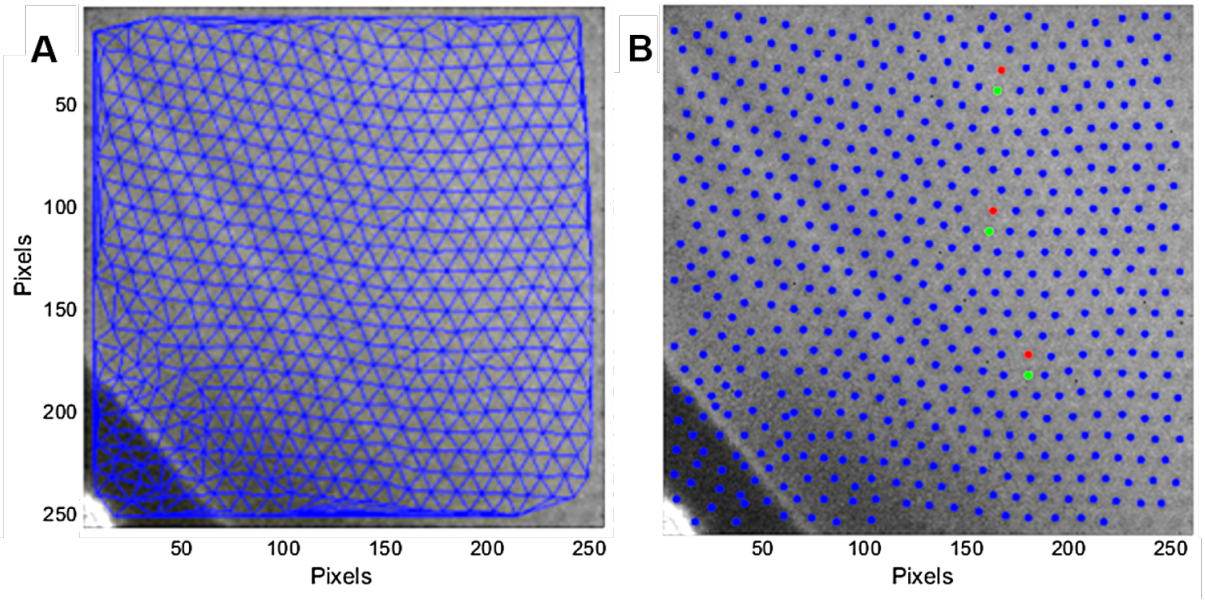

Figure 3.16: A Delaunay triangulation mesh is applied to the skyrmion points to highlight any defects within the image. Figure A shows the mesh overlaid to the image and figure B shows the individual skyrmions coloured by the number of Delaney triangles they are members of. Green = 5, Blue = 6, Red = 7.

peaks which can vary between 0°to 30°. The membership of a single skyrmion to either lattice is slightly more difficult to decide computationally. To determine membership of a single skyrmion to either of the skyrmion domains, the relative angles of the nearest neighbours are used to provide a metric for determining its local orientation. Figure 3.17 shows two frames picked from different data sets highlighting the increase in the density of defects by angle. The 9°misorientation gives an average of three full lattice spacings while 14°gives an average of one lattice spacing.

3.7.3 Time-resolved 5-7 defect trajectory analysis

We have demonstrated the presence of 5-7 defects and the proportionality between defect density and adjacent skyrmion domain angle. The benefit of imaging skyrmions with the Medipix3 detector is the capability to visualise the evolution of the defects in time. To demonstrate this, two consecutive frames #553 and #554 have been trimmed to show a

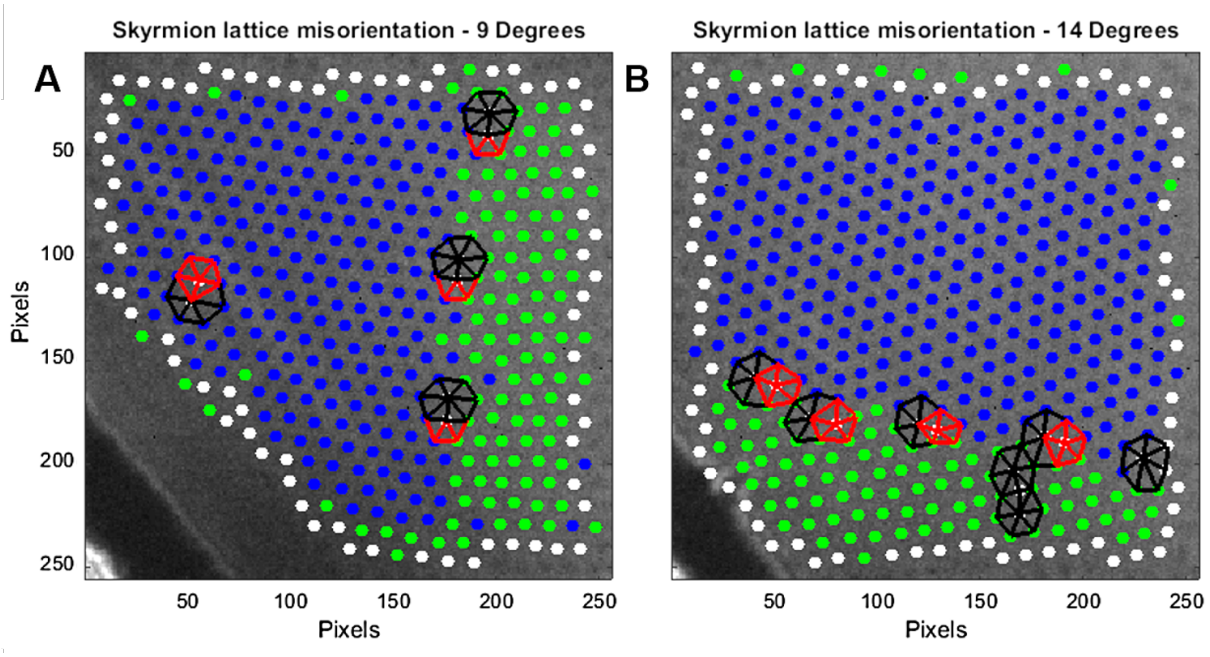

Figure 3.17: Two examples of the correlation between 5-7 defect density and skyrmion boundary misorientation. Figure A shows a 9°misorientation causing a skyrmion grain boundary with three lattice spacings between the defects. Figure B shows the density of the defects increase to only one lattice spacing, separating the defects caused by a 14°misorientation.

single defect. Skyrmions in frame 553 are connected to their nearest neighbour skyrmions in the following frame. Figure 3.18A shows a filtered image of frame 553 with skyrmions of that frame overlaid in red and skyrmions of the next frame overlaid in blue. Figure 3.18B replaces the positions with arrows to form a trajectory map of the motion between frames. For clarity, five skyrmions along a single skyrmion vector are labelled so that their motion in response to a defect position move can be discussed.

In frame 553, the defect can be identified as the skyrmion with five nearest neighbours. In figure3.18A, this is the skyrmion at position marker 4. The trajectory shows the defect moving by two lattice periods to the left by pressing the skyrmion at marker 2 half a period into the row below. This causes it to become the 5 nearest neighbour skyrmion of the 5-7 pair. The skyrmions on the rows above shift right to compensate for the movement and the original defect position gains an extra nearest neighbour, bringing the lattice at

position marker 4 back to symmetry, as shown in figure3.18B. Skyrmions 3&5 move very slightly to accommodate the skyrmion at marker 4 gaining this symmetry. Interestingly skyrmion 1 which shows the smallest movement between the two frames is directly next to skyrmion 5 which shows the most movement suggesting that the forces pressing the skyrmions are either very directional and/or localised.

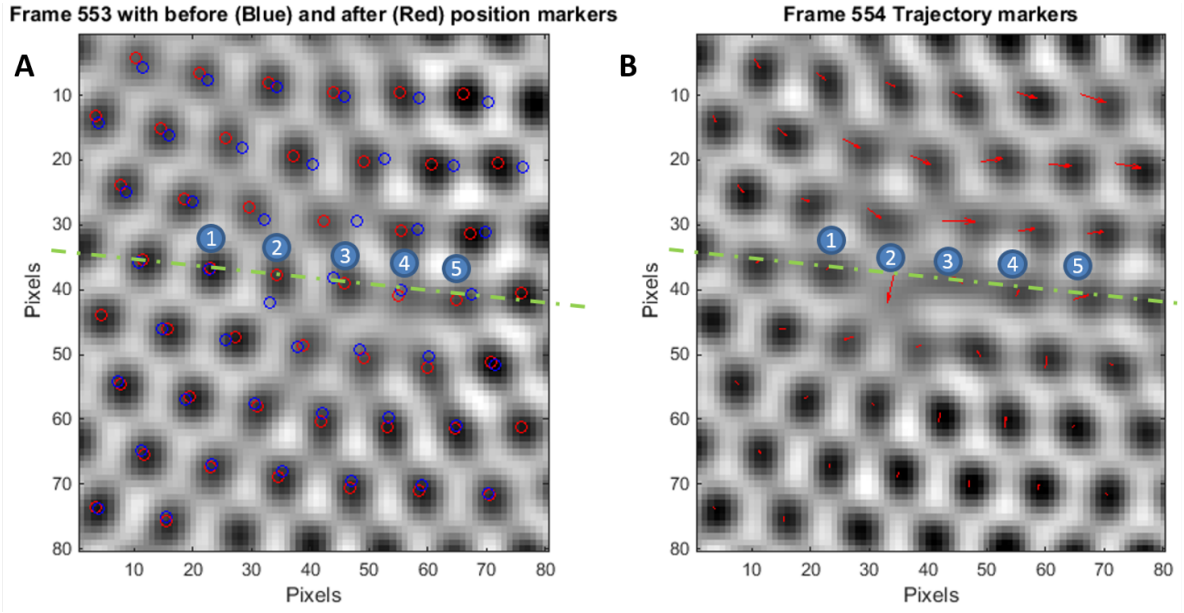

Figure 3.18: Trajectory analysis of the skyrmion defect is performed on two sequential frames in which there is a motion of the defect. Figure A shows frame 553 with current skyrmion locations in red and positions of skyrmions in the next frame in blue. Figure B shows frame 554 with the nearest neighbour trajectory plotted with arrows to produce a trajectory map. Five key skyrmions along a single skyrmion vector (labelled in green) are identified for discussion and numbered 1-5.

3.8 Discussion

In systems such as crystal lattices, the physical mechanisms of lattice motion play an important role in the macroscopic properties of the material. Although skyrmion lattices have significantly different physical properties, systems featuring competing long range

attraction and short range repulsion can often be compared. Two important material systems are of great relevance in discussing skyrmion lattices. Firstly, bubble rafts: these arrays of millimetre to micrometre sized bubbles suspended on water naturally pack themselves into a hexagonal lattice similar to skyrmions [95]. These were originally proposed as a convenient method of demonstrating defects in atomic lattices from slip planes to impurities caused by varying the space of the enclosure thus applying strain to the system. Due to the macroscopic size of the bubble raft system, the reorientation of the individual bubbles and the defects are on a time scale perceivable to the human eye which provides a useful reference for identifying similar phenomena in skyrmion lattices. [96, 97, 98, 99]. A second system that has had more recent scientific interest for potential technological applications is graphene. Each carbon atom is adjacent to only three nearest neighbours. However, the graphene rings form a hexagonal structure which has been shown to have important applications in electronics, where the properties of conductance and electron mobility are linked to defects and grain boundaries between non-colinear graphene sheets [100, 101, 102, 103, 104]. The organisation of the carbon atoms in graphene grain defects can present as 5-7 defects, which have been identified in skyrmion lattices by Rajeswari *et al.* [94]. The optical conditions required for atomic scale imaging of graphene in TEM makes time resolved imaging a challenge therefore further understanding of time resolved skyrmion lattice dynamics could provide data on a geometrically similar structure furthering the understanding of graphene physics.

The investigation of field induced phase transitions in Cu_2OSeO_3 has displayed the potential of time resolved imaging in an unmodified TEM through the use of the Medipix3 single electron counting solid state pixel detector. The image quality, which is ultimately determined by the magnetic contrast, is sufficient to begin not only identifying magnetic dynamics but applying computational methods to rapidly process large data sets. The magnetic contrast proves to be the primary limit in this experiment which prevented the 5ms and lower data sets from being useful. The contrast of the skyrmions could be improved with optimisation of beam conditions however the thickness of the sample is still the greatest cause of magnetic contrast reduction.

The analysis and presentation of the 3D dataset without the aid of video posed a challenge in itself. The symmetry data of the primary skyrmion movie is presented in a novel method through the use of the TEP. This method provides a convenient way of displaying the key phase information from the 3D dataset in 2D and conveniently breaks the dynamics into six definable segments for discussion.

The imaging of the helical lattice has produced the unique observation of helical folding as a means of facilitating dynamics helical vector changes. The appearance of this helical folding is striking in the real space images. However, the reciprocal space images only see slight modification due to relatively small volume the helical folds exist over. Therefore, this phenomenon seems to only be observable through use of real space imaging methods. The reason behind the helical direction change was not identified. However, the alignment of the helical lines parallel to the direction of skyrmion ingress provides an observation to be considered in further work.

The expulsion of the helical phase by the skyrmion lattice is imaged in real space with a higher time resolution than previously achieved. The results however suggest that 10ms exposure is still slightly too slow to capture some of the faster dynamics where blurring and single image events could be improved with lower exposures.

The rotation of the skyrmion lattice observed is in agreement with that seen in previous neutron scattering experiments [25] and proves real space information about the position of skyrmions during the rotation process inaccessible through reciprocal imaging techniques. Observations of 5-7 defects provide greater understanding about how skyrmion lattice rotation is facilitated and potentially about the energy barriers involved. The experiment draws similarities to both bubble rafts and graphene to aid the explanation of geometrically constrained system dynamics. Ophus *et al* [105] investigate static grain boundaries in both experimental and simulated graphene grain boundaries. The image processing performed on the experimental images demonstrate local intensity ordered filtered images which appear very similar to skyrmion images. As expected due to the hexagonal ordering it is demonstrated that the peak dislocation density occurs at 30 degrees. Although there were not enough images to provide a statistical investigation of the same scale, there may be

enough similarities between the work shown here and the work by Ophus *et al.* that similar methodologies may be implemented in the future if further time resolved skyrmion data is taken. The experiments presented in this chapter successfully expanded on previous static identification of 5-7 defects in the skyrmion lattice specifically that presented in the paper by the Lumes group, EPFL [94]. The physical means by which 5-7 defects change location is identified including how multiple lattice periods can be moved simultaneously. The spacing of the 5-7 defects being proportional to misorientation of two adjacent skyrmion lattices is in agreement with graphene literature however only 5-7 defects were observed in these experiments unlike the more complex armchair type defects in graphene. The highest angle observed in these experiments is 14 degrees therefore more complex defects being present in higher angle boundaries in skyrmion lattices is possible. Significant research into understanding the defects in graphene have been performed computationally to understand the energy landscape. The boundary angle, defect motion frequency and defect type could provide a greater understanding about the energy landscape the skyrmions experience. This concept is partially continued in chapter 4 in FeGe skyrmion lattice boundaries. The source of the continuous rotation displayed is speculated to be caused by thermal gradients caused by beam heating of the sample and is an area which warrants further investigation.

Finally, the exact method of skyrmion creation and annihilation is not identified, however, valuable information on the appearance of meta-stable skyrmions and the local magnetic state is gathered. It has been shown previously that the area on a $B-T$ phase diagram over which skyrmions are stable can be extended into the conical phase by the presence of electric fields [106]. The phase boundary dividing the skyrmion phase and conical phase is shown to be significantly effected by applied electric fields with the emergence of meta-stable phases. In this research there is observations of isolated/clusters of skyrmions with a lifetime on the order of 10s of milliseconds within material exhibiting contrast expected of the conical phase. Although the skyrmions in this region do not demonstrate the same stability, the potential of creating isolated skyrmions in conical phase regions has been demonstrated.

Chapter 4

Instability of high angle skyrmion lattice grain boundaries in FeGe

4.1 Introduction

In the previous chapter, skyrmion lattice dynamics in Cu_2OSeO_3 were investigated in response to a rapidly applied magnetic field. It was observed that the presence and motion of skyrmion domain boundaries were facilitated by 5-7 defects, where the defect density along the skyrmion domain boundary is proportional to the angle between the lattices. In the previous chapter single-shot millisecond time resolved imaging of these 5-7 defects provided insight into the motion of skyrmion lattices during rotation. However, the skyrmion boundaries were rapidly expelled from the field of view preventing investigation into the local energy landscape. In this chapter, the motion of individual skyrmions forming a defect within a stable skyrmion domain boundary is investigated. Fresnel mode imaging is performed on the near room temperature (T_c ~250k) chiral material FeGe [22], where the thermal energy available in the system will encourage reorientation of the skyrmion lattice to reach an energy minimum. In section 4.2, the experimental method of both sample fabrication and imaging of the skyrmion lattice boundary in FeGe is detailed. We demonstrate the impact of the magnetic starting state on the presence and density of defects in section 4.3. Section 4.4 focuses on a single mobile defect containing what

appears to be a paired skyrmion structure. The meta-stable states that the defect moves between are identified throughout the image sequence. The contrast level and large areas of stationary skyrmions enable the application of 2D Gaussian fitting which is explored in section 4.5. This position data is used in section 4.6 to identify the motion of the skyrmion pair defect which is analysed using an Néel-Arrhenius law type method to provide an understanding of the energy barriers of the system. In section 4.7, the identification of the defect position in individual images and low individual exposure durations are combined to create composite 'Long exposure' images. In section 4.8, the motion of the defects and the surrounding skyrmions are analysed on a frame by frame basis to give motion vector maps of the transition between meta-stable lattice states. Finally, in 4.9 the results of the chapter are discussed with focus on the nucleation of skyrmion lattice boundaries, identification of skyrmion motion and the application of the Medipix3 in meta-stable skyrmion imaging.

4.2 Experimental setup

The FeGe bulk material was thinned to electron transparency using the focused ion beam (FIB) instrument. The lamella of material was then removed using an Omniprobe lift-out device as previously in chapter 3 and attached to a copper finger using tungsten. The sample was then inserted into the Gatan liquid nitrogen cooling holder HC 3500 to decrease the temperature to significantly below the critical skyrmion temperature of 270K. The liquid nitrogen rod was stabilised at 253K by use of a PID controller with a stability of $\pm$0.1K. The weakly excited objective lens was used to provide a magnetic field out-of-plane to the sample at zero tilt. As the sample is tilted, the effective magnetic field in-plane to the sample increases while the out-of-plane field decreases. Sufficient field is used to prevent a phase transition during tilting. Static imaging of the magnetic states in section 4.3 was taken using a Gatan Orius CCD camera. This provided wide-field imaging of the sample for identification of defects while investigating methods of high angle lattice boundary nucleation. Time-resolved imaging was provided by the Medipix3 detector, used in a similar manner to the Cu_2OSeO_3 data acquisition described in chapter 3. Continuous

mode acquisition was used whereby images are captured with zero gap time for readout by alternating between two separate pixel counters. The Medipix3 detector was used in this experiment to maximise the signal-to-noise ratio in the images taken. An energy threshold value of 4.5keV was used before an electron is registered as a count for exclusion of thermal noise. The exposure time used was 10ms and the total recording length of the movies was 10s (1000 frames).

4.3 Nucleation of high angle skyrmion boundaries

High angle skyrmion lattice boundaries were nucleated in FeGe from a helical state at remanent field by introducing a small tilt of 0.5° followed by an applied field of 510G, which, due to the small angle is a near out-of-plane field to the sample. This field is sufficient to cause the transition from the helical to the skyrmion phase. However, the uniformity of the helical starting state appears to influence the appearance of skyrmion boundary defects in the resulting skyrmion lattice.

Here, two methods of initialising the helical starting state are investigated before increasing the field and assessing the impact on the skyrmion phase. The first method of reaching the helical phase is by first heating the sample above the Curie temperature T_c. The sample is heated to 293K which is above the Curie temperature of FeGe and then allowed to cool back down to the helical phase temperature, while at remanent field. This causes the helical lines to nucleate uniformly with very few defects in place and no isolated skyrmions present from previous experiments. Figures 4.1A-C show images of the helical state created after the Curie heating cycle. The skyrmion states created after the 510G field is applied is shown in figures 4.1D-F. Figure 4.1F does contain a skyrmion boundary along multiple skyrmion lattice vectors. This boundary is highlighted with red arrows.

Alternatively, the nucleation of a non-uniform starting state in which the helical lattice contains multiple defect types is demonstrated through rapid field variation. The objective lens relaxation cycle was used to cyclically oscillate the field initially up to 5000G reducing the magnitude of the oscillations over time. Figures 4.2A-C show the resulting magnetic

ordering caused by this process. The helical lattice contains many defects, especially line defects where new helical rows cause a forking pattern to appear highlighted in 4.2B&C with yellow arrows. In addition to the helical lines there are clusters of skyrmions persisting in the remanent field of the objective lens which are expected to be meta-stable at the field value. This is caused by the field cycle changing the position on the B-T phase diagram, moving through the skyrmion phase repeatedly during the oscillations. Skyrmions nucleated during this time become trapped within the helical lattice after the phase transition from skyrmion into helical phase. In the images multiple clusters of skyrmions are present with examples highlighted with blue arrows in figures 4.2A-C. The resulting skyrmion lattices formed after the transition from this non-uniform helical phase to the skyrmion phase - shown in figure 4.2D-F - appears to contain more skyrmion boundary defects and discontinuities than the sample heated above the Curie temperature causing a phase change. Lattice boundaries are observed in all three images with red arrows annotated along the boundary.

The standard B-T phase diagram does not differentiate systems at the same point arriving from different paths. However, these experiments seem to suggest a form of magnetic hysteresis in which the magnetic disorder of a previous phase can influence the magnetic disorder of a phase after transition. This is a common property of first order phase boundary systems. The helical grain boundary defects increase the total energy in the system. However, due to the finite mobility of these defects during the transition to the skyrmion phase, the skyrmion phase forms around these defects causing a higher density of skyrmion grain boundaries after the transformation.

An example of a defect present after transition to the skyrmion phase from a field influenced helical state is shown in figure 4.3 which is an extract taken from figure 4.2E. In the centre of the image there is a line of white contrast that is four lattice spacings in length. This feature has similar contrast to a helical line inside the skyrmion phase, however, there also appears to be structure to the line. The left hand end of the line appears to have the contrast of a skyrmion within a helical line. It is predicted that this is not a helical line, but a set of skyrmions which due to the local energy landscape exhibit

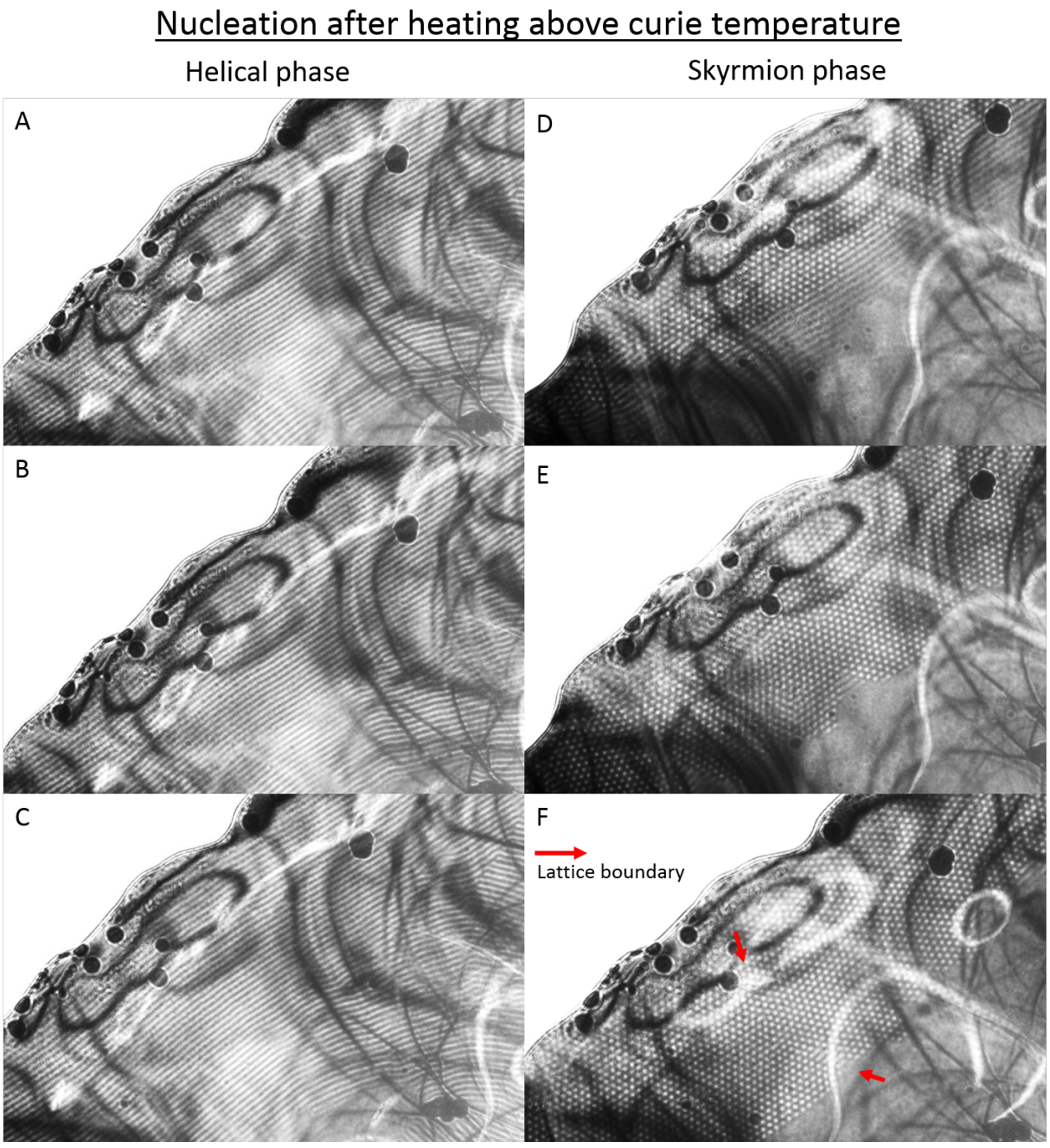

Figure 4.1: Figures showing the helical phase (A-C) of FeGe at remanent field (253K) after heating above the Curie temperature and, subsequent re-cooling, forming a uniform helical lattice. Figures (D-F), show the resulting skyrmion lattice after a magnetic field of 510G is applied out-of-plane causing a transition into the skyrmion phase.

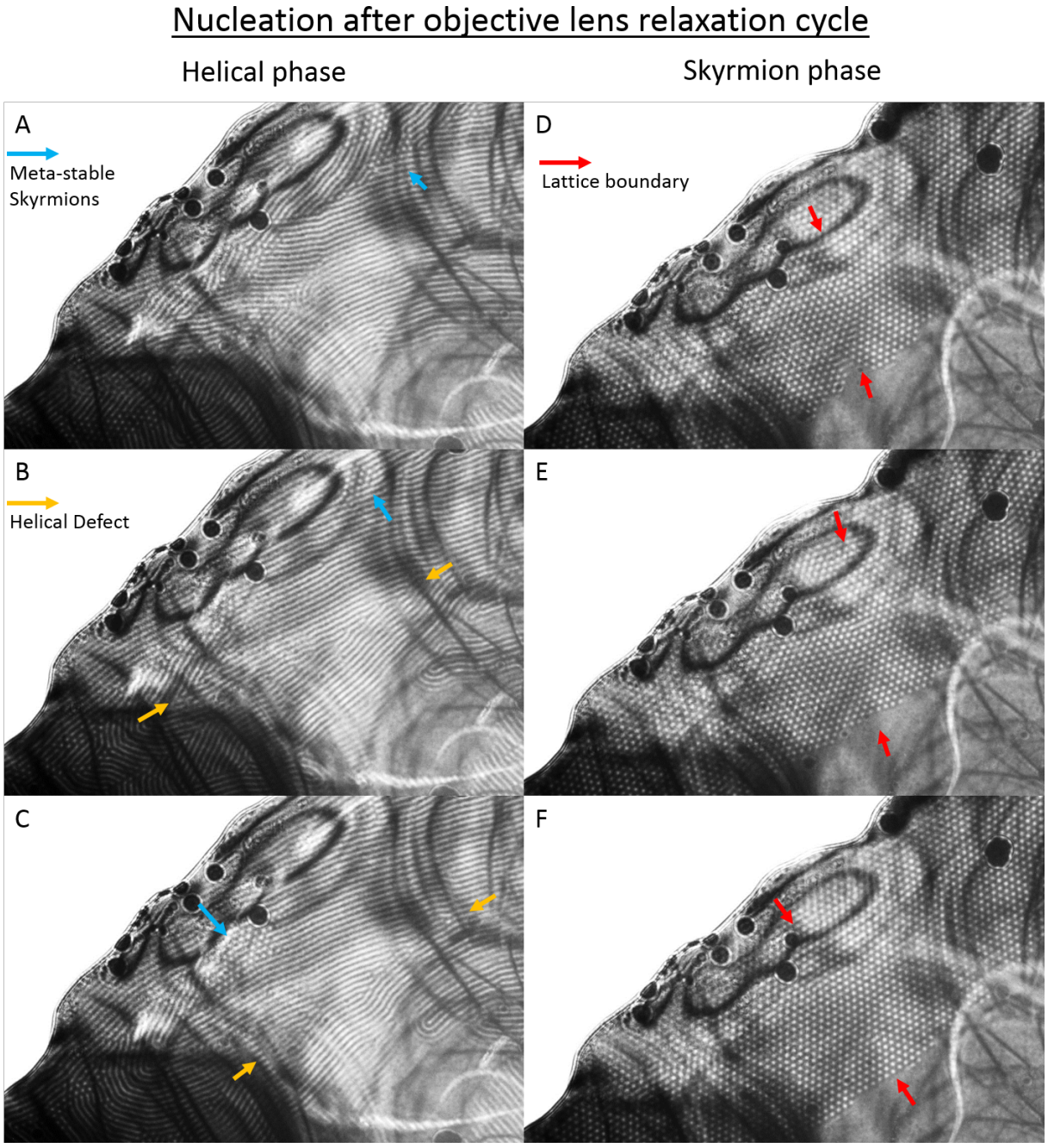

Figure 4.2: Figures showing the helical phase (A-C) of FeGe at remanent field (253K) after oscillation of the magnetic field, forming a high density of defects in the helical lattice. Figures (D-F), show the resulting skyrmion lattice after a magnetic field of 510G is applied out-of-plane causing a transition into the skyrmion phase.

motion in response to geometric frustration. This motion conjunction with the white dot contrast of the skyrmions in Fresnel mode imaging causes a time averaged blurring effect giving the appearance of white lines of contrast. The length of the line suggests that four skyrmions are present in this motion. Above this line defect we see two skyrmions paired closely together in a defect which is discussed in detail later.

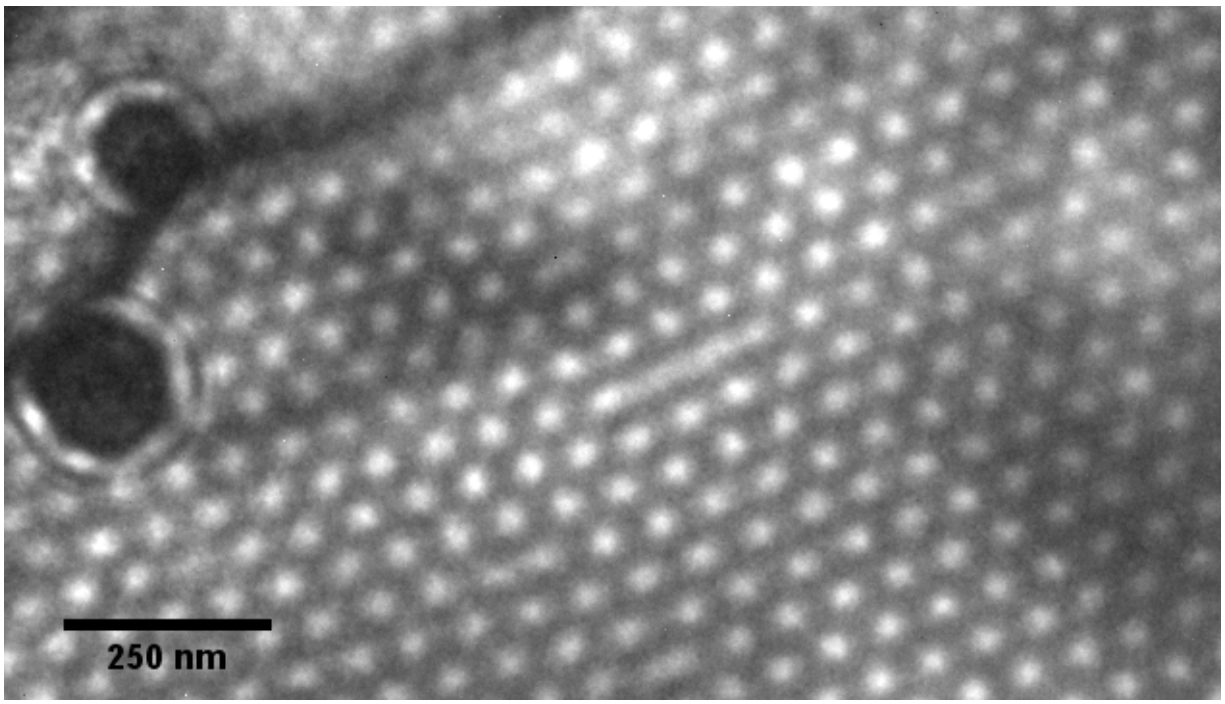

Figure 4.3: This extract from figure 4.2E, shows a line of contrast within the skyrmion lattice which is predicted to be rapid skyrmion motion caused by geometric frustration.

4.4 Analysis of Images and defect identification

In this chapter, a single set of image data is the primary focus for the analysis performed. The image set was taken for a duration of 1000 frames at a temperature of 253K. The image shows that the field of view area is entirely in the skyrmion phase apart from the bend contour contrast in the top right hand corner where the skyrmion contrast is shadowed and the two small defect objects at the top left and bottom left areas of the image showing dark contrast. Figure 4.4 shows frame #1 of the movie stack. The field

of view contains three defects in the skyrmion lattice, highlighted with red rings. The defects are labelled 1-3, from top to bottom. In this image the defects appear as a pair of skyrmions apparently so closely spaced that there is an overlap in their contrast, potentially making them appear like a single stretched skyrmion. This skyrmion pair is surrounded by 7 nearest neighbour skyrmions. The angle between the skyrmion domains that the boundary divides is calculated by taking the difference of the two near horizontal skyrmion vectors of both lattices. In figure 4.4 the plane of the left skyrmion domain is shown in green, the plane of the right skyrmion domain is shown in yellow. The angles of the three defects are calculated to be 16° for defect 1, 15° for defect 2 and 12° for defect 3.

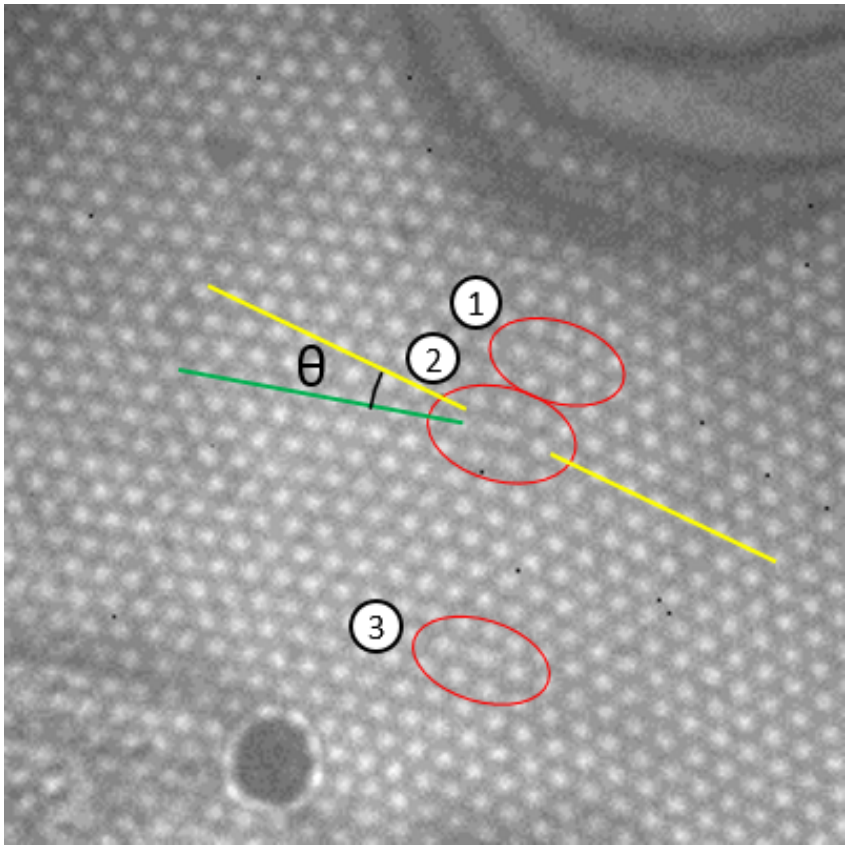

Figure 4.4: A figure showing the first frame of a high angle grain boundary in FeGe featuring three defects. Defect 1 exhibits infrequent motion, defect 2 exhibits regular motion where the defect moves between two meta-stable sites and defect 3 exhibits no motion during the recording duration

During the course of the movie the position of the defects appear to change location. The skyrmion pair position appears to hop laterally along the horizontal line of skyrmions. Defect 1 at the top of the image shows a few dynamic events during the course of the recording however not enough to build up a good statistic base. Defect 2 displays dynamics where a line of skyrmions regularly rearrange causing the defect to change position. Defect 3 at the bottom of the image displays no observable motion during the recording duration.

Observation of this skyrmion hopping motion shows that there are two meta-stable positions in which the skyrmion defect position has a lifetime longer than a single frame. This motion suggests that the two positions are separated by an energy barrier that is comparable to the thermal energy of the system. In addition to these two meta-stable sites, there are comparably rare frames which capture the more rapid transition between meta-stable sites. The presence of these transition images suggest that the motion between sites goes through a complex energy landscape with smaller local energy minima between sites. Examples of both sites and the unstable transition frames are given in figure 4.5.

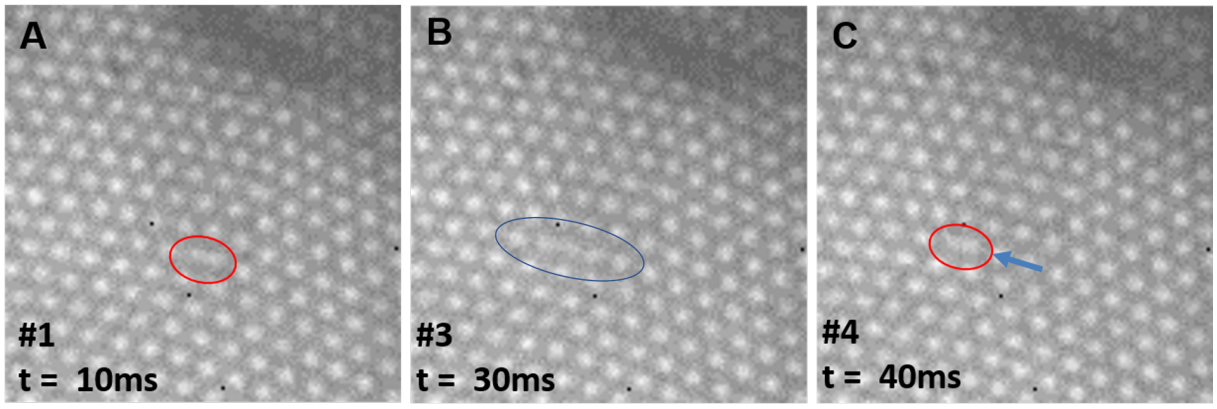

Figure 4.5: A figure showing the positions of defect sites and an example of a frame catching the transition. Image A shows site one, Image B shows a partial transition and Image C shows site one with a blue arrow overlaid to give a scale of distance the defect moves.

Figure 4.5A, shows a magnified extract from frame #1 with only a single skyrmion defect highlighted (Previously 4.42). Figure 4.5B, shows the transition frame captured where the skyrmions appear to now be no longer in a paired state but three skyrmions are

pushed into a space that should only contain two. Figure 4.5C shows the second position of the skyrmion pair after the transition. The blue arrow is used to highlight the distance of motion and alternatively the dead pixels provide another reference feature for indication of motion.

4.5 Skyrmion finding via 2D Gaussian fitting[1]

The level of contrast for the 10ms exposure images in this experiment is greater than those of the 10ms images presented in chapter 3 using Cu_2OSeO_3. This improved contrast has enabled more advanced skyrmion finding techniques to be employed in the analysis. The program Atomap, written by Dr Magnus Nord [107], which is used to analyse atomic resolution scanning transmission electron microscopy images, has been implemented here as a method of skyrmion finding. This program uses a series of processing steps including centre of mass fitting followed by 2D Gaussian fitting to find the positions of atoms in crystal lattices. The skyrmions in this Fresnel mode imaging present as white dots in a hexagonal lattice and therefore with only minor adjustment could be processed by this Atomap code. Each frame in the movie was first scaled to 4x the original image size using a bi-linear interpolation method. This step enabled the program to provide sub-pixel resolution position data on each skyrmion, where sub-pixel resolution is needed to fully understand the motion of the skyrmion pair due to small variations in the inter-skyrmion distances.

Figure 4.6 shows the position data generated by the Atomap code. Blue dots have been placed on each skyrmion at the calculated position. Defect 2 shows the pair of skyrmions identified. However, defects 1&3 only display a single skyrmion in the centre. This ability to resolve defect 2 and inability to resolve defects 1&3 is a consistent feature during the course of the movie where defects 1&3 are rarely resolved as separate skyrmions. It is predicted that the closer skyrmion pairing of defects 1&3 cause the suppressed dynamics.

[1]Skyrmion finding code adapted from the program 'Atomap', developed by Dr Magnus Nord, School of Physics & Astronomy, University of Glasgow

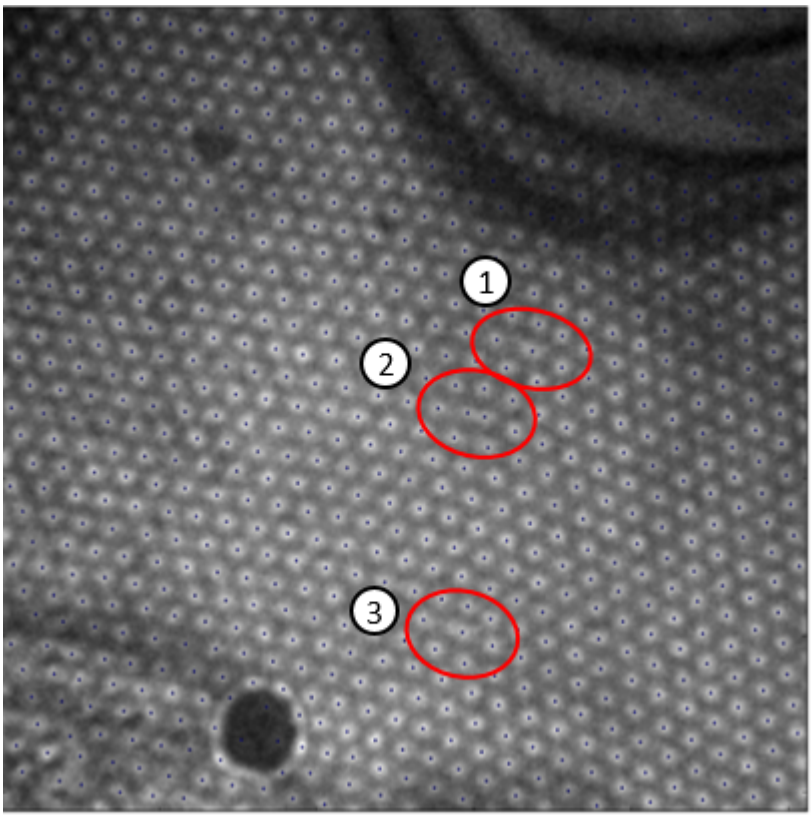

Figure 4.6: A figure showing the application of the Atomap code on a single frame after 4x bi-linear scaling. Blue dots highlight skyrmions identified through the 2D Gaussian fitting procedure.

4.6 Defect motion frequency and energy barriers

The frequency of motion of the defect skyrmion pair provides direct insight into the lattice energy landscape. In this experiment there are two meta-stable sites which can therefore be thought of as a double potential well shown in figure 4.7. Here the meta-stable skyrmion states are described by the two local minima. The red ball shows the defect position and the energy barrier E_a needed to move into the adjacent local minimum.

The probability of the skyrmion pair overcoming the energy barrier in a single attempt is exponentially dependent on the thermal energy of the skyrmions and the magnitude of the energy barrier together giving a Boltzmann factor. The skyrmion pair attempts to separate with a frequency called the attempt frequency. The probability per attempt

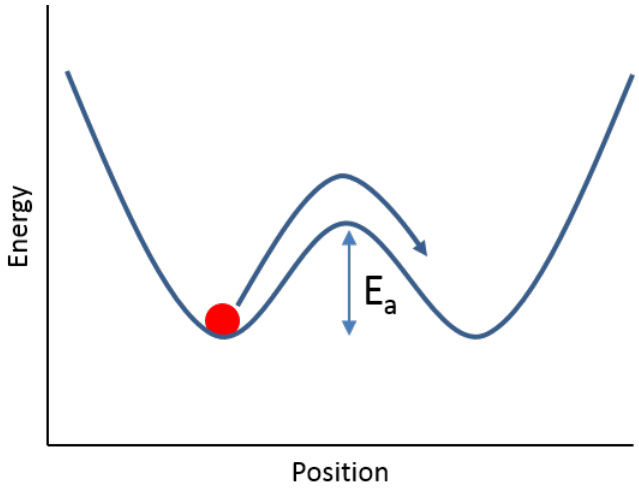

Figure 4.7: This image shows a representation of the meta-stable skyrmion defect local energy landscape with respect to position. The red ball represents the skyrmion defect being at site 1 with an energy barrier E_a between it and the skyrmion defect being at site 2.

and the attempt frequency together give the average time required for the skyrmions to overcome the energy barrier, as shown by the Néel-Arrhenius law in equation 4.1.

$$\frac{1}{\tau} = f_o e^{\frac{E_a}{kT}} \tag{4.1}$$

where τ is the state lifetime, f_o is the attempt frequency, E_a is the energy barrier, k is the Boltzmann constant and T is the temperature of the system.

To calculate the energy barriers we must first identify the position of the defect itself. Several methods were tested such as difference image analysis and several methods using the position. The method chosen used the fact that the motion occurred linearly along one of the lattice vectors. Figure 4.8A shows an extract from frame #1. In this frame there are four skyrmions of note; the pair that form the skyrmion defect at site 1 and the pair forming a defect at site two. These four skyrmions are directly adjacent to one another as shown in figure 4.8B and have been labelled 1-4. To determine computationally the defect position a reference skyrmion is used at the end of the chain with which the distances between the skyrmions can be calculated and compared. These relative distances are shown in figure 4.8C for the first 100 frames.

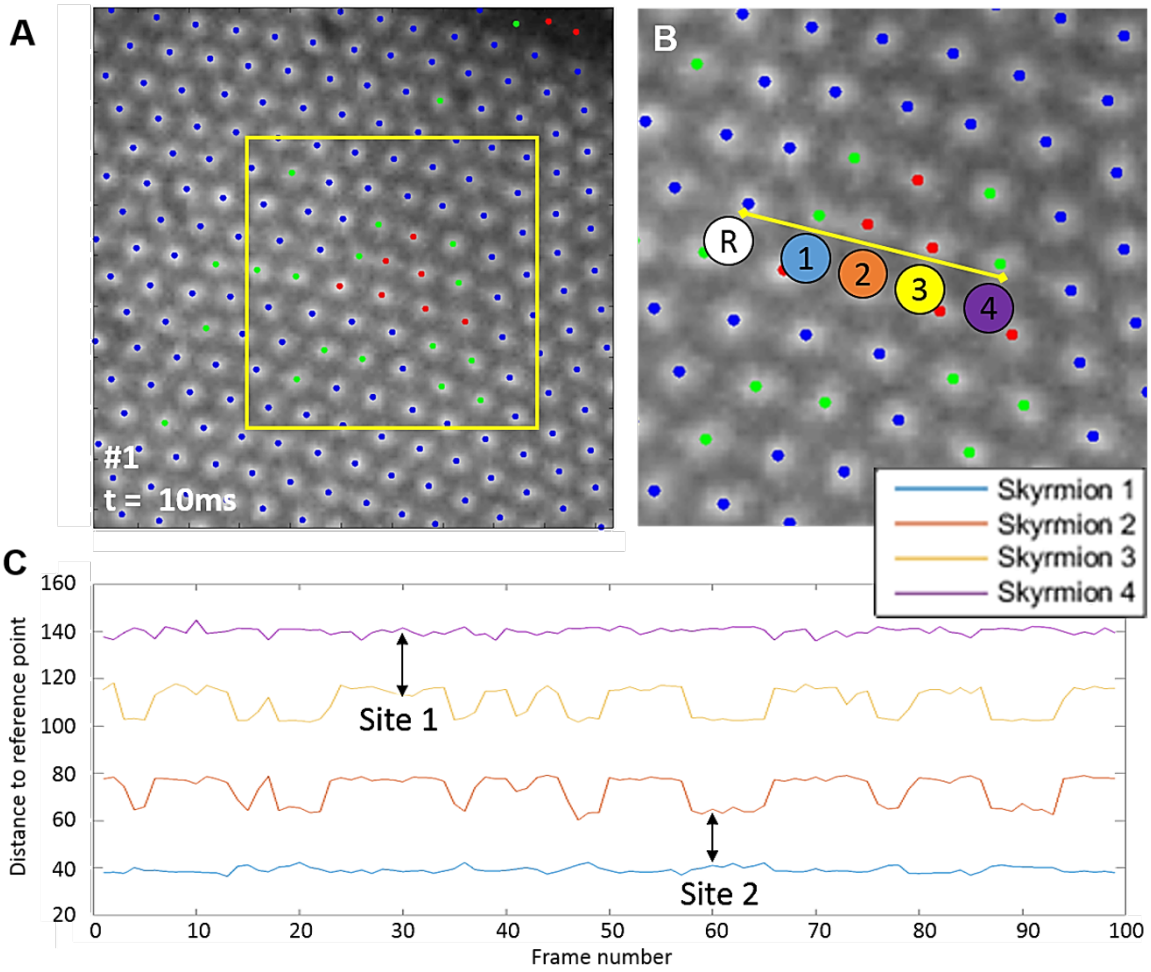

Figure 4.8: Figure A, shows an extract from frame #1 with a yellow region of interest shown in figure B. Figure B, shows five skyrmions in a line labelled. The skyrmion labelled R, is used as a reference skyrmion from which the distances to the other skyrmions 1-4, are used for determining defect site position. Figure C, shows a graph of the skyrmion distances to the reference point plotted for the first 100 frames. Skyrmions 2&3 are shown to exhibit mirrored motion while skyrmions 1&4 remain near stationary.

The position of the defect can then be identified based as the skyrmion pair with the shortest between them as calculated from the reference point. Figure 4.8C has highlighted the smallest difference for frames #30&#60 which show the defect sites at positions 1&2 respectively. Figure 4.8C shows that skyrmion 1&2 move in phase with skyrmions 1&4 exhibiting small correlated movements with 2&3. Skyrmions 2&3 clearly undergo the largest motion of the four skyrmions showing that as one pair of skyrmions overcomes an energy barrier it causes the other pair to become closer together. This analysis makes finding the average duration spent at either site possible by using an average position threshold to determine if the system is currently paired in site 1 or 2. Although this gives us position information it also gives us an understanding of the dynamics happening. Skyrmions 1&4 appear to have much smaller motion during the pairing and unpairing events. This suggests that the energy barrier enabling the reorientation of skyrmion 2&3 is extremely localised. The lifetimes of the skyrmion pair at each location are calculated for the full 1000 frames and presented in the histograms in figure 4.9 in a normalised form showing the lifetime probability fitted with an exponential trend-line.

In order to calculate the energy barrier using equation 4.1 an attempt frequency is needed, however, at the time this research was conducted there appears to be no value in skyrmion literature suitable. Therefore an approximation for this value is used until further research can be conducted by comparing the attempt frequency to a similar system. The system chosen is the motion of superconducting vortexes. Research carried out investigating the motion and reordering of superconducting vortexes have estimated values for the attempt frequency up to 10^{13}Hz [108, 109]. For the purposes of calculations in this project an attempt frequency of 10^{14} was chosen. However, it would be expected that a more accurate value for the attempt frequency will emerge in future research and consequently alter the scaling of the calculated energy values as described in equation 4.1.

The results of this experiment show that the local energy landscape in this region has a near symmetric energy barrier meaning the probability of the skyrmion pair occupying either site is approximately equal. The energy barrier E_a is calculated using equation 4.1 to be 0.56eV where an attempt frequency of $1x10^{14}$Hz is used. The kT value for this system

is calculated to be 0.022eV. The system appears to exhibit magnetic viscosity where the term magnetic viscosity has been used to define systems time dependence of magnetization during constant field and constant temperature. This term is part of the Néel relaxation theory developed by Louis Néel [110]. The energy of this energy barrier may be used to determine the response of the motion to changes in temperature of the specimen assuming there is no phase change.

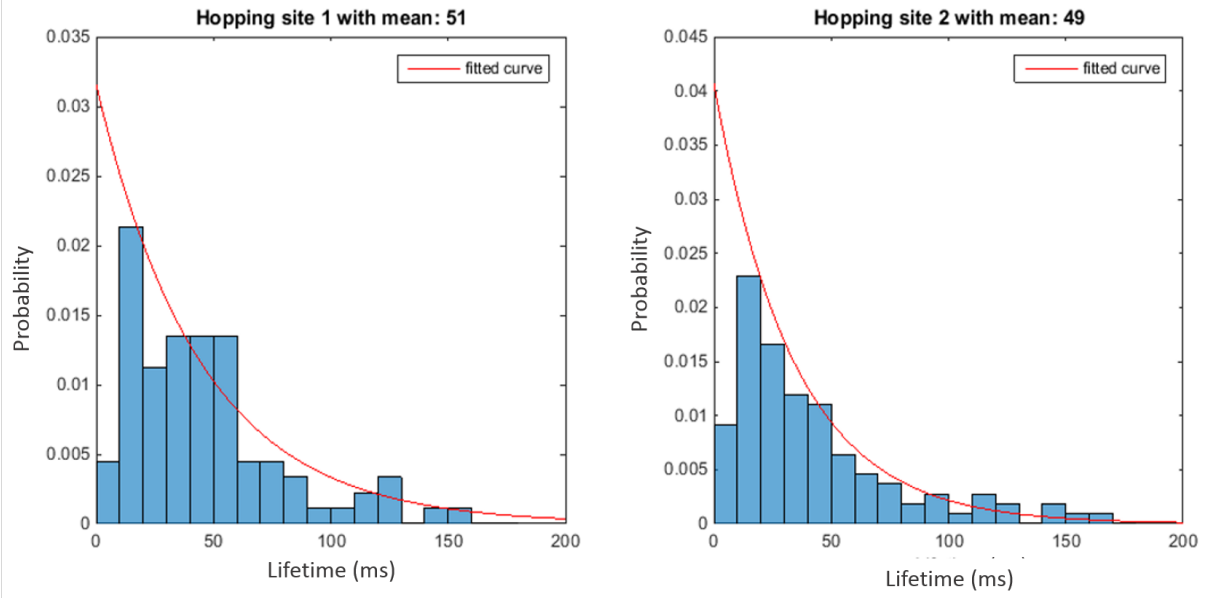

Figure 4.9: The calculated lifetimes of the defect at site 1 (left) and site 2 (right). The lifetime is normalised to give a probability of the defect for a given lifetime.

4.6.1 Asymmetric energy landscapes in high angle grain boundaries

In this section a second set of defect data is introduced to demonstrate alternative skyrmion pair motion probabilities. This experiment was performed using the same field and temperature conditions as the previous data set however the magnification is increased to focus on a specific defect. The defect exhibits similar bi-stable skyrmion pairing however in this example the skyrmion pairing moves only one lattice spacing rather than the

symmetric energy barrier example where the defect moved by two skyrmion spacings. The two skyrmion states are shown in figure 4.10

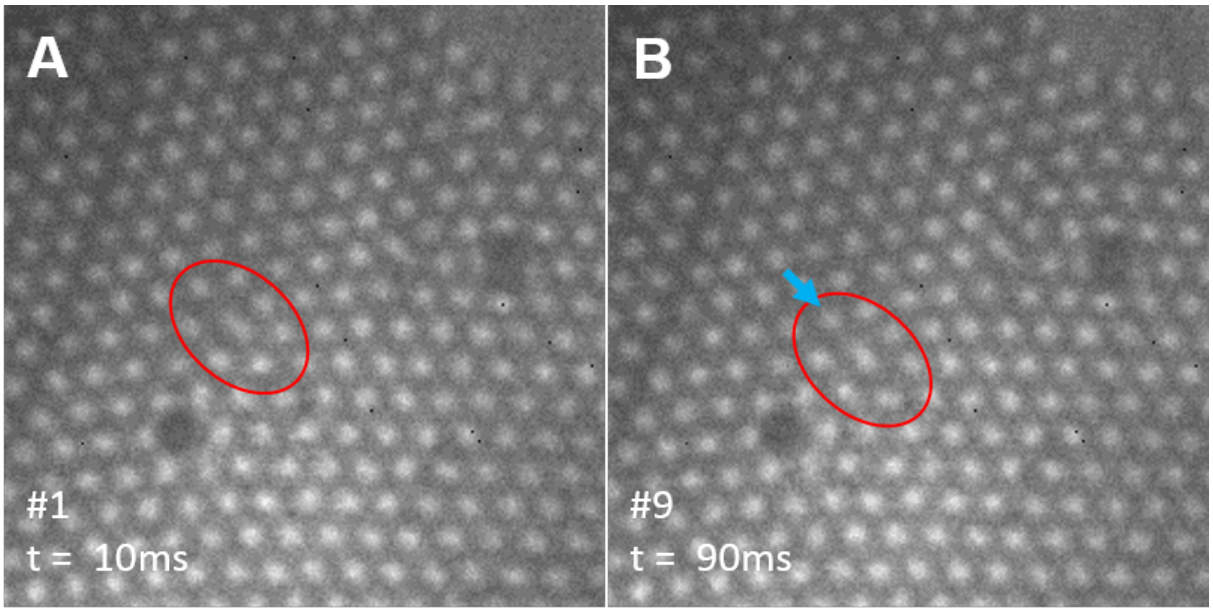

Figure 4.10: Fresnel images of an alternate high angle skyrmion lattice boundary exhibiting similar bi-stable motion of a paired skyrmion object. Figure A highlights the position of the defect at site 1 and figure B highlights the site at site 2 with a blue arrow indicating the distance.

In this system the skyrmion configuration shown in site A of figure 4.10 has a significantly longer lifetime than site B. This suggests there is an asymmetric energy landscape where the energy barrier is smaller moving from case B to A than the reverse direction. The lifetimes are calculated using the same method as the previous section and presented in figure 4.11

The results of this experiment prove that the local energy landscape in this region has an asymmetric energy barrier. The energy barrier of sites A&B are calculated using equation 4.1 as 0.586eV and 0.559eV respectively, where an attempt frequency of $1x10^{14}$Hz is used. The reason for the difference in energy landscape between the asymmetric and symmetric data-sets is not identified in this experiment however the Medipix3 detector is shown to be capable of resolving the motion of these defects at the 10ms timescale.

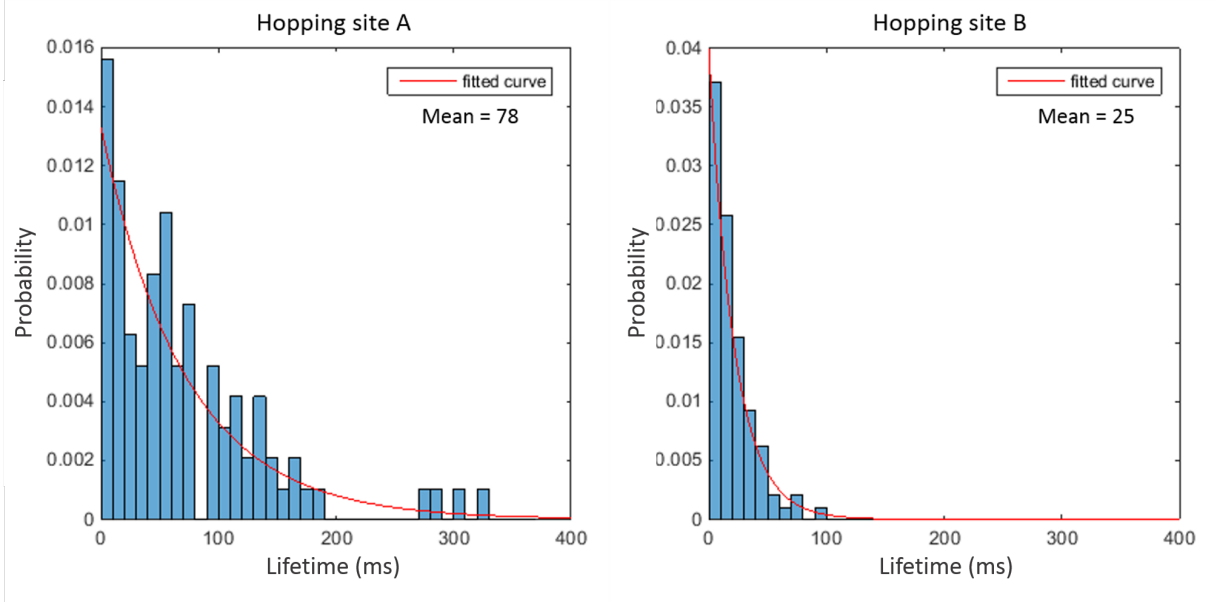

Figure 4.11: Normalised probability curves of the lifetime at site A in figure A and site B in figure B. The curves show a clear asymmetry in the lifetime of the defect at both sites.

4.7 Composite images of paired skyrmions

The magnetic structure of the skyrmion pair defect is important in understanding the physics of the energy landscape. However, the rapid motion of the skyrmion pair defect causes acquisition of high contrast, long exposure images of the pair while at either of the two meta-stable sites using a standard CCD camera difficult. The individual 10ms images have sufficient contrast between the centre of the skyrmion and the surrounding area to identify the skyrmion position however, a line profile taken across a skyrmion is prone to shot noise. In this section we investigate post-processing the image stack to retrieve composite images of the skyrmion defects at both sites 1&2. Using the defect position data gathered in the previous sections we remove all images from the stack where the skyrmion is at site 2. This leaves approximately half the images where every image has the defect at site 1. The image is then averaged into a single composite image. This single image has an equivalent exposure of the sum of the exposures in the contributing images. To demonstrate this, composite images have been formed by summing 10 sequential frames together resulting in a total exposure time of 100ms. These composite images are shown

in figure 4.12, where figure 4.12A shows the composite image for site 1. Figure 4.12B shows a magnified image for the defect. Figure 4.12C shows the composite image for site 2. Similarly, figure 4.12D shows the magnified image of site 2.

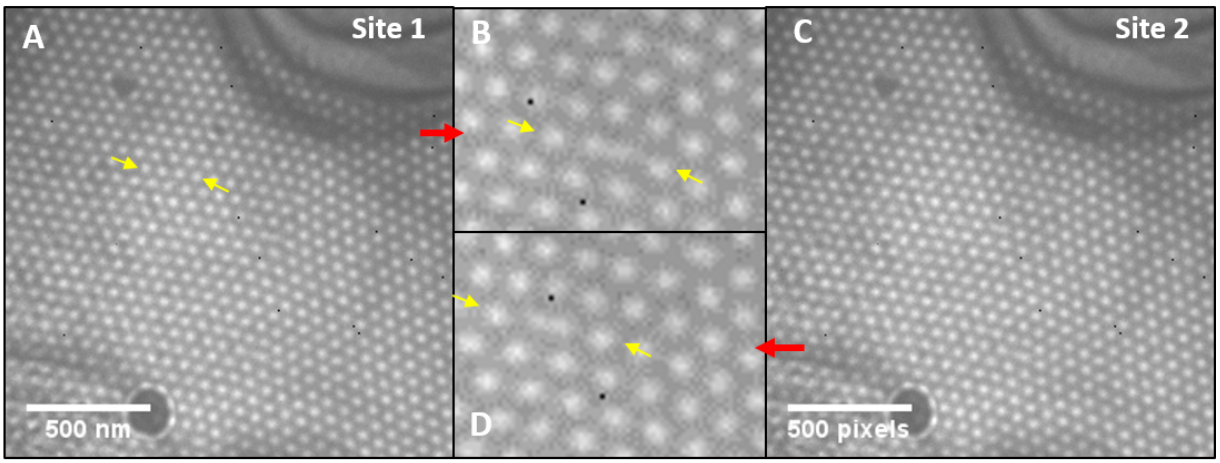

Figure 4.12: A figure showing composite images created from 10 frames where the skyrmion pair is at a single site respectively. The central images show a magnified section to highlight the skyrmion pairs.

Line profiles are taken of the defect sites in both composite images, these line profiles start and end positions are highlighted with yellow arrows in figures 4.12C&D. Additionally, to compare the difference between the defect skyrmions and the uniform lattice skyrmions a line profile is taken from the left hand skyrmion domain of figure 4.12A. Figure 4.13 shows the line profiles taken from the two composite images and the background skyrmion line profile offset vertically by 500 for clarity. The paired skyrmion peaks are shown to have weaker contrast than their single skyrmion counterparts in both cases. Site 1 appears to have a significantly more distinguished separation between the paired skyrmions than site 2. Site 1 has a skyrmion pair local minima that is 94% of the average pair peak height compared to site 2 where the local minima is 97% of the average peak height. The background skyrmion separation is an average of 10 pixels (Taken over 10 skyrmions) equivalent to 70nm. The separation of the skyrmion pairs by site is significantly lower than the background where site 1 has a separation distance of 4 pixels (28nm) and site 2 has a separation distance of 5 pixels (35nm). The distances between the nearest neighbour

skyrmions to the skyrmion pair is the same as the background skyrmions where the average of the four distances is 10 pixels (70nm) suggesting that the strain is localised to the skyrmion pair itself.

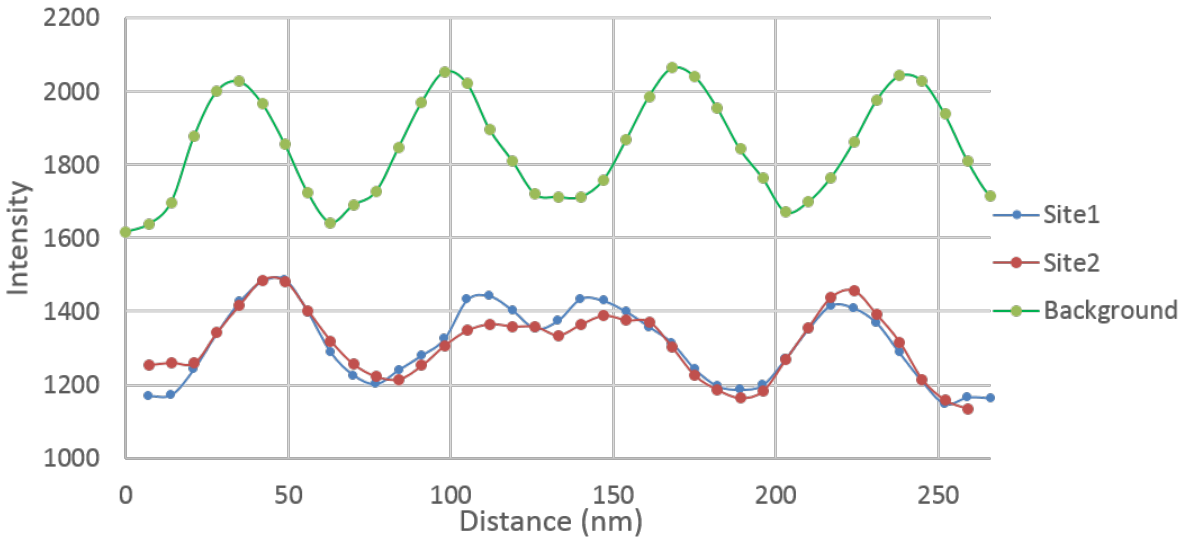

Figure 4.13: The graph contains the line profiles of the skyrmion pairs at both site 1&2 with the adjacent skyrmions included for reference. Additionally a line profile for the background skyrmions is added for comparison.

4.8 Skyrmion pair defect dynamics

The confined structure of the skyrmion lattice enables analysis of the motion of skyrmions with the assumption that they are not being created or destroyed in the region of the defect. The position of the skyrmions frame to frame can be identified allowing a vector map of skyrmion motion to be created. Skyrmion planes shifting in opposite directions to accommodate the motion of the skyrmion pair defect are identified. Figure 4.14 shows two images, each containing their own vector map created by sequential frames. In both images the plane of the defect is highlighted by the red bar and the skyrmion pair is highlighted with a red ring. Figure 4.14A shows frame #5 with the positions of the skyrmions in frame #6 indicated by the vectors in blue. The image shows the frame directly before the defect

position moves from site 2 to site 1. The pair separates in the sequential frame in which two skyrmions move to the right. The row above has a smaller magnitude of motion in the same direction. The row below shifts in an opposite direction to the motion of the defect skyrmions. Conversely, figure 4.14B shows frame #5 connected to frame #5 showing the transition from site 1 to site 2. The opposite direction of the defect shift is mirrored by the surrounding skyrmions where the row above follow the direction of motion and the row below oppose it. In both images the grain boundary separating the two skyrmion domains is positioned at an angle of 14 degrees along the plane lateral to the skyrmion pair as shown previously in figure 4.4. Figure 4.14C shows the same frame as figure 4.14A with a Burgers circuit overlaid to highlight the Burgers vector, b. The Burgers vector is defined as a representation of the magnitude and direction of the lattice distortion resulting from a dislocation in a lattice. Although this is usually applied to crystal lattices it still provides a useful metric when describing the impact on the hexagonal symmetry of the skyrmion lattice. Figure 4.14C demonstrates that the Burgers vector is one lattice spacing in the plane of the defect motion. Figure 4.14D shows the same frame as figure 4.14B overlaid with a nearest neighbour map in which a skyrmion above the defect connects to five neighbours in red and the skyrmion pair centre point is connected to seven neighbours. This 5-7 geometry is similar to those presented previously in figure 3.17.

The defect dynamics are consistent in all transitions between the two defect sites. The opposing directions of motion appear to minimise energy by maintaining the maximum area of skyrmion lattice at the standard inter-skyrmion distance. The skyrmion vector map shows the impact of the motion on surrounding skyrmions as a function of distance and location to the defect. The skyrmions below the defect have significantly more motion than those above the defect. This is likely caused by the direction of the defect angle, where the skyrmions above and below the defect have different levels of geometric frustration. The skyrmion rows greater than one away from the defect have very little motion, which highlights the very localised energy landscape change around the defect during motion.

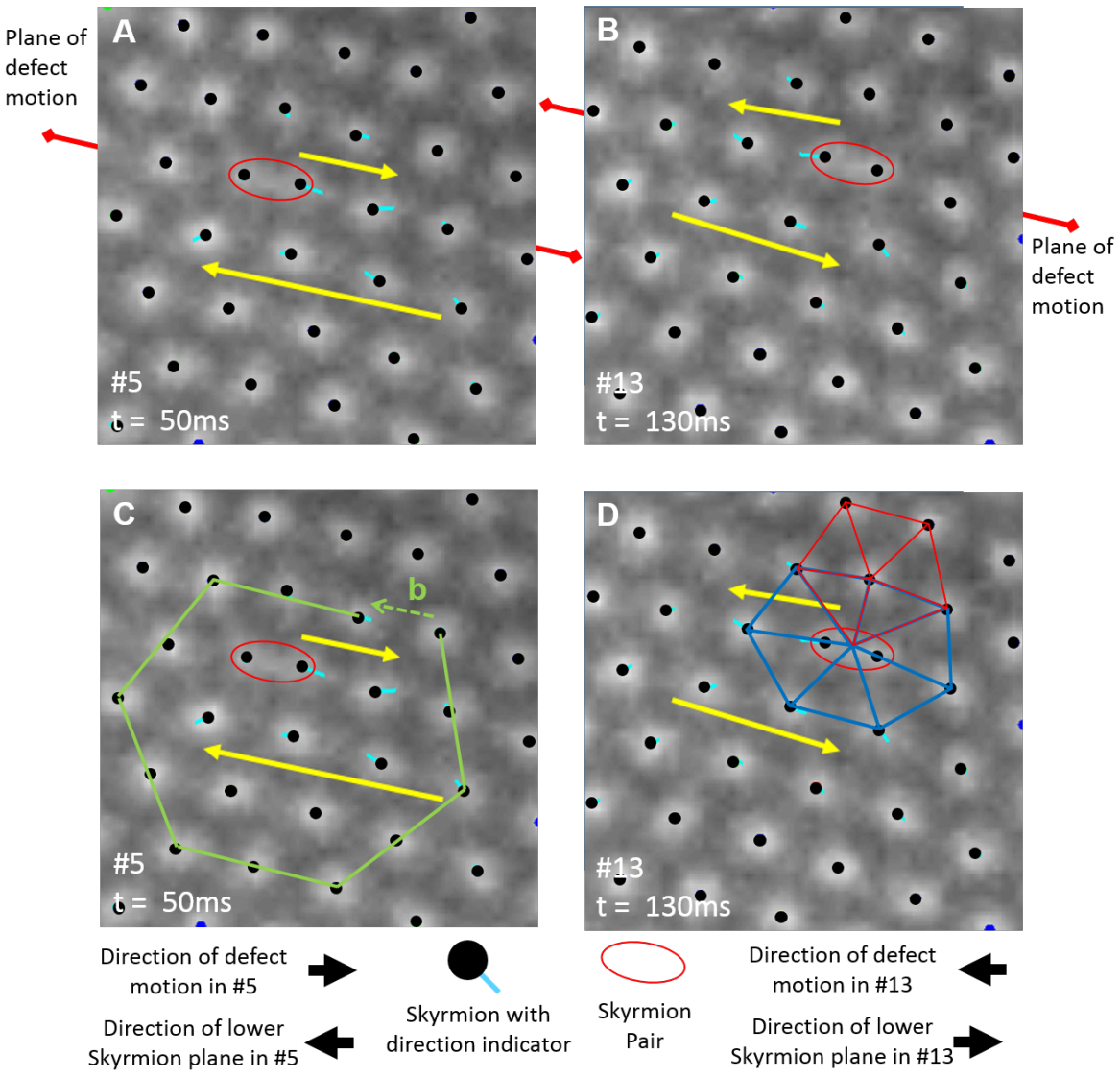

Figure 4.14: The impact of defect motion on the surrounding skyrmion lattice rows is highlighted in this figure through skyrmion vector maps. Figure A shows the skyrmion defect in the frame immediately before a shift to the left, similarly figure B shows the skyrmion defect in the frame immediately before shifting to the right. Figure C is duplicate of figure C with a Burgers circuit constructed to show the Burgers vector of the defect. Figure D is a duplicate of figure D with a 5-7 defect overlaid to demonstrate the nearest neighbours of the pair defect.

4.9 Discussion

An important aspect of investigating the dynamics of skyrmions at high angle grain boundaries was the nucleation of the skyrmion boundaries and defects exhibiting motion. Nucleation of skyrmion lattice defects such as dislocations and grain boundaries have been demonstrated in locations of structural defects such as at crystalline grain boundaries [111], near grain boundaries [112] and near the edges of samples [113]. However, the method of inducing grain boundaries has not been fully explored in previous research. We have investigated the effect of raising the sample above the Curie temperature and then back to the experimental temperature of 253K. This process results in a uniform helical lattice which is likely caused by the lack of magnetic structure present before the transition from the paramagnetic phase into the helical phase. In comparison to this, we have investigated oscillating the magnetic field at a magnitude which will cause the sample to pass from the helical, through the skyrmion and into the field polarized phase. This oscillation is reduced in magnitude until the field no longer causes field polarisation and finally comes to rest in the remanent field corresponding to the helical phase. The process appears to trap both skyrmions and helical discontinuities into the magnetic structure where the field oscillate faster than the time required to expel the defects. In our results we observe a form of structural magnetic hysteresis in the helical lattice. We observe that two separate paths of reaching the same point on the B-T phase diagram cause helical structure with different levels of dislocations and isolated skyrmions. This effect is important as it allows some control over the presence of defects for study. It has been observed that the uniformity of the helical phase may directly impact the density of defects in the skyrmion phase. The comparison of the skyrmion phase structure from the two types of helical phase initialisation; Curie heating and lens relaxation, show that the grain boundary defects and dislocations present in the helical phase may persist into the skyrmion phase with applied field.

The improvement in the SNR between the skyrmion core and surrounding area presented in the FeGe compared to the images taken in chapter 3 is clearly shown through implementation of 2D Gaussian fitting as a form of skyrmion finding rather than the tech-

nique previously implemented. Skyrmion identification was performed using the program 'Atomap' which was able to correctly identify the skyrmion pair at the defect primarily analysed in these results however had difficulty separating skyrmion pairs at other defects. The distance between the peaks appears to be short enough that the resolution of the Fresnel imaging technique is insufficient to clearly resolve the structure of the skyrmion pair. Alternative imaging techniques may give sufficient spatial resolution to resolve the position of these skyrmion pairs.

This chapter identified an object that appears to be a pair of skyrmions in close proximity, however, this is determined by the fact that the contrast shows the object dividing during the transition between skyrmion defect sites. In previous work on $FeGe_{1-x}Si_x$, observations of skyrmions in close proximity at crystal grain boundaries are demonstrated with predictions on the possible cross-sectional configurations of the skyrmion pair [112]. Stretched skyrmions have also been imaged in $FeGe_{1-x}Si_x$ using DPC scanning transmission electron microscopy [111]. It is observed that some skyrmions in a skyrmion domain boundary stretch in a single axis becoming elliptical. In the research presented here we have used composite images to determine if the object is two definitive skyrmions in close proximity rather than a single stretched skyrmion. The distance between the skyrmions is calculated from the composite images to be 28nm-35nm depending on defect site location, which is approximately half of the 70nm of the surrounding skyrmions including skyrmions within one lattice spacing of the defect itself. The hopping motion of the defect itself has not previously been identified in the skyrmion phase for FeGe. However, the motion of defects in FeGe has been documented previously in the helical phase where motion of magnetic edge dislocations are detected through scanning MFM showing discontinuities in the rastering image [114]. The observed structure of this object may give support to the possibility of skyrmions connecting at a Bloch point midway though a sample as a method of skyrmions merging [115].

It was proposed by Milde *et al* [115], that skyrmions in $Fe_{1-x}Co_xSi$, may merge at some point within the centre of the material therefore presenting as a single skyrmion on one side of the material and two skyrmions on the opposing side. This prediction uses a magnetic

anti-monopole to explain the change in topology through the material. In these predictions it appears to suggest that the structure of the single skyrmion may be warped into a elongated shape due to the merging of the two skyrmions on the opposite side however no length scale is given for this effect. In this experiment a thin lamella is imaged and therefore may be a method of examining a cross section of this system in a experimental application. Further investigation into the structure of this defect is needed using a high spatial resolution technique such as DPC to fully understand this magnetic object.

In this experiment the pairing and unpairing of the skyrmions at each site in the form of a potential energy barrier was investigated. It had been initially intended to use an Arrhenius law approach calculating the energy barrier using the hopping frequency as a function of temperature. Although data sets at different temperatures had been acquired, the modification of the skyrmion domain boundary during temperature changes has caused sudden removal or suppression of the skyrmion motion. This meant that the energy landscape was predicted using an attempt frequency approach which gave results within an order of magnitude of that predicted.

An important feature of this work is the capability of the Medipix3 to create composite images of systems with multiple states. In a standard CCD camera an image with exposure t is not equivalent to two exposures of $t/2$ because the integrated image contains double the read noise created by the detector. Therefore a single long exposure image usually gives a greater signal to noise ratio (SNR). The Medipix3 device has zero readout noise and therefore in the above case the images should be equivalent in SNR. Assuming that the magnetic state observed can be identified in a single short exposure and the duration between transitions is less than the exposure, then a composite image can be created. There is no limit to the number of states that the system can occupy if the previous conditions are met as an identified state can be integrated with images of identical states to create high SNR images. In section 4.7 this was demonstrated by identifying two states separated by a rapid transition. The image SNR is improved to the level that line profiles provide insight into the skyrmion pair structure. This technique however could provide a powerful tool in imaging repetitive millisecond magnetic dynamic systems.

Chapter 5

Investigating the ultimate time resolution of the Medipix3 as a direct electron detector

5.1 Introduction

In this chapter the experimental capabilities of the Medipix3 single electron detector are investigated through *in-situ* imaging of a time varying electron beam. The initial section, 5.2, describes details of the Medipix3 detector hardware and Merlin readout system. The time response of key hardware components is explored for a single pixel during the detection of an electron. It is discussed in relation to the ultimate time resolution achievable by the Medipix3 architecture. The impact of primary electron energy was investigated through Monte Carlo simulations to determine the spread of energy between adjacent pixels on the detector. In section 5.3, we characterise the time resolution of the electrostatic deflection plates in response to voltages applied at MHz frequencies. This characterisation is used to determine the suitability of the electrostatic deflection plates as a method of creating a time varying signal in the nanosecond regime. In section 5.4, we investigate the hardware variable threshold energy level impact of this on time resolution performed in single pixel mode (SPM). In section 5.5, we attempt to synchronise the image acquisition delay with

a single deflection state, to prove that the maximum exposure duration is equal to half of the oscillation time period. In section 5.6, we compare the time resolution of charge summing mode (CSM) to imaging with SPM during a delay sweep of a single deflection transition. In section 5.7, the results of the chapter are discussed in the wider context of time resolution in TEM and the motivations using detectors to achieve time resolution. The time resolution achieved in these experiments are compared to other modern pixelated detectors available.

5.2 Medipix3 Hardware

The imaging capabilities of the Medipix3 detector demonstrated in this chapter come directly from the silicon detector technology and the unique hardware architecture [116]. A schematic diagram showing a cross section of the Medipix3 is shown in figure 5.1 with reference to the key features. The Medipix3 detector is composed of an electronic chip with integrated logic bump-bonded with solder to a slab of silicon providing the conversion of electrons to a charge current. Silicon is a direct band gap semiconductor in which the valence band and the conduction band are separated by an optical band gap of 1.14 eV [117] and an electrical band gap of 3.6 eV. When an electron is inelastically scattered by a silicon atom, there is some energy imparted to a valence electron, promoting it to the conduction band creating an electron hole pair. The electronics-facing side of the silicon slab is patterned by dopant implantation to create a region of p-type material. This effectively creates a p-n junction with the surrounding n-type silicon material. This material is implemented in a range of thicknesses dependent on application. The material thickness used here is 300μm thick to provide adequate material to stop 200keV electrons discussed fully later. This silicon is sandwiched between thin layers of aluminium to provide conductive material for application of a biasing voltage. The default bias applied to the Medipix3 chip during these experiments is 90V, however, it has a maximum of 120V (typically used in 500μm silicon). This silicon structure is then bump-bonded directly to the single pixel logic circuitry mounted on the electronics board. Figure 5.1 shows the pitch

between the single pixel bump-bonds as 55μm which extends in two dimensions to create a 256 x 256 array. Each of the single pixel logic circuits feature two 12-bit counters which can read/write independently or together form a 24-bit counting register. The Medipix3 chip is controlled by a Merlin readout system produced by Quantum Detectors Ltd, Harwell Oxford.

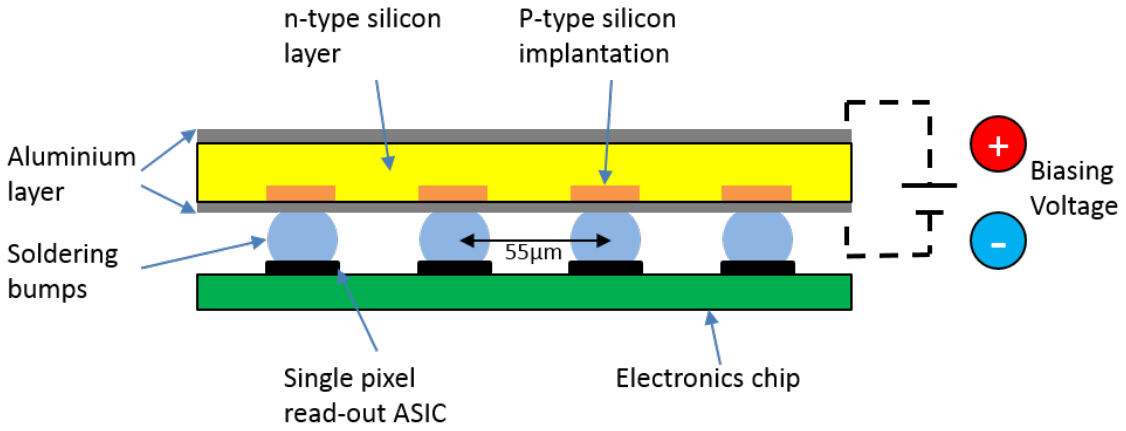

Figure 5.1: A schematic diagram of the Medipix3 device with the up most layers removed to reveal the position and geometry of the bump-bonding and circuitry.

The Merlin system runs on a 110 MHz internal clock (≈10ns) which is used for all timing such as the internal shutter, which dictates the duration of exposures and the acquisition trigger delay mechanism used for pump-probe type imaging. The jitter of the trigger response is in the region of 10ns (1 cycle) with a maximum of 20ns (2 cycles). The exposure trigger may either be activated by the internal clock, or in response to an external time to live (TTL) trigger signal [5].

The readout time of a detector is a primary limitation in the speed in frames per second (FPS) that can be achieved during acquisition. In the 12-bit operation the pixel readout takes a minimum of 820μs into the internal buffer of the Merlin system, after which time another exposure can be taken. This readout time provides a maximum frame rate of 1200 fps. The read action of the 12-bit counters can be limited to 1-bit or 6-bit to provide a reduction in the readout time. The pair of 12-bit counting registers can be used in tandem as a feature of continuous operation mode. Continuous operation mode enables

gapless sequential imaging where the dead time between frames is zero. The two counters take turns acting as the current counting registry and the counter being read out. The primary limitations of continuous operation mode are that the alternating purpose of the registers prevent the Medipix3 from using a 24-bit counter in this mode. Additionally, for the image acquisition to be gapless the acquisition time must be greater than the readout time ensuring the registry acting as the readout counter is empty and ready to start image acquisition.

The detection of a single electron is a process with multiple steps in analogue to digital conversion. Acquisition modes available to the Medipix3 detector, such as charge summing mode and colour mode, have increased the complexity of the hardware significantly over previous models. A block diagram of the components involved in the analogue to digital conversion process in a single pixel is shown in figure 5.2. Connections in green are only important when the detector is used in charge summing mode (CSM), discussed in detail later in this chapter. In figure 5.2 the area highlighted in orange is the analogue part of the system where the energy from the electron is interpreted as a voltage. Between the orange and blue areas are the discriminators used to digitally resolve when the voltage is above a threshold level. The blue area contains the logic circuitry where many of the detector configurations are used such as gapless acquisitions and CSM. Finally the area in purple encompasses the pair of counters with the shutter input that defines the duration of the exposure by allowing the counter to increase. This diagram is used as a reference for the hardware layout for the duration of this chapter.

To assist in understanding of the block diagram in figure 5.2 further, a simplified model of the response of key components to the arrival of a single electron is shown in figure 5.3. The diagram shows the timing of four important events in processing an electron impact. Figure 5.3A shows the arrival of the electron at the silicon slab which then causes electron-hole pair generation in the semiconductor material. The diffusion of the electron-hole pairs cause a current to flow through the bump-bond into the pixel logic. The arrival of the electron is presented as being instantaneous on the time line, the process of electron scattering occurs at relativistic speeds which are prompt compared to the other

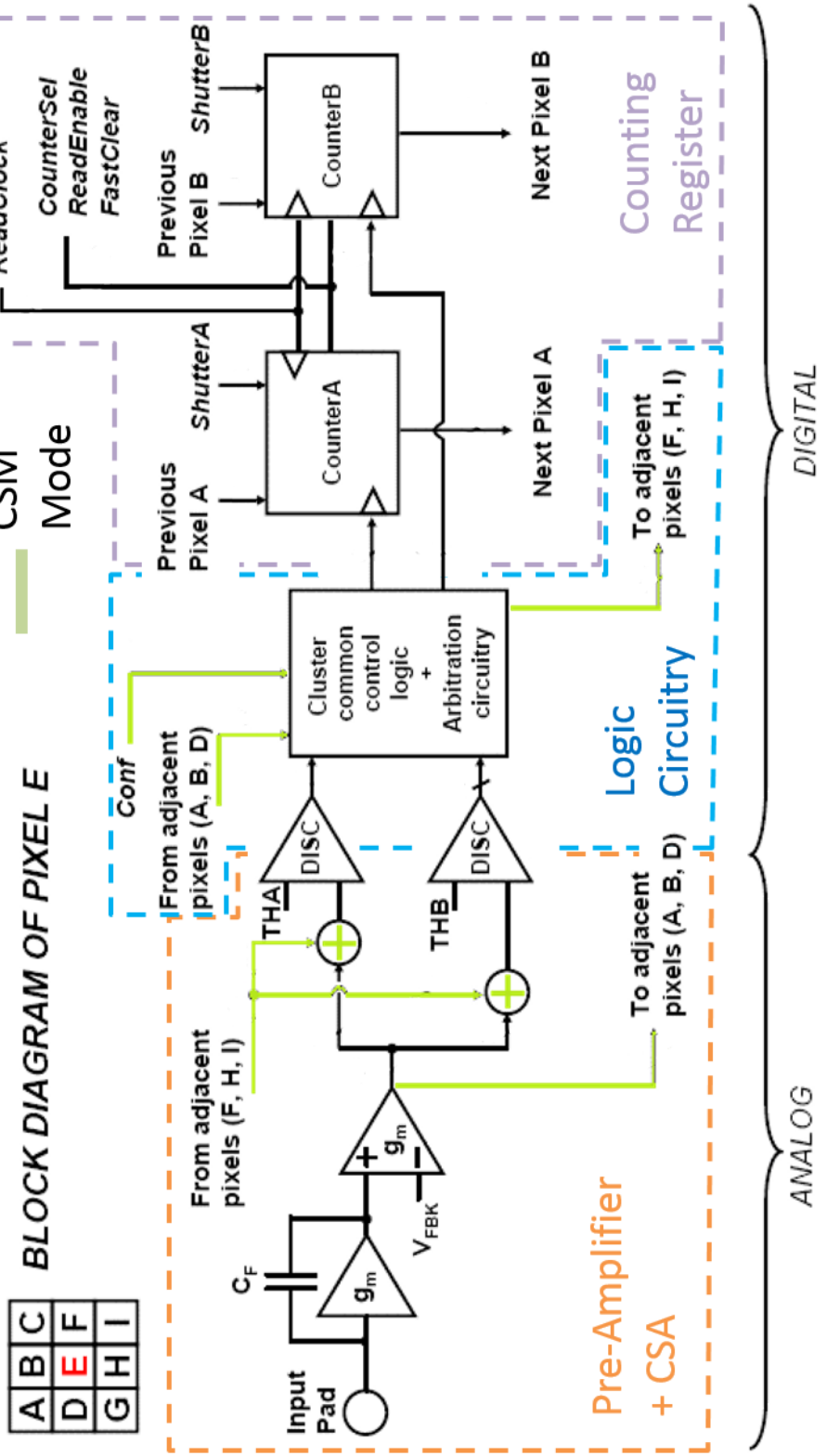

Figure 5.2: A block diagram of the important components in the analogue to digital conversion process. The figure is a simplified and annotated version of the figure published by Ballabriga *et al.* (2011) [5]

processes shown. Figure 5.3B shows the induced voltage of the charge sensitive amplifier (CSA) in response to the current flow created by the electron strike. The shape of the CSA response is replicated from recorded experimental response of the Medipix2 [118]. The shape features a sharp increase in voltage output followed by a slower decay of the voltage. The rate of voltage decay can, to a small degree, be controlled by the CSA variable Ikrum. The electron arrival and the voltage response of the CSA are the analogue sections of the electron processing. Figure 5.3C shows the digital response of the comparator to the CSA voltage. The CSA voltage output is compared to a user defined threshold THO - shown by a dashed line in figure 5.3C - which defines the minimum energy an electron must impart to that specific pixel before a count is registered. Above this threshold a discriminated pulse is triggered. The logic circuit triggers from low to high when the voltage increases above the threshold. After the voltage decays to below threshold, the logic output falls from high to low. The threshold of the comparator allows thermal noise to be rejected from the system. Our experiments have shown an adequate threshold for the removal of thermal noise to be ~2.7keV. The fall of the comparator in figure 5.3C causes the pulse in figure 5.3D which is directed to the counting registry, increasing it by one. The potential jitter of the digital processes is again determined by the internal clock. The pulse in figure 5.3D will only trigger an increase in the counter if the detector is currently set to expose.

The current detected by the CSA of each individual pixel is dependent on both the electron impact location and electron energy E_0. A single electron undergoes multiple scattering events when imparting its energy to the silicon. The energy required to create an electron hole pair in silicon by simple ionization (without momentum transfer) is ~3.6eV [119]. Therefore, the maximum electron hole pairs that can be created for a single 200keV electron hit is approximately 53,000. The maximum electron hole pairs for a 60keV electron hit is approximately 15,700. Each scattering event has the potential to increase the lateral scattering of the electron in the silicon. Monte Carlo simulations provide analysis of the distribution of energy in the silicon slab and approximate the effect on the analogue to digital conversion process. The Monte Carlo software used here, CASINO was originally developed by Raynald Gauvin at Université de Sherbrooke [120]. The simulations are

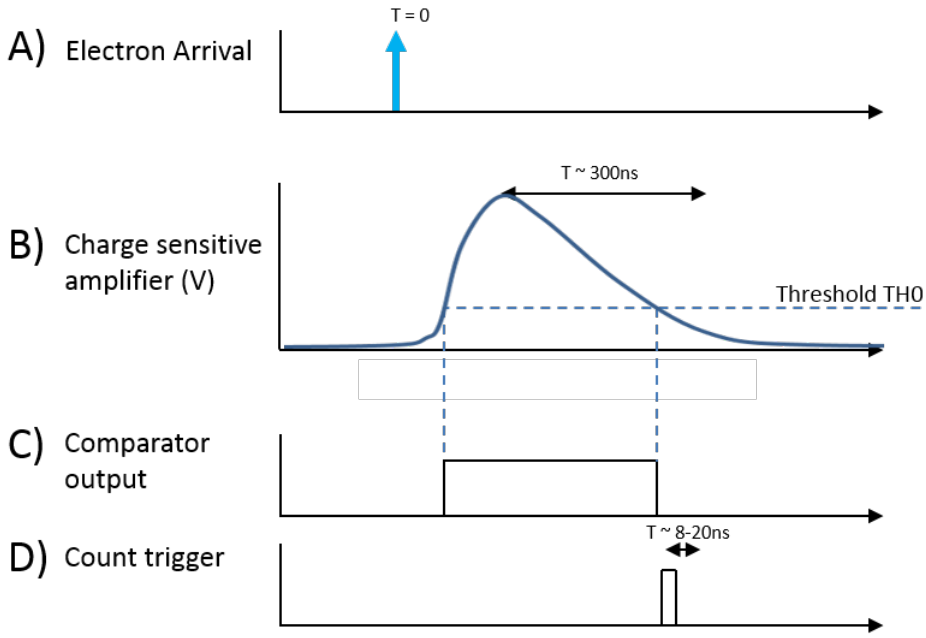

Figure 5.3: A figure showing a simplified model of the triggering sequence and timing of hardware processes for a single Medipix3 pixel in response to an electron impact.

performed on 300μm of silicon with scattering properties from the predefined CASINO material database. Monte Carlo simulations for two commonly used accelerating voltages are shown in figure 5.4. Electron trajectory data for voltages of 60keV and 200keV are shown with corresponding graphs showing the imparted energy contours. The trajectory data is centred at -27.5μm and the spacing of the vertical major grid lines are set to 55μm to represent the pixel spacing of the Medipix3. The trajectory data is formed from 1,000 electron hits and the statistics of the energy contours from 10,000. The red 300μm line on the trajectory data denotes the thickness of the sample and it can be shown that for all energies, transmission rate through the silicon is zero. Figure 5.4A shows that no 60keV electrons are scattered into silicon material attributed to an adjacent pixel. The energy contours in figure 5.4C show that 95% of the electrons have imparted their energy within a lateral spread of 7.9 μm. This means that a large area can be the impact point of a single electron, yet still attribute the majority of its energy to one pixel. Figure 5.5A provides a comparison of the lateral spread of a 60keV electron shown as a blue circle with radius 7.9μm. The square area shown bordered by the red dashed line encloses the area which

an electron could be assumed to undergo no charge sharing between pixels. A simple geometrical calculation shows this area to only be 50% of the pixel area. In contrast to this, the 200keV trajectory data in figure 5.4B shows many electrons reaching silicon in adjacent pixels. Importantly, the energy contours in figure 5.4D show that the 95% of the lateral energy loss has only been reached by 72μm. This is emphasised in figure 5.5B where the size of the pixel has been down-scaled by a factor of four to show that the full pixel area has the possibility of charge sharing. This potentially causes current flow in multiple pixels, especially where the impact of the electron is at the border between pixels. Single electrons triggering counting in multiple pixels appear as clusters up to four or more.

It is clear from the Monte Carlo simulations that the magnitude of lateral scattering is directly proportional to the primary electron energy used in the TEM. For both 60keV and 200keV there is a significant probability of electrons losing a portion of their energy to adjacent pixels depending on the impact location. The phenomenon of electrons depositing energy in multiple pixels is called charge sharing. This effect is well documented in pixelated detectors and has been a primary motivation in the development of the Medipix3 from its predecessor the Medipix2 [118]. However the impact on the ultimate time resolution has previously not been demonstrated. We postulate that charge sharing between pixels directly affects delay between electron arrival at the silicon and the increase in the counter. Therefore, this adversely affects the ultimate time resolution attainable by the Medipix3 detector. Figure 5.6 compares the response of the CSA and comparator output in the case of a 60keV electron depositing 100% of its energy into a single pixel, and the case where only 75% of the total energy is deposited into the pixel of interest with the rest charge shared to neighbouring pixels. As demonstrated in figure 5.5A the loss of energy is dependent on the proximity to the edge of the pixel. Case 1 simulates a strike to the centre of the pixel while case 2 simulates a strike close to a corner. Both electrons are shown to reach the silicon material at the same time. The rapid increase in the voltage response causes the discriminated pulse for the comparators in both cases 1&2 to trigger on similar timescales. However the voltage peak in case 2 is proportionally smaller based on energy lost to surrounding pixels. Therefore the time taken for the voltage in case 2

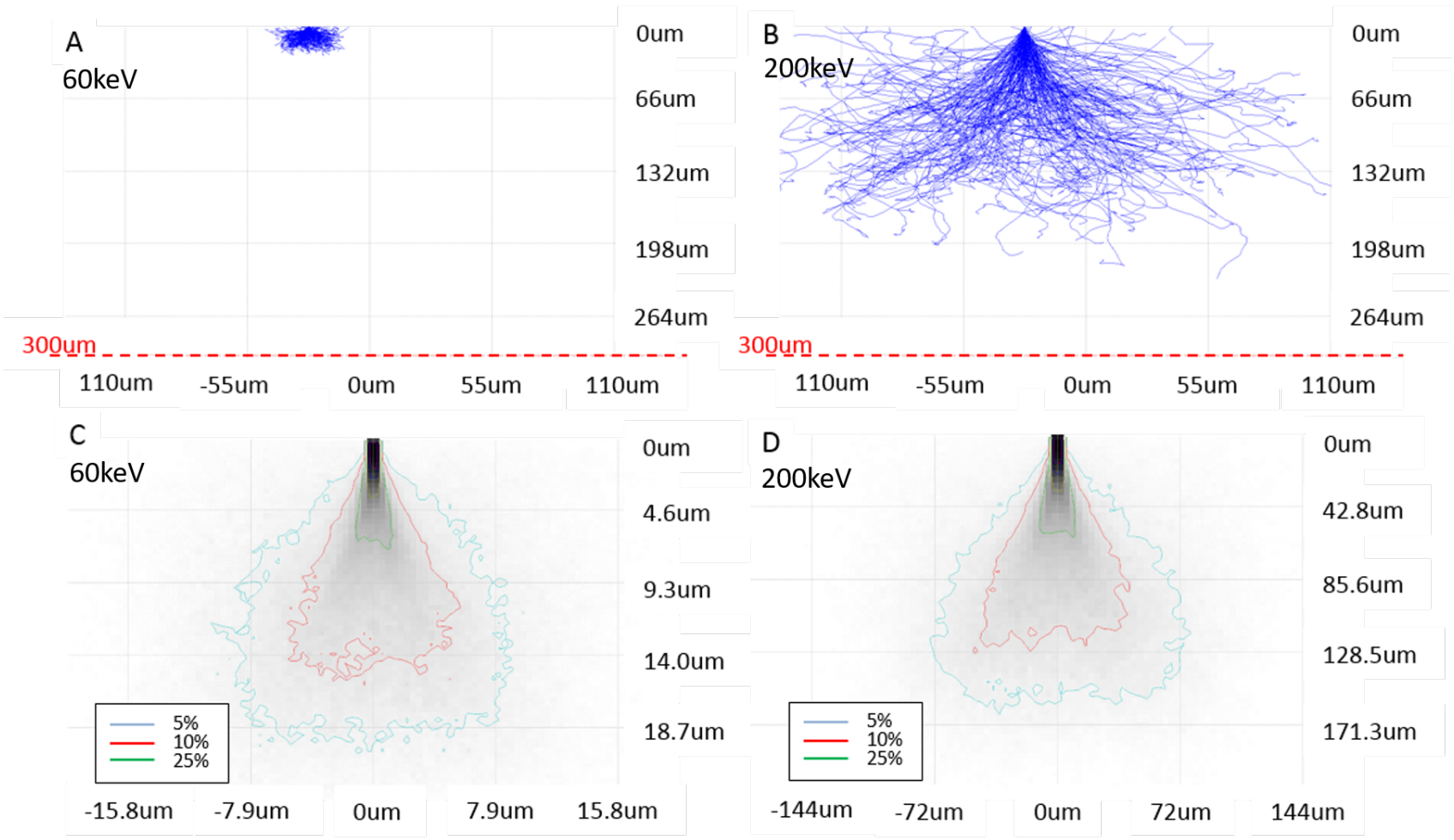

Figure 5.4: This figure shows Monte Carlo simulations performed on CASINO software for 200keV and 60keV electron impact events in 300μm silicon. The top row, A&B show traces of the individual electrons scattered through the material. The bottom row C&D show the probability of electron energy deposition in a region.

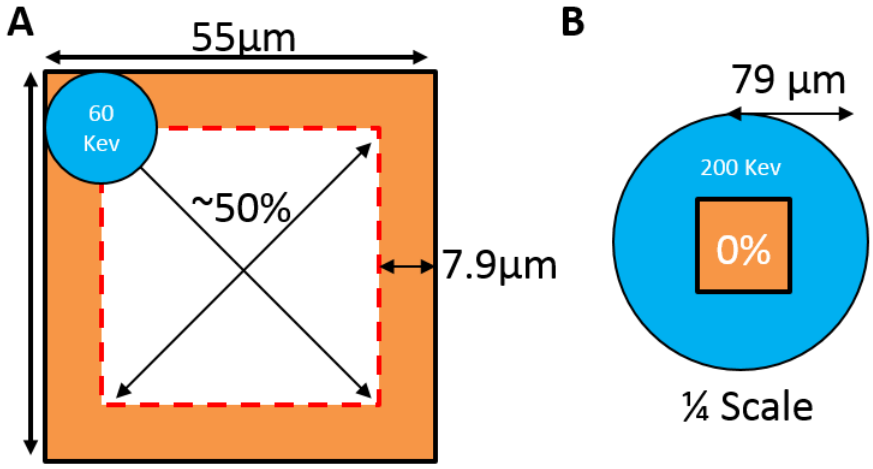

Figure 5.5: A geometric illustration of charge sharing compared to pixel area. Figure A shows that for 60keV electrons approximately 50% of the area of the pixel can be the impact point of the electron without charge sharing. Figure B shows that the area of a single pixel can be fully encapsulated by the scattering probability of a 200keV electron.

to decay below the threshold level TH0 is shorter than in case 2. As shown previously in figure 5.3 the trigger to increase the internal counter happens directly after the fall of the discriminated pulse. This demonstrates that the delay between electron impact and count triggering is proportionally smaller for an electron that has undergone charge sharing. This suggests that the magnitude of charge sharing is smaller for 60keV electrons than 200keV electrons. Therefore to access the greatest time resolution available, 60keV electrons should be used.

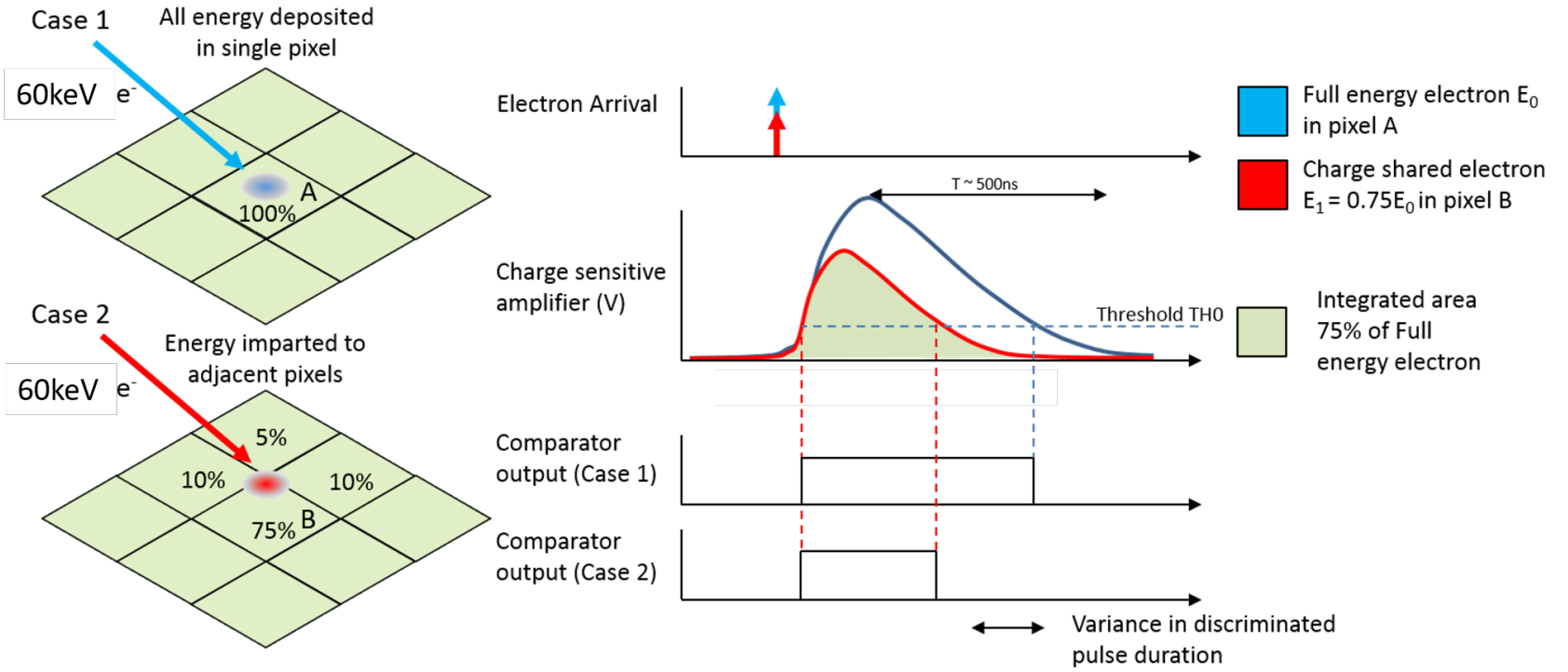

Figure 5.6: A figure showing the detection of both an electron depositing its total energy into a pixel (Blue) and an electron scattering through multiple pixels creating electron hole pairs in both (Red). The charge shared electron causes a smaller voltage response from the CSA causing the voltage to drop below the threshold faster. This demonstrates how a charge sharing electron causes an early electron counting event.

A single electron strike is capable of triggering counts in multiple adjacent pixels where the energy lost to adjacent pixels via charge sharing is greater than the threshold level. This can cause single electron impacts to appear as clusters effectively creating a point spread function for individual pixels, adversely impacting the modulation transfer function of the detector. Increasing the threshold level can prevent the triggering of multiple pixels by preventing the discriminated pulse where the CSA peak voltage response is smaller than the threshold level. Figure 5.7 shows both the total integrated counts in an image and the number of clusters in the image as a function of the threshold level in keV for 60keV electrons. At low threshold energies figure 5.7 shows that the number of integrated counts is greater than the number of clusters suggesting that the average cluster size is greater than one. At high threshold energies figure 5.7 shows the number of integrated counts are equal to the cluster sizes, however the number of cluster has decreased showing that some of the electron impacts have not created any counts. Therefore the DQE of the detector is lower at high threshold energies. This suggests that the ideal threshold value for detecting real counts is the intercept point where cluster counts and integrated counts are equal, meaning there is only one electron per cluster. Figure 5.7 shows this to be where TH0 = $E_0/2$.

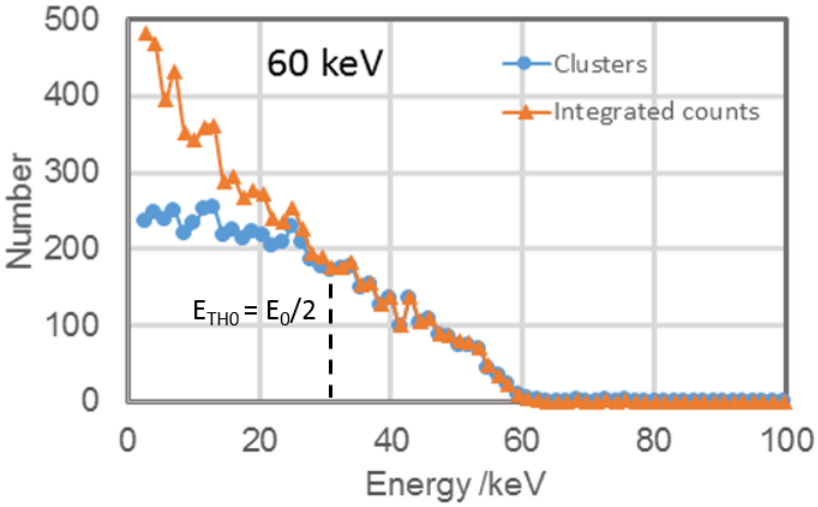

Figure 5.7: The total integrated counts detected compared to the number of clusters of electron counts as a function of threshold energy. This demonstrates the impact charge sharing between pixels where the integrated counts is greater than the cluster number, showing multiple pixels have triggered a count for only one electron arrival.

5.3 Characterisation of electrostatic deflection plate time resolution [2]

Before we explore the time resolution of the Medipix3, we needed a benchmark system which could be driven on the nanosecond timescale. We took advantage of the electrostatic beam deflection plates installed on the ARM200, located pre-sample in the TEM column to rapidly alter the beam position on the detector thereby creating an artificial dynamic process within the microscope. A voltage passed to these low capacitance deflection plates causes the illumination spot of a focused beam to shift position proportionally to an applied voltage and inversely proportional to the primary electron energy. A square wave therefore causes the beam to appear to split into two separate intensity spots during a long exposure image.

This experiment was performed with a primary accelerating voltage of 60keV. The

[2]Analysis performed by Dr Gary Paterson, Department of Physics & Astronomy, University of Glasgow

voltage applied to the deflector plates is a 5MHz square wave with a peak voltage of 10V and low voltage of 0V. The voltage source is connected directly to the plates with one meter of BNC cable. In principle, the shutter capacitance of 9.6pF and the supply impedance of 50Ω gives a time constant of approximately 0.5ns which should allow for a sub-nanosecond blanking. However, parasitic impedance in the test setup is predicted to increase the deflection transmission time. The exposure duration is set to one second so that the SNR of the resulting image is high. There is no sample inserted into the microscope so that the imaging is performed on free space.

Figure 5.8A shows a long duration image of a 5MHz square wave applied to the plates. It appears to split the beam into two separate beams where the distance between the disks is proportional to the voltage applied to the deflection plates. The intensity between the two disks is caused by the transition of the beam from the undeflected position to the deflected position. The image displayed has been rotated to align the displacement vertically so that the image can be integrated horizontally to provide a 1D profile. Figure 5.8B shows an image taken without any voltage applied to the deflection plates. This creates an image to be used as a point spread function to calculate the time spent at each position during the transition from undeflected to deflected. Once again the image is integrated horizontally to give a 1D profile. Figure 5.8C shows the integrated horizontal profiles taken from the 5MHz long exposure image shown as a red dashed line in figure 5.8A and the line profile taken from the static beam shown as a blue dashed line in figure 5.8B. The final solid line is discussed later. Figure 5.8D shows the probability distribution function (PDF) which is created by deconvolving the 5MHz profile with the point spread function (PSF) using 256 iterations of a Richardson-Lucy algorithm. The Richardson-Lucy algorithm is an iterative method for recovering an image that has been convolved with a point spread function. However, additional broadening was required to obtain a good fit. The sources of such broadening are most likely to be ringing and reflections from impedance mismatches, and this was approximated by introducing a small Gaussian convolution into the modelled PDF. To confirm that the PDF is accurate after convolution with the Gaussian and processing by the Richardson Lucy algorithm, we re-convolved the PDF with the PSF and compared

this to the 5MHz profile. This re-convolved profile is shown in solid black in figure 5.8C.

The results from this characterisation show that the time constant τ varies slightly where the beam transitions towards or away from its deflected state with $\tau_{\text{Rise}} = 4.00$ns with an error ($\sigma$) of 0.51ns and $\tau_{\text{Fall}} = 1.53$ns with a σ of 0.07ns. Weighted mean time constant τ is 3.8ns with an error of 0.5ns. This gives a 3σ transition time of around 11ns. We expect that the time resolution available by the Medipix3 is an order of magnitude greater than this and therefore the deflection transition will not pose a problem as the imaged dynamic process.

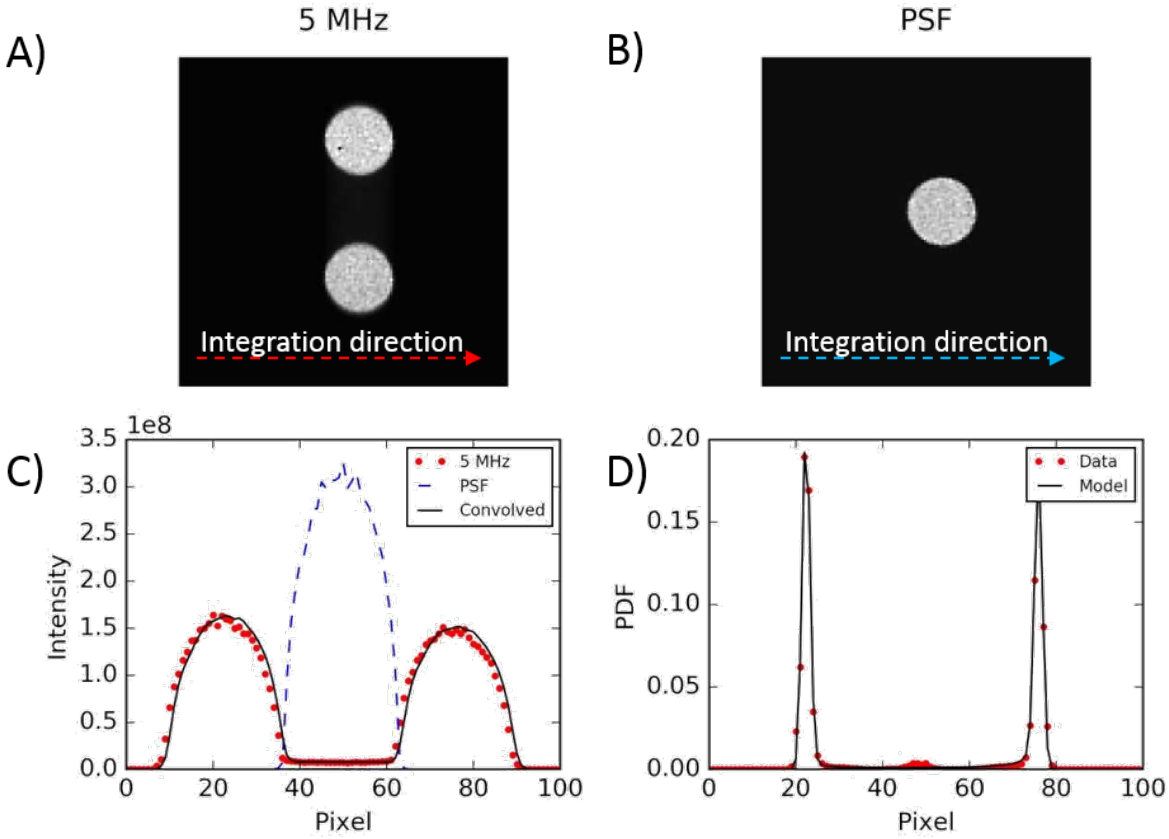

Figure 5.8: A figure showing the properties of the beam split by a 5MHz beam deflection. The long exposure image is deconvolved to produce a point spread function which can then provide an analysis of average beam position in time.

5.4 Impact of threshold level on stroboscopic imaging of electrostatic deflection

In the previous section 5.2 we postulated that charge sharing between pixels directly affects delay between electron arrival and counter trigger, as explained in figure 5.6. In this section, we investigate the impact of threshold energy level TH0 as a method of mitigating the impact of charge sharing on the variance in the discriminated pulse created by the comparator. Figure 5.9 shows the response of the CSA while set with a low threshold value in figure 5.9A, and set with a high threshold value in figure 5.9B. Both figures include four voltage responses, (1-4) in figure 5.9A and (5-8) in figure 5.9B. These voltage responses show greatly different peak voltages and decay times however remain relatively constant in shape to simulate electrons imparting different proportions of their charge into the pixel. The electrons decrease in imparted energy where the blue curves 1&5 have the greatest energy, down to the red curves 4&8 having the smallest simulated energy. Below each of the CSA voltage curves are the binary discriminated pulses created by the respective comparators. Figure 5.9A shows all four energy levels having voltage peaks above the low threshold energy level. Therefore all four simulated electrons produce discriminated pulses. The maximum difference in pulse finish time is shown by the red arrow. Figure 5.9B shows only electron responses 5&6 have a voltage peak greater than the high threshold energy level and therefore electron responses 7&8 do not create discriminated pulses and are thus not counted. This effect was previously shown in figure 5.7 where the DQE decreased as the threshold energy level began to exceed half of the primary electron energy. The discriminated pulses created by the two electrons 5&6 are shown to have a shorter total duration than their low threshold counterparts 1&2, respectively. This suggests that the delay between electron arrival and the trigger to count the electron will be on average shorter when a higher threshold level is used. Finally the maximum difference in pulse finish time is shown to be smaller for the high threshold because the high threshold level reject a proportion of electrons. This smaller difference in maximum pulse difference is the primary reason for the predicted difference in time resolution. If the pulses are aligned so

that the discriminated pulse finishes simultaneously, then the variation in pulse finish time becomes the variation in electron arrival time that can trigger an electron at the same time.

To investigate the impact of charge sharing and threshold level on the time resolution of the Medipix3, we employed a pump-probe type experiment to image the beam during the proven rapid transition between a deflected and undeflected state. The pump here is the deflection driven by the electrostatic beam deflector as discussed in section 5.3. The probe is the image acquisition triggered by the deflection pulse. The internal Medipix3 delay provides a method of altering the respective delay between the voltage signal to the plates and the image acquisition start. This allows the acquisition of sequential images with increasing delays forming a scan of the response in time. It may be naively assumed that as the deflection voltage changes we would see a single beam move position. However the variance in the discriminated pulse shown in 5.9 will cause electrons arriving at different times to be imaged in the same frame.

The pump-probe experiment is performed with the beam rapidly deflected from the electrostatic deflector plates by a single square wave pulse of 10V for a duration of 50ns. To maximise beam deflection, the primary accelerating voltage of the TEM used in this experiment is 60keV. The two TH0 energy levels reported in this experiment are 28keV and 51keV. The acquisition is achieved stroboscopically with the final image for each delay point integrated from 50,000 images of 50ns exposure (2.5ms total).

Figure 5.10 shows the results for the deflected beam intensity for both threshold energies. The intensity is calculated using a region of interest (ROI) ring positioned around the deflected beam where counts in this area are summed. The position of both ROI is gathered from a reference long exposure image showing the beam at both positions in detail. An example of the ROI applied to an image is shown as an insert corresponding to the position on the delay sweep denoted by the green asterisk. The insert shows the deflected beam appearing in both positions which has been coloured to provide good display contrast. The mean counts at the position of the deflected beam are then calculated for all delay points shown in the primary graph of figure 5.10.

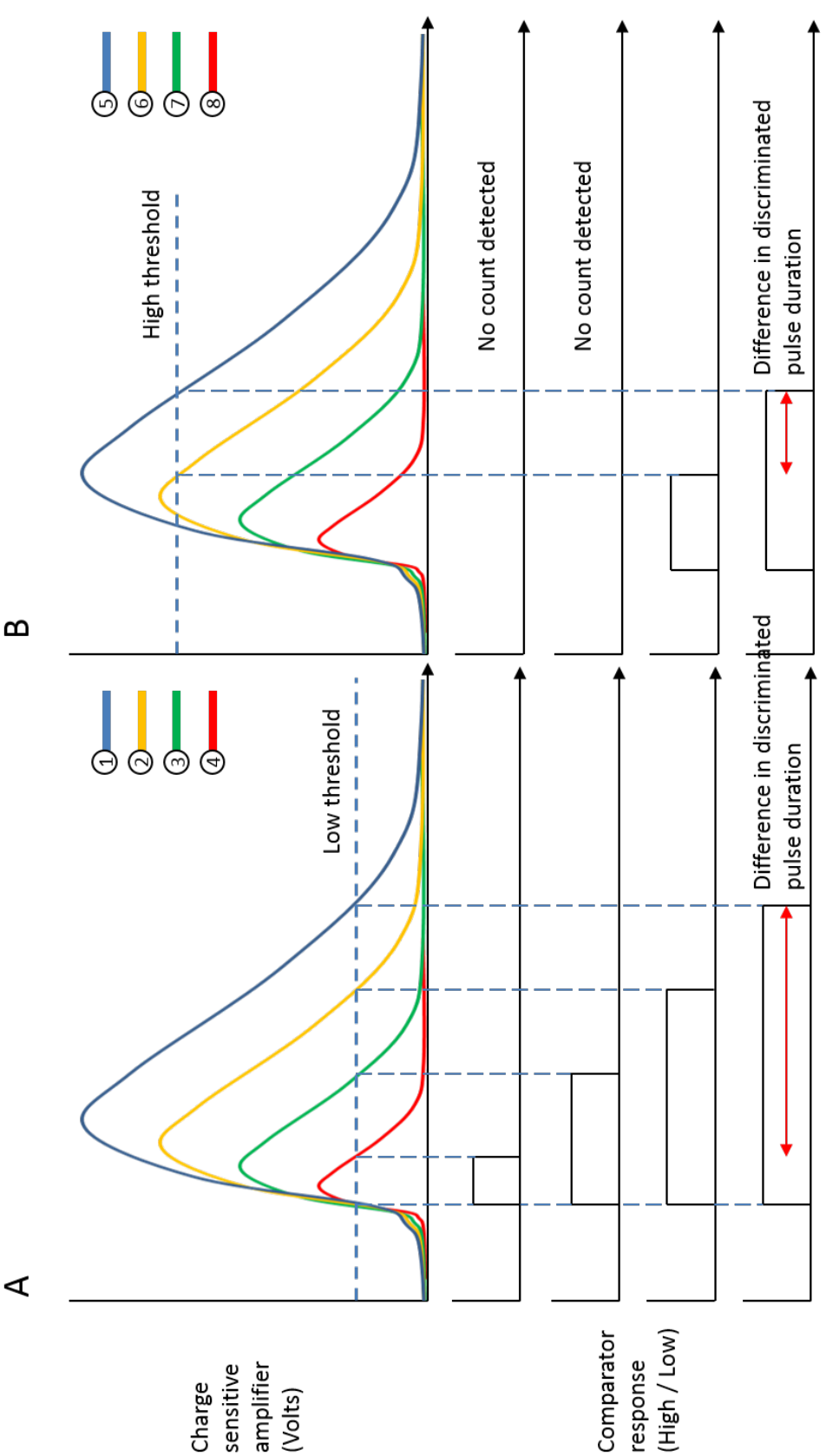

Figure 5.9: This figure demonstrates the impact of threshold on time resolution. The difference in the discriminated pulses generated by the CSA for a low threshold (A) compared to a high threshold (B). Both figures show four voltage responses corresponding to electrons with different energies. The difference between the discriminated pulses with the earliest end and latest end is highlighted with a red arrow, showing the variance in counter response time.

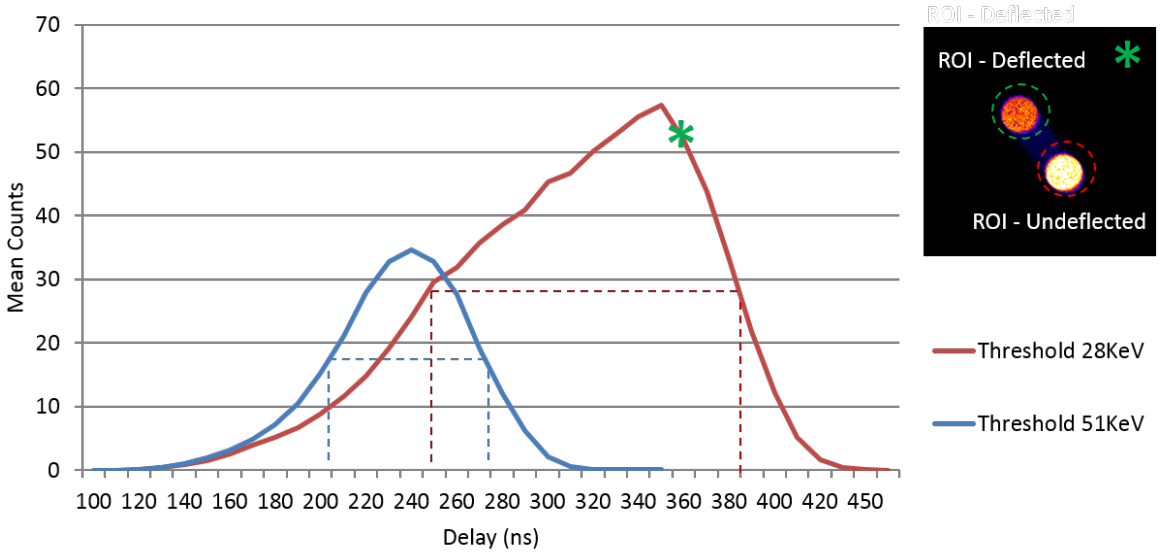

Figure 5.10: A figure showing the mean intensity at deflected beam region of interest for delay sweeps performed at threshold energy levels TH0 28keV and 51keV. An insert of the image acquired for TH0 at 360ns is included to demonstrate how the mean counts of the deflected region of interest is acquired.

The important features of the results from figure 5.10 are: the centre position of the curve, which indicates the average delay between electron impact and electron count; the full half width maximum (FHWM) of the curve, which indicates the variance of the discriminated pulse produced in response to the CSA; the integrated number of counts, which indicates the total number of electron counts for all delays thereby assessing the DQE of the detector at that TH0; and finally the shape of the curve.

Firstly, the position of the curve peak position is shifted from 350ns for TH0-28keV to 240ns for TH0-51keV. This means that for two electrons arriving at the same time, a pixel with a higher threshold has a higher probability of counting the electron first, compared to a pixel with a lower threshold. This is in agreement with the prediction from figure 5.9 that the delay to count an electron will be shorter, due to the decreased level of decay needed from the peak current before decreasing below threshold and being counted.

Secondly, the full width at half maximum (FWHM) of TH0-28keV is significantly larger than TH0-51keV. In figure 5.10 the full width half maximum is annotated with dashed

lines for both threshold values. The FHWM increases from 70ns at TH0-51keV to 140ns at TH0-28keV showing an increase in variance of 70ns. This means electrons arriving at the same time have been counted over a broader time range for TH0-28keV than TH0-51keV, which agrees with the prediction in figure 5.9 that a low TH0 will accept a greater range of electron energies than a high TH0. The physical impact on the image during high frequency beam deflection is that a broadening of the variance increases the amount of time that electrons can appear from both beam locations as demonstrated in the insert of figure 5.10. Low energy electrons appear to return to the undeflected beam position before the high energy electrons.

Next, the integrated area of the TH0-51keV curve is significantly less than the TH0-28keV curve. The TH0-51keV data has an integrated deflected-ROI count total of 141,751 whereas the TH0-28keV data was 408,846. As shown by figure 5.9B, a high threshold causes a significant amount of electrons to be excluded where the peak voltage response by the CSA is smaller than the threshold for any pixels that the electron has deposited energy into.

Finally the shape of the TH0-28keV curve clearly does not have the same clean rounded shape as TH0-51keV. The reason for this is not immediately apparent in this data set and cannot be explained by figure 5.9.

The energy level of TH0 clearly has a major impact on the counts, DQE, MTF and time response of the detector which has significant implications on the limits and functionality of the detector when attempting to perform time-resolved imaging. Although we demonstrate that the time resolution could be increasingly improved by increasing the threshold level there would rapidly become a point where so few electrons triggered a count that the SNR would become to low to constitute a usable image. The threshold level used in future time-resolved experiments clearly needs to reflect the application by maintaining the SNR while maximising time resolution.

5.5 Stroboscopic temporal aliasing

To experimentally determine the minimum time resolution of the detector, a repeatable dynamic process can be imaged with increasingly small time intervals until the dynamic process can no longer be resolved. The visual phenomenon is called the stroboscopic effect or sometimes informally called the "wagon-wheel effect". This phenomenon causes a revolving object to appear stationary because the shutter exposure frequency matches the revolution frequency.

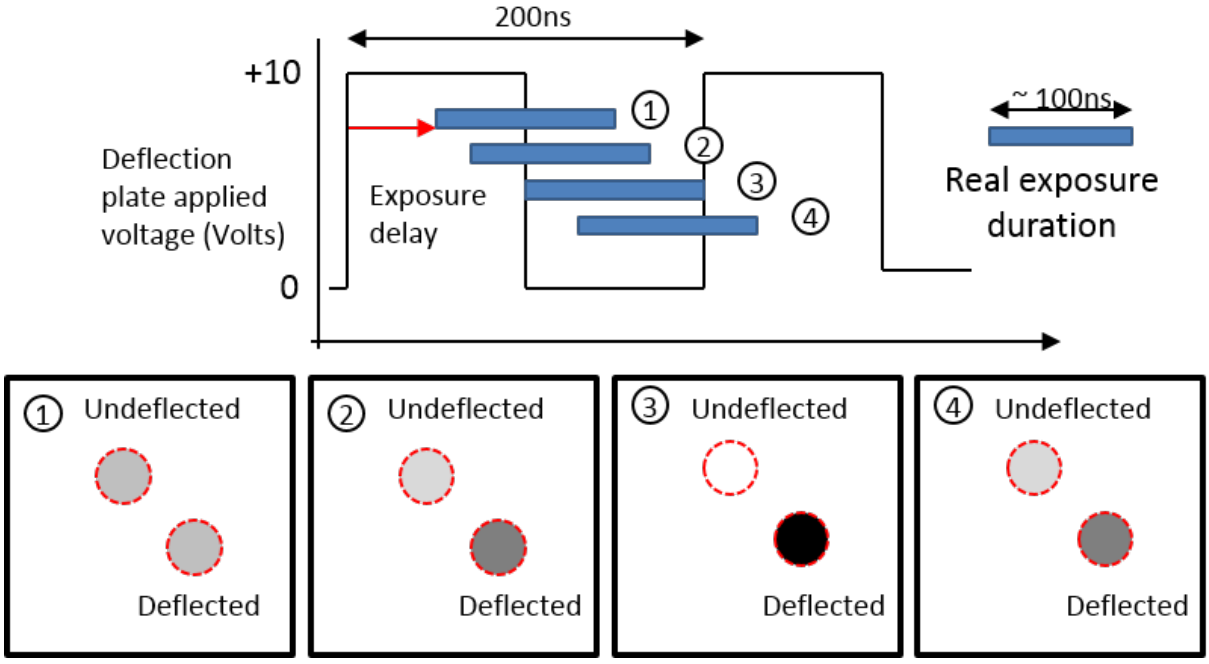

Figure 5.11: Imaging a single side of a repetitive signal in which the exposure is synchronised to the frequency. Sub-figures 1&2 show the delay too short and still including intensity in the beam during deflection. Figure 3 shows the exposure perfectly synchronized with the frequency where there is no deflected beam intensity. Figure 4 shows the delay once again unsynchronised.

In this experiment, the beam was oscillated with a fixed frequency and a delay sweep performed. If the time resolution was less than half of the oscillation period, the delay sweep would include an image where there is intensity in only the deflected beam position. Alternatively, if the time resolution was greater than half the period then at all delays there

would remain some counts in both deflected and undeflected positions. The oscillation of the beam via the deflector plates was increased to a frequency of 5MHz. The Medipix3 was configured to trigger the delay count on the square wave voltage rise provided to the deflection plates. An exposure time of 20ns was used and the final image was integrated from 100,000 individual images equivalent to a total exposure time of 2ms, although the real exposure is predicted to be longer. The delay sweep is performed at intervals of 20ns due to the time taken for a full integrated acquisition to be performed. 5MHz was chosen to acquire the full delay sweep as this was the final frequency at which the beam spot could be frozen at one side, meaning the entirety of the real exposure was contained during the time the beam is deflected. Figure 5.11 shows a diagram of this process with four images being taken at increasing delays labelled 1-4. In figure 5.11 exposures 1&2 are shown to have the transition from +10V to 0V happening during the image. Therefore we would expect there to be some intensity in both the deflected and undeflected beams, which is shown in inserts 1&2. In figure 5.11 exposure 3 is shown to be perfectly within the duration where the deflection plate applied voltage is 0. This would cause the undeflected beam to contain the full intensity of the image as shown in insert 3. Finally, in figure 5.11 exposure 4 shows the beam once again going through a transition and intensity reappearing in the deflected beam position, as shown in insert 4.

Figure 5.12 shows eleven frames A-K corresponding to a delay sweep between 0ns and 200ns (inclusive). To assist in viewing contrast the images have been recoloured from black and white to a 'fire' colour scheme where white is high intensity to blue with low intensity and black still where zero counts were detected. Frame A shows the majority of the intensity in the undeflected side. The fact that the delay time zero does not feature a fully deflected or undeflected state is due to the internal delay of the Medipix3 therefore, the real delay here is greater. Frame B shows the frame with the maximum deflected intensity. Frames C-F show a gradual transition where the proportion of the total intensity shifts from deflected to undeflected. Frame E shows the point closest to equal intensity present on both sides. Frame G shows the frame with the minimum deflected intensity. Frames H-K show the gradual return of the proportion of the total intensity to the deflected

side however does not reach full deflection being approximately equivalent to Frame A. The annotation of frame J is briefly discussed as it shows where the deflected and undeflected ROI are determined. These circular regions of interest consist of 1020 pixels each. The transition region in between is calculated as the total counts of the frame minus the counts of both ROI.

Figure 5.13 shows a graph of the total counts, Undeflected ROI counts, Deflected ROI counts and calculated transition counts. The results in figure 5.13 show that the total counts have an average counts of 26,756 which equates to less than one count per frame. The total counts have a standard deviation of 587 which is significantly larger than the expected shot noise variation for this counts number of 163. The most likely cause of this variation is the change in beam position through the column optics changing the total number of electrons that can reach the detector. In this experiment however we do not have enough data to definitively reach that conclusion. Figure 5.13 marks the position of minimum and maximum deflection where the real exposure of the beam is primarily contained in a single ROI, giving the SNR of the detector at this time resolution. The 20ns delay gives the maximum deflection intensity with 91.6% of the total intensity contained within the ROI. There is shown to be some intensity outside of the deflected ROI with 5.4% in the undeflected ROI and only 3.0% of the intensity in the transition region. The 120ns delay gives a similar result for the maximum undeflected intensity with 91.3% of the total intensity contained within the ROI. The remaining intensity is 5.3% in the deflected ROI and 3.4% of the intensity in the transition region. To calculate the maximum signal to noise ratio of this experiment we take the signal to be the intensity of the ROI for that deflection state and the noise as the intensity outwith this area. For the minimum deflection (20ns) we have SNR of 10.9 and for the maximum deflection (20ns) we have an SNR of 10.5. Finally figure 5.13 shows that the maximum transition intensity is found at the two time delays 80ns and 180ns where the pair of ROI have the smallest intensity. The maximum transition intensity percentage is found to be 11.6% and 10.9% respectively.

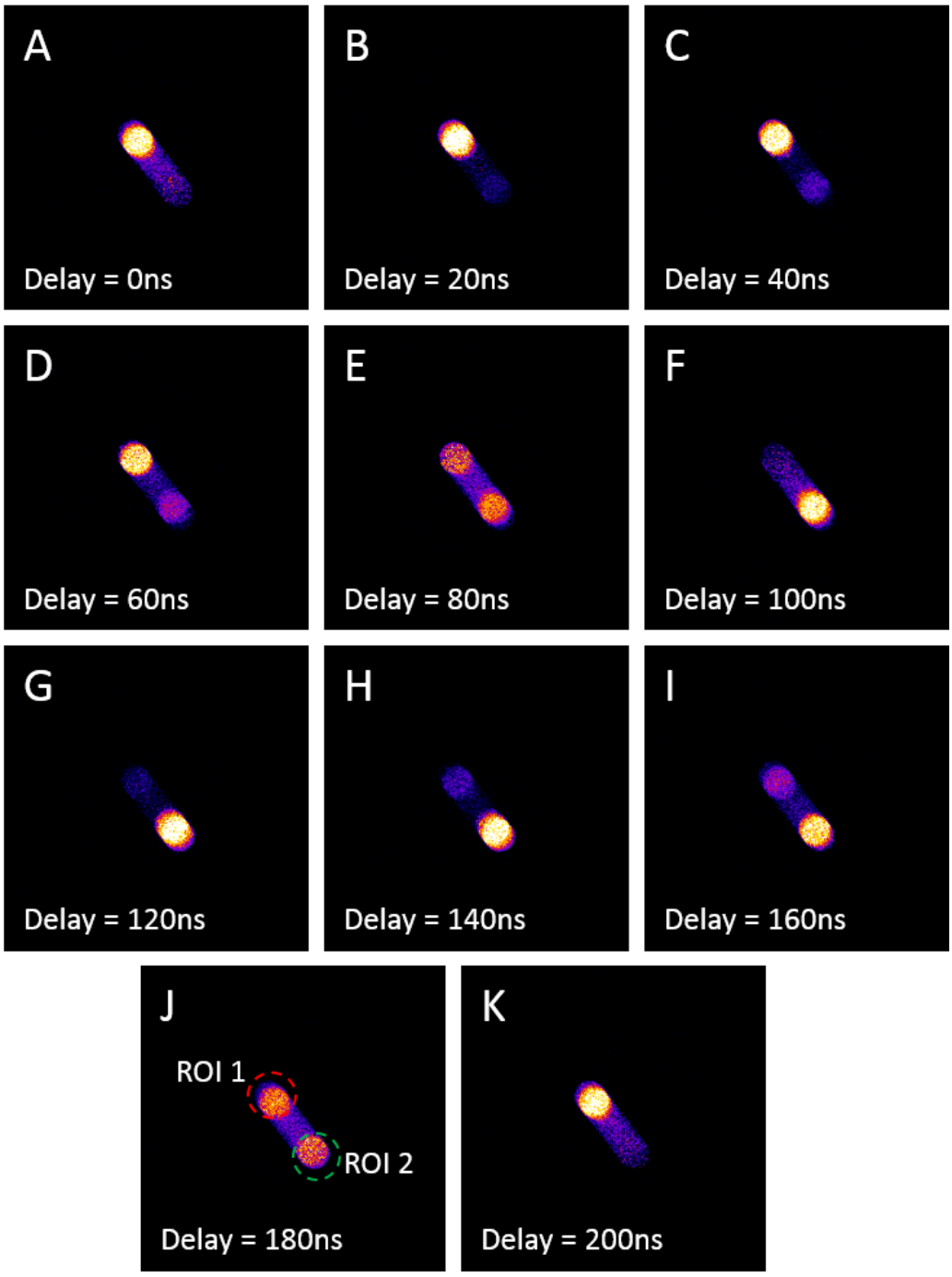

Figure 5.12: A sequence of images (A-K) from a pump-probe type delay sweep which was performed on a 5MHz beam oscillation. Frame B shows the beam at minimum deflection and frame G shows the beam at maximum deflection. Frame J is annotated with two region of interest markers used on all images for calculating statistics.

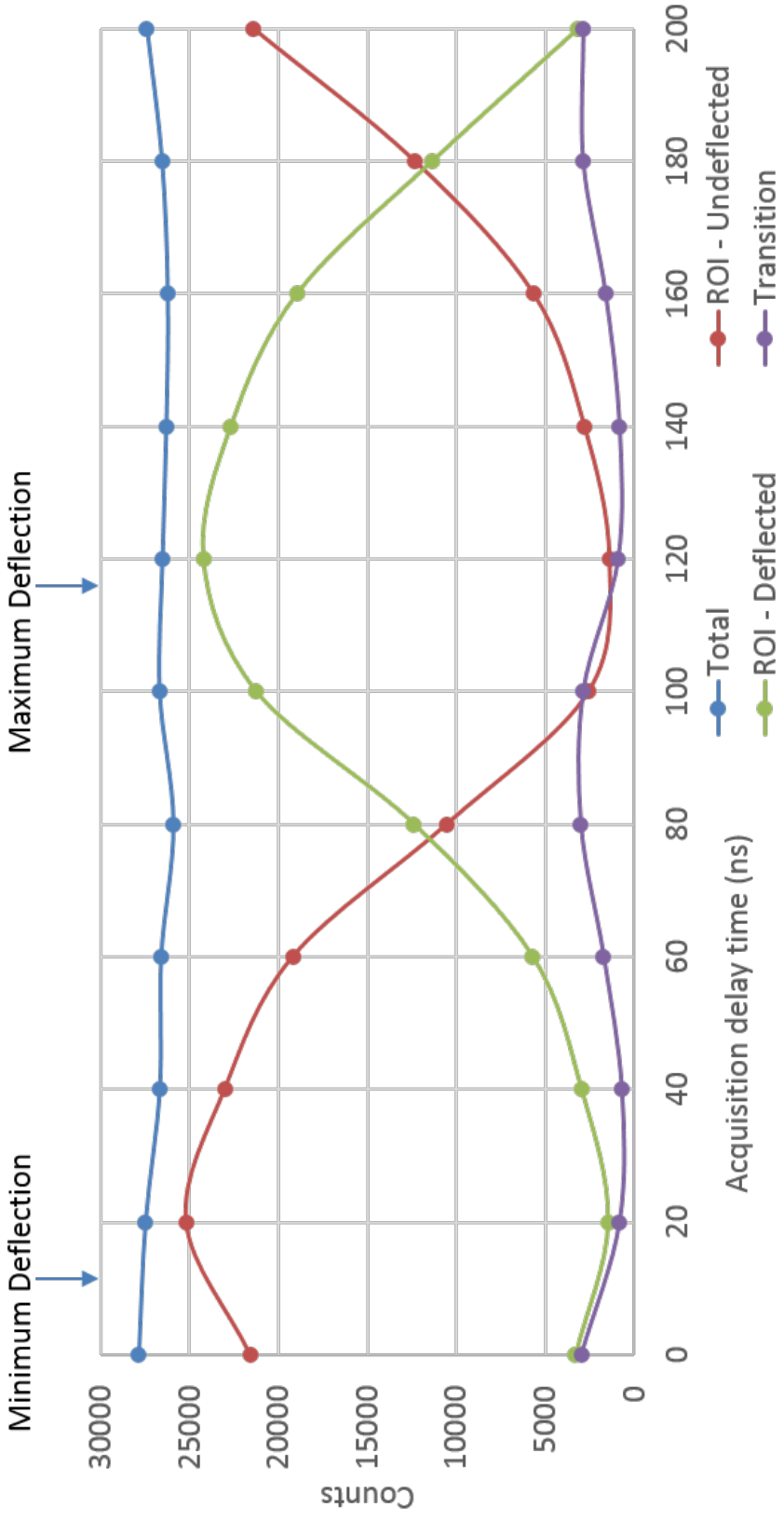

Figure 5.13: The total counts from specific regions of interest during the delay sequence capturing the 5MHz oscillation. The total, deflected and undeflected ROI are totalled directly from the images with the transition total calculated by subtracting both ROI from the total.

5.6 Investigating time-resolved imaging with charge summing mode

One of the features introduced into the Medipix3 hardware as an improvement to its predecessor is an imaging mode called charge summing mode (CSM). CSM was introduced as a method of reducing the impact of charge sharing on MTF whilst maintaining the DQE of low threshold energies. CSM works by comparing the induced current of the pixel with the induced current of the surrounding pixels. This was shown previously in figure 5.2, where the pixel of interest, E, receives signals from the adjacent pixels, F, H and I. Pixel E distributes its own signal to adjacent pixels, A, B and D. The pixel communication is present in both the analogue and digital sections of the electron processing circuitry, allowing the voltages to be compared and the largest be assigned the electron hit. This interconnected circuitry effectively create 2x2 blocks in which the electrons are assigned in a winner takes all situation. The pixel with the largest voltage is most likely to be the site of electron impact. However, it is possible that an electron arriving near the edge of a pixel may scatter towards the adjacent pixel. A limitation of the CSM mode is that the comparison algorithm is performed only on the 2x2 blocks. Therefore, charge sharing with spread greater than neighbouring pixels cannot properly be corrected for by this architecture. This limits the effectiveness of CSM at higher primary electron voltages. However CSM remains effective for a range of energies such as 60keV electrons.

An unexpected consequence of the CSM mode architecture and the motivation for this experiment is that the temporal spread in the fall of the disseminated pulse caused by charge sharing may be partially mitigated. The currents of each pixel in the 2x2 block are summed and compared to a threshold value at the corner intersection of the four pixels. This summation effectively recreates the full electron charge from across the 2x2 block. Therefore the triggering of discriminated pulse should have a reduced effect from charge sharing, which we had shown previously in section 5.2 to be the origin of the temporal spread of the pulse to counter.

In this experiment we investigate if CSM mode has a detectable impact on the ultimate

time resolution by imaging a single transition from a deflected to an undeflected beam condition. The width of a single transition provides direct insight into the variance of the count triggering. The experiment used a square wave with a time period of 10μs ensuring only a single transition in the time space of the delay sweep. This prevents electrons from the following oscillation period impacting the exposure. The exposure time is set to 20ns. The exposure is triggered by the initial deflection with a delay of 10μs to image the return transition. CSM is used with TH0-4.5keV to prevent thermal noise. SPM experiments with TH0-4.5keV & TH0-28keV are used to compare the transition delay and width.

The intensity of both the deflected and undeflected beams are recorded and presented in figure 5.14. The intensities for the deflected and undeflected beams are calculated using the same region of interest scheme shown in figure 5.12J. To define the start and the end of the transition, the intensity at 10% of the maximum, $I_{0.1}$, and the intensity at 90% of the maximum, $I_{0.9}$ are used. In figure 5.14 these intensity boundaries are highlighted with vertical dashed lines. The difference between these gives the variation in electron counting time. The intercept where $I_{\text{Deflected}}$ is equal to $I_{\text{Undeflected}}$ was used as the centre point of the transition. The delay in the detector is then calculated as the difference between transition centre point and voltage increase.

The results for the SPM modes are shown in figure 5.14A & 5.14B featuring similar transition structures with a smooth reversal of the intensity levels. SPM TH0-4.5keV shows ~6,000 more counts than TH0-28keV and a broader time of transition. Figure 5.14C shows an unusual shape in the undeflected beam intensity featuring an increase in brightness before the transition. In contrast the response of the deflected beam shows a simple transition without an increased intensity peak above average. This feature of the undeflected state is not explained during this experiment; however, the transition width and delay is compared.

Table 5.1 summarises the timing of both CSM and SPM. CSM mode is shown to have the smallest variance at 110ns thus confirming that the internal electron charge recombination is directly impacting the time resolution of CSM mode compared to SPM mode.

Calculated results of intensity curves				
Mode	$I_{0.1}$ (ns)	$I_{0.9}$ (ns)	Δ_t (ns)	Delay (ns)
SPM 4.5keV	290	470	180	380
SPM 28keV	170	300	130	250
CSM 4.5keV	380	490	110	450

Table 5.1: A table of the CSM & SPM transition profile timing. The transition start and end times are extracted where the intensity crosses the first and tenth intensity decile. The variance in electron arrival time is calculated as the difference between the two intensity boundaries. The delay is calculated as the difference between the real fall of the voltage pulse and the centre of the transition.

The large difference in variance between SPM TH0-4.5keV and SPM TH0-28keV is expected due to the time differences between charge shared electrons and electrons imparting all their energy to a single pixel. The small variance between SPM TH0-28keV and CSM TH0-4.5keV suggests that when the threshold is high enough, the contribution of charge shared electrons to the increase in variance is small. The delay of CSM TH0-4.5keV is 70ns longer than the SPM experiments. This proves that the additional analogue and digital processing steps when comparing adjacent pixels causes a delay in the electron counting.

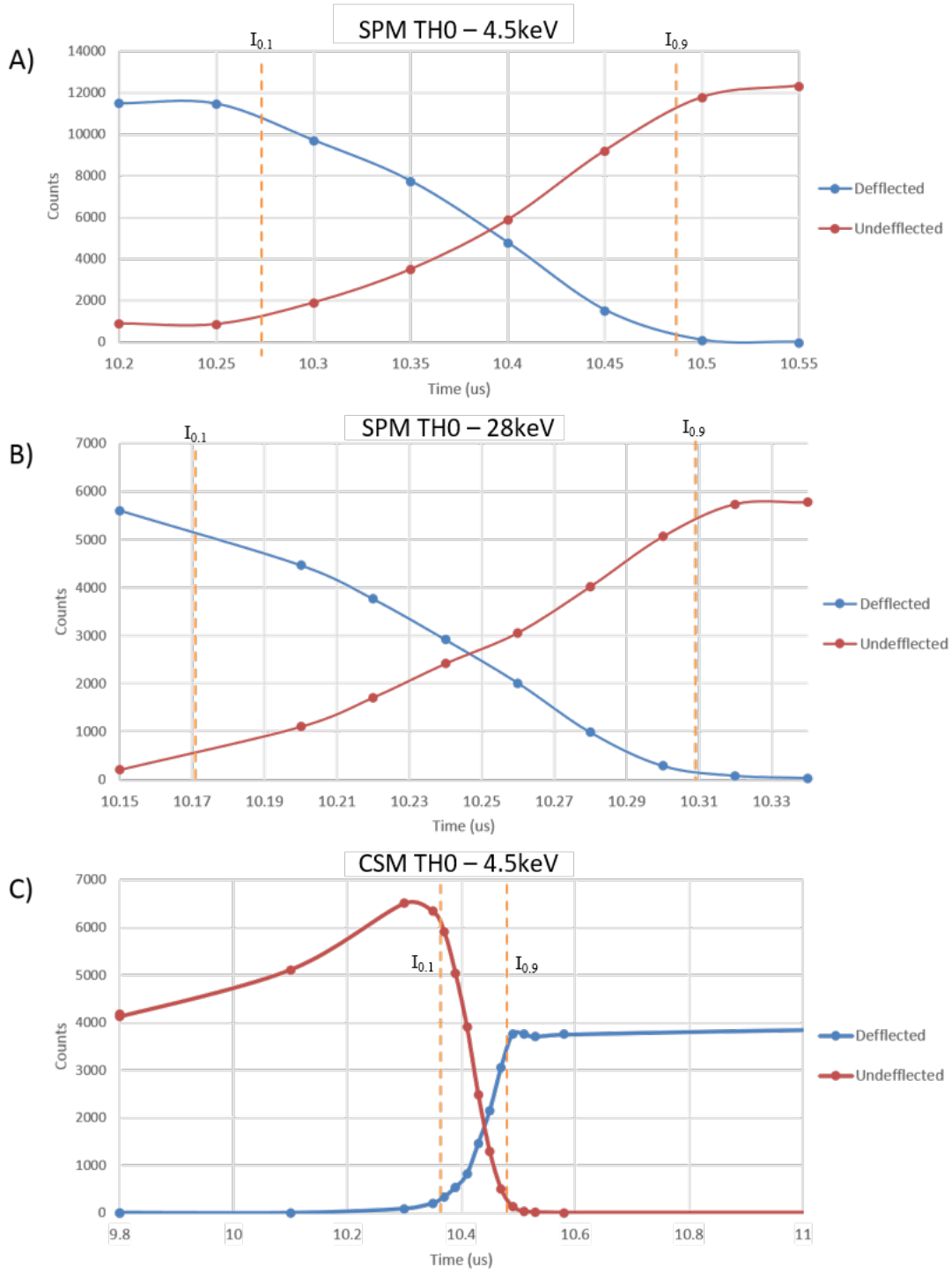

Figure 5.14: A delay series imaging a 60keV beam during transition from deflected to undeflected for: A) single pixel mode with a threshold level of 4.5keV, B) single pixel mode with a threshold level of 28keV and C) charge summing mode with a threshold level of 4.5keV.

5.7 Discussion

The time resolution on a TEM is limited by the signal-to-noise ratio, where live imaging is often performed with exposures of ~100ms, and images taken for data acquisition or publication can be collected for upwards of 1000ms. Chapter 2 discussed the sources of noise in a TEM image, specifically the shape of the SNR vs exposure curve, featuring a limit where the readout noise becomes a significant fraction of the total exposure. In the previous results chapters 3 & 4 we have shown that single shot imaging using the Medipix3 detector has given access to new lattice dynamics in TEM. However, we also recognise the barrier to single shot imaging will always be the limited number of electrons available. In this chapter, we have investigated the stroboscopic imaging capabilities of the Medipix3 device as a method of bypassing limited electron count at fast exposures. The current method of accessing sub-millisecond data in TEM uses a photo-emission electron gun - discussed in detail in chapter 2 - to generate electrons over a short space of time. The time resolution afforded to the TEM is therefore approximately the duration which the photo-emission element is illuminated by a laser. TEM using photo-emission sources are built with optical ports for laser injection incorporated into the column. Therefore TEM without optical access would require introduction of new components to the column in order to utilise a photo-emission source. The research performed in this chapter presents an alternative, non-invasive method of accessing the nanosecond time regime in conventional TEM by using a post-specimen method of achieving time resolution - the Medipix3 detector. The use of the Medipix3 detector is of great importance to the wider TEM community as a method of updating standard TEM with time resolved capability without any decrease in spatial resolution often found in photo-emission TEM.

It was predicted that charge sharing between pixels would be greater for higher primary electron energies due to scattering. Monte Carlo simulations shown in figure 5.4, show that 200keV electrons have a 95% probability contour lateral spread of 72μm compared to only 7.9μm at 60keV. Therefore it is clear that compared to the 55μm pitch pixel width of the Medipix3 the 200keV electron was unlikely to deposit all of its energy in a single pixel. The 60keV is even shown to only have a geometric area equal to 50% of the total pixel area that

is outside this scattering range. In figure 5.6, we compared the impact on charge sharing on time resolution. The range of electron energies caused by charge sharing is shown to directly impact the variance in detection delay of electrons. Therefore 200keV electrons, capable of scattering to a pixel's second nearest neighbour are capable of depositing the greatest range of energies, negatively impacting the ultimate time resolution. Therefore to provide the optimum time resolution conditions we chose to use 60keV electron energies rather than 200keV, that are preferable when performing high spatial resolved experiments.

In section 5.3, we demonstrated the process of characterising the transition speed of the electron beam between an undeflected state and a deflected state when driven by the electrostatic beam plates. The two identified dynamics that prevented this process from providing an ideal illumination were the transition time, and ringing in the system once the maximum deflection had been reached. The location of the electrostatic deflection plates at the top of the column made it a challenge to connect the voltage supply without introducing significant extra capacitance from BNC cables (100pF/m), which increases the time constant of the deflection. The use of an operational amplifier with a high operating voltage and slew rate is proposed as an alternative. This could be placed to generate a high voltage close to the source without adding significant extra capacitance. The predicted maximum transition speed was calculated based on the capacitance of the plates (9.7pF) and the supply voltage resistance (50Ω) giving a time constant of 0.5ns. Implementation of a low capacitance means of providing the voltage supply such as an operational amplifier could provide a time varying illumination with sub-nanosecond transition times for future time resolved detector bench marking.

The results from section 5.4 prove the link between threshold level and time resolution with the SPM results from section 5.6 in agreement. The investigation of a single transition event from deflected to undeflected in figures 5.14A & 5.14B, compared to the top-hat type transition of 5.10 does not show a change in the normalised shape. This suggests the flattening of the TH0-28keV curve in figure 5.10 is an anomaly due to the width of the beam deflection and the returning transition. The results documented linking threshold level and time resolution could potentially expand the use of the Medipix3 colour mode,

where eight threshold levels are used and recorded separately. This would potentially allow electron counts excluded at high threshold levels to be recorded separately. The eight data sets could then be combined later to scan between time resolution and total counts. This methodology would be helpful when investigating processes where the exact time scale is not known.

The primary user controlled variable investigated in this experiment is TH0 when performing single pixel mode. However, the Medipix3 manual and understanding of the pixel hardware suggests that there are other variables which may be tuned in order to attain a higher time resolution from the Medipix3 device. Firstly, the biasing voltage across the pixel directly influences the drift velocity of the electron-hole pairs. Therefore, increasing the applied voltage would potentially shorten induced voltage of the charge sensitive amplifier for all electrons detected. Assuming the voltage response remains the same, the proportionally shorter response time would result in a smaller variance in possible electron arrival times, increasing the maximum time resolution. Secondly, the CSA contains an extended list of fine tuning variables, of which one of particular note is Ikrum. Ikrum changes the rate of decay of the output voltage produced by the CSA by altering the resistance and therefore the expulsion of current. Increasing Ikrum causes the voltage response to decay quicker, this would potentially cause all voltage responses from both electrons depositing all energy and electrons undergoing charge sharing to exhibit reduced decay times. Therefore if the response is shortened proportionally the variance in discriminated pulse fall time should decrease. In the original testing of these elements in the PhD thesis of Rafael Ballabriga Suñé [121], the values were not optimised for maximum time resolution and this could be a method of pushing the time resolution further in future work.

In the final results section 5.6, we investigated the potential of CSM as a method of increasing the time resolution of the detector. The method of charge reconstruction used in CSM mode potentially reduced the variance in electron count triggering thereby reducing the impact of charge sharing without increasing threshold level. We found that a time resolution of 110ns could be achieved for a threshold energy of 4.5keV compared to a time

resolution of 180ns for the same threshold implemented in SPM. As expected, CSM mode has an increased delay time of 450ns compared to 380ns from SPM-4.5keV. Although CSM mode was not designed as a method of increasing time resolution we have proven it to be a useful bi-product of the charge reconstruction hardware.

Chapter 6

Time-resolved small angle electron scattering of thermally induced phase changes in FeRh

6.1 Introduction

Iron rhodium (FeRh) exhibits a unique property in which it undergoes a phase change between anti-ferromagnetic (AFM) to ferromagnetic (FM) in response to temperature increasing above a critical threshold T_t whilst undergoing no crystallographic structure change. The mechanism enabling this change has been a topic of intense debate in the scientific community and continues to provide an ideal specimen for the study of fundamental magnetism. Iron and rhodium alloy with compositions of 49% - 53% iron, forming a B2 cubic crystal unit cell [122]. Bulk FeRh is shown to have an AFM to FM transition temperature T_t = 380K [122, 123], with this temperature increasing as the material is thinned [124]. The underlying microscopic mechanism for this transformation is still unclear. Kittel originally proposed a model based on lattice expansion driven exchange inversion [125], although models based on electronic heat capacity [126] and spin fluctuation [127] have also been discussed. FeRh has been identified as a promising material for memristors, a device exhibiting resistance dependent on the previous history of applied

current [128, 129, 130] and for solid state cooling due to the large magneto-calorific effect during the phase transition [131, 132, 133]. The ability to perform *in situ* measurement of the changes of the magnetic state of FeRh is therefore an important aspect of progressing research in this field.

The aim of this chapter is to apply the stroboscopic time resolved capabilities of the Medipix3 detector, demonstrated in chapter 5, on the material FeRh. Investigation into thermal timescales is performed by imaging the transition from AFM to FM of a lamella of FeRh in response to rapid heating generated by voltage pulses across a resistive material in close proximity to the sample. By demonstrating the ability to resolve the magnetic moment on the microsecond scale using an imaging technique called small angle electron scattering patterns (SAES) we hope to provide a novel method of investigating thermally induced magnetic transitions in TEM. As discussed in section 6.2 the experimental method used in this chapter is discussed with focus on sample fabrication from bulk FeRh to electron transparent lamella on electrically contacted chip and the imaging mode SAES. In section 6.3 the contrast present in the static temperature images is discussed where the range of temperatures between 293K and 423K spanning the AFM to FM transition are imaged. Initial time resolved measurements are performed in at millisecond timescales to demonstrate the time resolution of single shot imaging in section 6.4 before attempting stroboscopic imaging of the transition in section 6.5. Finally, in section 4.9 the results of this time-resolved experiment and their implication on the role of TEM at thermal timescales is discussed.

6.2 Experimental Design[3]

The time resolved capabilities of the Medipix3 detector were used to investigate both the magnetic and thermal response of a thin lamella of FeRh. Fabrication of the sample used in this chapter was primarily performed by Dr Trevor Almeida [7]. The FeRh alloy

[3]Sample fabrication performed by Dr Trevor Almeida, Department of Physics & Astronomy, University of Glasgow

was epitaxially grown by means of DC magnetron sputtering co-deposition to a thickness of 50nm on a NiAl buffer (40nm) on a GaAs substrate (500 μm). The substrate was mechanically thinned to ~5μm using diamond paper with paper grades ranging from 30μm to 1μm grit. The sample was inserted into the FEI Dual Beam FIB Nova 200 where the MgO substrate was back thinned using progressively smaller beam currents (9.0nA, 2.7nA, 0.9nA) to bring the sample to a thickness of ~1μm. The lamella is then detached from the bulk material by creating an undercut using FIB milling and transferred to the chip by securing the sample to an *in-situ* micro-manipulator using Pt deposited with a gas injector [134, 135]. The sample is then attached to a DENSsolutions micro-electro-mechanical system (MEMS) Wildfire heating chip shown in figure 6.1, which is discussed later in this section. The lamella of material is attached above a 5μm wide sample window shown in figure 6.1C using FIB Pt deposition. The sample is then detached from the micro-manipulator before being secured on the opposite side. At this stage the lamella of FeRh undergoes a second round of thinning to electron transparency. The milling uses currents from 0.26nA to 90pA at 30keV followed by a low energy polish at 5keV at 47pA. This brings the sample to electron transparency. An example of a lamella of FeRh on a Wildfire chip is shown in figure 6.2 where deposited platinum securing the FeRh above free space can be seen.

The DENS Wildfire chip shown previously in figure 6.1A and heating rod provides a method of heating and controlling temperature of the sample. The Wildfire chip is used both in conjunction with a PC controlling the temperature via a 4-point-probe controlling the local temperature on the chip to an accuracy of ±0.001K. The patterned heating element in figure 6.1B is designed to provide uniform heating in the region designated the research area. The PID controller provides a heating rate of 200K ms^{-1}, however by accessing the heating element directly voltages higher than used by the PID controller allowed this heating rate to be bypassed. A breakout box enabled direct access to the heating element which was connected to a signal generator capable of voltage pulses up to 10V.

Small angle electron scattering imaging mode was used in the TEM to provide data

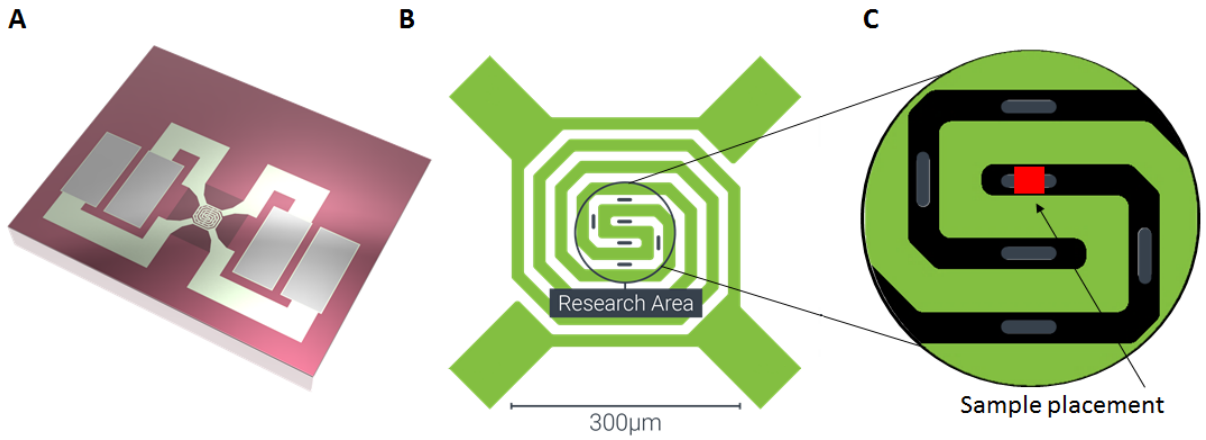

Figure 6.1: The wildfire MEMS-based heating chip produced by DENSsolutions. Figure A shows the full chip design with contact pads designed for use in DENS TEM holders. Figure B shows the heating element (Green) with the electron transparent windows as black ovals in the research area. Figures are adapted from DENSsolutions website [6]

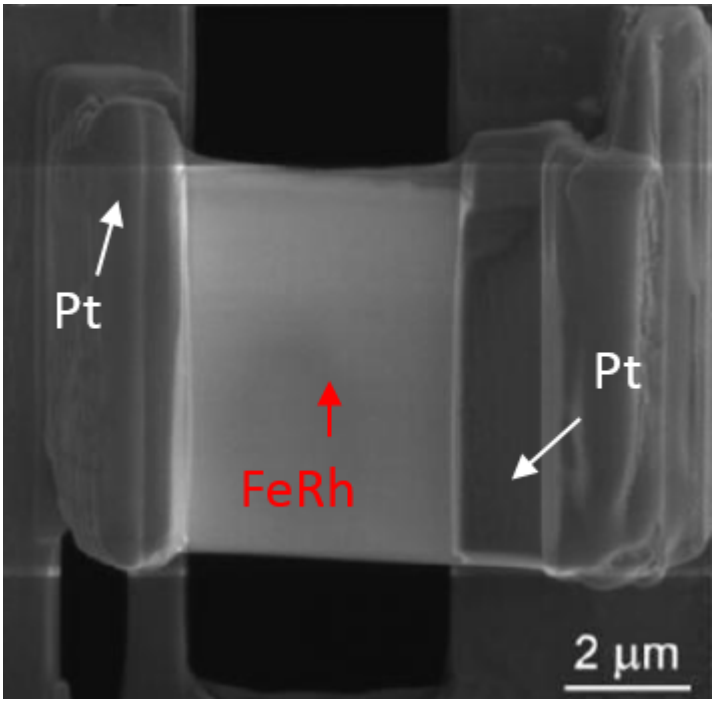

Figure 6.2: An electron transparent lamella of FeRh attached to a Wildfire chip above a free space window. The FeRh is secured by Pt deposited via a gas injector. The figure is adapted from the JEMS conference paper produced by Dr Trevor Almeida [7]

on the magnetic moment of the material. As discussed in section 2.4 magnetic phase of an object requires a quantum interpretation using the Aharonov-Bohm effect to properly describe the contrast. The incoming electron waveform shows in equation 6.1 is convoluted with the sum of both the electrostatic and magnetic potentials where the transmitted wave has the form 6.2. The sum of the potentials in equation 6.3 can be re-written as shown in equation 6.4 where the deflection from the electrostatic component is given on the left and the magnetic phase change from the Aharonov-Bohm effect is given on the left.

$$\Psi_I = \Psi_o e^{2\pi \mathrm{ikz}} \tag{6.1}$$

$$\Psi_T = \Psi_I e^{\mathrm{i}\Phi(\mathrm{x,y})} = \Psi_I e^{\mathrm{i}\Phi(\mathrm{x,y})} e^{2\pi \mathrm{ikz}} \tag{6.2}$$

$$\Phi = \Phi_{\mathrm{electrostatic}} + \Phi_{\mathrm{magnetic}} \tag{6.3}$$

$$\Phi = \frac{\pi V(x,y)t(x,y)}{\lambda_e E} + \frac{2\pi et}{h} \tag{6.4}$$

where Ψ_0 is the emitted wave function, Ψ_I is the wave function incident to the sample, Ψ_T is the transmitted wave function, Φ is the total phase, $\Phi_{\mathrm{electrostatic}}$ is the electrostatic component of the phase shift and Φ_{magnetic} is the magnetic component of the phase shift.

To image this deflection the beam can be imaged in the back focal plane where the image formed by the lens is proportional to the square of the Fourier transform of the back focal plane according to Abbes theory. The back focal plane is described in equation 6.5. The intensity of the beam imaged in the back focal plane as shown in equation 6.6 has a deflection spacing directly proportional to the phase Φ. In this experiment the transition from AFM to FM will cause the beam in the back focal plane to shift from undeflected to deflected.

$$F(k_x, K_y) = \Psi_o \iint e^{\mathrm{i}\Phi(\mathrm{x,y})} e^{-2\pi \mathrm{ik_x x}} e^{-2\pi \mathrm{ik_y y}} dxdy \tag{6.5}$$

$$I = |FT[\Psi_T]|^2 \tag{6.6}$$

The PID temperature control system was initially used to provide SAES patterns at fixed temperatures. In the static temperature experiments the Gatan Orius CCD camera is used to take high resolution images of the SAES pattern. In the time resolved experiments voltage pulses from a signal generator were used to rapidly heat the wildfire chip which is in thermal contact with the FeRh causing a transition from anti-ferromagnetic to ferromagnetic. The voltage and duration of the pulse determine the thermal energy available to the system with a minimum required to cause the transition. Several voltages were tested with 1.5V clearly demonstrating a transition and used as the minimum voltage in the time resolved experiments. Using a pump-probe approach the magnetic moment of the FeRh was investigated by triggering the Medipix3 detector on the rising edge of the pulse with the internal detector clock allowing a delay in the exposure. The limit in the SNR of single shot imaging prompted a change in the detection mode to stroboscopic with the exposure still triggered in a pump-probe approach except with the final exposure constructed from the sum of many images. In order to compensate for reducing the duration of the voltage pulse for investigating microsecond exposures in the stroboscopic experiments, the voltage was increased in order to provide enough thermal energy to cause a phase transition. In this experiment the voltage was increased to a maximum of 10V at which point the thermal conduction of the DENS Wildfire rod became a limiting factor in the time response of the system.

6.3 Static imaging of temperature response

The incident electron beam was positioned at the edge of the sample so as to incorporate both electron transmission through the FeRh and also electrons passing through free space. Electrons passing though the FeRh lamella are small angle scattered whereas the electron passing do not. This provides a reference point for calculating the change in the beam deflection when temperature and consequently magnetic moment changed. In the image

this presents itself as two spots where one is the SAES pattern and the other is the free space signal. This positioning of the electron beam is shown in figure 6.3.

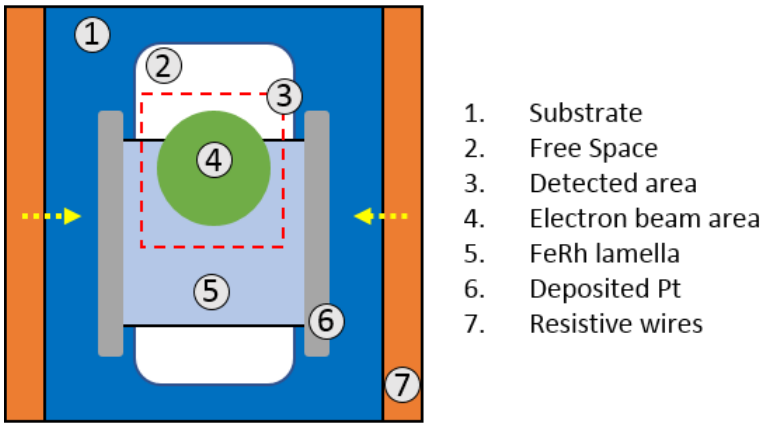

Figure 6.3: A schematic of the beam position with respect to the FeRh sample and Wildfire chip. The detected area is overlaid in dashed red to explain the contrast in the real space images shown later. The direction of thermal energy transfer is annotated in yellow.

Figure 6.4 shows both the Fresnel and SAES images side by side for comparison where the temperature is maintained at 293K. Figure 6.4A shows the FeRh illuminated by a beam area 1.8μm of which 0.1μm is passing through free space away from the sample at the top right. The magnetic structure of the FeRh is visible due to the defocus of the Fresnel mode imaging. Figure 6.4B shows the SAES contrast corresponding to the illuminated area in figure 6.4A. The contrast has been inverted and coloured to enhance visibility of key features. Towards the top of figure 6.4B is the illumination from the electrons passing through free space. The diffraction electrons are those separated from the free space signal. The spread of the contrast is potentially due to both the different directions of magnetisation within the sample and electrostatic contributions. The FeRh sample when in an AFM state should not cause a deflection in the SAES pattern and therefore it would be expected that the contrast should display only a single peak in intensity. However, even at 20K a separation is observed which suggests that the sample is not completely in the anti-ferromagnetic state which is thought the be due to strain introduced during the sample fabrication process.

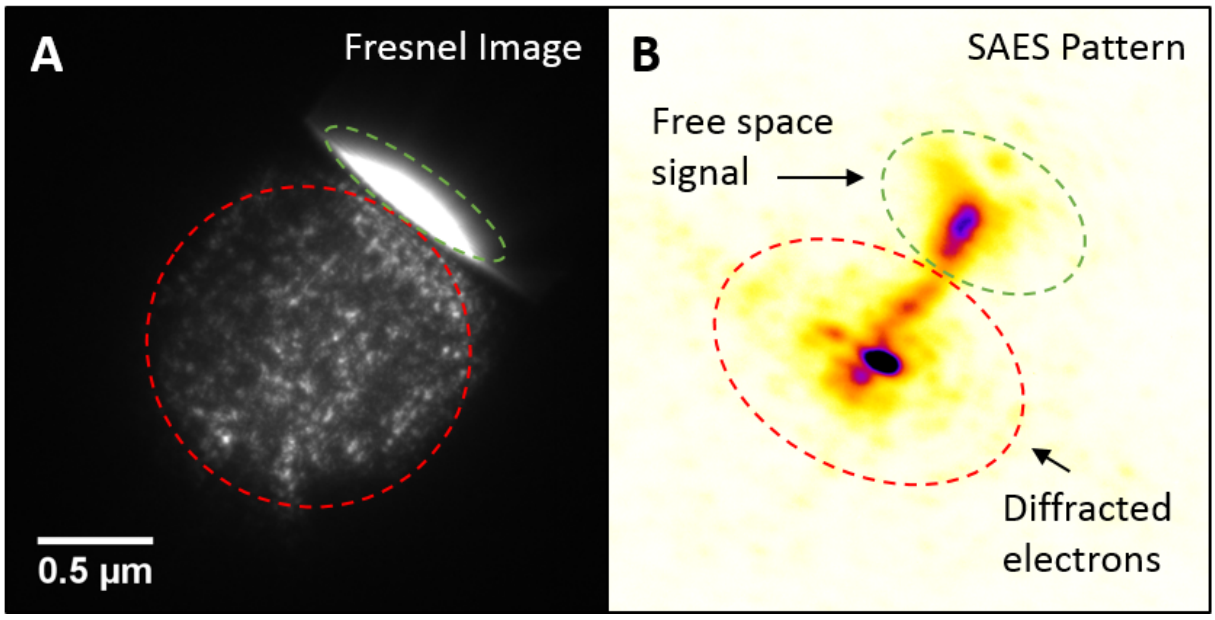

Figure 6.4: FeRh imaged with both real space Fresnel image in figure A and SAES in figure B. The intensity of the two main contrast features in the SAES pattern can be seen to correspond with the beam position at the edge of the sample.

To give a reference for the change in magnetisation with temperature we take both Fresnel and small angle diffraction images at temperatures between 293K and 423K in 10K increments which documents in real & reciprocal space the transition from AFM to FM. Figure 6.5 shows four pairs of scattering pattern images during the temperature increase. Figures 6.5A-D show the real space images of the SAES patterns in figures 6.5E-F which have been rotated so that the direction of deflection is vertical and the position of the free space signal centred. Figure 6.5E shows the SAES pattern that was presented previously with the real space Fresnel image. In figure 6.5F the diffracted electron intensity has become more widely spread and shows increased angular separation from the free space signal. To determine the distance between the free space beam and the scattered region we used a centre of mass fitting. In figures 6.5G and H the deflected electron intensity reaches a maximum angular separation from the free space signal indicating that the FeRh has saturated in an FM state. The change in intensity and shape of the free space beam suggests that the heating is causing some motion of the sample relative to the beam.

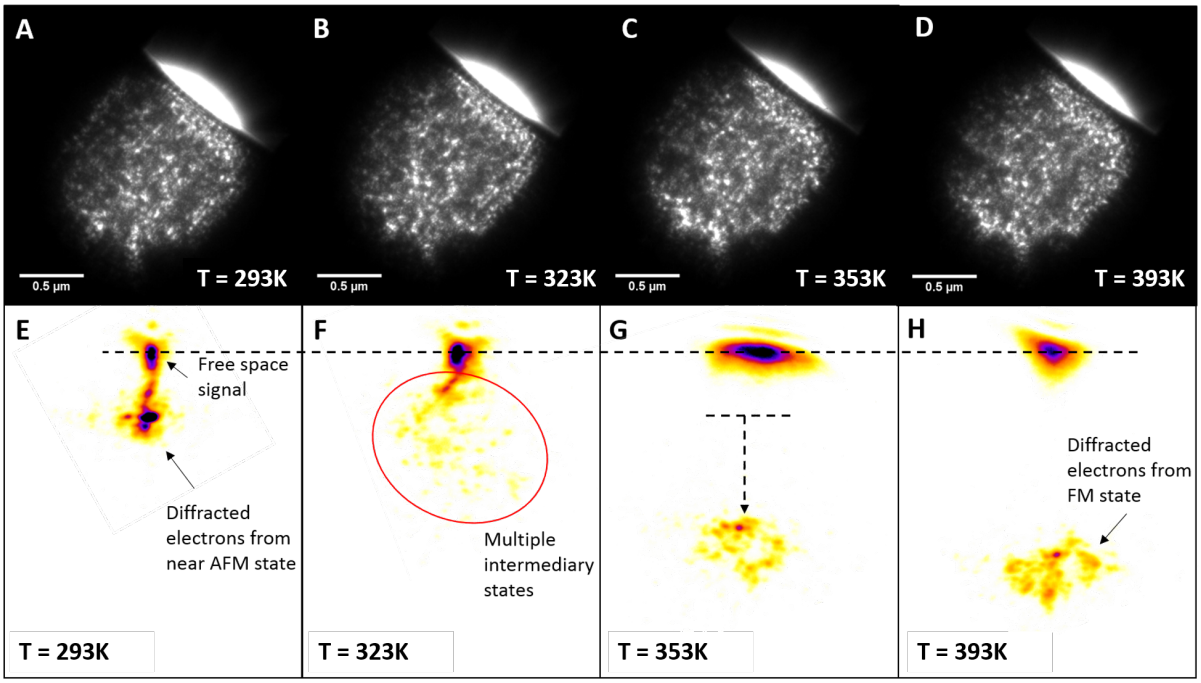

Figure 6.5: Static temperature evolution of both real space & SAES patterns for FeRh imaged at static temperatures; A&E) 293K, B&F) 323K, C&G) 353K, D&H) 393K. The temperature range is shown to span the AFM to FM magnetic transition.

Figure 6.6 plots the change in the separation of the free space beam and the diffracted beam. The transition starts at 313K and plateaus at 373K up to the final data point at 423K. This transition width and position is in agreement with results from literature showing an increase from the AFM/FM T_t of 10K in bulk FeRh to higher temperatures through thinning [123].

6.4 Direct filming of pulsed AFM/FM transition

The change in the magnetic moment of the FeRh in response to a voltage pulse driving the magnetic state from AFM into FM is investigated initially in single shot mode. In the previous chapters 3&4, direct filming was limited to 10ms when detecting a broad beam covering the sample. However, because SAES converges the beam into scattering spots the intensity is sufficient to image at 1ms while maintaining an intensity sufficient to

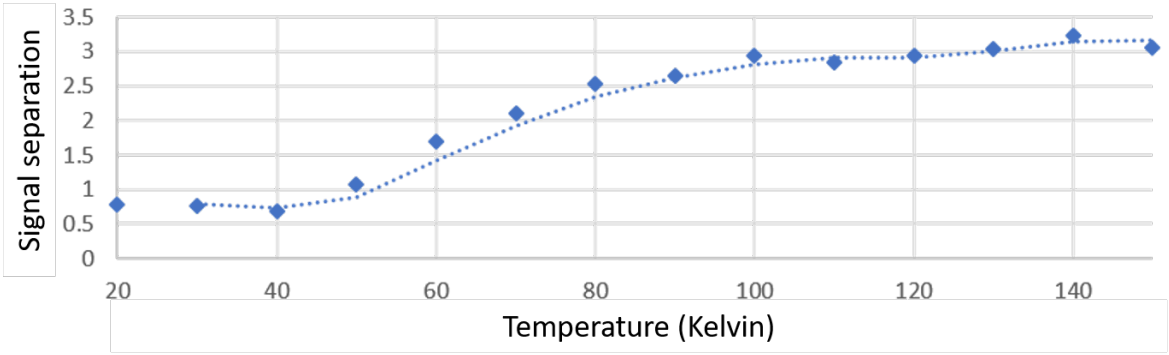

Figure 6.6: A plot of the calculated separation distance between the diffracted electron signal and free space beams as a function of temperature.

identify the position of the beams. The imaging is performed in continuous acquisition mode allowing for gapless imaging of the magnetic response. The imaging is triggered from the start of the 1.5V pulses with durations 5ms and 10ms. Figure 6.7 shows the separation of the SAES centre of mass and the free space beam peak plotted against time for both the 5ms (Blue) and 10ms (Orange) pulse durations. The end of each of the pulses is indicated by a dashed line.

Both curves show similar response to initial heating in which the first three data points show a small increase in separation followed by a rapid heating phase during the pulse between 3ms and 4ms. In the case of the 5ms pulse saturation of the magnetic moment is reached within 4ms and then following the end of the pulse cooling occurs over 20ms (5ms to 25ms). The 10ms pulse requires cooling over a much longer duration of 27ms (10ms to 37ms) before returning to the AFM state. This suggests that SAES provides a proxy measurement for temperature only up to the saturated FM transition temperature T_t. This is demonstrated in figure 6.8 where both the 10ms and 5ms responses have been analysed. The graph indicates both the magnetic moment between AFM and FM on the left hand axis and FeRh temperature T on the right hand axis. Temperature can be increased beyond T_t and is predicted to do more in the case of the 10ms pulse T_{10ms}.

The near identical initial response is expected as the thermal energy applied into the system is equal at each point until the 5ms mark and therefore the responses should

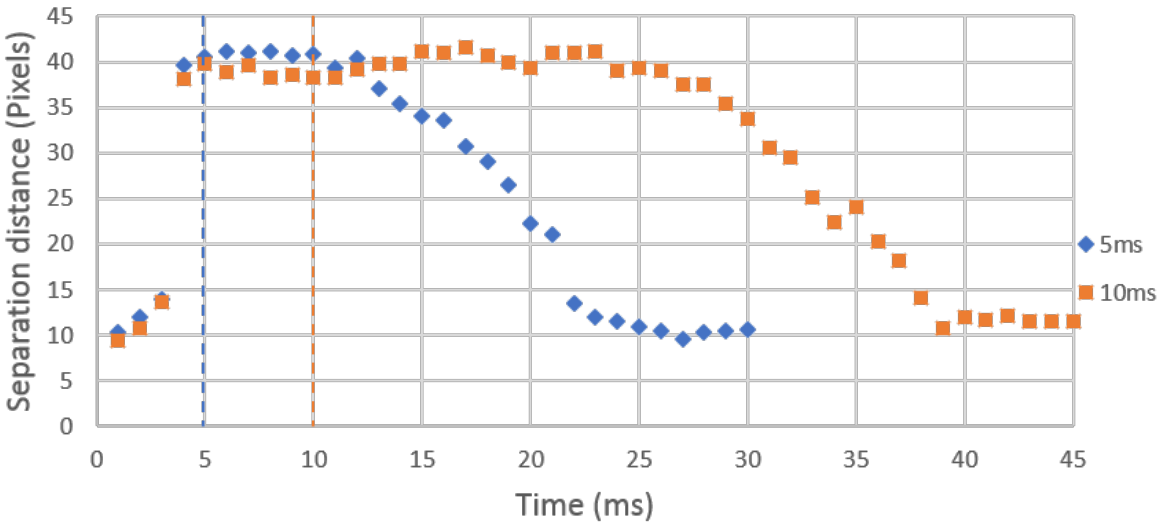

Figure 6.7: The change in the separation distance between the SAES and free space beam in FeRh as a response to a 1.5V pulse of 5&10ms. Imaged in single shot mode with an exposure of 1ms.

be the same. We see that the time resolution of 1ms is not enough to identify the intermediate material temperatures during the heating due to the large gap in imaged separation distances corresponding to ~323K. The similar duration between the end of the FM saturation state at which the magnetic moment begins to decline and the AFM state suggests that the rate of thermal energy removed from the sample is equal at these timescales. The peak intensities for the free space beam and SAES are 304 and 181 electrons per pixel. Exposures below this duration are beam current limited with currents between 100pA and 1nA corresponding to a single pixel intensity less than $1e^{-}\mu s^{-1}$. As demonstrated in the previous chapter microsecond and below exposures are capable in stroboscopic mode and would improve the ultimate resolution with which the magnetic moment of the AFM to FM transition could be resolved.

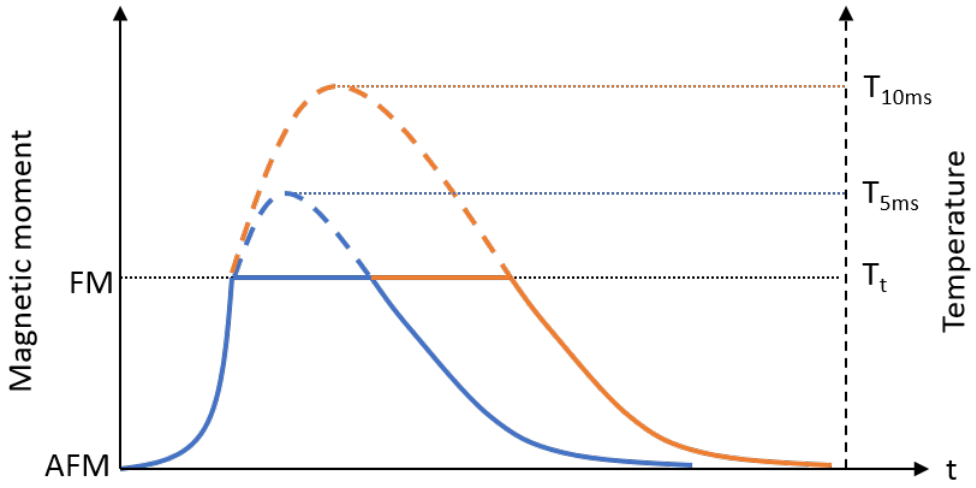

Figure 6.8: The predictions of the real FeRh temperature compared to the FeRh magnetic moment acting as a proxy for temperature. The increased pulse duration causes $T_{10ms} > T_{5ms}$ resulting in a longer duration before reaching the AFM state.

6.5 Stroboscopic imaging of pulsed AFM/FM transition

In this section we demonstrate the capability of stroboscopic imaging in acquiring SAES patterns at microsecond exposures exploiting the time resolution of the Medipix3 as explored in chapter 5. We perform stroboscopic imaging with a total exposure duration of 1ms by summing 100 frames of 10μs. The 10μs exposure duration allows us to investigate shorter heating pulses. The magnetic transition is driven by heating pulses of 2.5ms duration at 1.5V and 1ms duration at 2V.

Figure 6.9 shows the results of the two stroboscopic pump-probe experiments where the time axis is displayed in log form. The trend in the data points, as expected, remains consistent with the trend from the previous single shot imaging. Both figures show how the reduction in the image exposure time enables significantly more data points to be gathered during the period in which the magnetic moment in the FeRh is changing. The change in the FM separation distance between the 1ms and 2.5ms pulse duration data-sets was caused by alteration in the column optics to maximise the SAES pattern contrast. In the

1ms pulse dataset the spacing between the delay intervals is 100μs for the first 1000μs. The greatest change is seen between 800μs and 900μs with a change in separation distance of 14.7 pixels.

Finally, we investigate a pulse duration to 100μs and increase the voltage up to the maximum voltage provided by the signal generator used in the experiment of 10V in order to provide enough thermal energy to cause a transition at small pulse durations. In the previous experiment it was clear that a pump-probe delay spacing of 100μs was not sufficient to capture the full range of magnetic states during the transition and therefore a spacing as fine as 5μs at specific points to maximise the demonstrated time resolution. Figure 6.10 shows the SAES response for pulse voltages 7V, 8.5V and 10V plotted against a logarithmic time axis. The end of the 100μs is highlighted by a red dashed line and the data is connected by a moving average trend line.

One of the primary reasons for increasing the voltage up to 10V is apparent in the separation distance at the end of the voltage pulse. It can be seen that the 8.5V and 7V pulses have a 6.1px and 4.3px separation distance respectively after the voltage pulse is finished. The separation increases between T = 100μs and T = 400μs after which the sample saturates in the FM state. This shows a different profile than the previous experiments where the FM state has always been reached before the end of the voltage pulse. This effect can be understood by considering the system as three connected temperature reservoirs, where the components are the heating element, the silicon nitride substrate and platinum as intermediary material and the FeRh as the final temperature reservoir. In the case of both the 7V and 8.5V data the voltage pulse causes the temperature to rapidly rise in the heating element. The maximum temperature and therefore thermal gradient between the heating element determine the rate that thermal energy enters the intermediary material. Similarly, the temperature of the intermediary material and the thermal gradient between it and the FeRh determine the temperature at the end of the pulse. The gradient between the three is not sufficient for the FeRh to receive enough thermal energy in 100μs to fully reach the FM state. However, when the pulse is turned off the remaining thermal energy and rate of thermal energy transfer from the intermediary

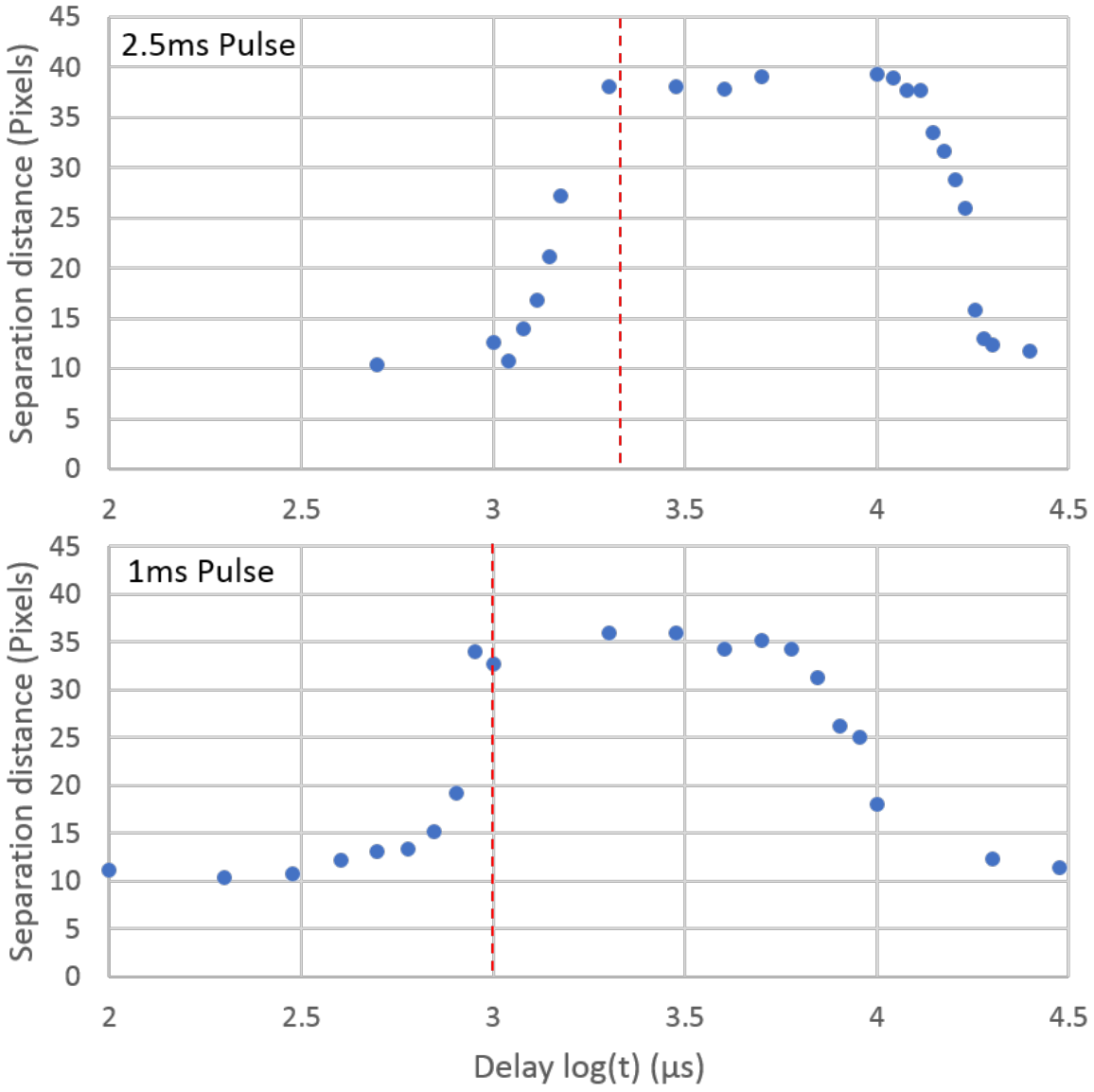

Figure 6.9: The change in the separation distance between the SAES and free space beam in FeRh as a response to a 2V pulse of 2.5ms duration and a 1.5V pulse of 1ms duration. Imaged stroboscopically with an exposure of 10μs.

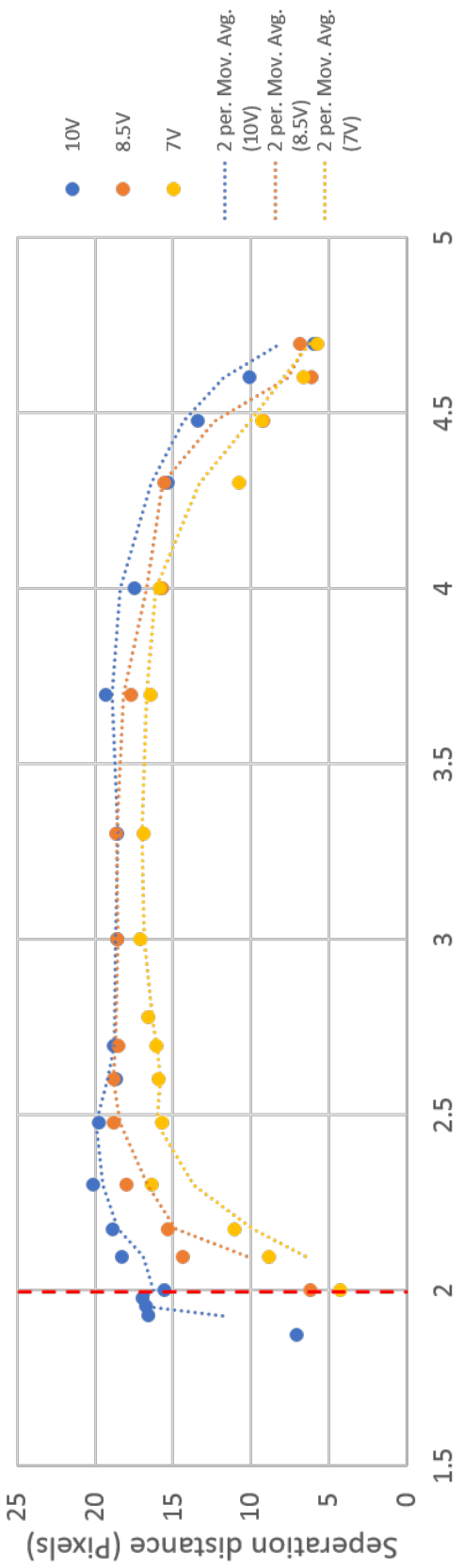

Figure 6.10: Thermally induced transitions between AFM and FM in FeRh in response to voltage pulses of 100μs duration with peak voltages of 10V, 8.5V and 7V.

material into the FeRh is sufficient to cause the transition into the FM state. Therefore, this must mean that in the 10V case the temperature of the wire and subsequently the thermal gradient across the reservoirs is sufficient to cause the FM transition before the end of the pulse. The time resolution of stroboscopic SAES performed on the Medipix3 detector therefore allows us to access the thermal timescales of the heating chip itself allowing for understanding of the response and limits of thermal activation of the FeRh AFM to FM transition.

6.6 Discussion

The fabrication of the sample played an important role in the quality of the results from this experiment. The variation in temperature during the experiment appeared to cause thermal expansion in the sample resulting in a change in the position of the sample imaged. This effect is evident from both the real space Fresnel images in which the bright free space region changes size between images and seen in the SAES images as a change in the free space beam intensity. This thermal motion is likely caused by a combination of thermal expansion of the FeRh during heating and the adhering of the FeRh in position above the free space whole in the Wildfire chip using Pt.

The initial separation between the SAES beam and the free space beam suggests that the material is not entirely in the AFM state. An electron beam passing through an AFM sample should experience no deflection due to the magnetism. This is thought to be caused by damage in the process of thinning the sample and strain caused when adhering the sample to the DENS Wildfire chip. Although this does not change the investigation into the time resolution attainable by both the Wildfire chip and the Medipix3 it does prevent calibration of the separation in terms of magnetic moment without further investigation to identify the moment of the near-AFM starting state.

Single shot mode imaging of SAES patterns is shown to be limited to 1ms by the electrons available in the column. Exposure durations of 1ms were tested and are capable of identifying the pair of frames between which the AFM to FM transition occurred. However,

these single shot images are mostly unable to capture the intermediate transition between the AFM and FM state. This gives an approximate boundary between the time resolution available for imaging reproducible and non-reproducible thermal experiments.

The final stroboscopic dataset identified a thermal latency in the increase in the temperature of the FeRh in response to the voltage pulse. This latency is important in determining the ultimate time resolution which the AFM to FM transition can be driven using the DENS Wildfire chip. In the results although we determine a 10V pulse with a duration of 100μs is capable of driving the sample state into FM, however, voltage pulses of 8.5V and 7V must rely on stored thermal energy in the chip to provide thermal energy after the pulse. The distance between the heating element and the chip window is 4μm which along with the physical heating element itself is predicted to be the cause of this latency. This latency could potentially be avoided by directly attaching the sample directly to the heating element.

The manual method of both controlling the pump-probe imaging delay sweep and identifying the position of the SAES beam and free space beam caused there to be significant gaps in the delay sweep. The density of data-point acquisition needed to be approximated via coarse identification of key points visually. However, automating this process would allow for identification of separation distance over a time line with finer continuous time resolution.

Although the thermal latency in the system provided a limit to the time resolution in this AFM to FM experiment it does indicate the potential of TEM in studying temperature changes in stroboscopic imaging. Image exposure in this experiment is demonstrated as short as, but not limited to 10μs, where exposures as short as 100ns - based of results of chapter 5 - could be envisioned assuming that the summed exposure of the stroboscopic dataset was sufficient to provide enough contrast and the sample conditions are right. In this experiment the real time resolution is also limited by the area of sample illuminated by the beam forming the SAES. The large sample area and local magnetic domains within caused there to be a spread in the intensity from the SAES beam. In this experiment the position was calculated by a centre of mass calculation. However, this did appear to cause

some noise in the calculated position of the order of 2px. Therefore, the ultimate time resolution attainable also appears to be negatively impacted by the presence of multiple magnetic domains in a sample. To maximise the possible time resolution a single domain sample would be used.

Chapter 7

Summary and future work

7.1 Introduction

In this thesis, methods of attaining time resolution in an unmodified TEM have been investigated extensively in single-shot mode in chapters 3&4, and in stroboscopic mode in chapters 5&6. The magnetic structure of samples were investigated using Lorentz imaging techniques where Fresnel mode imaging was performed providing real-space time resolved imaging in single shot mode and SAES patterns were imaged providing magnetic moment data at microsecond time resolution. The Medipix3 direct electron detector features heavily in this thesis and provides the technological advance to enable investigation of new time regimes in TEM by removing the read noise that had previously limited the signal-to-noise ratio. In the case of single-shot mode, experiments were performed on the skyrmion materials Cu_2OSeO_3 and FeGe with the prediction that skyrmion lattice dynamics would present new and unique processes that had not been previously imaged in real space. In Cu_2OSeO_3 it was discovered that the field-induced phase transition between helical and skyrmion state exhibited interesting magnetic phenomena such as meta-stable skyrmions ahead of the skyrmion-lattice, stretching of the inter-skyrmion lattice spacing on the tens of millisecond timescale and the role of 5-7 defects in skyrmion lattice boundaries during rotation of skyrmion domains. In FeGe observations of a paired-skyrmion like state exhibiting millisecond timescale repeatable motion was imaged and estimates of the energy

barrier overcome made. This motion enabled testing of a method of image reconstruction, unique at this timescale to the Medipix3.

In the case of stroboscopic mode imaging, initial experiments were performed to determine the ultimate time resolution of the recently developed Medipix3 direct electron detector where the temporal response of the APS architecture had not previously been investigated directly for attaining time resolved images in TEM. The original Medipix chip had been previously investigated in conjunction with pulsed deflection using a bifilar rod to determine the application of APS in temporal deflection imaging proposed in the thesis of Dr Robert Beacham [136]. In this work the beam was swept across the detector during magnetic propagation. This imaging mode called streak imaging effectively created a profile of the magnetic moment across the detector. Although simulations produced in the Beacham thesis suggest this to be possible experimentally this proved difficult. In this thesis, low-capacitance deflection plates were used as a method of deflecting the electron beam at near nanosecond frequencies and used as a probe for the time resolution of the Medipix3. The time resolution of single pixel mode at two energy thresholds and charge summing mode were determined providing understanding of the potential time resolution available for future time resolved TEM experiments. This knowledge was applied to FeRh samples providing microsecond time resolution SAES patterns during thermally induced transition from AFM to FM states. This provided an insight into the thermal control of thin film material using MEMS based chips.

7.2 Summary

In chapter 3, we have shown the successful application of TEM in accessing the millisecond time regime of magnetic dynamics with real space imaging. The implementation of the Medipix3 single electron detection device provides a method of removing the readout noise from the image acquisition increasing the signal-to-noise ratio at exposure durations previously inaccessible. Lorentz TEM at millisecond timescales opens up a wide field of research into skyrmion lattice control through magnetic fields and local thermal heating

both of which can provide dynamics changes on a similar timescale.

The image quality in these experiments is limited due to the thickness of the Cu_2OSeO_3 suggesting that the Medipix3 detector could enable single shot imaging into the microsecond range with correct beam optimisation and sample thickness. Current research into thin film chiral materials provide a perfect system for maximising single shot TEM time resolution using this technology.

Three key dynamic processes are presented in these results: skyrmion lattice rotation, dynamics of skyrmion slip planes with tracking of individual skyrmion and the emergence of meta-stable skyrmions in confined regions. None of these had previously been accessible without the Medipix3 technology. The skyrmion lattice rotation dynamics imaged in this experiment improve upon the XMCD and neutron diffraction experiments. The presence of multiple skyrmion domains is confirmed and the structure of skyrmion lattice boundaries imaged dynamically for the first time by providing resolution allowing identification of individual skyrmion positions and trajectories. Finally, although millisecond time resolution was not fast enough to directly image the creation and annihilation of skyrmions themselves, it did provide an understanding of where skyrmions can dynamically nucleate in the B-T phase map while out of equilibrium.

In chapter 4, it was demonstrated that the ability to detect skyrmion defect dynamics at high angle skyrmion boundaries with a time resolution of 10ms is possible. This research has been performed as an extension to the work performed in chapter 3 using the Medipix3 detector to access ten millisecond exposure images in which the SNR of skyrmions is sufficient for computational image processing and skyrmion position finding. We have used the spatial resolution of Fresnel mode TEM to identify paired skyrmion system where the inter-skyrmion distance is approximately half of the background skyrmion lattice. The frequency of motion by the skyrmion defect at the high angle grain boundary has provided a method of quantitatively assessing the magnitude of the energy barrier controlling the rate of skyrmion motion has been approximated for both symmetric and asymmetric skyrmion defect sites. Finally, we used the discrete positions occupied by the skyrmion pair defect and the comparably short ten millisecond exposures to compile select images in

the skyrmion stack to construct a single composite image with reduced noise.

In chapter 5, we demonstrated a novel method for providing sub millisecond time resolution in an unmodified transmission electron microscope. We have demonstrated that a time resolution of 100ns is achievable in an electron microscope where a continuous beam, produced by a cold field emission gun is imaged using the Medipix3 detector. This feat is unachievable by CCD cameras for continuous emission electron guns where the readout noise causes images with insufficient SNR at sub-millisecond time resolutions. Imaging a sharp beam position change provided a method of probing the time resolution by effectively capturing the variance in the delay of electrons during the analogue to digital conversion process. The imaging and analysis of an *in-situ* dynamic process has determined the Medipix3 to be capable of imaging down to 100ns. The stroboscopic temporal aliasing captures the beam with an intensity above 90% of the total image intensity providing an estimated SNR above 10 for imaging at this time resolution. The results of image capture on a single sided transition show CSM has a variance of 110ns and SPM a minimum variance of 140ns when performed with a threshold energy of 51keV. SPM is confirmed to be capable of isolating an electron beam oscillating at 5Mhz through stroboscopic temporal aliasing. Electrostatic beam deflection provides a time varying image with a transition time of approximately 11ns, which is appropriate for this experiment and may potentially provide a means in itself for time resolution in the microscope through time resolved beam deflection. The voltage supply and parasitic impedances could be significantly reduced to provide a detectable intensity variation in the nanosecond time regime.

The application of stroboscopic imaging mode to FeRh in chapter 6 provided proof that the removal of readout noise though use of the Medipix3 detector could unlock access to new fields of magnetic study such as investigation of microsecond thermal processes. It was demonstrated that the transfer of thermal energy through the MEMS based chip delayed the transition from AFM to FM of FeRh depending on the voltage supplied. Voltage pulses as short as 100 μs and with amplitude as large as 10V were investigated for the purposes of driving the phase transition, however, the limiting factor proved to be the carrying chip.

The SAES images taken at 20° provided evidence of some deflection of the electron

beam indicating that the FeRh may have some contribution that is still FM even though at bulk this material should be AFM. This phenomenon had been identified previously and attributed to damage caused by ion implantation by McLaren [137]. The key mechanisms through which the FM transition point is believed to decrease are diffusion of Fe into surrounding material, a release of strain in the material and an alteration in the crystal structure. It was experimentally confirmed in the thesis of McLaren that this effect occurred during FIB thinning however not during ion polishing.

7.3 Future work

In this section we explore the future work identified for continuing the investigation into time resolved dynamic imaging in transmission electron microscopy. Each chapter is visited in turn with suggestions to the improvement of the current experimental set-up and potential wider field applications.

In chapter 3 we demonstrated that using the Medipix3 detector, 10ms exposure images provide useful magnetic contrast in Lorentz imaging mode. In light of imaging performed at much faster timescales in chapters 5&6 it is clear that the time resolution is not detector limited. Although 10ms imaging is a significant improvement of CCD cameras dedicated thin film samples such as spin-ice arrays and domain walls in nano wires could lend themselves to significantly higher contrast. Images with higher contrast than the Cu_2OSeO_3 would potentially enable demonstration of faster single shot imaging. Additionally, if the magnetic structure was not the primary purpose of imaging but the overall state, then the imaging could be pushed faster still, such as imaging spin-ice domain reversal where the direction of magnetisation is identifiable at low contrast.

The method of creating vector maps when analysis of subsequent frames such as those shown in section 3.6.2 highlights the motion of skyrmions within those frames. However, improvements could be made to this process, specifically removing the edge artefacts introduced at the Fourier filtering step. This process is unnecessary if imaging a sample away from the edge of the specimen.

The composite images generated in chapter 4 provided magnetic resolution of the paired skyrmion object down to 10nm in Fresnel mode imaging. This resolution allows for successful identification of individual skyrmion positions and measurement of the distance between skyrmions. However, it did not allow for a full analysis of the interior structure. Differential phase contrast imaging is proposed as a method of accessing the internal structure of the paired skyrmion object to enhance understanding of the modification of inter-skyrmion distance and its effect on the skyrmion structure. DPC is not a time resolved imaging technique however we identified defects with little or no movement during the experiment which would prove ideal candidates for performing DPC imaging.

Nucleation of skyrmion lattice defects as a result of disorder in the helical state was investigated briefly, capturing images of initial and final states. The hypothesis that increased helical disorder resulted in a higher probability of a high angle lattice boundary being present was supported by evidence, however, the mechanism and dynamics that cause this were not investigated. Investigating this phenomenon using the same experimental conditions as demonstrated in chapter 3 reveals how the disorder evolves between magnetic phase states.

The time resolution determined in chapter 5 may be optimised further. However, it is unlikely that the Medipix3 can reach a time resolution significantly faster than 100ns, and would require hardware changes in the future iterations of the device to achieve significant improvement. The following are proposed hardware changes identified during the course of these experiments which could contribute to lowering the maximum time resolution of the Medipix3 detector.

Firstly, the choice of silicon as the semiconductor material for production of electron-hole pairs could be replaced with an alternative semiconductor material. Materials such as GaAs or CdZnTe feature significantly higher atomic mass numbers. Therefore, the stopping distance for an electron would be significantly less and consequently the electron-hole pair distribution density would increase. Increasing the density of the electron-hole pair distribution would not only reduce the possibility of pixel-wise charge sharing, but could ultimately impact the time resolution. The voltage response from the CSA would be

compressed in time giving a shorter time response with an increased peak voltage.

The second proposed hardware change that could dramatically increase the time resolution of the Medipix3 is the option to trigger the pulse to counter using the rise of the CSA voltage above threshold rather than the current implementation which uses the CSA voltage decaying below threshold. The voltage response curve features a sharper rise time than fall time. Therefore, the variation in the triggered count time for two electrons with different charge distributions would be smaller if triggered as the voltage reached the threshold.

Finally, the stroboscopic imaging performed in this experiment was integrated to an image with a total exposure in the order of milliseconds. However, the total acquisition time, including gaptime, was significantly longer than this. The read time of the Medipix3 detector is 860μs, therefore the 50,000 image acquisitions performed for the threshold tests resulted in an image recording duration of 43 seconds. The trigger to readout the pixel counts could be frozen so that the full 50,000 frames become integrated into one image, while still only triggering electron counting events within the defined exposure times. The second benefit in only capturing the integrated image is that only one data set needs to be stored immediately after the acquisition, decreasing the overall data storage footprint compared to temporarily storing thousands of images.

If these changes were implemented, the Medipix3 device would potentially achieve significantly faster time resolutions than reported in this work. The ten to single nanosecond time regime is an important goal for electron detectors in TEM, as many macroscopic processes such as domain dynamics and propagation occur at those timescales. Therefore, realising pump-probe type imaging of nanosecond magnetic dynamics has gone from being impossible to achievable in the next iteration of Medipix-like devices.

In chapter 6 the time resolution tested reached a minimum of ten microsecond increments, however, the thermal response of the MEMS chip prevented investigation of the nanosecond capabilities suggested in chapter 5. Joule heating as a method of generating thermal energy in samples may continue to limit the investigation into thermal response. Laser induced heating using nanosecond lasers could provide the thermal change in future pump-probe

type experiments. The application of Medipix3 detectors in stroboscopic imaging DTEM instruments could reveal a whole field of research in the thermal responses of both magnetic and non-magnetic materials.

Bibliography

[1] Nakatania Y. Thiaville A. and Miltat J. Head-to-head domain walls in soft nano-strips: a refined phase diagram. *Journal of Magnetism and Magnetic Materials*, 290–291:750–753, 2005.

[2] Marrows C. H. Spin-polarised currents and magnetic domain walls. *Advances in Physics*, 54(8):585–713, 2005.

[3] Mougin A. et al. Domain wall mobility, stability and walker breakdown in magnetic nanowires. *EPL 78* (2007), 57007, doi:10.1209/0295-5075/78/57007.

[4] Kézsmárki I. et al. Neel-type skyrmion lattice with confined orientation in the polar magnetic semiconductor GaV_4S_8. *Nature Materials*, 14:1116–1122, 2015.

[5] Ballabriga R. et al. Characterization of the Medipix3 pixel readout chip. *Journal of Instrumentation*, 6(01):01052, 2011.

[6] DENSsolutions. Wildfire in situ tem heating. `http://denssolutions.com/products/wildfire`, 2017.

[7] Almeida T. P. et al. Preparation of high-quality planar ferh thin films for in situ tem investigations. *Journal of Physics: Conference Series*, 903, 2016.

[8] Jiles D. *Introduction to Magnetism and Magnetic Materials*. Chapman and Hall, CRC, 1995.

[9] Stoner E. C. Atomic moments in ferromagnetic metals and alloys with non-ferromagnetic elements. *Philosophical Magazine Series 7*, 15, 1933.

[10] Klaui M. Head-to-head domain walls in magnetic nanostructures. *Journal of physics: Condensed matter*, 20(31), 2008.

[11] Schryer N. L. and Walker L. R. The motion of 180° domain walls in uniform dc magnetic fields. *Journal of applied physics*, 45:5406, 1974.

[12] Beach G. S. D. et al. Dynamics of field-driven domain-wall propagation in ferromagnetic nanowires. *Nature materials*, 4:741, 2005.

[13] Leliaert J. et al. Thermal effects on transverse domain wall dynamics in magnetic nanowires. *Appl. Phys. Lett.*, 106:202401, 2015.

[14] Hayashi M. et al. Direct observation of the coherent precession of magnetic domain walls propagating along permalloy nanowires. *Nature Physics Letters*, 3:21–25, December 2006.

[15] Dzyaloshinsky I. A thermodynamic theory of "weak" ferromagnetism of antiferromagnetics. *Journal of Physics and Chemistry of Solids*, 4(4):241–255, 1958.

[16] Moriya T. Anisotropic Superexchange Interaction and Weak Ferromagnetism. *Phys. Rev.*, 120(1):91–98, 1960.

[17] Yamamoto K. et al. Interfacial Dzyaloshinskii-Moriya interaction and orbital magnetic moments of metallic multilayer films. *AIP Advances*, 7:056302, 2016.

[18] Mühlbauer S. et al. Skyrmion Lattice in a Chiral Magnet. *Science*, 323(5916):915–919, 2009.

[19] Neubauer A. et al. Topological Hall Effect in the A Phase of MnSi. *Phys. Rev. Lett.*, 102(18):186602, 2009.

[20] Munzer W. et al. Skyrmion lattice in the doped semiconductor. *Phys. Rev. B*, 81(4):041203, 2010.

[21] Milde P. et al. Unwinding of a Skyrmion Lattice by Magnetic Monopoles. *Science*, 340(6136):1076–1080, 2013.

[22] Yu X. Z. et al. Near room-temperature formation of a skyrmion crystal in thin-films of the helimagnet FeGe. *Nature Materials*, 10:106–109, 2011.

[23] Bode M. et al. Chiral magnetic order at surfaces driven by inversion asymmetry. *Nature*, 447(7141):190–193, 2007.

[24] Uchida M. Onose Y. Matsui Y. and Tokura Y. Real-Space Observation of Helical Spin Order. *Science*, 311(5759):359–361, 2006.

[25] Seki S. Yu X. Z. Ishiwata S. and Tokura Y. Observation of Skyrmions in a Multiferroic Material. *Science*, 336(6078):198–201, 2012.

[26] Ehlers D. et al. Skyrmion dynamics under uniaxial anisotropy. *Phys. Rev. B*, 94(1):014406, 2016.

[27] Je S. el al. Asymmetric magnetic domain-wall motion by the dzyaloshinskii-moriya interaction. *Phys. Rev. B*, 88:214401, 2013.

[28] Boulle O. et al. Domain wall tilting in the presence of the dzyaloshinskii-moriya interaction in out-of-plane magnetized magnetic nanotracks. *Phys. Rev. Lett.*, 111:217203, 2013.

[29] Skyrme T. H. R. A unified field theory of mesons and baryons. *Nuclear Physics*, 31:556–569, 1962.

[30] Fert A. Cros J. and Sampaio J. Skyrmions on the track. *Nature Nanotechnology*, 8:152–156, 2013.

[31] Yu X. Z. et al. Near room-temperature formation of a skyrmion crystal in thin-films of the helimagnet FeGe. *Nature Materials*, 10:106–109, 2011.

[32] Zhang S. L. et al. Room-temperature helimagnetism in FeGe thin films. *Scientific Reports*, 7(1):123, 2017.

[33] Romming N. et al. Field-Dependent Size and Shape of Single Magnetic Skyrmions. *Phys. Rev. Lett.*, 114(17):177203, 2015.

[34] Müller J. Magnetic Skyrmions on a Two-Lane Racetrack. *New Journal of Physics*, 19(2):025002, 2017.

[35] Zhang X. et al. Skyrmion-skyrmion and skyrmion-edge repulsions in skyrmion-based racetrack memory. *Scientific Reports*, 5:7643, 2015.

[36] Zhang X. Ezawa M. and Zhou Y. Magnetic skyrmion logic gates: conversion, duplication and merging of skyrmions. *Scientific Reports*, 5:9400, 2015.

[37] Xing X. Pong P. W. T. and Zhou Y. Skyrmion domain wall collision and domain wall-gated skyrmion logic. *Phys. Rev. B*, 94(5):054408, 2016.

[38] De Broglie L. Recherches sur la théorie des quanta. *Ann. de Physique*, 3(10):22, 1925.

[39] Williams D. B. and Carter C. B. *Transmission Electron Microscopy*. Springer US, 2 edition, 2009.

[40] Busch H. Über die Wirkungsweise der Konzentrierungsspule bei der Braunschen Röhre. *Arch. Elektrotech*, 18:583–594, 1927.

[41] Ruska E. The development of the electron microscope and of electron microscopy. *Reviews of Modern Physics*, 59:627–638, 1987.

[42] Kisielowski C. et al. Detection of single atoms and buried defects in three dimensions by aberration-corrected electron microscope with 0.5-Å information limit. *Microscopy and Microanalysis*, 14(5):469–477, 2008.

[43] Smith D. J. Progress and perspectives for atomic-resolution electron microscopy. *Ultramicroscopy*, 108(3):159–166, 2008.

[44] Fowler R. H. and Nordheim L. Electron emission in intense electric fields. *Proceedings of the Royal Society*, 119:173–181, 1928.

[45] Lobastov V. A. Srinivasan R. and A. H. Zewail. Four-dimensional ultrafast electron microscopy. *Proc. Natl. Acad. Sci. U.S.A.*, 102(20):7069–7073, March 2005.

[46] Brüche E. Elektronenmikroskopische Abbildung mit lichtelektrischen Elektronen. *Z. Phys*, 86(448), 1933.

[47] Barwick B. et al. Laser-induced ultrafast electron emission from a field emission tip. *New J. Phys*, 9(141), 2007.

[48] Berger J. A. et al. DC photoelectron gun parameters for ultrafast electron microscopy. *Microscopy and Microanalysis: The Official Journal of Microscopy Society of America, Microbeam Analysis Society, Microscopical Society of Canada*, 15(4):298–313, 2009.

[49] Rutherford E. The scattering of α and β particles by matter and the structure of the atom. *Philosophical Magazine*, 21:669–688, 1911.

[50] Aharonov Y. and Bohm D. Significance of electromagnetic potentials in the quantum theory. *Phys. Rev.*, 115:485–491, 1959.

[51] Dekkers N. H. and deLang H. Differential phase contrast in a STEM. *Optik*, 41:452–6, 1974.

[52] Dekkers N. H. and deLang H. A detection method for producing phase and amplitude images simultaneously in a scanning transmission electron microscope. *Philips Tech. Rev.*, 37:1–9, 1977.

[53] Chapman J. N. and Morrison J. Quantitative determination of magnetisation distribution in domains and domain walls by scanning transmission electron microscopy. *Journal of Magnetism and Magnetic Materials*, 35:253, 1983.

[54] Dekkers N. H. McVitie S. and McFadyen I. R. A detection method for producing phase and amplitude images simultaneously in a scanning transmission electron microscope. *Scanning Microscopy Supplement*, 1:221, 1987.

[55] Majert S. and Kohl H. High-resolution STEM imaging with a quadrant detector—Conditions for differential phase contrast microscopy in the weak phase object approximation. *Ultramicroscopy*, 148(Supplement C):81–86, 2015.

[56] Krajnak M. et al. Pixelated detectors and improved efficiency for magnetic imaging in STEM differential phase contrast. *Ultramicroscopy*, 165:42–50, 2016.

[57] McMullana G. Faruqi A. R. Clare D. and Henderson R. Comparison of optimal performance at 300 kev of three direct electron detectors for use in low dose electron microscopy. *Ultramicroscopy*, 147:156–163, 2014.

[58] Clough R. N. Moldovan G. and Kirkland A. I. Direct detectors for electron microscopy. *Journal of Physics: Conference Series*, 522(012046), 2014.

[59] McMullan G. Chen S. Henderson R. and Faruqi A. R. Detective quantum efficiency of electron area detectors in electron microscopy. *Ultramicroscopy*, 109(9):1126–1143, 2009.

[60] Milazzo A. et al. Characterization of a direct detection device imaging camera for transmission electron microscopy. *Ultramicroscopy*, 110(7):744–747, 2010.

[61] Sander B. Golas M. M. and Stark H. Advantages of CCD detectors for de novo three-dimensional structure determination in single-particle electron microscopy. *Journal of Structural Biology*, 151(1):92–105, 2005.

[62] Bammes B. E. Rochat R. H. Jakana J. and Chiu W. Practical performance evaluation of a 10k $\times$ 10k CCD for electron cryo-microscopy. *Journal of Structural Biology*, 175(3):384–393, 2011.

[63] Gamo K. Focused ion beam lithography. *Nuclear Instruments and Methods in Physics Research Section B*, 65:40–49, 1992.

[64] Lin J. et al. Polarization-Controlled Tunable Directional Coupling of Surface Plasmon Polaritons. *Science*, 340(6130):331–334, 2013.

[65] Lummen T. T. A. et al. Ultrafast imaging of plasmons in a transmission electron microscope. *SPIE OPTO*, 9746:974610, 2016.

[66] Lummen T. T. A. et al. Imaging and controlling plasmonic interference fields at buried interfaces. *Nature Communications*, 7:13156, 2016.

[67] Bogdanov A. N. and Rößler U. K. Chiral Symmetry Breaking in Magnetic Thin Films and Multilayers. *Phys. Rev. Lett.*, 87(3):037203, 2001.

[68] Tomasello R. et al. A strategy for the design of skyrmion racetrack memories. *Scientific Reports*, 4:6784, 2014.

[69] Sampaio J. et al. Nucleation, stability and current-induced motion of isolated magnetic skyrmions in nanostructures. *Nature Nanotechnology*, 8(11):839–844, 2013.

[70] Albert A. Vincent C. and João S. Skyrmions on the track. *Nature Nanotechnology*, 8(3):152–156, 2013.

[71] Xing X. Pong P. W. T. and Zhou Y. Skyrmion domain wall collision and domain wall-gated skyrmion logic. *Phys. Rev. B*, 94(5):054408, 2016.

[72] Rebei A. and Hohlfeld J. The magneto-optical Barnett effect: Circularly polarized light induced femtosecond magnetization reversal. *Physics Letters A*, 372(11):1915–1918, 2008.

[73] Bigot J. Y. Vomir M. Andrade L. H. F. and Beaurepaire E. Ultrafast magnetization dynamics in ferromagnetic cobalt: The role of the anisotropy. *Chemical Physics*, 318(1–2):137–146, 2005.

[74] van Kampen M. et al. All-Optical Probe of Coherent Spin Waves. *Phys. Rev. Lett.*, 88(22):227201, 2002.

[75] Boeglin C. et al. Distinguishing the ultrafast dynamics of spin and orbital moments in solids. *Nature*, 465(7297):458–461, 2010.

[76] Stamm C. et al. Femtosecond modification of electron localization and transfer of angular momentum in nickel. *Nature Materials*, 6(10):740–743, 2007.

[77] Beaurepaire E. Merle J. C. Daunois A. and Bigot J. Y. Ultrafast Spin Dynamics in Ferromagnetic Nickel. *Phys. Rev. Lett.*, 76(22):4250–4253, 1996.

[78] Zhou Y. et al. Dynamically stabilized magnetic skyrmions. *Nature Communications*, 6:8193, 2015.

[79] Wang W. et al. Driving magnetic skyrmions with microwave fields. *Phys. Rev. B*, 92(2):020403, 2015.

[80] Zhang S. et al. Current-induced magnetic skyrmions oscillator. *New Journal of Physics*, 17(2):023061, 2015.

[81] Mochizuki M. et al. Thermally driven ratchet motion of a skyrmion microcrystal and topological magnon Hall effect. *Nature Materials*, 13(3):241–246, 2014.

[82] DuttaGupta S. et al. Adiabatic spin-transfer-torque-induced domain wall creep in a magnetic metal. *Nature Physics*, 12(4):333–336, 2016.

[83] Lemerle S. et al. Domain Wall Creep in an Ising Ultrathin Magnetic Film. *Phys. Rev. Lett.*, 80(4):849–852, 1998.

[84] Cayssol F. et al. Domain Wall Creep in Magnetic Wires. *Phys. Rev. Lett.*, 92(10):107202, 2004.

[85] Krajnak M. et al. Pixelated detectors and improved efficiency for magnetic imaging in STEM differential phase contrast. *Ultramicroscopy*, 165:42–50, 2016.

[86] Shibata N et al. Differential phase-contrast microscopy at atomic resolution. *Nature Physics*, 8(8):611–615, 2012.

[87] Langner M. C. et al. Coupled Skyrmion Sublattices in Cu_2OSeO_3. *Phys. Rev. Lett.*, 112(16):167202, 2014.

[88] S. L. et al. Zhang. Multidomain Skyrmion Lattice State in Cu_2OSeO_3. *Nano Letters*, 16:3285–3291, 2016.

[89] H. Marayama M. Howe J. M. Hidaka and Takaki S. Atomic-level observation of disclination dipoles in mechanically milled, nanocrystalline Fe. *Science*, 29:2433, 2002.

[90] Yuan H. Y. and Wang X. R. Skyrmion creation and manipulation by nano-second current pulses. *Scientific Reports*, 6:22638, 2016.

[91] Wang C. et al. Enhanced stability of the magnetic skyrmion lattice phase under a tilted magnetic field in a two-dimensional chiral magnet. *Nano Lett.*, 17(5):2921–2927, 2017.

[92] Kleman M. and Friedel J. Disclinations, dislocations, and continuous defects: A reappraisal. *Rev. Mod. Phys.*, 80:61, 2008.

[93] Schoenherr P. et al. Topological domain walls in helimagnets. *Nature Physics*, 14:465–468, 2018.

[94] Rajeswari J. et al. Filming the formation and fluctuation of skyrmion domains by cryo-Lorentz transmission electron microscopy. *Proceedings of the National Academy of Sciences*, 112(46):14212–14217, 2015.

[95] Bragg L. and Nye J. F. A dynamical model of a crystal structure. *Proc. R. Soc. London, Ser. A*, 190(1023):474–481, 1947.

[96] Abd el Kader A.. and Earnshaw J. C. Stability of two-dimensional foam. *Philosophical Magazine A*, 76:1251–1260, 1997.

[97] Fukushima E. and Ookawa A. The transition structure of the grain boundary observed in soap bubble raft. *J. Phys. Soc. Jpn.*, 8:129–130, 1953.

[98] Fukushima E. and Ookawa A. Observation of the grain boundary in soap bubble raft part i. static feature of the grain boundary. *J. Phys. Soc. Jpn.*, 8(5):609–614, 1953.

[99] Fukushima E. and Ookawa A. Some characters of the soap bubble raft in a vibrating state. *J. Phys. Soc. Jpn.*, 10(11):970–981, 1955.

[100] Lahiri J. et al. An extended defect in graphene as a metallic wire. *Nature Nanotechnology*, 5(5):326–329, 2010.

[101] Liu L. Qing M. Wang Y. and Chen S. Defects in Graphene: Generation, Healing, and Their Effects on the Properties of Graphene: A Review. *Journal of Materials Science & Technology*, 31:599–606, 2015.

[102] Cervenka J. and Flipse C. F. J. The role of defects on the electronic structure of a graphite surface. *Journal of Physics: Conference Sees*, 61(1):190, 2007.

[103] Červenka J. Katsnelson M. I. and Flipse C. F. J. Room-temperature ferromagnetism in graphite driven by two-dimensional networks of point defects. *Nature Physics*, 5(11):840–844, 2009.

[104] Leonardo V. Heerema S. J. Dekker C. and Zandbergen H. W. Controlling Defects in Graphene for Optimizing the Electrical Properties of Graphene Nanodevices. *ACS Nano*, 9(4):3428–3435, 2015.

[105] Ophus C. Shekhawat A. Rasool H. and Zettl A. Large-scale experimental and theoretical study of graphene grain boundary structures. *Phys. Rev. B*, 92:205402, 2015.

[106] Okamura Y. Kagawa F. Seki S. and Tokura Y. Transition to and from the skyrmion lattice phase by electric fields in a magnetoelectric compound. *Nature Communications*, 7, 2016.

[107] Nord M. et al. Atomap: a new software tool for the automated analysis of atomic resolution images using two-dimensional gaussian fitting. *Advanced Structural and Chemical Imaging*, 3(1):9, 2017.

[108] Nappi C. et al. Current induced resistive state in fe(se,te) superconducting nanostrips. *Scientific Report*, 7:4115, 2017.

[109] Cohen L. F. and Jensen H. J. Open questions in the magnetic behaviour of high-temperature superconductors. *Rep. Prog. Phys.*, 60:1581, 1997.

[110] Ewing J.A. *Philosophical Transactions*, 176:569, 1885.

[111] Matsumoto T. et al. Jointed magnetic skyrmion lattices at a small-angle grain boundary directly visualized by advanced electron microscopy. *Scientific Reports*, 6:35880, 2016.

[112] Matsumoto T. et al. Direct observation of $\sum 7$ domain boundary core structure in magnetic skyrmion lattice. *Science Advances*, 2(2):1501280, 2016.

[113] Li Z. et al. Magnetic Skyrmion Formation at Lattice Defects and Grain Boundaries Studied by Quantitative Off-Axis Electron Holography. *Nano Letters*, 17(3):1395–1401, 2017.

[114] Dussaux A. et al. Local dynamics of topological magnetic defects in the itinerant helimagnet FeGe. *Nature Communications*, 7:12430, 2016.

[115] Milde P. et al. Unwinding of a skyrmion lattice by magnetic monopoles. *Science*, 340(6136):1076–1080, 2013.

[116] Anderson P. W. Theory of flux creep in hard superconductors. *Phys. Rev. Lett.*, 9:309–311, 1962.

[117] Kittel C. *Introduction to Solid State Physics*. Wiley, Hoboken, New Jersey„ 8 edition, 2004.

[118] Llopart X. et al. Medipix2: A 64-k pixel readout chip with 55- mu;m square elements working in single photon counting mode. *IEEE Transactions on Nuclear Science*, 49(5):2279–2283, 2002.

[119] Scholze F. Rabus H. and Ulm G. Mean energy required to produce an electron-hole pair in silicon for photons of energies between 50 and 1500 eV. *Journal of Applied Physics*, 84(5):2926–2939, 1998.

[120] Drouin D. et al. CASINO V2.42—A Fast and Easy-to-use Modeling Tool for Scanning Electron Microscopy and Microanalysis Users. *Scanning*, 29(3):92–101, 2007.

[121] Ballabriga R. *The Design and Implementation in 0.13µm CMOS of an Algorithm Permitting Spectroscopic Imaging with High Spatial Resolution for Hybrid Pixel Detectors*. PhD thesis, Universitat Ramon Llull, 2010.

[122] Fallot M. Alloys of iron with the metals of the platinum group. *Ann. Phys.*, 10:291–332, 1938.

[123] Kouvel J. S. and Hartelius C. C. Anomalous Magnetic Moments and Transformations in the Ordered Alloy FeRh. *Journal of Applied Physics*, 33(3):1343–1344, 1962.

[124] Le Graët C. et al. Sputter growth and characterization of metamagnetic B2-ordered FeRh epilayers. *Journal of Visualized Experiments: JoVE*, 5(80):50603, 2013.

[125] Kittel C. Model of exchange-inversion magnetization. *Phys. Rev.*, 120:335, 1960.

[126] Gruner M. E. Hoffmann E. and Entel P. Instability of the rhodium magnetic moment as origin of the metamagnetic phase transition in α-FeRh. *Phys. Rev. B*, 67:064415, 2003.

[127] Gu R. Y. and Antropov V. P. Dominance of the spin-wave contribution to the magnetic phase transition in FeRh. *Phys. Rev. B*, 72:012403, 2008.

[128] Chua L. Memristor-The missing circuit element. *IEEE Transactions on Circuit Theory*, 18(5):507–519, 1971.

[129] Chua L. Memristor, Hodgkin–Huxley, and Edge of Chaos. *Nanotechnology*, 24(38):383001, 2013.

[130] Strukov D. B. Snider G. S. Stewart D. R. and Williams R. S. The missing memristor found. *Nature*, 453(7191):80–83, 2008.

[131] Nikitin S. A. et al. The magnetocaloric effect in Fe49rh51 compound. *Physics Letters A*, 148(6):363–366, 1990.

[132] Liu Y. et al. Large reversible caloric effect in FeRh thin films via a dual-stimulus multicaloric cycle. *Nature Communications*, 7(11614), 2016.

[133] Manekar M. and Roy S. B. Reproducible room temperature giant magnetocaloric effect in Fe–Rh. *Journal of Physics D*, 41(19):192004, 2008.

[134] Randolph S. J Fowlkes J. D. and Rack P. D. Focused, nanoscale electron-beam-induced deposition and etching. *Critical Reviews in Solid State and Materials Sciences*, 31:55–89, 2006.

[135] Furuya K. Nanofabrication by advanced electron microscopy using intense and focused beam. *Sci Technol Adv Mater*, 9(1):014110, 2008.

[136] Beacham R. J. *pplication and development of advanced Lorentz microscopy techniques for the study of magnetic nanostructures*. PhD thesis, University of Glasgow, 2013.

[137] McLaren M. J. *Transmission Electron Microscope Characterisation of Iron-Rhodium Epilayers*. PhD thesis, University of Leeds, 2014.